UNIVERSITY OF OKLAHOMA

GRADUATE COLLEGE

DEVELOPMENT OF A NOVEL APPARATUS TO DETERMINE THE MULTIAXIAL TENSILE FAILURE CRITERIA FOR ULTRA-HIGH PERFORMANCE CONCRETES

A DISSERTATION

SUBMITTED TO THE GRADUATE FACULTY

in partial fulfillment of the requirements for the

Degree of

DOCTOR OF PHILOSOPHY

By

TREVOR JAY LOONEY
Norman, Oklahoma
2021

DEVELOPMENT OF A NOVEL APPARATUS TO DETERMINE THE MULTIAXIAL TENSILE FAILURE CRITERIA FOR ULTRA-HIGH PERFORMANCE CONCRETES

A DISSERTATION APPROVED FOR THE
SCHOOL OF CIVIL ENGINEERING AND ENVIRONMENTAL SCIENCE

BY THE COMMITTEE CONSISTING OF

Dr. Jeffery S. Volz, Chair

Dr. Royce Floyd

Dr. Kanthasamy Muraleetharan

Dr. Chris Ramseyer

Dr. Shideh Shadravan

ABSTRACT

The use of ultra-high performance concrete (UHPC), a stronger and more durable class of concrete, has increased in recent years. Large-scale production has been limited due to the cost of proprietary UHPC products, but the development of less expensive, non-proprietary mix designs has the potential to change that. However, this material has much larger tensile strengths than conventional concrete, in large part due to the presence of steel fibers. The traditional concrete analysis and design method of ignoring tensile strength would be overly conservative and would not accurately predict behavior. Therefore, there is a need to understand the multiaxial tensile behavior of UHPC to facilitate creating accurate analysis models and design guidelines.

The purpose of this research was to develop a novel apparatus with the ability to conduct triaxial tension, biaxial tension, and tension-tension-compression testing on UHPC cube specimens. Once the apparatus, the Looney Bin, was designed and fabricated, trial tests were conducted for each of the stress conditions to develop test procedures. Then, a comprehensive set of multiaxial tension data was collected on a non-proprietary UHPC mixture with fiber contents of 0%, 1%, 2%, 4%, 5%, and 6% fibers by volume. The collected data showed that the triaxial tension strength was approximately 6.2% of the uniaxial compressive strength for fiber contents ranging from 1% to 4% and was approximately 5.8% for 0% fibers. Also, exponential decay functions were fitted to the tension-tension-compression data to estimate the reduction in compressive strength as the applied tension in two orthogonal directions increases.

Lastly, the finalized multiaxial dataset was combined with previously published data encompassing the compression end of the failure surface for curve fitting. Nonlinear

regression analyses were conducted to fit two separate failure surface functions to the combined dataset. Arbitrary parameters were determined for each general equation that provided the best fit to the combined dataset. The fitted equations could be implemented in analysis models to more accurately predict the strength and behavior of full-scale UHPC structural elements.

ACKNOWLEDGMENTS

I first would like to thank my advisor, Dr. Jeffery Volz. Working with him again for my dissertation has been a tremendous pleasure. I very much appreciated his advice when I felt stuck on a problem and his patience when I was frustrated with setbacks. I certainly could not have developed the Looney Bin without his guidance. Even though he is my academic advisor, I will always consider him a dear friend.

I would also like to thank Mike Schmitz for all of his help in the development of the Looney Bin. Making this test setup would not have been possible without his fabrication expertise and his amazing problem-solving skills. On top of all that, he was a great guy to work and hang out with. I truly enjoyed getting to know him through the years and I wish him all the best on his very well-earned retirement.

I would like to thank my committee members for taking the time to read this lengthy tome and for providing valuable comments for its improvement.

I would like to thank all of the students I had the pleasure of working with and teaching throughout the years. They really made my time as a Ph.D. student special, and I enjoyed watching them grow as engineers. This was my first experience watching students I taught continue on to do research with me. It was a unique pleasure to help them throughout their academic career and to hear their thanks for that help. A special thanks to Steve Roswurm for being one of the few people crazy enough to be at the lab near constantly with me. I have truly enjoyed our friendship.

I want to thank John Bullock for joining our team at OU for my final year here. It was awesome having him back in the lab, just like old times. I could not think of a better way to finish my time at OU than hanging out with John!

I cannot thank my family enough for their continued support no matter how many times I decided to go back to school. I would not be the man I am today without my parents, Scott and Traci Beckham. All of my accomplishments were possible because of them.

Last, I want to thank my wife, Krista. Words cannot express how much I appreciate having her in my life. I would never have been able to finish this massive undertaking without her. She sat through countless hours of me complaining and reasoning through all of my work, and most of the good ideas in my research came from these conversations. Her willingness to listen as I verbalized my frustrations was nothing short of superhuman. She is the cornerstone of my life and I would be lost without her. Thanks to her help, I was somehow able to make my research “sciency enough.” I love you, Krista, and I can’t wait to see what life brings us next!

TABLE OF CONTENTS

LIST OF ILLUSTRATIONS

LIST OF TABLES

1. INTRODUCTION

1.1. BACKGROUND AND JUSTIFICATION

Conventional concrete is one of the most widely used structural materials in the world. It is a cost-effective construction material that is relatively easy to make, transport, and place. However, conventional concrete has its limitations when it comes to strength gain and durability. There is currently a large effort in the research community to mitigate these issues. One such solution to both issues was the creation of a unique new class of concrete, referred to as ultra-high performance concrete (UHPC). The enhanced mechanical and durability properties of UHPC make a strong case for this material replacing or at least augmenting conventional concrete construction.

UHPC differs from conventional concrete in a number of distinct ways. Where conventional concrete utilizes large volumes of coarse aggregate, UHPC does not use any. The largest aggregate size in UHPC is typically less than 0.05 in. in diameter. Due to the lack of coarse aggregate, UHPC has a much larger volume of cementitious material than conventional concrete. Also, UHPC typically has a much lower water-to-cementitious material ratio (*w/cm*) than conventional concrete. The *w/cm* ratio is typically less than 0.25. Finally, steel fibers are typically added to the cementitious matrix to improve post crack behavior. The Federal Highway Administration (FHWA) also states that UHPC should have uniaxial compressive strengths over 21.7 ksi and post-crack tensile strengths of at least 0.72 ksi (Haber et al., 2018).

UHPC has been implemented in numerous applications in the United States for several decades. The most common use thus far has been as a precast deck panel connection material in bridges due to the high cost of the material (e.g., Russell and

Graybeal, 2013; Graybeal, 2019). Another common use for UHPC has been for bridge deck overlays due to its excellent durability performance (e.g., Haber et al., 2017; Wibowo and Sritharan, 2018). Also, precast columns have been connected to precast concrete footings by inserting column longitudinal bars extending out of the column into formed pockets filled with UHPC (Graybeal, 2016). There have also been large-scale uses in bridges in Iowa and Virginia where the bridges were constructed using UHPC bulb-tee bridge girders (Russell and Graybeal, 2013). Currently, the Precast Concrete Institute (PCI) is developing design guidance for using UHPC in precast, prestressed elements to facilitate future design and increase the use of UHPC in construction of precast bridge and building structural members (eConstruct-WJE-UNL-NCSU, 2020).

1.1.1. Concerns with UHPC

With the creation of any new structural material comes the complications of incorporating that material without major changes to current construction practices. Ideally, UHPC would be used as a direct replacement of conventional concrete for all structural applications. However, due to the lack of awareness and knowledge of UHPC, it cannot currently directly replace conventional concrete. While there have been recent studies examining the fresh and hardened properties of UHPC (Haber et al., 2018), the high cost of commercially available UHPC products inhibits its use in large-scale structural applications. There have also been studies evaluating the performance of non-proprietary UHPC mix designs meant to reduce the cost, with results showing comparable performance to proprietary products (e.g., Wille and Boisvert-Cotulio, 2013; Looney et al., 2019; Looney et al., 2020).

1.1.2. Reasons for Varying Fiber Content

A large part of the expense related to UHPC lies in the steel fiber content. Steel fibers are added to UHPC to increase the post-cracking flexural strength, as well as to reduce shrinkage and creep. However, steel fibers are very expensive and drastically increase the cost of any concrete mix design. While 2% fibers by volume is the most common fiber percentage used, such a large quantity may not be required for adequate performance. Reducing steel fiber contents for certain applications could help reduce the cost of UHPC while maintaining many of its benefits.

1.1.3. Roadblocks to Accurate Analysis

An added complication of changing the fiber content is altering the material's structural response. There have been studies conducted showing existing models work reasonably well at predicting the behavior of UHPC in typical structural applications when using 2% fibers by volume (Kwak et al., 2009; Chen and Graybeal, 2012). However, there are few studies evaluating the behavior and failure surface of UHPC at different fiber contents, and none are very thorough (Wille et al., 2014; Savino et al., 2018). Without an understanding of the material's behavior at different fiber contents, particularly under multiaxial stress states, alterations to the fiber content are less likely for most structural applications.

1.2. OBJECTIVES AND SCOPE OF WORK

The objective of this study was to evaluate the failure surface of UHPC with different fiber contents using a novel, multiaxial tension test setup with the ability to apply tension forces in three orthogonal directions simultaneously. A non-proprietary

UHPC mix design developed at the University of Oklahoma was used as the base mixture, and the fiber contents were varied to evaluate changes in the failure surface. The fiber percentages evaluated were 0, 1, 2, 4, 5, and 6% by volume. These fiber contents were chosen to mirror a similar study evaluating other fresh and hardened properties of this mix design that was conducted in tandem with this study.

1.3. RESEARCH PLAN

The research plan focused on the goal of developing the multiaxial failure surface for UHPC at various fiber percentages. To that end, the first step was the development of a novel test apparatus. The test setup was designed to be easily maneuvered by one person, easily deconstructed to accommodate quick turnover for testing, able to test a standard concrete specimen size with the ability to be easily altered to accommodate different specimen sizes, and able to apply compressive forces in one direction by a separate load frame while simultaneously applying tensile forces in the other two directions. The apparatus was meant to test for triaxial tension, biaxial tension, and tension-tension-compression stress conditions.

Once the apparatus was designed, the individual components were fabricated and trials were conducted on UHPC specimens. A load cell coupling nut was constructed and calibrated to use the program LabVIEW^{TM} to track load applied by the apparatus and fixtures during testing. Different epoxies were evaluated during these trial tests for their bond strength between the fixture and the concrete specimen. The trial process was also used to develop test methods for each stress condition evaluated.

Once the test methods were determined, the non-proprietary UHPC mix design was adjusted to accommodate the fiber percentages to be studied. Then, a minimum of ten data points were collected for each of the fiber contents evaluated. The data points encompassed all three stress conditions the apparatus was designed to test and each data point was the average of at least two individual tests. Statistical limitations were developed to determine outliers in replicate tests for each fiber content and stress condition. In addition to the stress values at failure, a study of failure morphology was also undertaken in order to better understand the behavior of UHPC and verify the robustness of the data.

Once the data was finalized, literature was evaluated to add to the data collected in this study for the development of a complete failure surface. Different published failure surface equations were chosen to be fit to the finalized dataset. Nonlinear regression analyses were conducted using MATLAB to determine the arbitrary parameters of each equation that created the best fit. Once the fit was determined for each equation, they were plotted in two and three dimensions for comparison of shapes and estimation of uniaxial and multiaxial tensile strengths.

1.4. OUTLINE

This dissertation consists of eight chapters and one appendix. Chapter 1 briefly explains the characteristics, benefits, and concerns of UHPC, as well as the study's objective and the manner in which the objectives were attained.

Chapter 2 details a literature review conducted to evaluate previously published mix designs, uniaxial and biaxial UHPC testing, concrete failure models, examples of UHPC use in construction, and the reasoning for the need of this study.

Chapter 3 details the UHPC mix design used for each of the fiber percentages, specimen curing methods, and fresh and hardened properties.

Chapter 4 details the development of the novel test apparatus, including describing the initial concept, design of each fixture associated with the apparatus, developing the data collection method, and finalizing the test method.

Chapter 5 details the finalized test procedures for each stress condition tested, explains how the raw data was processed, and discusses the troubleshooting process for the tension-tension-compression test.

Chapter 6 details the collection, evaluation, and statistical analysis of the collected data, as well as including detailed evaluations of failed specimens from each of the fiber contents and test methods to better understand failure of UHPC subjected to multiaxial tensile stresses.

Chapter 7 focuses on finding trends in the data collected, adding the collected data to previously published data, and finally using the entire dataset for nonlinear regression of the failure equations considered.

Chapter 8 restates the findings that were established during the course of this study and presents conclusions and recommendations.

2. LITERATURE REVIEW

2.1. ULTRA-HIGH PERFORMANCE CONCRETE MIX DESIGN

There have been numerous studies outlining the design of non-proprietary UHPC mix designs. Wille and Boisvert-Cotulio (2013) conducted a study developing various UHPC mix designs using materials in the Northern United States to facilitate use of the material by contractors. The researchers evaluated mixes containing various cements, silica fumes, supplementary cementitious materials, and fine sands. The weight ratios for the constituents were set to 1:0.25:0.25 for cement:silica fume:supplementary cementitious material, 0.25 maximum water-to-cementitious material ratio, 1.0-2.0 for aggregate:cement, and 1.0-2.0% fibers by volume. The researchers first determined an optimum cementitious paste, then aggregates were introduced to the paste, lastly the fibers were evaluated to improve ductility and tensile strength. The final mix design cost approximately $850 per cubic yard and utilized a Type II/V cement, silica fume, fly ash, basalt fine aggregate, and 1.5% fibers by volume (Wille and Boisvert-Cotulio, 2013).

Later, a similar study at the University of Arkansas was conducted using locally available materials (Alsalman et al., 2017). The available cementitious materials consisted of Type I cement, silica fume, and Class C fly ash. Three types of natural sand, ranging in size, were used as aggregate sources. The steel fiber content was set to 3% by volume and a carboxylate high range water reducer was used. Three separate total paste contents were maintained while proportions of the silica fume and fly ash were varied to find the optimum ratios. Cube compressive strengths were used to evaluate the effectiveness of the mix designs. The final mix design was able to achieve a compressive strength of 22.5 ksi (155 MPa) at 90 days. The silica fume content was set to 10% of the

total cementitious content since no significant gain was observed at higher contents. The fly ash content was set to 20% of cementitious material since higher contents appeared to have a detrimental effect on compressive strength (Alsalman et al., 2017).

The University of Oklahoma also conducted a study to develop a UHPC mix design using locally available materials (Looney et al., 2019). A comprehensive study was conducted evaluating Type I/II and Type III cement, different proportions of supplementary cementitious materials such as silica fume, fly ash, and slag cement, various water-to-cementitious materials ratios, natural river sands at various proportions, and the effect of particle packing using the Andreasen and Anderson model (Funk and Dinger, 1994). A target flow was set to 7.5 in. to maintain fiber suspension. The mix development study was narrowed down to three mixes that had the highest strength while maintaining the target flow. The most effective mix design contained cementitious material consisting of 60% Type I/II cement, 30% slag cement, and 10% silica fume by weight, an aggregate-to-cement ratio of 1:1 by weight, a water-to-cementitious material ratio of 0.2, and fiber content of 2% by volume (Looney et al., 2019).

More recently, a UHPC mix design template was developed by El-Tawil et al. (2020). The authors establish an "open-recipe UHPC" that provided guidance on what constituents to add to the mix design and how to mix the constituents. The cementitious material consisted of a half-and-half mixture of slag cement and Type I cement. The cement must have a C_3A content of less than 8%. The UHPC mixture also used silica fume that was approximately 20% of the total cementitious content by weight. A fine and coarse silica sand were also used. Several mixture designs were developed with water-to-cementitious material ratios ranging from 0.16 to 0.17. Steel fibers were dosed at 2% by

volume. The published mix designs were stated to reach 28 ksi without applying heat curing. The cost of these mixtures were estimated to range from $726 to $856 per cubic yard when using domestically sourced materials (El-Tawil et al., 2020).

2.2. UNIAXIAL TENSION TESTING

Uniaxial tension testing is the simplest method for obtaining tension behavior of structural materials. In conventional reinforced concrete design, the tension strength of the concrete is ignored since it is negligible when compared to the overall strength of the member. However, the increased compressive strength of UHPC, coupled with the addition of steel fibers, provides enough tension strength to significantly increase a UHPC member's overall strength. Unfortunately, there has not been a widely adopted, standardized test method or specimen geometry established for determining the direct tension strength of concrete.

Researchers at the Federal Highway Administration (FHWA) have developed a new tension test setup to determine direct tension constitutive behavior through testing prisms (Graybeal and Baby, 2013). The researchers initially referenced ASTM E8/E8M (2009) to establish a specimen cross section. However, the specimen outlined in the ASTM was modified from a tapered section to a straight prismatic section due to the complications tapering caused when casting the UHPC specimen, as well as to reduce stress concentrations. To facilitate gripping, aluminum plates were glued to the two opposite, formed sides. The aluminum plates were tapered to alter the stress transfer to the UHPC specimen in a way that would increase the likelihood of failure occurring near the center of the prism. The displacement was also measured on all four sides to capture

any non-uniform cracking behavior throughout testing. The specimen ends were clamped at the glued aluminum ends to apply loads. A specimen in the test setup is shown in Figure 2.1.

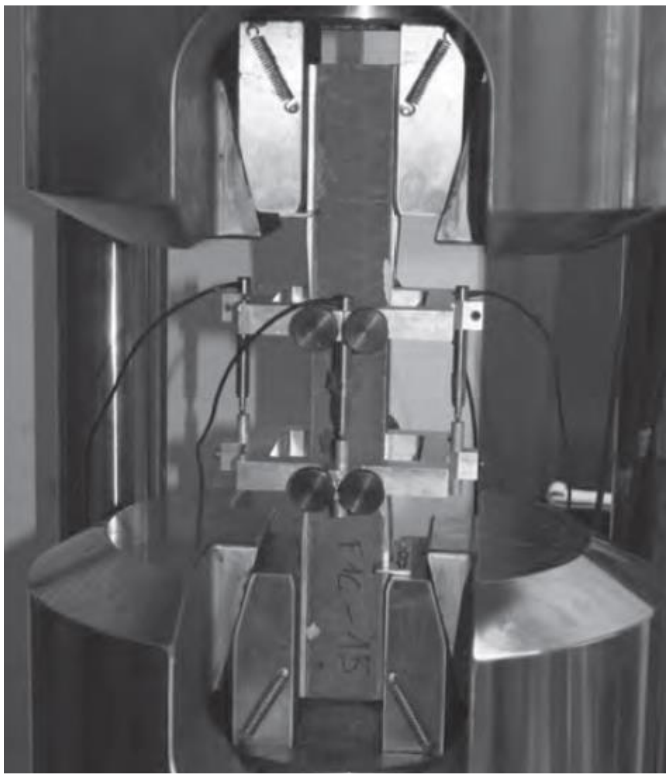

Figure 2.1 – Prism specimen in test setup (Graybeal and Baby, 2013)

Two specimen lengths were evaluated: 12 in. and 17 in. The aluminum plate length and gauge length for the 12 in. specimen were 4.5 in and 3 in., respectively. The aluminum plate length and gauge length for the 17 in. specimen were 10.25 in and 4 in., respectively. The aluminum plates were 0.188 in. where they were gripped within the test setup. Load was applied at a deflection rate of 0.0001 in./s until a limit strain of 25,000 με or the stress was transferred to a crack outside of the gauge length. After conducting

trials of tests using various mixes with different fiber types and lengths with each of the specimen lengths, the researchers were able to obtain direct tension strength data including modulus, initial crack strength, and post cracking behavior with each of the specimen lengths. However, the longer specimen was recommended to increase the likelihood the crack would initiate within the gauge length (Graybeal and Baby, 2013).

Another study evaluating new direct tension test specimen types for UHPC considered multiple different test setups and specimen cross sections (Wille et al., 2014). A comprehensive examination of different specimen geometries and load application methods was conducted to determine which may provide the most accurate results. The geometries considered included dogbone, unnotched prisms and cylinders, and notched prisms and cylinders. The load application methods included friction clamping, end anchored, side friction grip, end glued, side glued, and several combinations thereof. The researchers noted that end glued specimens were not adequate for capturing post-crack and strain hardening behavior due to the weak bond of the glue to the end caps, where failure tended to occur first. Also, notched specimens were not considered ideal due to stress concentrations that occur with abrupt changes in geometry, resulting in inaccurate tension strengths. Further, the dogbone specimens evaluated all had large ends to force failure in a specific area, long center portions of consistent cross section, and smooth cross section transitions. After evaluating the different specimens and test setups used by past studies, the researchers chose a specimen that met the following criteria: small specimens that were easy to cast, demold, and align in the test setup, had a constant cross section in the center gauge length, were not glued to ensure no bond failures, and were

easily aligned during testing. The final specimen and test setup chosen is shown in Figure 2.2.

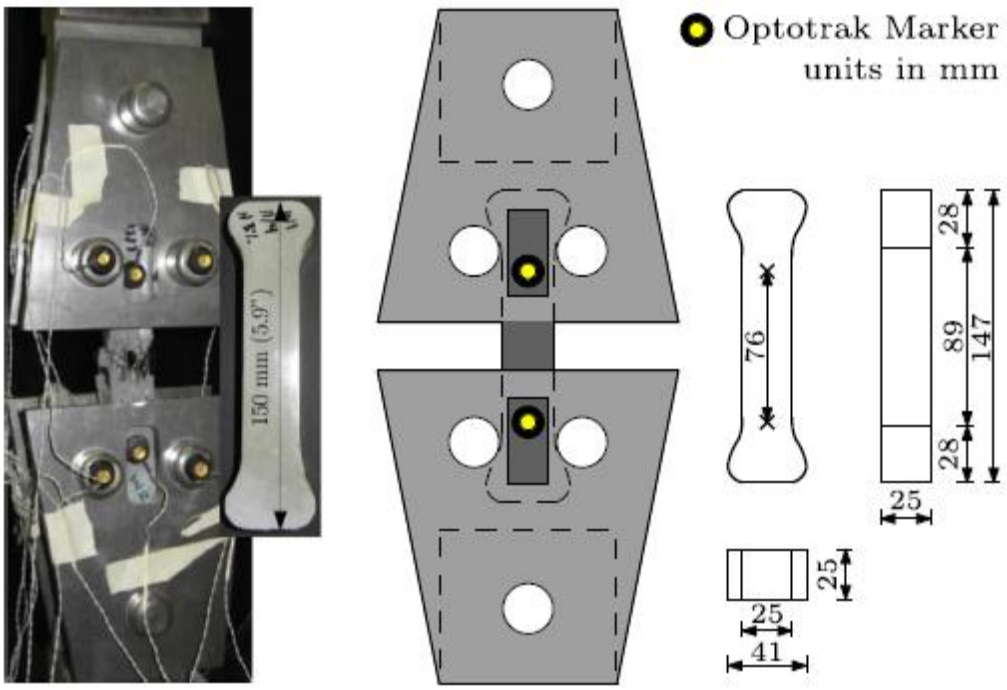

Figure 2.2 – Optimized specimen geometry chosen for trials (dimensions in mm) (Wille et al., 2014)

The load rate of this test was set to 0.025 in./min. Using this test setup, UHPC mixes with three different fiber types at various fiber percentages were tested to develop standard uniaxial constitutive models. Figure 2.3 shows the bilinear failure models established using the collected data for each of the fiber types (Wille et al., 2014).

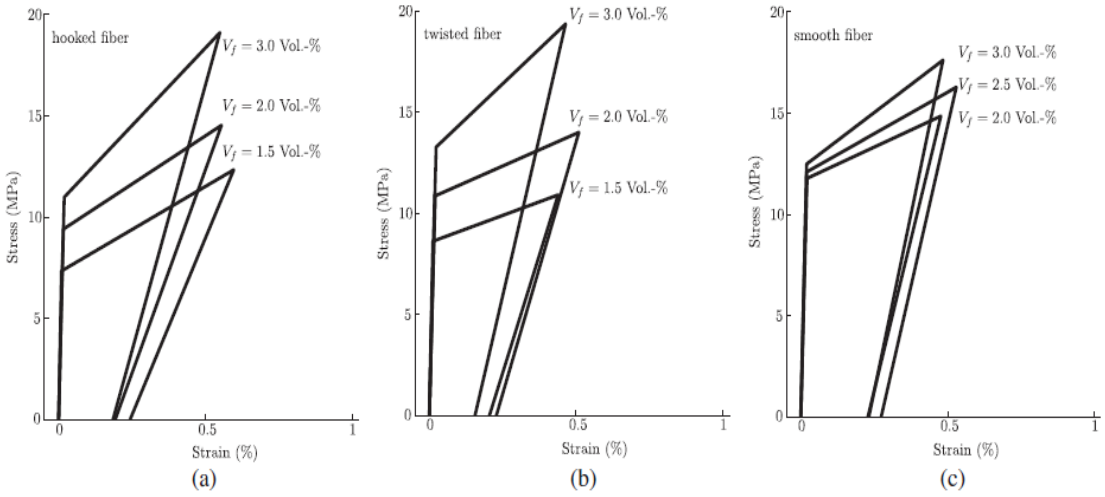

Figure 2.3 – Bilinear uniaxial models for (a) hooked fibers, (b) twisted fibers, and (c) straight fibers (Wille et al., 2014)

The tensile behavior of fiber reinforced UHPC was also recently tested using rectangular dogbone specimens by Savino et al. (2018). Three different commercially available UHPC blends were tested, and each used different fiber types and volumes similar to the studies discussed previously, as shown in Figure 2.4. The volume for Mix *a* was 1.7%, Mix *b* was 2.5%, and Mix *c* was 3.8% by volume (Savino et al., 2018).

Figure 2.4 – Fiber types used in mix a, b, and c (Savino et al., 2018)

The direct tension test used a dogbone specimen that was clamped at each end with ends that were free to rotate to allow for load alignment. Square aluminum plates were glued to the ends of the specimen to facilitate testing. The load was applied at a deflection rate of 0.002 in./min. and the strains were determined from 3 in. strain gauges attached to each of the wide faces of the specimen. The specimen and test setup are shown in Figure 2.5 (Savino et al., 2018).

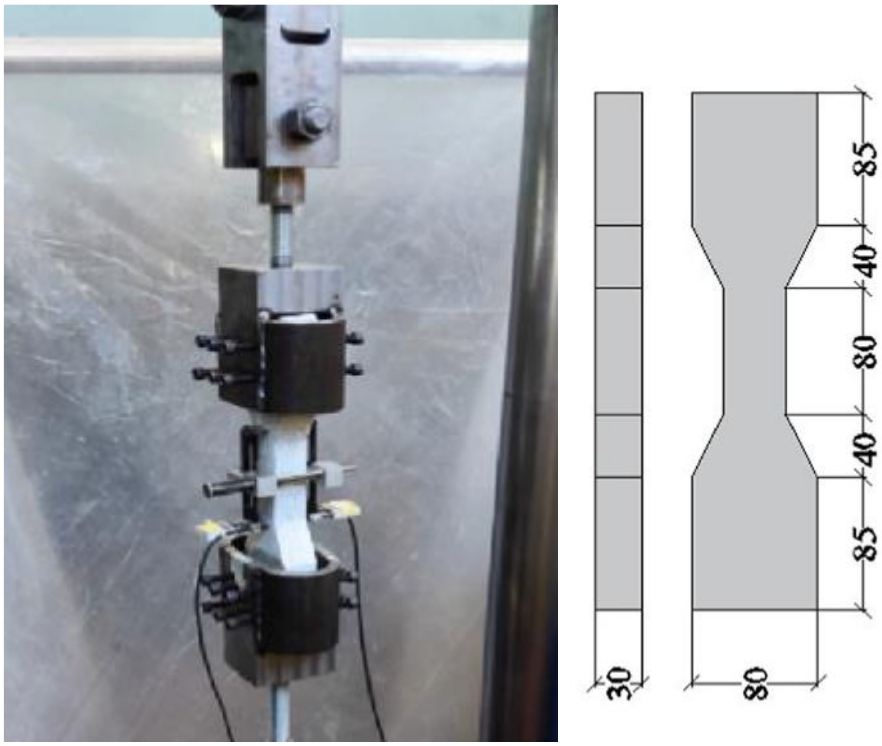

Figure 2.5 – Dogbone test specimen (dimensions in mm) (Savino et al., 2018)

The study was conducted to develop a composite material theory-based model to estimate flexural test results using results of direct tension test. The authors identified a change in behavior based on fiber content. At a fiber content above the critical content, the specimens exhibit increased post-cracking strength. At a level below that critical

content, a softening behavior occurs. The equation for calculating that critical content in direct tension is presented as Equations 2.1. The developed model highlights two different behaviors of UHPC in tension, shown in Figure 2.6, based on their fiber content. (Savino et al., 2018).

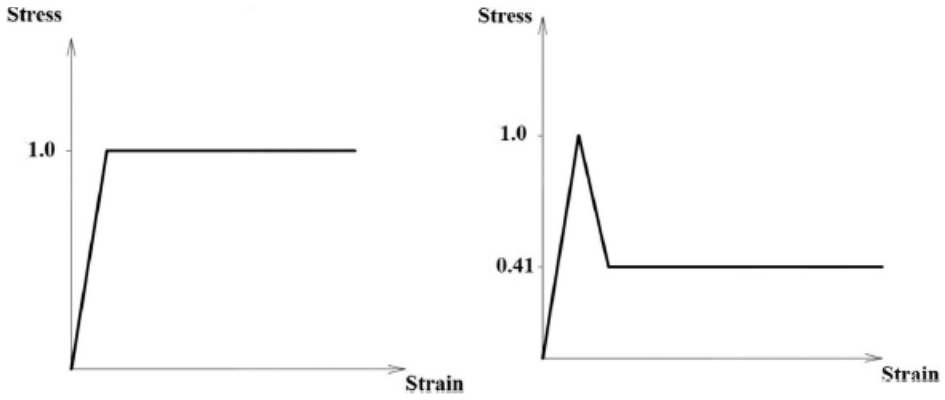

Figure 2.6 – Tensile constitutive models based on fiber contents above (left) and below (right) the critical fiber content (Savino et al., 2018)

$$V_{f,crit} = \frac{\sigma_{mu}}{\sigma_{fu} - E_f \varepsilon_{mu}} \quad \textbf{(2.1)}$$

Where $V_{f,crit}$ is the critical fiber content, σ_{mu} is the unreinforced UHPC ultimate tensile strength, σ_{fu} is the fiber ultimate tensile strength, E_f is the steel fiber modulus of elasticity, and ε_{mu} is the strain at which σ_{mu} occurs. If the fiber volume is kept above that critical volume, increased post-cracking strength would be expected in that specimen (Savino et al., 2018).

Recently, researchers at the University of Oklahoma evaluated the effect of various steel fiber contents on the direct tension strength of a UHPC mix design

developed at the university (Lepissier, 2020). For this testing, the researchers designed a dogbone specimen with a circular geometry that was 15 in. long with an end diameter of 3 in. and a center diameter of 2 in. The dogbone specimen is shown in Figure 2.7.

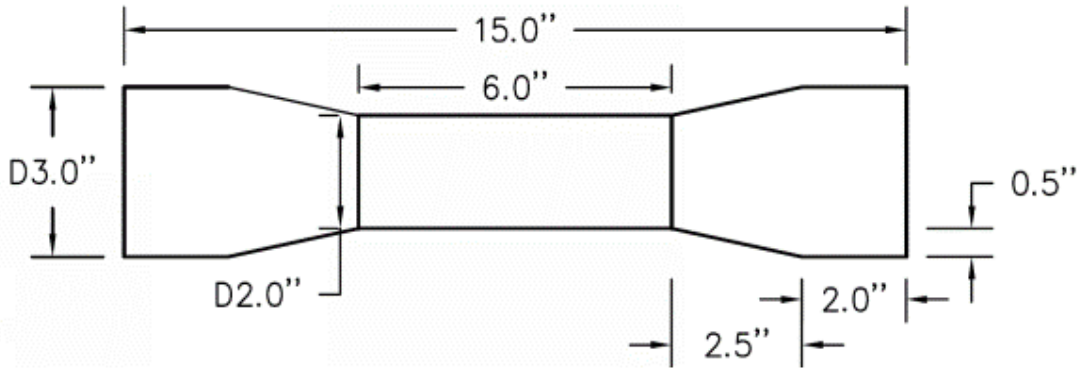

Figure 2.7 – Cylindrical dogbone specimen (Lepissier, 2020)

The load was applied through aluminum end caps that were epoxied to the 3 in. diameter ends of the specimens 24 hours prior to testing. The aluminum clamps were then fixed to the load-controlled testing machine by clamping to ensure no rotation of the ends was permitted upon crack development. Displacement measurements were obtained using linear variable differential transformers (LVDTs) that were place diametrically opposite from each other on the 2 in. diameter length in an effort to capture the deflection pre- and post-crack. Failed specimens with different crack patterns are shown in Figure 2.8.

Figure 2.8 – Failed specimens with a single crack (left) and multiple cracks (right) (Lepissier, 2020)

Direct tension testing was conducted on specimens with 0, 1, 2, 4, and 6% steel fibers by volume. The fibers used in this study were Dramix® OL 0.2/13 steel fibers. The researchers noted that, as the fiber percentage increased up to 4%, the tension strength also increased. There was a drop in tension strength at the 6% fiber dosage. Also, strain plateau was observed with up to 2% fibers, with 4 and 6% fibers not exhibiting any additional post crack strength (Lepissier, 2020).

The researchers also conducted a strain distribution study on three different specimen geometries to determine which specimen had the lowest level of stress concentrations. The geometries evaluated were the dogbone specimen used for the fiber content study, a 2 in. diameter, 4 in. long standard cylinder with load application similar to the dogbone specimen, and a prismatic section similar to the one that was developed by Graybeal and Baby (2013) in both geometry and loading mechanism. Strains were

measured by attaching 6 mm (0.24 in.) strain gauges directly to the surface of the specimens. For the cylindrical specimens, four strain gauges were spaced evenly around the diameter where the failure was anticipated, with the dogbone specimens having an additional four strain gauges applied near the bevel to evaluate the potential for stress concentrations at those locations. The prismatic specimen had strain gauges applied in the center and on one edge of each face to evaluate the strain change at corners. The strain gauge locations are shown in Figure 2.9.

Figure 2.9 – Strain gauges applied to the dogbone (left), cylinder (middle), and prismatic (right) specimens (Lepissier, 2020)

The strain distributions determined from testing were then compared to a finite element analysis of each specimen conducted in the program ANSYS©. The strain distributions from both the analytical and experimental results showed that the cylindrical dogbone specimen was the ideal geometry for direct tension testing among the geometries tested. While there were strain concentrations at the bevel of the dogbone and none on the cylinder, the larger ends of the dogbone ensured a larger epoxied area than

the cylinders, decreasing the likelihood of failure of the glued surface prior to failure of the concrete. The strain at the corner of the prismatic section was approximately 80% higher than that at the center, increasing the likelihood of premature concrete failure due to strain concentrations (Lepissier, 2020).

Another study conducted at the University of Oklahoma focused on evaluating the uniaxial tension strength of UHPC using prismatic specimens (Campos, 2020). The author sought to develop a modified version of the tensile test developed by Graybeal and Baby (2013) due to the lack of availability of the test equipment required for that test. The specimen had a 2 in. x 2 in. cross section and was 17 in. long. Aluminum plates were epoxied to the sides of the specimen such that the ends of the aluminum plates were 4.5 in. apart. In lieu of clamping the aluminum plates, the plates extended beyond the ends of the UHPC specimen where a steel clevis was attached using two bolts. An aluminum spacer was placed between the two extended aluminum plates to ensure the plates did not rotate inward upon application of the tensile load. The clevises had steel plates extending out with bolt holes for a second set of clevises that were attached to the test frame. This configuration allowed for slight rotation of the specimen ends to reduce the effect of load eccentricity caused by misalignment in the test frame (Campos, 2020). The specimen configuration is shown in Figure 2.10.

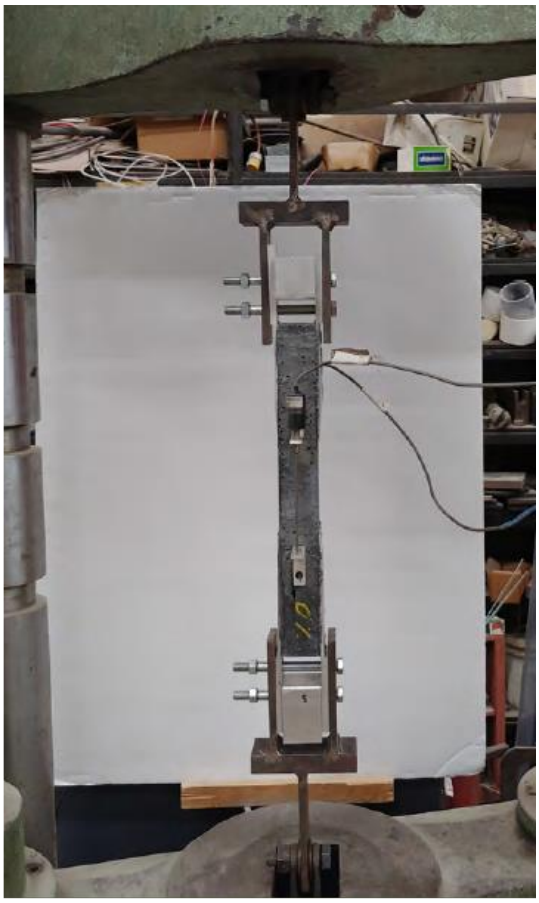

Figure 2.10 – Uniaxial tension test specimen in load frame (Campos, 2020)

Deflections were measured using two LVDTs placed on opposite sides of the specimen and the load was applied at a rate between 100 and 150 lb/s. Uniaxial tension tests were conducted using the same UHPC mix design and fiber percentages as Lepissier (2020). The data showed that the first-crack stress was not well correlated to the fiber content. However, the maximum post-crack strength increased as the fiber content increased, except in the case of 6% fibers, where it decreased. Also, the 2%, 4%, and 6% fiber content specimens developed multiple cracks before a single crack was extended upon failure, while the 0% and 1% only developed a single crack upon failure. The

largest tensile strength as observed with the 4% fiber content. Post-crack strength increases were also observed with the 2%, 4%, and 6% fiber content specimens (Campos, 2020).

2.3. MULTIAXIAL TESTING

Several studies have been conducted to develop failure criteria for UHPC subjected to biaxial loading as well. D'Alessandro et al. (2013) conducted biaxial testing of the UHPC blend Ductal®. The fiber content was 2% by volume per the manufacturer's recommendations. The test specimens were 12 in. x 12 in. x 1 in. panels subjected to bending stresses. The panels were tested in a load frame, shown in Figure 2.11, meant to create a maximum stress state at the top and bottom of the panel through bending.

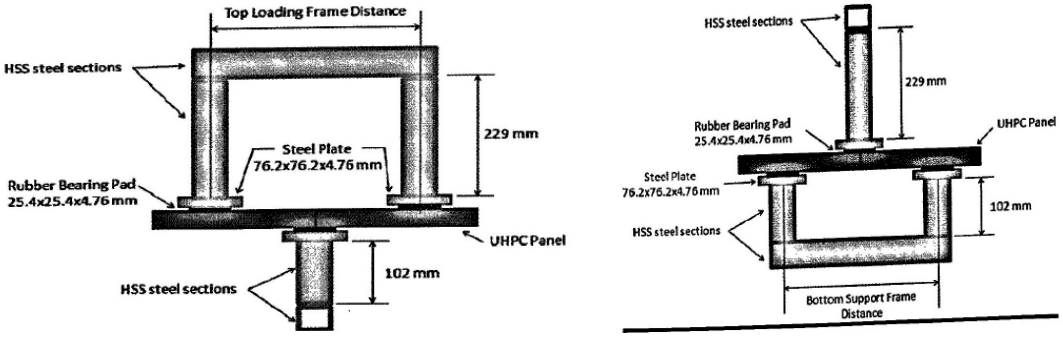

Figure 2.11 – Test setup for biaxial testing (D'Alessandro et al., 2013)

The load was applied by a centrally located hydraulic ram attached to the top frame. The bottom frame remained stationary while the top frame was used to apply the load. The span between the bottom supports was adjusted to created different levels of tension-compression ratios to provide additional points on a failure curve. The load was

applied at a deflection rate of 0.03 in/s. Failure loads from the test were used in a finite element analysis using the analysis program ABAQUS^{TM} to determine the failure stress states at the center of the top surface for the biaxial failure curve. The preliminary cracking model developed from these tests is shown in Figure 2.12 (D'Alessandro et al., 2013).

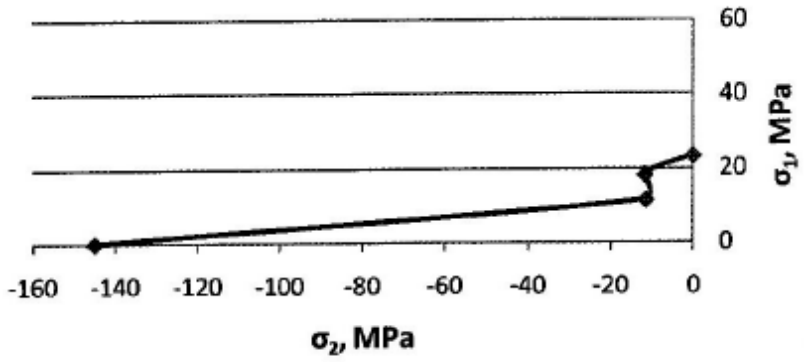

Figure 2.12 – Biaxial failure curve from panel testing (D'Alessandro et al., 2013)

Another study to assess the tension-compression biaxial behavior of UHPC was conducted by Lee et al. (2017) on UHPC panels. The panels tested were 9.5 in. x 7.5 in. x 3.5 in. All test specimens contained mild reinforcing steel, either horizontal or vertical and horizontal, and were tested with 0, 1, and 1.5% steel fiber reinforcement by volume. The tensile force was applied first by partially embedding reinforcing bars into the test panels and loading those bars to less than their yield stress. Once a target strain was reached on the partially embedded bars, compression was applied through the top ram to failure. No load rate was provided in the study. The test setup is shown in Figure 2.13.

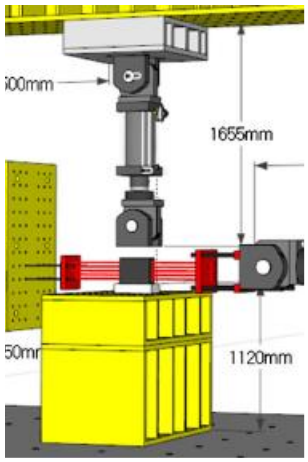

Figure 2.13 – Biaxial testing setup (Lee et al., 2017)

The test results determining the compression strength reduction with applied tension were used to compare to similar testing conducted by Fehling et al. (2008), shown in Figure 2.14. Also, the collected test data was plotted along the biaxial failure curve for conventional concrete created by Kupfer et al. (1969) and is shown in Figure 2.15.

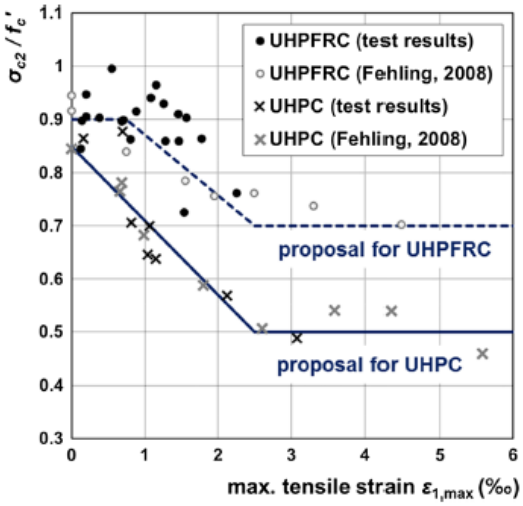

Figure 2.14 – Compressive strength reduction with tensile loading (Lee et al., 2017)

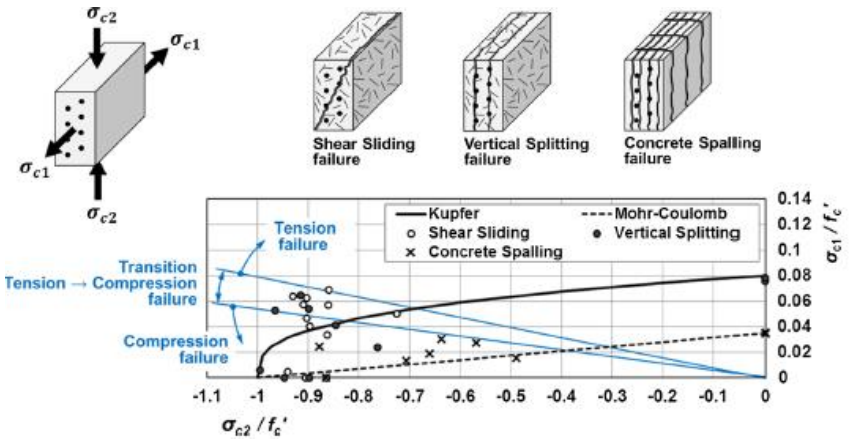

Figure 2.15 – Test data with Kupfer et al. (1969) failure surface (Lee et al., 2017)

The results showed that the compressive strength was reduced by up to 50% with the applied tensile loading. Also, the authors suggested that the test data collected followed the Kupfer model reasonably well (Lee et al., 2017).

Several studies have also tested for the behavior of UHPC under a triaxial compressive stress state. One such study was conducted by Williams et al. (2009) at the U.S. Army Engineering Research and Development Center on their UHPC mix design, Cor-Tuf®. The UHPC was tested with and without fibers. The fibers used in this study were Bekaert Dramix ZP305 hooked end fibers and the fiber content was set to a proportion by weight of cement of 0.31. The triaxial compression specimens consisted of 2 in. diameter, 4 in. tall cylinders placed in an 85 ksi capacity pressure vessel. Triaxial compression tests were conducted with confinement pressures of 1.5 (10 MPa), 2.9 (20 MPa), 7.3 (50 MPa), 14.5 (100 MPa), 29 (200 MPa), and 43.5 (300 MPa) ksi. The stress-strain curves for these tests are shown in Figure 2.16.

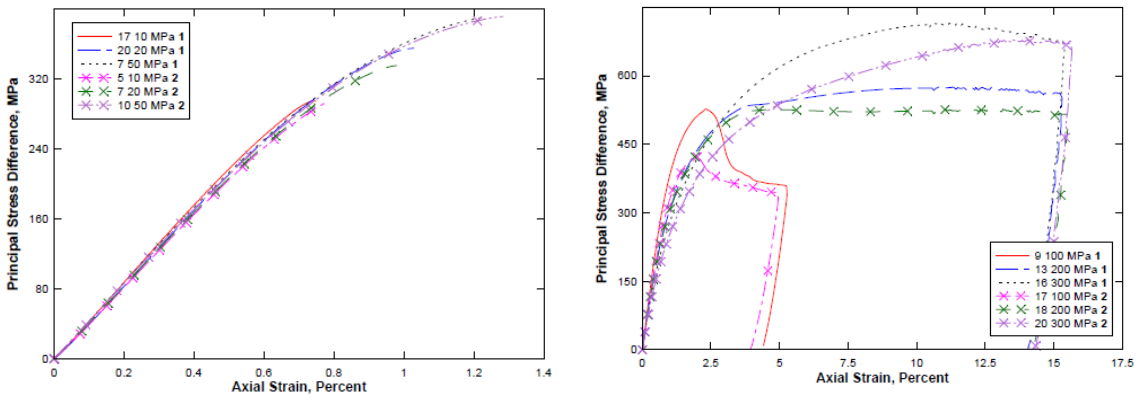

Figure 2.16 – Triaxial test results (Williams et al., 2009)

The number 1 at the end of the legend indicates that the UHPC specimens contained steel fibers, and the 2 indicates the UHPC specimens did not contain steel fibers. The overall trends of each test were similar, with the UHPC containing steel fibers being stronger than without steel fibers. Also, tensile strength tests were conducted to compare the tensile strength to the unconfined compression strength. The data showed that the tensile strength was less than 10% of the compression strength, showing that the relationship is not the same for UHPC as it is for conventional concrete (Williams et al., 2009).

Wang et al. (2016) conducted triaxial compression tests on a commercially available UHPC mix in Europe that did not contain steel fibers. However, this UHPC contained aggregate larger than 0.039 in. (1 mm), which is not standard for UHPC. Non-standard cylinders of 1.88 in. diameter and 3.77 in. height were cut from a block of cast UHPC for the test. The specimens were then placed in a 58 ksi capacity pressure vessel that was used to provide confinement pressure, and a separate ram was used to apply load on the round surface. The triaxial test was conducted with confinement pressures of 3.6

(25 MPa), 7.2 (50 MPa), 14.5 (100 MPa), 29 (200 MPa), and 58 (400 MPa) ksi. A plot of the stress versus axial and radial strain is shown in Figure 2.17 for each confinement pressure.

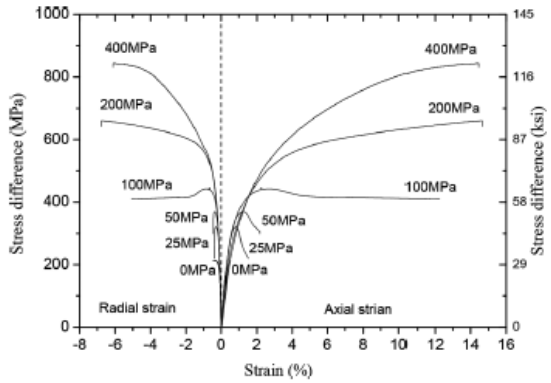

Figure 2.17 – Results of triaxial compression tests (Wang et al., 2016)

The data collected was then plotted against the failure envelope developed for conventional concrete by Ottosen (1977) and is shown in Figure 2.18. Also, a comparison of confined compressive strength was made to conventional concretes of different strengths and is shown in Figure 2.19.

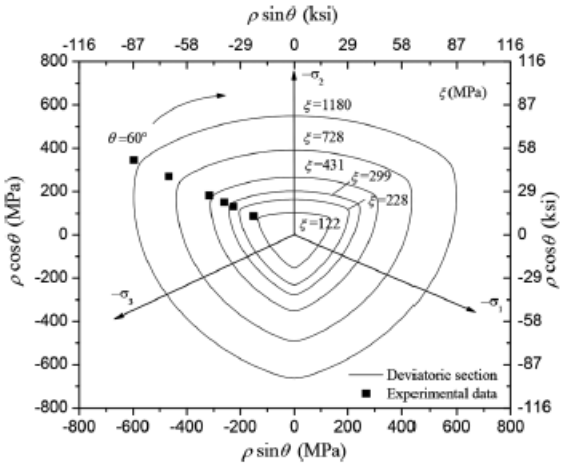

Figure 2.18 – Test data on Ottosen failure envelope (Wang et al., 2016)

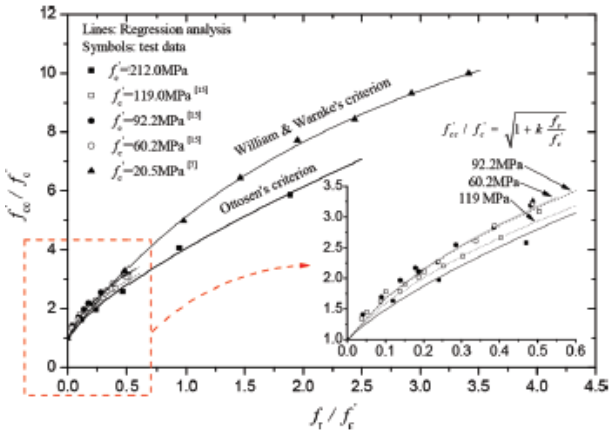

Figure 2.19 – Different concretes confined compressive strength (Wang et al., 2016)

The comparison of UHPC to conventional concrete shows that the benefit of confinement to conventional concrete is less pronounced with UHPC. Also, a brittle to ductile failure transition is seen in the compressive stress strain data. The authors state this transition occurs somewhere between the 14.5 and 29 ksi confinement pressures (Wang et al., 2016).

Wang et al. (2020) conducted triaxial compression tests on UHPC containing 1.5% fibers by volume. The steel fibers were 0.5 in. long and 0.008 in. in diameter. The triaxial test was conducted on 2 in. x 4 in. cylinders that were subjected to confining pressures of 0.725 (5 MPa), 1.45 (10 MPa), 2.9 (20 MPa), 4.35 (30 MPa), 5.8 (40 MPa), and 7.25 (50 MPa) ksi. The confining pressure was applied using a 20 ksi capacity pressure vessel. The test consisted of applying the confining pressure to the cylinder, then applying the longitudinal stress at a deflection rate of 0.0008 in./min. until failure. The stress vs. axial and radial strain response for each of the confining stresses is shown in Figure 2.20. The peak stresses for each confinement stress were also plotted against the Ottoson (1977) failure criteria and are shown in Figure 2.21.

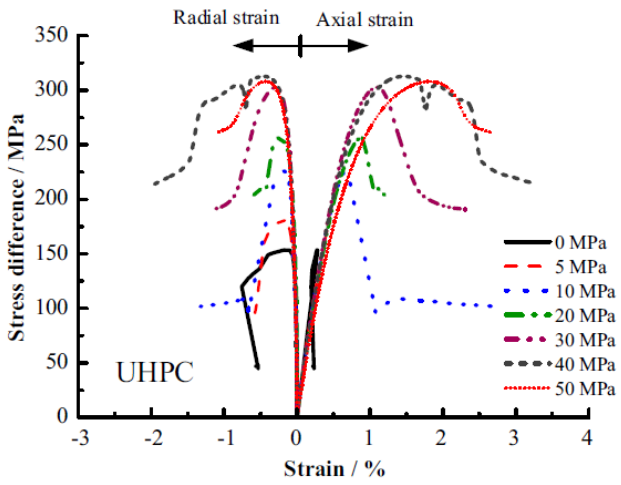

Figure 2.20 – Triaxial compression test results (Wang et al., 2020)

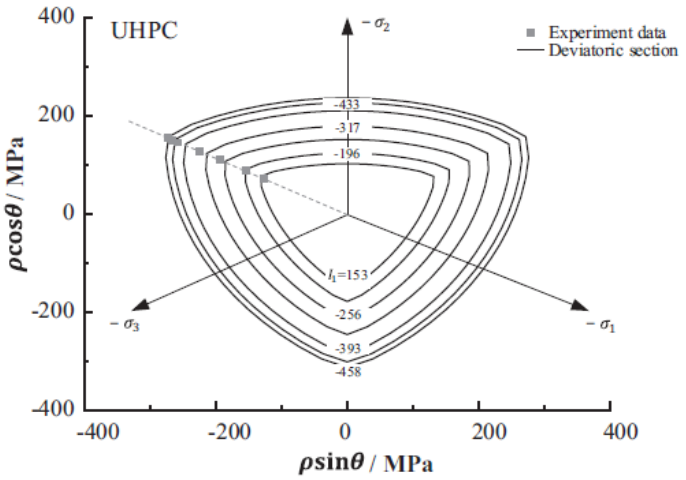

Figure 2.21 – Test data on Ottosen failure envelope (Wang et al., 2020)

This study also conducted the same tests and data comparison with a high performance concrete of a lesser compressive strength to compare the relationships these two concrete strength classes have to conventional concrete. The authors noted that the enhancement of the ultimate strength for UHPC was less pronounced than for the high performance concrete when compared to conventional concrete. However, the fibers present in UHPC provided additional ductility and higher failure strains (Wang et al., 2020).

The studies on triaxial compression summarized above were all conducted using cylindrical specimens. Due to their shape, it is extremely difficult to apply tensile stresses to cylindrical specimens. While there are apparatuses available that have the ability to apply tensile loading in the longitudinal direction (triaxial extension test), there does not appear to be a method for applying tensile stresses in the radial direction. Due to this shortcoming, cylinders are not optimal for applying multiaxial stresses with more than one tension component. However, cubes offer the ability to apply tensile stresses in

multiple directions simultaneously. Unfortunately, few studies have been conducted that apply multiaxial stress states to UHPC cubes. One such study was conducted on 3.94 in cube specimens by Ritter and Curbach (2015). The UHPC tested contained 0.035 in diameter, 0.59 in. long steel fibers at approximately 2.5% by volume. The average uniaxial tension and compression strength of the tested material was 1.16 and 25.24 ksi, respectively. The multiaxial testing consisted of applying load in three different directions simultaneously using hydraulic jacks while the opposite three sides of the cube were fixed. The loading was applied proportionally, with the ratios of all three stresses set and the load applied until failure. A total of 35 stress ratios were tested and no stress ratio contained more than one tension component. The load was applied at a deflection rate of 0.00004 in./s for the tension component at stress ratios higher than 0.1 and at 0.0002 in./s for all other stress ratios. The test setup is shown in Figure 2.22.

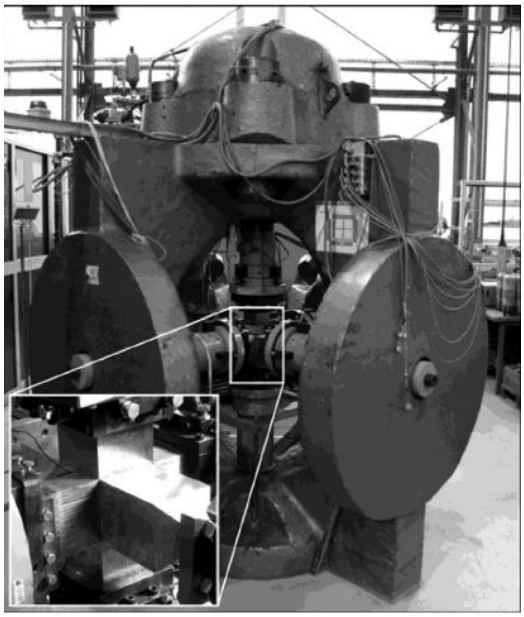

Figure 2.22 – Triaxial test setup (Ritter and Curbach, 2015)

Both compression and tension loads were applied through loading brushes to reduce the effect of confinement at the location of the applied load. To apply the tension load, the brushes had to be glued to the concrete surface. However, the authors noted that premature failure of the glued surface occurred when the brushes were glued directly to the concrete surface. A solution to this issue involved casting a 10x10 grid of screws into the cubes with the screw heads protruding 0.08 in. out of the concrete surface. The screws around the perimeter of the cube were embedded 0.39 in and the interior screws embedded 0.55 in. The brush heads were then glued to the heads of the screws, while the screw heads were completely covered by glue. A specimen with the embedded screws is shown in Figure 2.23.

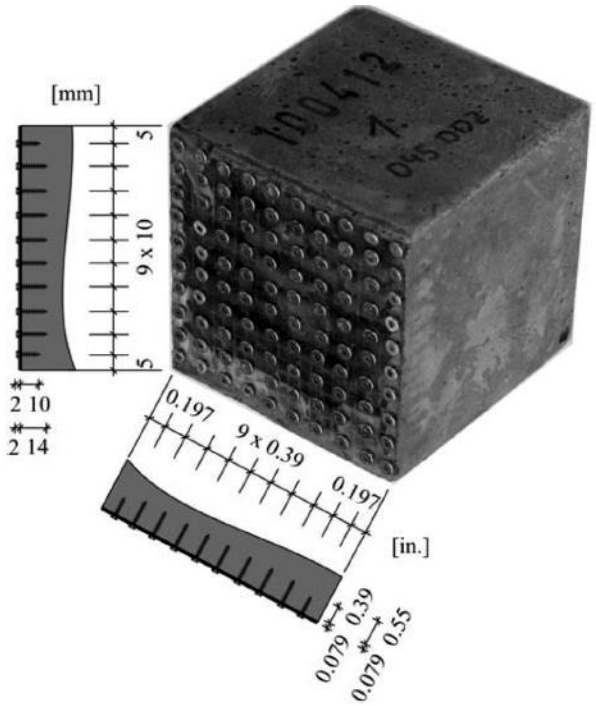

Figure 2.23 – Cube with embedded screws (Ritter and Curbach, 2015)

During testing, the strain in all three directions was measured using Fiber-Bragg gratings attached to a tetrahedral pedestal and embedded in each cube specimen. The data collected was used to develop approximate behavior and damage functions, shown in Equations 2.2 through 2.4 (Ritter and Curbach, 2015).

$$\begin{bmatrix}\boldsymbol{\varepsilon_1}\\ \boldsymbol{\varepsilon_2}\\ \boldsymbol{\varepsilon_3}\end{bmatrix} = \begin{bmatrix}\frac{1}{E_0\phi_1^2} & \frac{\nu_0}{E_0\phi_1\phi_2} & \frac{\nu_0}{E_0\phi_1\phi_3}\\ \frac{\nu_0}{E_0\phi_2\phi_1} & \frac{1}{E_0\phi_2^2} & \frac{\nu_0}{E_0\phi_2\phi_3}\\ \frac{\nu_0}{E_0\phi_3\phi_1} & \frac{\nu_0}{E_0\phi_3\phi_2} & \frac{1}{E_0\phi_3^2}\end{bmatrix}\begin{bmatrix}\boldsymbol{\sigma_1}\\ \boldsymbol{\sigma_2}\\ \boldsymbol{\sigma_3}\end{bmatrix} \quad \textbf{(2.2)}$$

$$\boldsymbol{\phi_i(\kappa_{di})} = \sqrt{\mathbf{1} - \boldsymbol{D_i(\kappa_{di})}} \quad \textbf{(2.3)}$$

$$\boldsymbol{D_i(\kappa_{di})} = \begin{cases} \mathbf{0}, & |\boldsymbol{\kappa_{di}}| \le |\boldsymbol{\varepsilon_{d0}}| \\ \boldsymbol{x1 - exp}\left[-\left(\frac{|\kappa_{di}|-|\varepsilon_{d0}|}{\varepsilon_d}\right)^2\right], & |\boldsymbol{\kappa_{di}}| > |\boldsymbol{\varepsilon_{d0}}| \end{cases} \quad \textbf{(2.4)}$$

Where $\varepsilon_1/\ \varepsilon_2/\ \varepsilon_3$ are the principal strains, $\sigma_1/\ \sigma_2/\ \sigma_3$ are the principal stresses, ν_0 is Poisson's ratio, E_0 is the modulus of elasticity, ϕ_i is the damage function for the principal directions, κ_{di} is the principal strain at the current load step, and ε_{d0} is the strain at initial damage. The damage at each load step is governed by the damage shape parameter equation shown in Equations 2.5 and 2.6.

$$\boldsymbol{\varepsilon_d(z^*, \varphi^\circ)} = \mathbf{0.05}\boldsymbol{exp}\left(-\mathbf{0.003}\boldsymbol{exp}\left[\mathbf{11.3}\boldsymbol{z'_{\varepsilon_d}(z^*, \varphi^\circ)}\right]\right) + \mathbf{0.0015}\boldsymbol{exp}\left[-\left(\mathbf{1.5}\text{^}\left\{\left(\frac{\mathbf{60^\circ - \varphi}}{\mathbf{25^\circ}}\right)\boldsymbol{z'_{\varepsilon_d}(z^*, \varphi^\circ)}\right\}\right)\right] \quad \textbf{(2.5)}$$

$$z'_{\varepsilon_d} = \begin{cases} z^* - (-0.000016\varphi^* - 0.0105\varphi), & z^* > -0.000016\varphi^2 - 0.0105 \\ 0, & z^* \leq -0.000016\varphi^2 - 0.0105 \end{cases} \quad \textbf{(2.6)}$$

Where ε_d is the shape parameter that describes the level of damage, z'_{ed} is the coefficient that describes the trend of the shape parameter curve, and φ is the angle of the stress ratio that defines the meridian (Ritter and Curbach, 2015).

2.4. CURRENT FAILURE MODELS

Development of multiaxial failure criteria for concrete has been a topic of study for decades. Popular failure models include Kupfer et al. (1969), Ottosen (1977), and Drucker and Prager (1952). More recently, Menétrey and Willam (1995) developed a generalized triaxial concrete failure model with three adjustable parameters to tailor the model to other brittle materials. The model was based on the criterion developed for rock masses by Hoek and Brown (1980), which does not account for the effect of the intermediate principal stress, σ_2. This was overcome by converting to a stress invariant based formulation using Hiagh-Westergaard coordinates ξ, ρ, and θ, shown in Equations 2.7 through 2.9.

$$\xi = \frac{1}{\sqrt{3}} I_1 \quad \textbf{(2.7)}$$

$$\rho = \sqrt{2J_2} \quad \textbf{(2.8)}$$

$$\cos 3\theta = \frac{3\sqrt{3}}{2} \frac{J_3}{J_2^{3/2}} \quad \textbf{(2.9)}$$

The generalized, three-parameter failure equation is shown in Equation 2.10.

$$\boldsymbol{F(\xi,\rho,\theta) = \left[A_f\rho\right]^2 + m\left[B_f\rho r(\theta,e) + C_f\xi\right] - c = 0} \qquad \textbf{(2.10)}$$

The three parameters A_f, B_f, and C_f can be calibrated to match testing results of different materials. The values *m* and *c* represent frictional and cohesion strength, respectively. For the generalized equation, *c* is set to a value of 1. The equation for *m* considers the uniaxial strengths of the material and is shown in Equation 2.11.

$$\boldsymbol{m = 3\frac{f_c'^2 - f_t'^2}{f_c' f_t'}\frac{e}{e+1}} \qquad \textbf{(2.11)}$$

The equation, *r*, is the elliptical function that creates a triple symmetric ellipse to represent the deviatoric space of the failure criteria. The elliptical function is shown in Equation 2.12.

$$\boldsymbol{r(\theta,e) = \frac{4(1-e^2)cos^2\theta + (2e-1)^2}{2(1-e^2)cos\theta + (2e-1)[4(1-e^2)cos^2\theta + 5e^2 - 4e]^{1/2}}} \qquad \textbf{(2.12)}$$

The parameter, *e*, adjusts the out-of-roundness of the deviatoric plane and is valid from 0.5 to 1. When $e = 0.5$, the deviatoric plane is a triangular shape, and when $e = 1$, the deviatoric plane is a circle. An example of the failure shape with different values for *e* is shown in Figure 2.24.

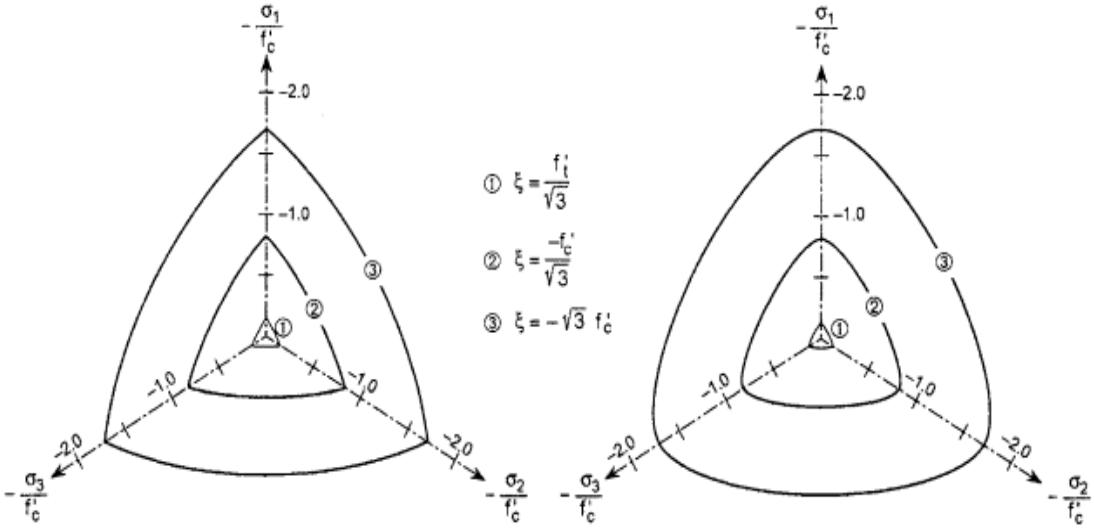

Figure 2.24 – Deviatoric plane shapes at three values for ξ for e = 0.5 (left) and e = 0.6 (right) (Menétrey and Willam, 1995)

Upon developing the generalized, three-parameter equation, the authors were able to calibrate the parameters of the equation to generate several common concrete failure criteria equations. The calibrated parameters determined for the various failure criteria are shown in Table 2.1 (Menétrey and Willam, 1995).

Table 2.1 – Parameters determined to match existing concrete failure criteria (Menétrey and Willam, 1995)

	A_f	B_f	C_f	m	e
Huber-Mises	0	$\sqrt{\frac{3}{2}}\frac{1}{f'_c}$	0	1	1
Drucker-Prager	0	$\sqrt{\frac{3}{8}}\frac{f'_c + f'_t}{f'_c f'_t}$	$\frac{3}{2}\frac{f'_c - f'_t}{f'_c f'_t}$	1	1
Rankine	0	$\frac{1}{\sqrt{6}f'_t}$	$\frac{1}{\sqrt{3}f'_t}$	1	$\frac{1}{2}$
Mohr-Coulomb	0	$\frac{1}{\sqrt{6}}\frac{f'_c + 2f'_t}{f'_c f'_t}$	$\frac{1}{\sqrt{3}}\frac{f'_c - f'_t}{f'_c f'_t}$	1	$\frac{f'_c + 2f'_t}{2f'_c + f'_t}$
Parabolic Leon	$\sqrt{\frac{1.5}{f'_c f'_t}}$	0	$\sqrt{3}\frac{f'_c - f'_t}{f'_c f'_t}$	1	No e
Three-Parameter Concrete	$\frac{\sqrt{1.5}}{f'_c}$	$\frac{1}{\sqrt{6}f'_t}$	$\frac{1}{\sqrt{3}f'_t}$	$\sqrt{3}\frac{f'^2_c - f'^2_t}{f'_c f'_t}\frac{e}{e+1}$	$0.5 < e \leq 1$

While several failure criteria have been developed for conventional concrete, very few have been developed around UHPC. One such expression was developed by Ritter and Curbach (2016) using the data collected in the study mentioned above by the same authors (Ritter and Curbach, 2015). In lieu of using Haigh-Westergaard coordinates, the authors developed a new, rotated set of coordinates that are shown in Equations 2.13 through 2.16.

$$\boldsymbol{x'} = \frac{\boldsymbol{x-y}}{\sqrt{\boldsymbol{2}}} \tag{2.13}$$

$$\boldsymbol{y'} = \frac{\boldsymbol{x+y-2z}}{\sqrt{\boldsymbol{6}}} \tag{2.14}$$

$$z' = \frac{x+y+z}{\sqrt{3}} \tag{2.15}$$

$$\varphi = 60° - \arctan\left(\frac{x'}{y'}\right) = 60° - arctan\left(\frac{\sqrt{3}(x-y)}{(x+y-2z}\right) \tag{2.16}$$

This rotated coordinate system makes *z'* the x-axis when plotted in a two-dimensional format. A graphical representation of the rotated coordinate system is shown in Figure 2.25.

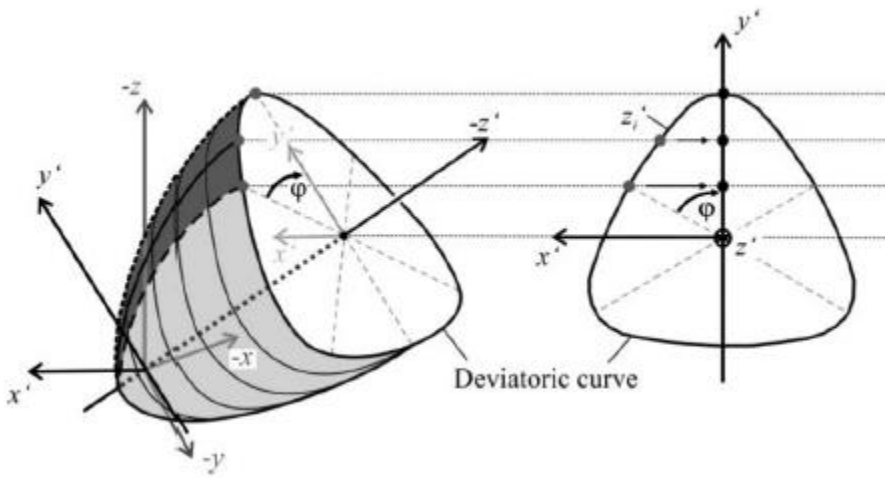

Figure 2.25 – Rotated coordinate system in relation to the original axes (Ritter and Curbach, 2016)

The generalized equation is shown in Equations 2.17 through 2.18.

$$y(z^*, \varphi) = \left[\frac{\sqrt{3}}{2}\tan(\varphi) + \frac{1}{2}\right] k(z^*, \varphi) y'_{tm} z^* \tag{2.17}$$

$$z^* = \frac{-z'}{|f_c|} + \frac{f_{ttt}}{|f_c|} \tag{2.18}$$

The values of z' were transformed into z^* to ensure that compression values were positive. The term f_{ttt} is the hydrostatic tension strength and must be estimated in most cases. To make the equation more generalized and allow for multiple deviatoric plane shapes and trends from hyrdrostatic tension to hydrostatic compression, the authors provide multiple equations to create these shapes. The deviatoric shape is determined by the term $k(z^*, \varphi)$. The equation for $k(z^*, \varphi)$ is shown in Equations 2.19 through 2.21.

$$\boldsymbol{k(z^*, \varphi) = 10.539 - \left(5.27 - r(z^*)\right)\left(\frac{\varphi^\circ}{60^\circ}\right)^2 - \left(\frac{\varphi^\circ}{60^\circ}\right)^{3.8138 r(z^*) - 2.8138}} \quad \textbf{(2.19)}$$

$$\boldsymbol{r(z^*) = \frac{r_1}{1 + exp[r_2 z^*]} + r_4} \quad \textbf{(2.20)}$$

$$\boldsymbol{r(z^*) = \frac{r_1}{1 + exp[r_2 z^*]} \frac{1}{1 + exp[r_3 z^*]} + r_4} \quad \textbf{(2.21)}$$

If the value of $r(z^*) = 1$, the deviatoric plane is circular, if $r(z^*) = 5.27$, the deviatoric plane is triangular, and if $r(z^*) > 5.27$, the deviatoric plane is a non-convex triangular shape. Two different equations for $r(z^*)$ are provided for further customization. The various r terms can be used to adjust the deviatoric shape as the surface transitions from hydrostatic tension to hydrostatic compression.

The final term in the general equation, y'_{tm}, defines the trend of the tension meridian (the line of the failure surface when $\varphi = 0°$). Five equations were provided that can be used in the general equation to describe various shapes. They are presented here as Equations 2.22 through 2.26.

$$\boldsymbol{y'_{tm}(z^*) = a_1(z^*)^{b_1}} \quad \textbf{(2.22)}$$

$$\boldsymbol{y'_{tm}(z^*) = a_1(1 - b_2{}^{z^*})} \quad \textbf{(2.23)}$$

$$\boldsymbol{y'_{tm}(z^*) = a_3(z^*)^2 + b_3 z^*} \quad \textbf{(2.24)}$$

$$\boldsymbol{y'_{tm,mod,1}(z^*) = (1 + c^{z^*})^d y'_{tm}(z^*)} \quad \textbf{(2.25)}$$

$$\boldsymbol{y'_{tm,mod,2}(z^*) = y'_{tm}(z^*)\left(\frac{-f_{ccc}}{|f_c|} - z^*\right)^f} \quad \textbf{(2.26)}$$

The last two equations are modified versions of the y'_{tm} equation for small values of z^*. The various equations for y'_{tm} can be used to describe both an open ended and closed ended shape in the hydrostatic compression direction by adjusting the values of the *a* and *b* terms. The limits to the *a* and *b* terms are shown in Table 2.2.

Table 2.2 – Limits of the *a* and *b* terms for each equation (Ritter and Curbach, 2016)

Eq. 2.21 (Opening)	Eq. 2.22 (Asymptotic)	Eq. 2.23 (Closing)
$a_1 > 0$	$a_2 > 0$	$a_3 < 0$
$0 < b_1 < 1$	$0 < b_2 < 1$	$b_3 > 0$

The authors then used the experimental data collected (Ritter and Curbach, 2015) to develop a failure surface for UHPC. Multiple combinations of the y'_{tm} equations and $r(z^*)$ with various r values were evaluated to develop the surface. Two different versions

were compared that show different trends of the surface in the hydrostatic tension direction. The final shapes and comparisons to experimental data are shown in Figure 2.26 (Ritter and Curbach, 2016).

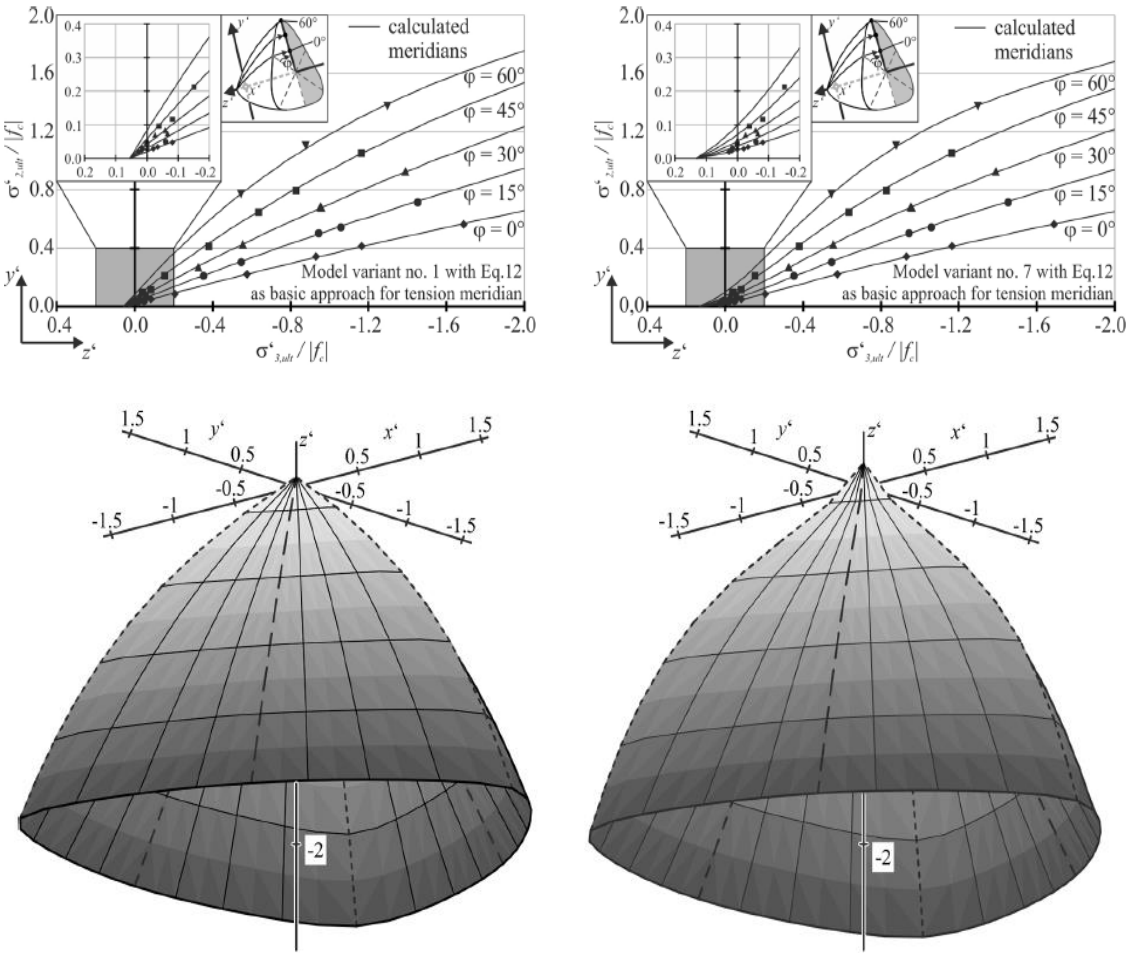

Figure 2.26 – Comparison of two failure surfaces with experimental data (Ritter and Curbach, 2016)

2.5. RESEARCH GAPS

The literature review highlighted a variety of studies evaluating the performance of UHPC in several different stress conditions. Noticeably absent is data representing

portions of the failure surface with two or more principal stresses in tension. In the case of conventional concrete, the absence of this data did not hinder design and analysis efforts since the tension strength is typically ignored due to its relatively low value when compared to its compressive strength. However, UHPC has a much higher tensile strength, especially when incorporating steel fibers, and ignoring the tensile behavior of UHPC could be considered overly conservative, may not accurately depict behavior, and would ignore the contribution of the most expensive component of UHPC – the steel fibers.

While collecting multiaxial tension strength data would be beneficial to UHPC design and analysis efforts, applying these stresses is exceptionally difficult and test equipment capable of applying those stress conditions is exceedingly rare. While the test equipment used by Ritter and Curbach had the potential to apply tension in more than one direction, the authors were unable to adequately attach the test fixtures without the addition of screws to the cube faces being placed in tension (2015). These screws could not be placed in an adjacent cube face for application of tension in more than one direction due to interferences. Therefore, a new method for this type of load application is necessary to fill the gap in tensile data that would better inform failure models. With multiaxial tensile data, a complete failure surface could be developed to help improve the understanding of UHPC behavior as well as improve the analysis and design of UHPC structural elements.

3. MIX DESIGN AND CONCRETE PROPERTIES

3.1. INTRODUCTION

The following chapter details the UHPC mix design used in this study, including a brief description of how it was developed. The mixing and curing procedure used for all the test specimens is also described. Finally, the procedures for conducting the fresh and hardened property testing are described and the corresponding results are provided.

3.2. MIX DESIGN REFINEMENT AND PROCEDURES

3.2.1. Mix Design Refinement

The UHPC mix design used for all testing in this study was originally developed at the University of Oklahoma. The initial mix design process was outlined by Looney et al. (2019) and is described in detail in Chapter 2. However, the original mix design utilized a relatively bulky fiber meant for refractory concrete. The large mass of the fiber required that the UHPC flow be set to a maximum of 7.5 in. to ensure the fibers stayed suspended in the cementitious matrix during the curing period. This flow made the mix less workable and reduced the working time of the UHPC. The mix design is shown in Table 3.1.

Table 3.1 – Mix design by Looney et al. (2019)

Type I Cement (lb/yd^3)	1180
Slag Cement (lb/yd^3)	590
Silica Fume (lb/yd^3)	197
Masonry Sand (lb/yd^3)	1966
Steel Fibers (lb/yd^3)	255
Water (lb/yd^3)	393
MasterGlenium 7920 (oz./cwt)	15.77

Refinements were conducted on this mix design to improve the rheology for use in this study. A smaller, lighter steel fiber was chosen to replace the larger fiber used in the original mix design study. The new fiber chosen was the Bekaert Dramix® OL 0.2/13 smooth steel wire fiber, which is 0.512 in. long and 0.008 in. in diameter, with a tensile strength of 313 ksi. This was a commonly used fiber size in UHPC. After changing the fibers, trials were conducted to find the flow where fiber segregation occurred, observed by cutting cylinders along their length for visual inspection. The trials were conducted using 2% fibers by volume to match the fiber content of the original mix design. The trials showed that the flow could be as high as 10 in. before fiber segregation occurred. The final mix design for 2% fibers determined from these trials is shown in Table 3.2.

Table 3.2 – UHPC mix design used in this study with 2% fibers

	2% Fibers
Type I Cement (lb/yd^3)	1180
Slag Cement (lb/yd^3)	590
Silica Fume (lb/yd^3)	197
Masonry Sand (lb/yd^3)	1966
Steel Fibers (lb/yd^3)	265
Water (lb/yd^3)	393
MasterGlenium 7920 (oz./cwt)	20

3.2.2. Mixing Procedure

The size of each batch used for casting test specimens was 0.12 ft^3 and all of the mixing was conducted in a Blakeslee tabletop planetary mixer with a 0.33 ft^3 capacity. The sand was first oven dried for approximately twenty-four hours to ensure it was completely dry prior to mixing. Once the sand cooled to ambient conditions, it was ready to be mixed. The Type I cement, slag cement, silica fume, and masonry sand were weighed and added to the mixing bowl. Then, the mixing bowl was placed on the mixer and turned to low speed (102 revolutions per minute) to blend the dry ingredients. The mixer was kept running at that speed for the entirety of the mixing process. After ten minutes of dry blending, half of the HRWR was added to the mixing water and the wet blend was slowly added to the dry blend over the course of approximately one minute. This blend was left to mix for two minutes, then the remainder of the HRWR was added to the blend over the course of approximately thirty seconds. Once all of the wet ingredients were added, the UHPC was left to mix until just before it was flowable. The process typically required twelve to fifteen minutes of mixing. Once the mix appeared flowable, the fibers were added to the mix over the course of approximately one minute.

The fibers were then allowed to disperse in the cementitious matrix for approximately three minutes. After dispersing, the mixer was turned off, the bowl was removed, and the UHPC was ready to be placed in the specimen molds. The entire mixing process lasted between twenty-three and twenty-nine minutes, depending on the fiber content and HRWR dosage.

3.2.3. Adjustments for Different Fiber Content

As the fiber content changed, it became apparent that the HRWR dosage determined in the trials for 2% fibers shown in Table 3.2 was not adequate for all fiber contents. Trial batches were required for each of the fiber percentages tested to ensure adequate flowability while maintaining fiber suspension. The final mix designs for each of the fiber percentages evaluated is shown in Table 3.3. During the course of the research, HRWR dosages required slight adjustments to account for constituent material variability.

Table 3.3 – UHPC mix design evaluated

	Fiber Content by Volume					
	0%	1%	2%	4%	5%	6%
Type I Cement (lb/yd^3)	1204	1192	1180	1156	1143	1131
Slag Cement (lb/yd^3)	602	596	590	578	572	566
Silica Fume (lb/yd^3)	201	199	197	193	191	189
Masonry Sand (lb/yd^3)	2007	1987	1966	1927	1906	1886
Steel Fibers (lb/yd^3)	0	132	265	529	661	793.5
Water (lb/yd^3)	401	397	393	385	381	377
MasterGlenium 7920 (oz./cwt)	19	19	20	24	26	28

The trials showed that, as the fiber percentage increased, the HRWR dosage was required to increase to maintain flowability. This makes sense since the addition of fibers inhibit flowability.

3.2.4. Curing Procedure

Cube specimens were cast for both multiaxial tension and uniaxial compression testing, and three cylinders were cast for uniaxial compression testing as well. Once the specimens were cast, they were placed in a curing room that was maintained at approximately 73°F and covered with plastic sheeting to trap in moisture evaporated from the specimens. Additionally, since the cube specimens meant for multiaxial tension testing required a moderately smooth surface to ensure an adequate surface for bonding the test fixtures, the cube specimens were covered with a plastic sheet, then a flat plate was placed over the plastic, and a concrete prism was placed over the plate to more effectively trap moisture in the specimen and maintain a moderately smooth top surface of the cube. The covered cube specimens are shown in Figure 3.1.

Figure 3.1 – Covered cube specimens immediately after casting

The specimens were allowed to cure in the curing room for approximately twenty-four hours. After this time, the specimens were demolded. The cube specimen edges were scraped with a putty knife to remove any projections to reduce the likelihood of stress concentrations during uniaxial compressive testing. After specimen removal, they were transported to an ESPEC Platinous H-Series temperature and humidity chamber for heat and moisture curing. The chamber was programmed to maintain a temperature of 194°F at 95% relative humidity for forty-eight hours. This curing regime was in accordance with ASTM C1856 (2017) for steel fiber reinforced UHPC. After the forty-eight hour heat and moisture curing, the chamber automatically turned off. The specimens were left in the chamber for an additional twenty-four hours before removal to more slowly cool down and ensure there were no sudden changes in temperature that could cause internal cracking. After removal, the specimens were transported to the same initial curing room until the start of testing preparation. This preparation process typically started one to three days after removal from the curing chamber.

An observation was noted concerning the post-heat and moisture curing behavior of specimens with 0% and 1% fiber contents. When tested, several sets of specimens would obtain what appeared to be a reasonable multiaxial tension strength result, while having a very low uniaxial compressive strength result for both the cube and cylinder specimens. These test results also appeared to occur when the cubes were stored in the lab when the ambient humidity was less than 50% after heat curing. This behavior led the author to believe that the reduced ambient humidity caused the specimens to lose moisture at an accelerated rate and increase drying shrinkage. The fiber content was too low to provide enough shrinkage restraint. After observing this behavior on a 0% fiber

specimen, a second set was cast the next day and cured in the same manner up to removal from the curing chamber. After removal from the curing chamber, the specimens were subjected to moist curing at the same temperature as all the previous specimens.

The method for providing moist curing is shown in Figure 3.2. All of the cube and cylinder specimens were place in a bucket and the bucket was placed on its side. Then, a small, cool-mist humidifier was placed in front of the bucket opening to propel moist air into the bucket. The bucket was tilted slightly to allow the condensate to be drained so the specimens were not submerged in water. This method provided a relative humidity of above 95%, ensuring no moisture was lost from the specimens prior to testing. The specimens meant for multiaxial tension testing were only removed to allow for the surfaces to dry prior to prepping the specimens. The prepared specimens were placed back in the moist environment until testing.

Figure 3.2 – Moist curing method for 0% specimens

The test results of the normally cured and the moist cured specimens are shown in Table 3.4, where σ_1, σ_2, and σ_3 are the three tensile principal stresses, and f_c is the uniaxial compressive strength.

Table 3.4 – Test results comparing the post-heat cure regime for 0% specimens

0%	(psi)			
	σ_1	σ_2	σ_3	f_c
Standard Cure	1026	498	488	15620
Moist Cure	1069	510	497	18330

The multiaxial test results were nearly identical, but the standard cured uniaxial compressive strength was approximately 15% lower than the moist cured specimen. This difference in uniaxial compressive strength appears to be due to some form of damage caused by drying shrinkage from being left in a low humidity environment for several days prior to testing. The fact that this was only observed in the 0% and 1% fiber specimens also provides evidence the reduction in strength was caused by shrinkage since the fibers appear to provide restraint against shrinkage.

3.3. FRESH AND HARDENED PROPERTIES OF MIX DESIGNS

3.3.1. Flow Procedure

The flow test was conducted in accordance with ASTM C1856 (2017) after the UHPC mixing procedure was completed. The flow table was wiped clean of any debris, the flow cone was centered on the flow table, and the UHPC was poured into the flow cone. No tamping was conducted on the UHPC, and the cone was filled in one lift. Excess UHPC was then screeded off the top to ensure the UHPC was level with the top

of the cone. Then the cone was slowly raised, allowing the UHPC to flow across the table. A timer was started as soon as the flow cone was raised. Any UHPC that adhered to the inside of the cone was removed and placed in the center of the flowing UHPC upon removal of the cone. The table was left stationary throughout the test. After two minutes, four measurements were taken of the diameter of the flowing UHPC, and the recorded flow was the average of those four measurements. Photos of flows measured on a 10 in. diameter flow table for each of the fiber contents at the target HRWR dosages are shown in Figure 3.3 through Figure 3.8.

Figure 3.3 – Flow of the UHPC mix with 0% fibers

Figure 3.4 – Flow of the UHPC mix with 1% fibers

Figure 3.5 – Flow of the UHPC mix with 2% fibers

Figure 3.6 – Flow of the UHPC mix with 4% fibers

Figure 3.7 – Flow of the UHPC mix with 5% fibers

Figure 3.8 – Flow of the UHPC mix with 6% fibers

Once the fiber content was above 2% by volume, the fibers tended to agglomerate and not flow with the cementitious matrix. This was caused by a large quantity of fibers becoming entangled. At 4% fibers, a portion of the fibers was able to flow with the cementitious matrix, while leaving the rest of the fibers as a tangled mound near the center of the flow. At 5% fibers, the majority of fibers appeared tangled, with the entire mass slumping slightly upon removal of the flow cone, with some of the cementitious matrix flowing out and creating a halo around the mass. At 6% fibers, the tangled mass of fibers only slumped slightly upon removal of the flow cone and the same cementitious material halo was observed around the edges of the mass. The tangle of fibers with the 4%, 5%, and 6% fiber contents reduced the self-consolidating nature of the UHPC even after adjustments to the HRWR admixture.

3.3.2. Cube Uniaxial Compressive Strength

The 2 in. x 2 in. x 2 in. cubes were cast in general accordance with ASTM C109 (2020), with some modifications. A demolding agent was applied to the inside of each cube mold. After conducting the flow test, the UHPC was slowly poured into each cube mold in a single lift. The UHPC was not tamped into the mold due to its self-consolidating nature. Once the molds were filled, the excess UHPC was screeded off, and the molds were tapped against the table to facilitate consolidation.

On test day, the specimens were oriented such that the uniaxial compressive loading would be applied to two of the formed surfaces. Then, the cubes were measured in that orientation in all three directions due to the potential for the specimens to have substantial differences in height since the top surfaces were not placed against the forms. The uniaxial compressive testing was conducted on a Forney© 450 Series compression machine with automatic controls. The specimen geometry was input into the console, the preload was set to approximately half of the anticipated failure load, and the load was set to 150 psi/s based on ASTM C1856 (2017). Once the parameters were set, the cube was centered in the test machine, and the test was started. The test was run until the applied load fell to 70% of the peak load. In the case of the 0%, 1%, and 2% fiber contents, this stop point was reached nearly instantaneously after the peak load was reached due to sudden and explosive crack development. For the higher fiber contents, the load exhibited a more gradual decrease after the peak load. This was caused by an increase in fibers bridging the initial cracks and sustaining a considerably slower post-peak load reduction as the fiber contents increased. A failed 2% fiber content cube is shown in Figure 3.9.

Figure 3.9 – Failed 2% cube after the uniaxial compression test

3.3.3. Cylinder Uniaxial Compressive Strength

Three 3 in. x 6 in. cylinders were cast and tested in accordance with ASTM C1856 (2017) for each batch. A demolding agent was applied to the inside of each cylinder mold. After casting the cubes, the UHPC was slowly poured into the cylinder molds in a single lift. After filling, the top was screeded off, and the sides were gently tapped to facilitate consolidation.

On test day, the specimens were placed in a machine to grind the ends of the cylinders with a diamond embedded steel grinding wheel to ensure the ends were smooth, parallel to each other, and perpendicular to the cylinder sides. Once the ends were ground, the specimens were ready for uniaxial compressive testing. The uniaxial compressive testing was conducted in the same test machine used on the cubes. The specimen geometry was input into the console, the preload was set to approximately half of the anticipated failure load, and the load was set to 150 psi/s. Once the parameters were set, the cylinder was centered in the test machine and the test was started. The test

was run until the applied load fell to 70% of the peak load. The same behavior after the peak load of the cubes was observed in the cylinders, except it was more pronounced. This could be due to the larger specimen size allowing for longer failure cracks, thus increasing the likelihood that more fibers would bridge the cracks after the peak load was reached. A failed 6% fiber content cylinder is shown in Figure 3.10.

Figure 3.10 – Failed 6% cylinder after the uniaxial compression test

3.3.4. Comparison of Cylindrical and Cube Uniaxial Compressive Strengths

The purpose of the following data is to determine the relationship between the cylindrical and cube compressive strengths. The flow and compressive strength data for each of the UHPC mixes cast for test specimens are shown in Table 3.5 through Table 3.10. The average of the cube uniaxial compressive strength multipliers to obtain the

cylinder uniaxial compressive strength for each of the fiber contents is shown in Table 3.11.

Table 3.5 – Flow and uniaxial compressive data for each 0% fiber content pour

		(psi)		$\frac{Cylinder\ f_c}{Cube\ f_c}$
	Flow (in.)	Cylinder f_c	Cube f_c	
0%	9.000	16200	13910	1.16
	9.500	17580	15530	1.13
	7.125	16110	14510	1.11
	9.875	16790	12230	1.37
	9.250	16320	15170	1.08
	8.313	15620	12850	1.22
	9.625	18330	11700	1.57
	9.188	14380	9000	1.60
	8.875	17420	17820	0.98
	9.325	16500	14580	1.13
	9.500	16220	10100	1.61
	9.500	16220	10100	1.61
	8.875	17420	17820	0.98
			Avg. =	1.27
			Standard Deviation =	0.24
			Coefficient of Variation =	0.19

Table 3.6 – Flow and uniaxial compressive data for each 1% fiber content pour

		(psi)		$\frac{Cylinder\ f_c}{Cube\ f_c}$
	Flow (in.)	Cylinder f_c	Cube f_c	
	9.563	16920	16920	1.00
	8.000	17950	18180	0.99
	9.500	17330	18420	0.94
	9.875	16570	15990	1.04
	9.625	17620	18200	0.97
	10.000	17560	17730	0.99
1%	9.500	17320	17950	0.96
	9.188	16430	16510	1.00
	8.500	17990	18640	0.97
	9.125	18190	16510	1.10
	10.000	18360	18810	0.98
	8.813	17770	17660	1.01
	9.625	18420	20240	0.91
			Avg. =	0.99
			Standard Deviation =	0.05
			Coefficient of Variation =	0.05

Table 3.7 – Flow and uniaxial compressive data for each 2% fiber content pour

		(psi)		$\frac{Cylinder\ f_c}{Cube\ f_c}$
	Flow (in.)	Cylinder f_c	Cube f_c	
2%	7.000	18720	19650	0.95
	9.313	18340	20210	0.91
	7.125	19170	19910	0.96
	8.938	18950	19310	0.98
	6.125	18810	19600	0.96
	8.500	18710	19270	0.97
	8.938	16630	19420	0.86
	8.688	19180	21110	0.91
	9.500	17770	19920	0.89
	6.875	18940	21110	0.90
	9.625	19500	20040	0.97
	9.000	18270	20000	0.91
			Avg. =	0.93
			Standard Deviation =	0.04
			Coefficient of Variation =	0.04

Table 3.8 – Flow and uniaxial compressive data for each 4% fiber content pour

		(psi)		$\frac{Cylinder\ f_c}{Cube\ f_c}$
	Flow (in.)	Cylinder f_c	Cube f_c	
4%	8.125	19650	21450	0.92
	4.500	19870	22240	0.89
	8.250	20520	22150	0.93
	6.375	20330	2219.	0.92
	6.313	20230	21850	0.93
	8.875	20380	23090	0.88
	8.375	19430	21980	0.88
	9.063	19520	23060	0.85
	8.375	20050	22760	0.88
	8.750	19050	22340	0.85
			Avg. =	0.89
			Standard Deviation =	0.03
			Coefficient of Variation =	0.03

Table 3.9 – Flow and uniaxial compressive data for each 5% fiber content pour

		(psi)		$\frac{Cylinder\ f_c}{Cube\ f_c}$
	Flow (in.)	Cylinder f_c	Cube f_c	
5%	5.750	20760	22690	0.91
	5.875	21050	23020	0.91
			Avg. =	0.91
			Standard Deviation =	0.00
			Coefficient of Variation =	0.00

Table 3.10 – Flow and uniaxial compressive data for each 6% fiber content pour

		(psi)		$\frac{Cylinder\ f_c}{Cube\ f_c}$
	Flow (in.)	Cylinder f_c	Cube f_c	
6%	5.125	21570	23970	0.90
	4.750	20880	23890	0.87
			Avg. =	0.89
			Standard Deviation =	0.02
			Coefficient of Variation =	0.02

Table 3.11 – Average cube strength multiplier to estimate cylinder strength

	Avg. $\frac{Cylinder\ f_c}{Cube\ f_c}$
0%	1.27
1%	0.99
2%	0.93
4%	0.89
5%	0.91
6%	0.89

The cylinder uniaxial compressive strengths were used to normalize the multiaxial test data points collected from the same UHPC pour. However, cube specimens were also tested in uniaxial compression to determine a relationship between the uniaxial compressive strengths of cubes and cylinders at various fiber contents. Table 3.11 shows

that, for a 0% fiber content UHPC, the cube strengths were lower than the cylinder strengths. For the UHPC with fibers, the cubes strengths were higher than the cylinder strengths, and the amount the cubes were stronger increased with an increase in fiber content. This data highlights that the size effect typically seen in testing of concrete specimens is altered by the presence of fibers and is dependent on the fiber content. This could be due to the change in the amount fibers that are able to mitigate microcrack expansion at higher percentages.

These results differ from Graybeal and Davis (2008), who did similar comparisons between the same size cubes and cylinders of UHPC with either 2% of the same fibers used in this study or no fibers. The authors determined that the cylinder uniaxial compressive strength could be estimated from a cube uniaxial compressive strength by multiplying the cube strength by 0.96 for either fiber content studied. The results in Table 3.11 are drastically different for no fibers with the results showing the cubes produced lower uniaxial compressive strengths. However, there was a large coefficient of variation in the collected data. The 2% fiber content results showed a cube strength multiplier of 0.93 to obtain cylinders strengths, which is lower than the value determined by Graybeal and Davis (2008). The different results could indicate further study is needed in determining the size effect of UHPC uniaxial compression testing at different fiber contents.

4. DEVELOPMENT OF "THE LOONEY BIN"

4.1. INTRODUCTION

The following chapter outlines the process by which the Looney Bin was developed and designed. The evolution of the test apparatus, the design and construction of the apparatus, the data collection method, and the evaluation of the fabricated test setup are discussed.

4.2. CONCEPT DEVELOPMENT

4.2.1. General Analysis of Problem

Before development of the triaxial tension test setup, a specimen geometry had to be chosen. As mentioned previously, the majority of triaxial testing that has been conducted on concrete used cylindrical specimens. However, application of tensile forces in more than one direction on a cylindrical specimen is extremely challenging without altering the specimen geometry in ways that create stress concentrations. Due to this difficulty and the need to reduce stress concentrations, cube specimens were chosen for this study. Cubes are ideal for triaxial testing since they provide flat faces in three orthogonal directions for load application.

The next step was determining the size of the specimen. Ritter and Curbach (2015) selected 3.94 in. cubic specimens. However, the use of a non-standard cube size would create issues with repeatability of testing and with form construction. A 2 in. x 2 in. x 2 in. specimen size is reasonable for testing due to it being a standard size for compression testing of grouts and mortars. Also, since the fibers used in this study were 0.5 in. long, the 2 in. dimension was still at least three times the size of the largest

constituent in the mix, thus meeting typical requirements for fiber-reinforced concrete test specimens (ASTM C1609, 2019). For these reasons, a 2 in. x 2 in. x 2 in. cube was chosen as the specimen size for this study. However, using this specimen size limits the fibers to a maximum length of 0.67 in. per ASTM C1609 (2019). Therefore, an attempt was made during the design of the triaxial test setup to provide the option of testing larger cube specimens. This consideration will create the opportunity for triaxial tension testing of larger fiber lengths.

Lastly, the tensile force transfer method had to be determined. Application of tensile forces to brittle materials is inherently complicated by the required load transfer mechanisms. For example, in uniaxial testing, tension is applied to steel specimens through the use of textured wedge grips that are designed to compress into the specimen as tension is applied (ASTM E8, 2021). This load transfer method is feasible due to the general malleability and ductility of steel. If this method were attempted with concrete, its brittle nature would not allow the wedge grip teeth to mold the surface without causing the concrete surface to fracture, thus losing grip strength.

There have been numerous studies evaluating the best method for applying tensile forces to concrete specimens for uniaxial testing (e.g. Lepissier, 2020; Savino et al., 2018; Wille et al., 2014; Graybeal and Baby, 2013). The most common method among these studies was applying tension through the use of collars on dogbone specimens. The use of collars to apply the tensile forces would require casting projections with angled faces on each side of the cube specimen for the collar to react against. This method would cause complications in the specimen fabrication since it would require specialized formwork to cast the bell shapes on each face. Also, the projections from the cube face

would inevitably create stress concentrations on the cube specimen, which are best avoided. Lepissier (2020) was successful in transferring tension stresses through aluminum end caps that were directly epoxied to the ends of dogbone specimens. While the specimen shape provided a larger area for epoxying the end caps than the center area, the epoxy used in that study was not the strongest available and using a stronger epoxy had the potential to mitigate the bond strength issues. Again, the cube specimen could be formed to provide projections on each cube face that creates a larger area for epoxy, but this route was not the most advantageous. Therefore, the method for load transfer would be through metal plates that were epoxied directly to the cube faces using a stronger epoxy than used by Lepissier (2020).

4.2.2. Original Concept

With the specimen geometry, size, and load transfer mechanism chosen, the next step was to design a test apparatus. The initial design consisted of a full test frame. One test frame is shown in Figure 4.1.

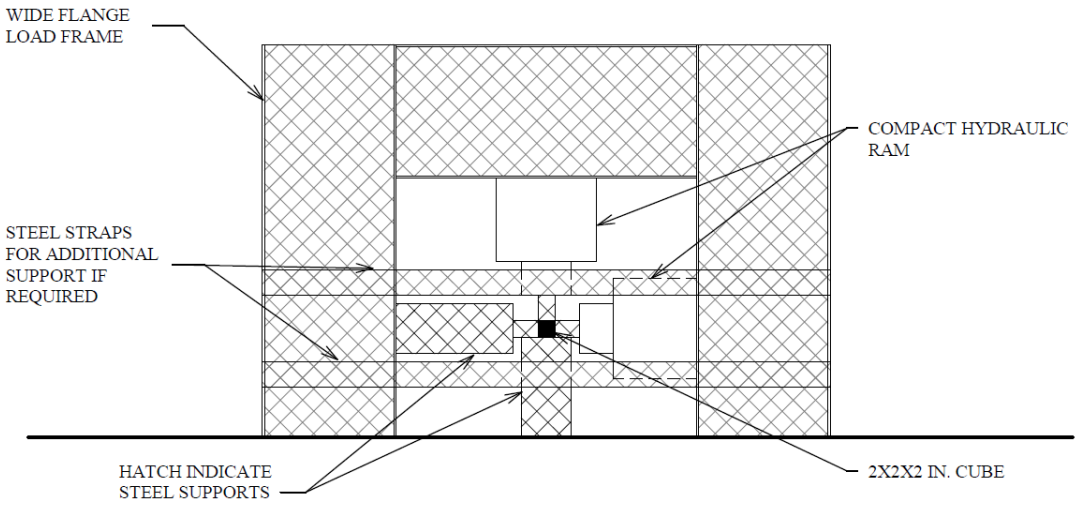

Figure 4.1 – Test frame for initial triaxial test setup

The frame would consist of wide flange steel sections with steel plate straps that straddle the test specimen to help resist the forces required to stress the cube horizontally. The frame would need to be bolted to the Fears Structural Engineering Laboratory (Fears Lab) strong floor to resist vertical loading. The frame would have the ability to apply loading in two of the principal directions. Loads would be applied in the third direction by reacting off steel bulkheads located at Fears Lab that were constructed for prestressing. A ram would be attached at the proper height on one bulkhead and the other would have a support block attached to it for supporting the other side of the cube. Square steel plates would be epoxied to each face for tensile force transfer.

While this test apparatus would be possible and fairly simple to construct, several issues were determined during concept development. The necessity to directly attach to the strong floor would require drilling and epoxying large diameter threaded rods a sufficient amount to withstand the anticipated forces. Doing so would damage the strong floor and the projected threaded rod would create tripping hazards when not in use. Damage to such an important aspect of a testing lab was not considered feasible at the time of initial concept development. Also, such a test frame would be very bulky to maneuver and keeping the frame in place on the strong floor when not in use would take up valuable floor space. Furthermore, the use of the bulkheads also creates movement issues due to their size. For these reasons, the initial concept was discarded.

4.2.3. Creation of a Self-Contained Test Setup

The size issues highlighted with the initial design concept created a new requirement for the triaxial tension test setup. The size of the apparatus must be such that it could be easily moved by a single person. This requirement would make it easier for

future researchers to use this test. However, a smaller apparatus size creates difficulty with load application and measurement since, typically, loads are applied using hydraulic actuators and measured using load cells, both of which impose physical limitations in terms of size, weight, and maneuverability. With these issues in mind, a load application method was developed that would not require the use of conventional hydraulic actuators and load cells. This thinking led to the design of a test apparatus consisting of a cube manufactured with metal plates that was hollow inside where the test specimen would be located. The load would be applied by threaded rods that would penetrate through the walls of the metal cube. On the outside of the cube, nuts would be attached to the threaded rod so that, as the nuts were fed down the length of the exposed rod, they would react on the outside face of the plate and pull the threaded rod. On the inside, a clevis would be epoxied to the cube face and the threaded rod would be attached to the clevis, completing the load path for the tensile forces. Tightening of the nut would then pull on the threaded rod, applying a tensile force to the clevis, which would be attached to the specimen. The use of individual plates to assemble the cube would also provide the ability to apply concurrent compressive forces along one of the three axes using the Baldwin test machine located in Fears Lab.

4.3. DESIGN AND FABRICATION OF THE LOONEY BIN

4.3.1. Design of the Looney Bin

After the initial analysis of the problem, the following requirements were set prior to design of the Looney Bin:

1. It must be small enough to be easily transported by one person.

2. Since the load application will occur in three orthogonal directions simultaneously, it must be a cube shape.
3. It must be easily deconstructed to ensure attaching and removing test specimens takes a reasonably small amount of time to complete.
4. It must be large enough to provide space for the test fixtures needed for tensile force application.
5. It must be possible to adjust the test setup for larger specimen sizes to facilitate future testing of longer fibers.
6. It must allow for the application of compressive loads along one of the three axes using the Baldwin test machine located in Fears Lab.

These requirements led to the test setup being constructed out of ASTM B209 (2014), Grade 6061 (yield strength of 35,000 psi) aluminum plates that were bolted together. Aluminum plates were chosen to reduce the overall weight of the test setup, while also making fabrication easier. Using bolts to connect the plates ensured ease of construction and deconstruction. The plate thickness would need to be large enough to accommodate bolts that are tapped through the plates thickness, large enough to withstand anticipated failure loads of the test specimens, and thin enough to keep the weight manageable for one person to maneuver. As a starting point for design, the bolt size was set to 0.25 in. in diameter. With this bolt size chosen, an initial plate thickness of 0.5 in. was chosen.

The next step was to determine the overall size of the test setup. To determine the required dimensions, the load application fixtures had to be designed first. An anticipated

peak tensile load of 5,000 lb was chosen for the design of the test setup. This load would represent a failure stress of 1,250 psi for the cube specimens, which is near the failure stresses of the UHPC test by Graybeal and Baby (2013). The load application method chosen involved tightening a threaded rod that would react off the plate wall and would be attached to a clevis that was epoxied to the cube. The other side of the cube would then need to be attached to the wall of the test setup to complete the load path. Epoxying directly to the plate wall would not be feasible since the process of running multiple tests would require replacing the plates for each test. Therefore, separate individual blocks of ASTM B221 (2020), Grade 6061 aluminum bars that would bolt directly to the plate wall would be epoxied to the cubes to act as plinths. This would allow for easy attachment and removal of test specimens without the need to disassemble the entire apparatus.

The plinths and clevis plates that would be epoxied to the cube faces were set to 1.875 in. x 1.875 in. in cross section to ensure that there were no interferences at the corners of the cube specimens. The aluminum plinths were machined out of 2 in. x 2 in. aluminum bar stock with the same dimensions as the clevises. No pre-manufactured clevises were found that had the required dimensions, so the clevises were fabricated out of steel plate stock. The clevises were designed to be attached to a 0.5 in. ball joint using a steel shank, and the ball joint would attach to the threaded rod. The ball joint size was chosen for its availability and has a tensile strength of 10,000 lb, which exceeds the anticipated peak load. ASTM A193 (2020), Grade B7 threaded rods with a diameter of 0.5 in. were chosen to simplify the connection to the ball joint. The 0.25 in. plates welded to the clevis plate were made the same size as the cube specimen to help when epoxying the clevis to the cube. The plinth height was set to 1.5 in. to allow for the bolts to thread 1

in. into the plinth and two offset bolts were used to reduce the risk of twisting the plinths when tightening the bolts. A total of nine plinths and nine clevises were constructed to allow for gluing and testing of three cubes during a single session. The fabrication drawings for the clevis and plinths are shown in Figure 4.2 and Figure 4.3, respectively. The American Institute of Steel Construction (AISC) Steel Construction Manual (14th ed., 2011) was used to determine the capacities of the steel fixtures and the yield stress was used to determine the axial capacity of the aluminum plinths to ensure they were adequately sized for the design force. The capacities are shown in Table 4.1.

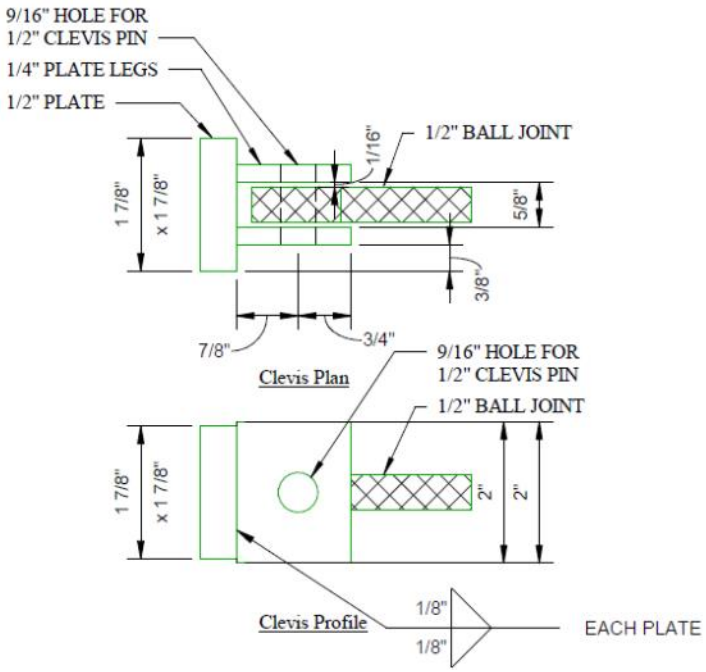

Figure 4.2 – Clevis fabrication details

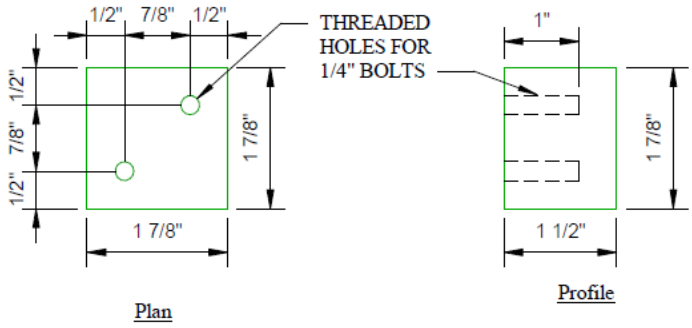

Figure 4.3 – Plinth fabrication details

Table 4.1 – Capacities of load application fixtures

Fixture	Material	Controlling Case	Capacity (lb)
Clevis Plate	ASTM A36	Bolt Bearing (Eq. J3.6b)	16,313
Clevis Plate Weld	ASTM A36	Base metal (Eq. J2-2)	32,625
Clevis Pin	ASTM A36	Shear (J3-1)	12,823
Plinth	Aluminum, Grade 6061	Axial Tension	123,047
Threaded Rod	ASTM A193, Grade B7	Bolt Tension (J3-1)	12,690

With the plinth and clevis sizes determined, the interior dimension required for the specimen and test fixtures could be determined. The length of each piece of the test setup in one direction was as follows: 1.5 in. plinth, 2 in. specimen, 2.125 in. clevis, and 1.5 in. shank thread length for the ball joint. The combined length (excluding epoxy thickness) was 7.125 in., which would set a minimum interior dimension of the test setup to 8 in. However, fibers with up to 1.3 in. lengths have been tested in UHPC (Wille et al., 2014). This fiber size would set a minimum cubic specimen dimension to 4 in. Accounting for this new size, the fixture length would increase to 9.125 in., with a

minimum interior dimension of 10 in. Aluminum plate stock with a 12 in. width was readily available at the time of fabrication and, using a 0.5 in. thickness, would allow for an interior dimension of 11 in. with inset plate construction. Therefore, the interior dimension was set to 11 in. with an outside dimension of 12 in. This width would provide a large enough interior section to house cubes with dimensions up to 4 in. while not being overly bulky. The next step in the design process was developing fabrication drawings for the plates. The fabrication drawings for the aluminum plates are shown in Figure 4.4.

With the plinth sizes chosen, the specimen would have to be attached to a corner of the cube test setup, which provided the benefit of increasing the stiffness of the overall test since the load would be applied close to a support (plate wall). The test apparatus was designed to have two plates that are inset on all four sides (labeled left and right plates), two plates that are inset on the top and bottom and directly supported by two side plates on the other two edges (labeled side plates), and the top and bottom plates would be directly supported on all four edges by the other four plates. The plates were attached together with three bolts on each edge to provide stability and stiffness. All edges that were inset had 1 in. deep threaded holes that were centered in the plate thickness. All edges that were supported by a plate edge had 9/32 in. holes for the 0.25 in. diameter bolts (provides 1/32 in. clearance for bolts).

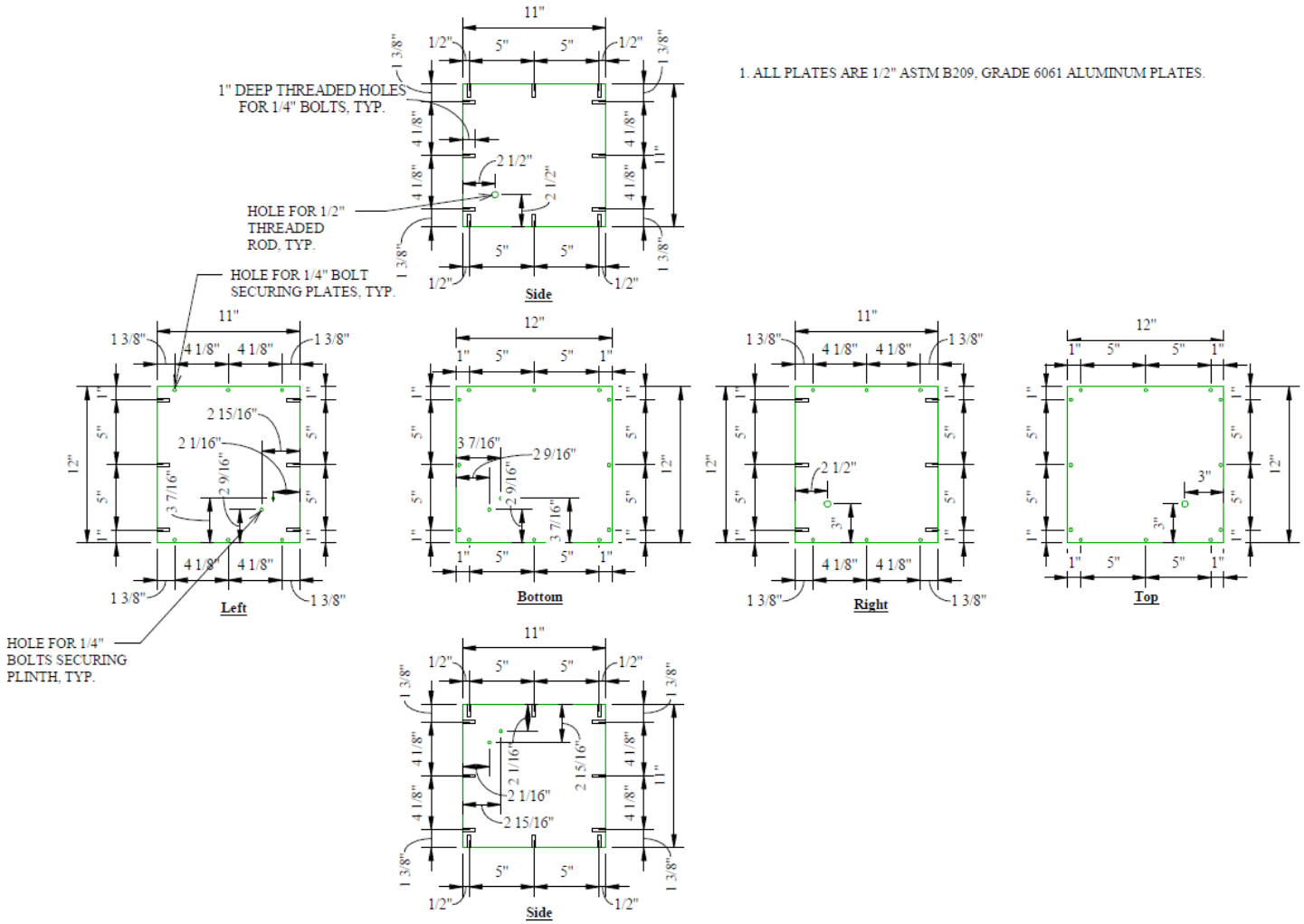

Figure 4.4 – Plate fabrication details

The final step in the Looney Bin design process was to ensure the plates and the bolts were adequate to resist the design force. The bolts chosen were SAE-J429 (2014) Grade 5 bolts, having a minimum tensile strength of 120,000 psi. The shear strength of the bolts was taken to be 45% of the tensile strength (nominal shear strength in bearing-type connections) per Table J3.3 of the ASCE Steel Construction Manual (14^{th} ed., 2011), or 54,000 psi. A 0.25 in. diameter bolt with 20 threads per inch has a solid cross-sectional area of 0.031 in^2 (Engineersedge.com). Therefore, the shear strength per bolt is 1,674 lb and a minimum of three bolts would be required to withstand the 5,000 lb design load. Each plate that was bolted has a minimum of six bolts, so the bolting pattern was sufficient.

A preliminary plate thickness was determined assuming the plate was simply supported on two edges and the 5,000 lb design force was applied directly in the center of the plate. With these assumptions, a minimum plate thickness of 0.45 in. was determined, which is smaller than the 0.5 in. thickness assumed when determining the interior clearances. Then, a finite element analysis was conducted on each of the plate types using ANSYS© Workbench V. 19.1. Analysis models were developed for each of the three plate edge support conditions to ensure the plates were not stressed above the yield strength of 35,000 psi. The plates were modeled with the appropriate dimensions and hole locations based on the fabrication drawings. The analysis was conducted using Grade 6061 aluminum material properties. The boundary conditions were set to displacement limits of zero at the plate supported edges and the fully bolted edges to allow for rotation of the plate ends, which is a conservative assumption since the bolt tightening would provide a level of fixity. The 5,000 lb load was applied as a stress on an

idealize area representing the size of a washer, since the use of washers was anticipated. Each of the models exhibited stress concentrations at the load application area above the yield strength of the material but, these were only small areas and the stress quickly dissipated to below the yield strength in the surrounding area. Therefore, the 0.5 in. thickness was deemed adequate for the Looney Bin. However, the use of larger specimens would require a higher design force. The 0.5 in. thick plates would then be inadequate and larger plate thicknesses would be required for larger specimen sizes. For this study only 0.5 in plates were fabricated. The models for each of the plate types are shown in Figure 4.5, Figure 4.6, and Figure 4.7.

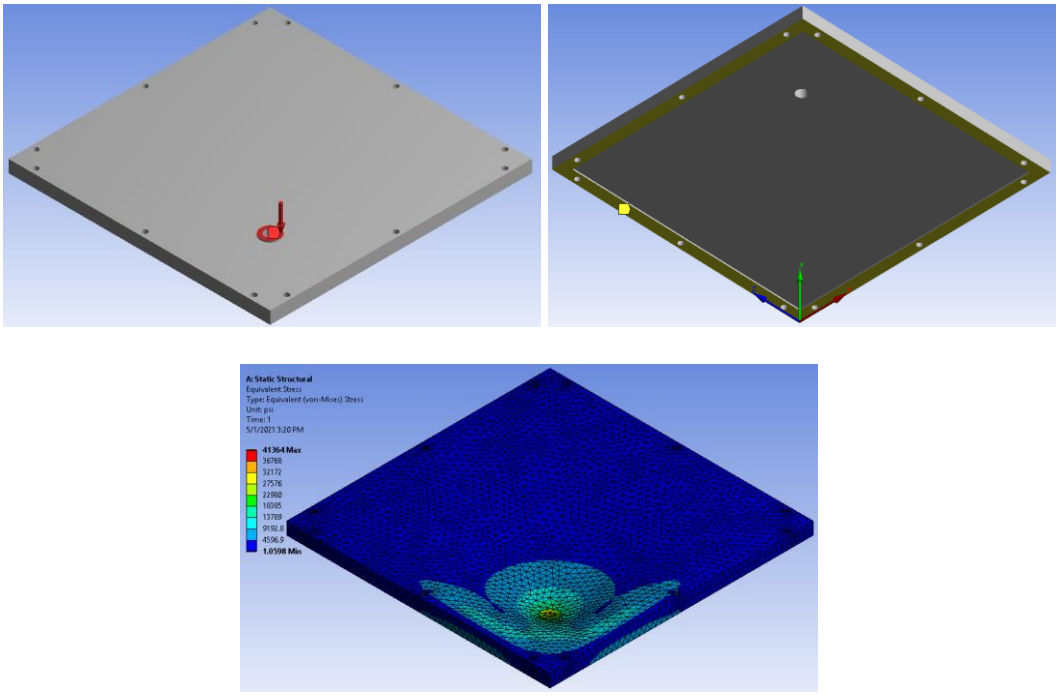

Figure 4.5 – ANSYS© model for top and bottom plates showing load (top left), boundary conditions (top right), and Von Mises stresses after analysis (bottom)

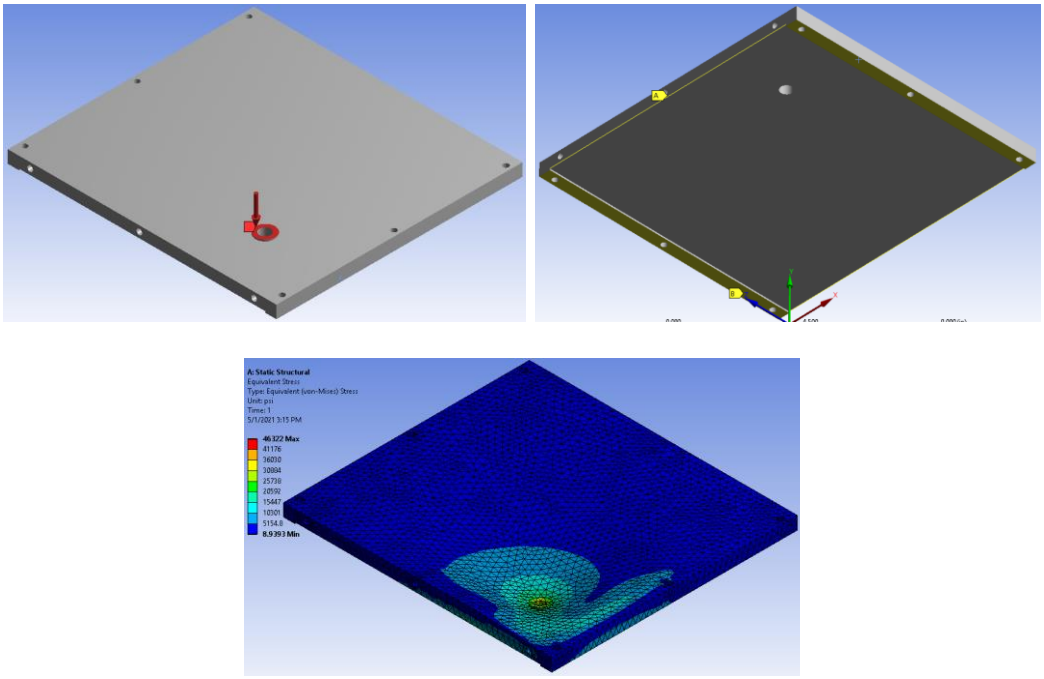

Figure 4.6 – ANSYS© model for left and right plates showing load (top left), boundary conditions (top right), and Von Mises stresses after analysis (bottom)

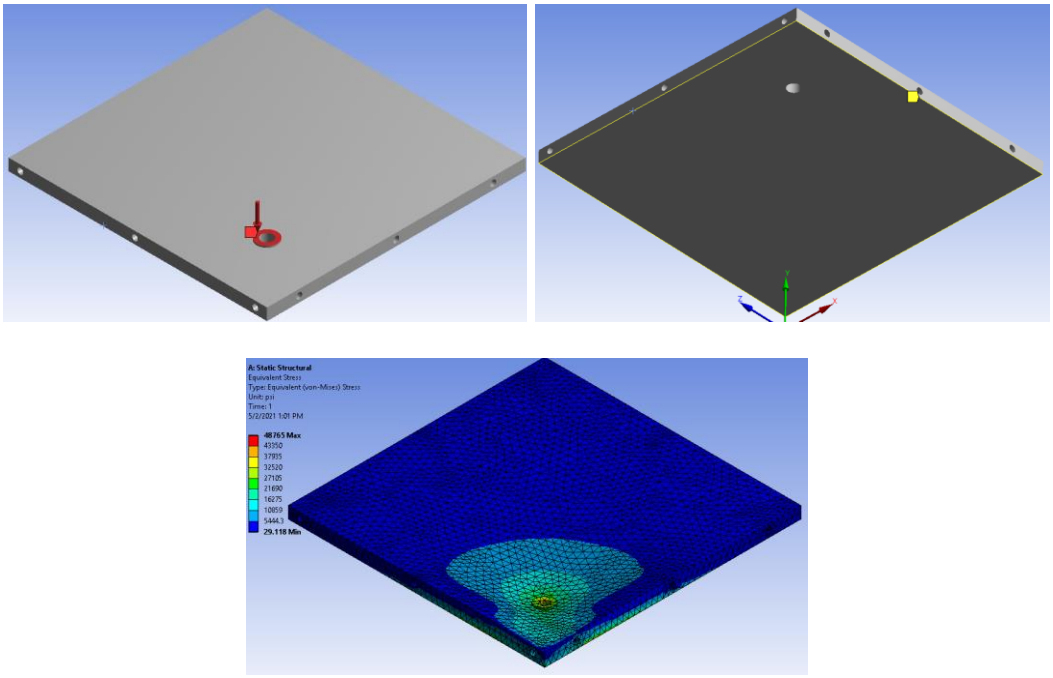

Figure 4.7 – ANSYS© model for side plates showing load (top left), boundary conditions (top right), and Von Mises stresses after analysis (bottom)

4.3.2. Fabricated and Assembled Looney Bin

The fabricated and assembled Looney Bin is shown in Figure 4.8 and Figure 4.9. Examples of the fabricated clevises and plinths are shown in Figure 4.10 and Figure 4.11, respectively. The plinths are shown bolted to the walls of the Looney Bin prior to gluing a cube in Figure 4.12. A fully glued specimen is shown in Figure 4.13.

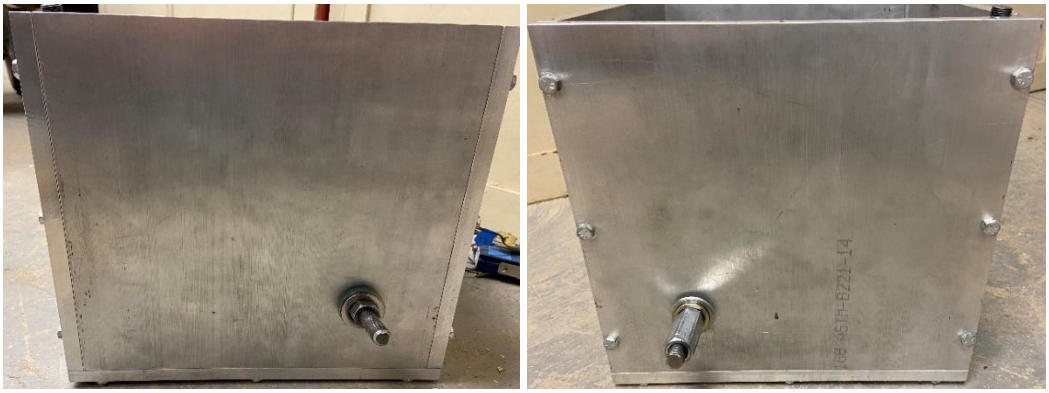

Figure 4.8 – Fully inset (left) and partially inset (right) plates on Looney Bin

Figure 4.9 – Constructed Looney Bin with top plate

Figure 4.10 – Fabricated clevises

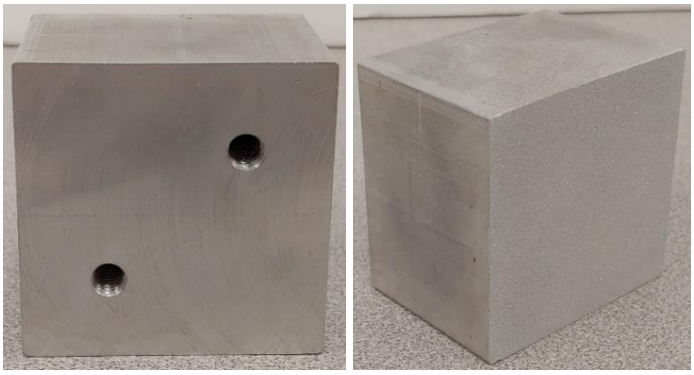

Figure 4.11 – Fabricated plinths

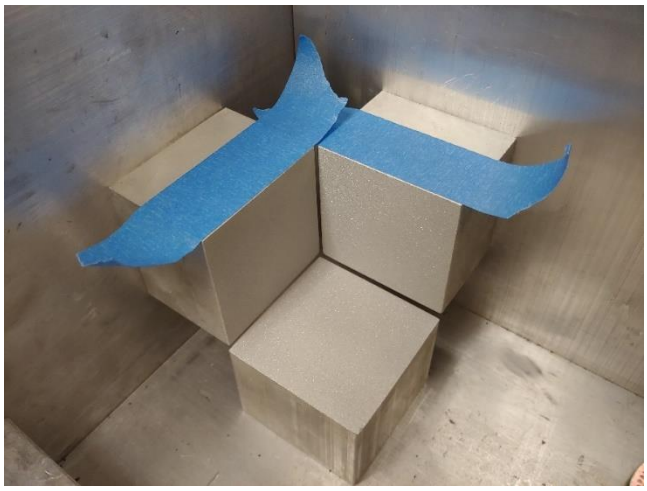

Figure 4.12 – Plinths bolted to the Looney Bin walls

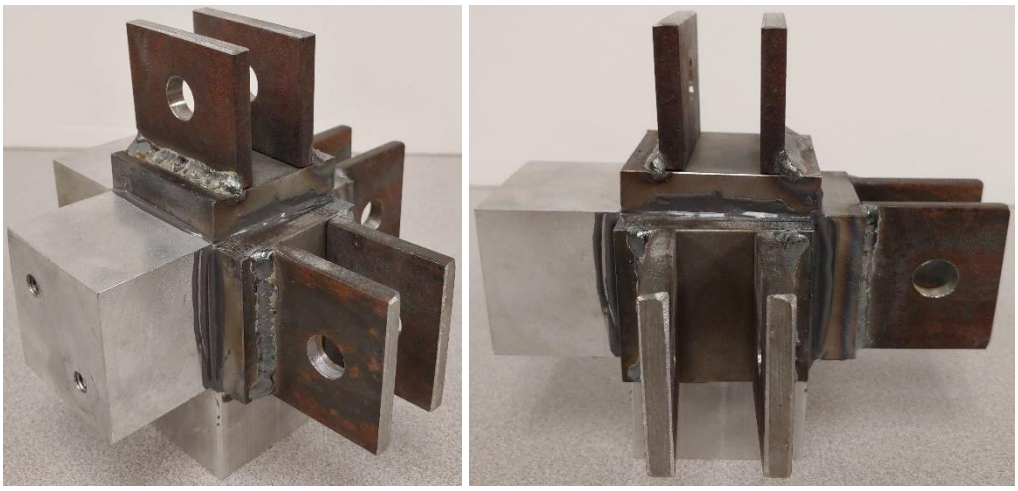

Figure 4.13 – Specimen with fixtures attached

4.4. DATA COLLECTION METHOD

4.4.1. Coupling Nut Load Cell Construction

With the apparatus fabricated, the load application method was designed. Earlier it was stated that the tensile force would be developed by tightening a nut on the threaded rod that would react off of the Looney Bin plate wall. A load cell would then need to be constructed to measure the load applied from tightening the nut and would connect the ball joint to the threaded rod. This was facilitated by construcing a load cell using a standard, 2 in. long coupling nut with strain gauges attached to measure the tensile force. Two strain gauges were attached on diametrically opposite sides of the coupling nuts along the centerline, then the strain gauges and their exposed wires were covered with RTV silicone to help protect them from accidental contact. The strain gauge wires were zip tied to the coupling nut approximately 0.5 in. from the strain gauge for strain relief. The Baldwin testing frame was used to calibrate the coupling nut load cells.

The strain gauge readings were collected using National Instruments™ (NI) data collection equipment coupled with the program, LabVIEW™. The strain gauge output was measured by attaching the wires to an NI 9236 quarter bridge, 350 Ohm strain gauge module. The module was then inserted into an NI CompactDAQ eight slot USB chassis, which was then directly connected to a computer using a USB cable. Since the Looney Bin was designed to be a closed system, a hole was required through a plate wall to allow the wires to be fed out of the apparatus for data collection. The hole for the wires and the wired module is shown in Figure 4.14.

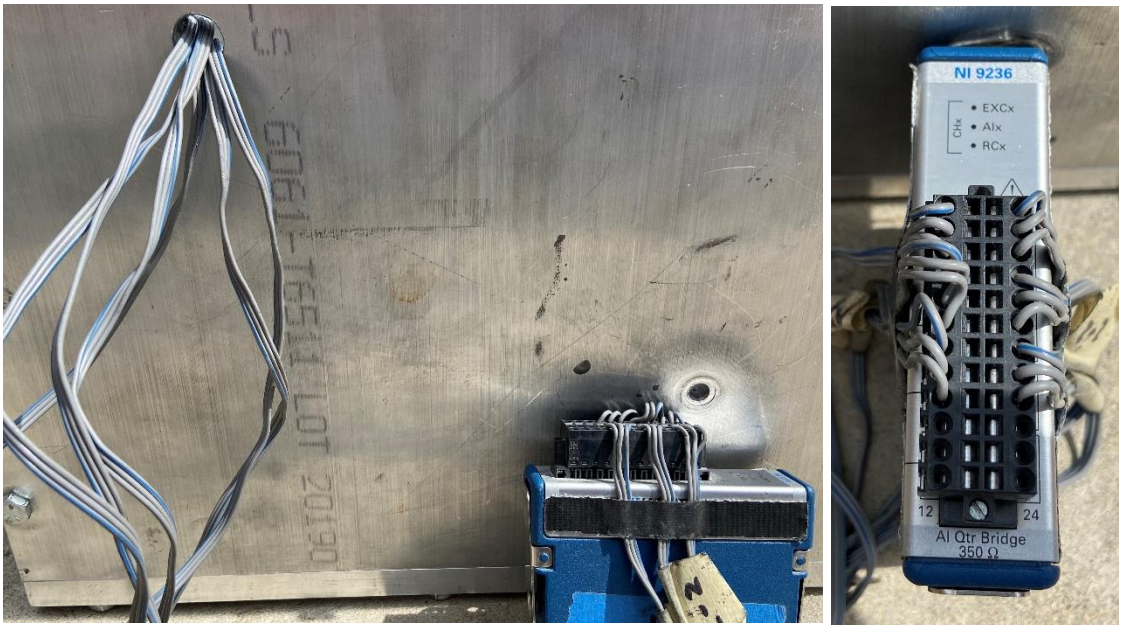

Figure 4.14 – Wiring setup for the Looney Bin

LabVIEW™ code was then written to read each of the attached strain gauges and average the readings of the two strain gauges attached to each coupling nut. The averaged strain readings were labeled to match one of the three principal stresses applied. The

averaged readings were then multiplied by a scalar number that would translate the strain readings to a load reading after calibration was conducted. The data was then fed through plotting programs so the load application could be monitored during testing and then it was written to a text file for post-processing. A tare button was also added to the program to allow for a non-zero start point in data collection. Also, the load cells were labeled one, two, and three to correspond to the same labels shown on the program screen (Figure 4.15). Sigma one was in the direction of the top and bottom plates, sigma two was in the direction of the fully inset (left and right) plates, and sigma three was in the direction of the partially inset (side) plates. The program was also capable of displaying the maximum value in the sigma one direction, which was the direction the load was applied to failure. The program display screen and block diagram are shown in Figure 4.15 and Figure 4.16.

Figure 4.15 - LabVIEW™ test program screen

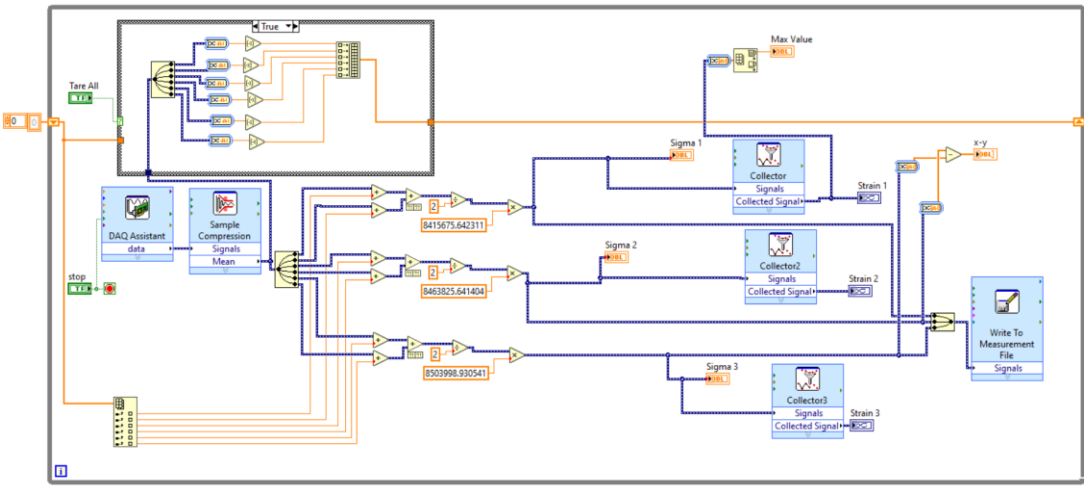

Figure 4.16 – LabVIEW™ block diagram showing coding

4.4.2. Coupling Nut Load Cell Calibration

The calibration of each of the coupling nut load cells was conducted using the two middle crossheads of the Baldwin testing machine. Long pieces of threaded rod were locked into the top and middle crossheads and the coupling nut load cell was connected to both pieces of rod. Then, tension was applied by tightening a nut on the outside of the cross head, thus pulling on the threaded rod and the connection to the opposite crosshead, to mimic the load application in the Looney Bin. Initally, the threaded rods were embedded approxmately halfway from each end of the coupling nut load cells (the rod ends would be touching at the center of the load cell). However, this method of attachment made calibration difficult since the rods were threaded over the area of the coupling nut load cell where the strain gauges were attached, causing the load transfer to occur in those locations and affecting the strain gauge readings. This would cause the coupling nut load cell calibration to appear incorrect when the coupling nut was removed and reinserted to be checked. If the threads were not in the exact location as the

calibration, then the strain readings would be different. To remedy this, the threaded rods were only inserted into each end of the coupling nut load cell a distance of 0.5 in. (the diameter of the threaded rod). This way, the threaded rods would not overlap with the attached strain gauges and no issues would occur during calibration.

Once the coupling nut load cells were calibrated, they were attached to the ball joint and threaded rod, ensuring only 0.5 in. of thread from each fixture was inserted into the coupling nut load cell. A smaller nut on each of the fixtures was used as a guide to ensure the appropriate amount of thread was inserted into each coupling nut load cell. The guide nut was located 0.5 in. from the end of the respective fixtures, then the fixture was threaded into the coupling nut load cell until it reached the nut. Once both fixtures were attached, the guide nuts were tightened on the coupling nut load cell a sufficient amount (applying slight compression) to ensure the threaded rod and ball joint did not come loose during testing. A completed coupling nut load cell is shown attached in the test fixture in Figure 4.17.

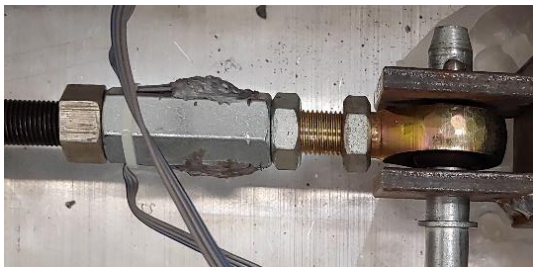

Figure 4.17 – Coupling nut load cell attached to test fixture

4.5. EVALUATION OF FABRICATED TEST SETUP

4.5.1. Establishing Specimen Gluing Procedure

Once the coupling nut load cell was calibrated, the Looney Bin fabrication was complete and trial runs could commence. The first step to the testing procedure was choosing a suitable epoxy to conduct the tests and to establish an appropriate method for gluing. The epoxy for this test must be able to withstand the design direct tensile force for the Looney Bin (5000 lb force, which equates to 1,250 psi on the specimen). Also, for ease of testing and to ensure testing continuity, the epoxy must be readily available and easy to obtain. While reviewing the literature for various epoxy brands, it became apparent that most companies do not publish direct tensile bond strengths. The lap shear strength with various materials was another test method used to show bonding strength. The direct tensile strength of the epoxy was also a commonly published value. A list of epoxies identified for potential use in this study is shown in Table 4.2.

Table 4.2 – Initially considered epoxies

Epoxy Brand	Strengths (psi)			
	Direct Tension	Tension Bond	Slant Shear	Lap Shear
Sikadur® -31 Hi-Mod Gel	3,300	420	2,900	NA
Loctite EA® 907™	3,100	NA	NA	3,000
J-B Weld™	5,020	NA	NA	NA
J-B Weld™ Clearweld™	3,900	NA	NA	NA
Devcon® 2 Ton® Epoxy	2,500	NA	NA	NA
Gorilla® Epoxy	3,300	NA	NA	NA

NA – Not Available

One aspect of these epoxies that made selection difficult was their lack of testing uniformity. The only epoxy brand to provide a tensile bond strength was far too weak to

be considered for this test. The only property that all the considered epoxies had in common was the direct tensile strength. While tensile strength may not have a proportional relationship with tensile bond strength, it was assumed that the largest tensile strength would have the largest bond strength. Therefore, the two J-B Weld™ epoxies were considered in the initial trials. Also, the J-B Weld™ epoxies were both readily available at local hardware stores, ensuring testing continuity. While the original J-B Weld™ showed the highest strength, the Clearweld™ epoxy had a faster set time, which would allow for faster testing. Therefore, initial cube tests were conducted using Clearweld™ epoxy. An epoxied specimen is shown in Figure 4.18.

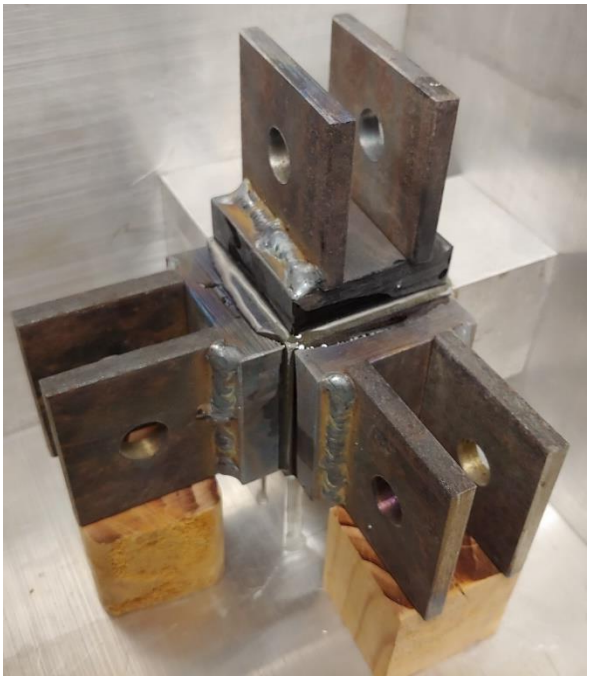

Figure 4.18 – Glued specimen

Prior to applying any epoxy, the cube specimens were measured in all three orthogonal directions for accurate stress calculations. Initially, each specimen was glued in the Looney Bin. The epoxy procedure started with applying the epoxy to the three faces of the cube specimen that would be in contact with the plinths (the plinth configuration just prior to cube placement is shown in Figure 4.12). Painter's tape was placed on the top of the plinths and side clevises to reduce the overlapping of epoxy from the top clevis with the side clevis. Once those three sides were covered with epoxy, the cube was carefully placed on the plinths. Then, the two clevises that would go on the sides of the specimen were coated in epoxy. Pieces of wood were machined to be exactly 1.5 in. tall (the same height as the plinths to ensure the clevises were centered on the cube) to act as stands for the side clevises while the epoxy was curing. Once the two side clevises were put in place, the top clevis was coated in epoxy and carefully placed on top of the cube. The Looney Bin was carefully leveled to ensure the top clevis stayed in place while the epoxy cured. After placement of the top clevis, a scraper was used to remove epoxy from the adjacent fixtures not protected by painter's tape. Painter's tape that was attached to both the Looney Bin plate wall and the clevis was also used to hold the top clevis in place. The specimens were then allowed to cure for one hour per the manufacturer's recommendations. The glued specimen is shown removed from the apparatus in Figure 4.19.

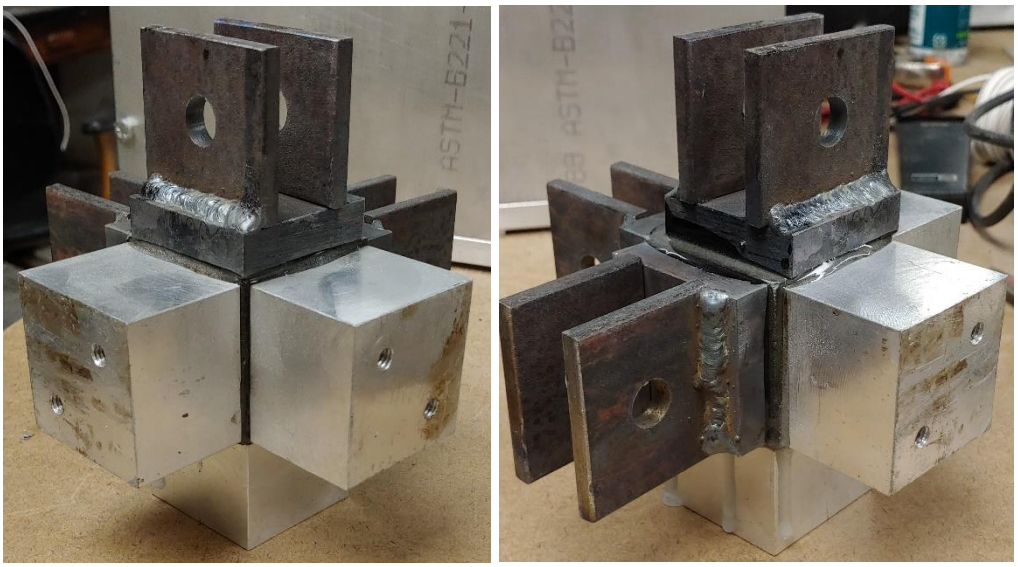

Figure 4.19 – Glued specimen after curing

One aspect of UHPC that drastically improves its durability performance is its very low permeably. While low permeability is great for durability, it drastically reduces the epoxy bond strengths. The first test was conducted using a cube with no surface preparation to enhance bond strength. This test only reached a stress of approximately 400 psi before bond failure between the concrete face and the epoxy. This issue led to the idea of sandblasting the cube faces prior to gluing. The sandblasting removes the outer surface of the concrete faces and helps to create a roughened surface, while not doing any internal damage to the specimen. The specimens were then measured after sandblasting. A comparison of a sandblasted cube to the cube as it looks after curing is shown in Figure 4.20. The same issue of bonding occurred when epoxying to smooth steel and aluminum. Therefore, all glued surfaces were sandblasted prior to gluing. Also, the metal fixtures were cleaned with acetone after sandblasting. Examples of the initial failures is shown in Figure 4.21 (bond with clevis) and Figure 4.22 (bond with plinths).

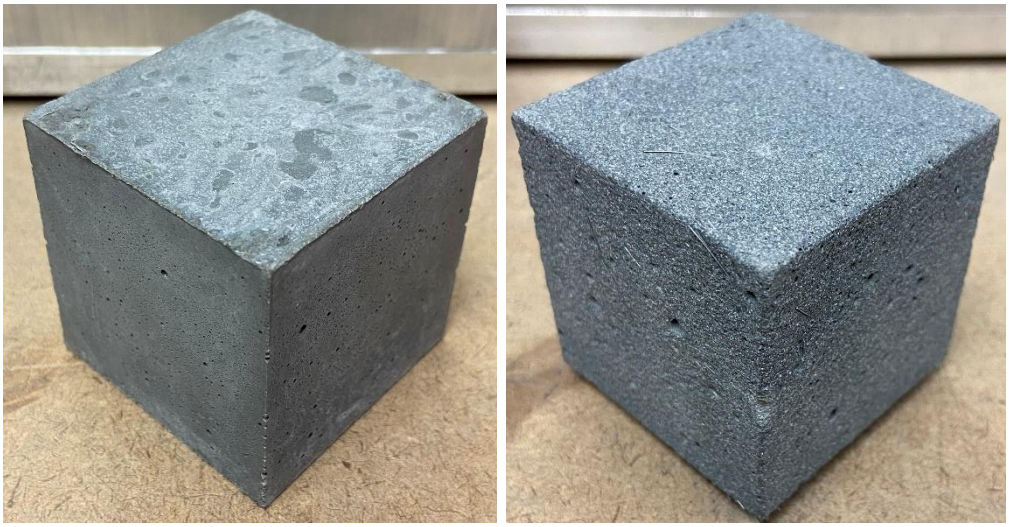

Figure 4.20 – Cube specimen before (left) and after (right) sandblasting

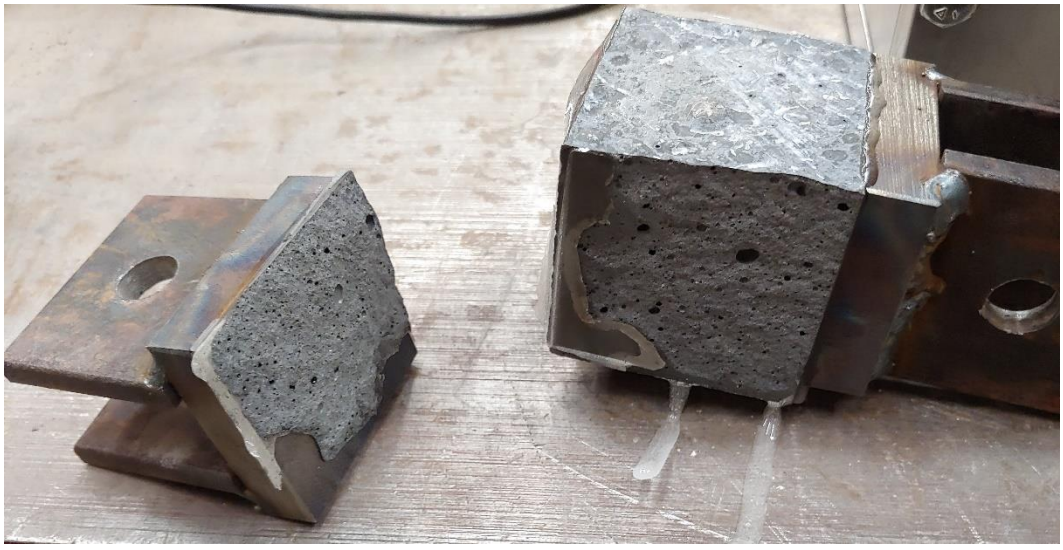

Figure 4.21 – Evidence of bond failure on clevis

Figure 4.22 – Evidence of bond failure on plinths

Another issue that was noted during the initial gluing attempts was caused by the epoxy viscosity. The photo on the right of Figure 4.19 shows signs that the viscosity of the epoxy was too low, causing it to leak down the specimen before it cured. This leaking created unbonded areas between the two surfaces, as shown in Figure 4.23. Due to this issue, the original J-B Weld™ was chosen for further testing since it has a much lower viscosity.

Figure 4.23 – Specimen exhibiting signs of epoxy leakage during curing

However, one issue with the original formula was its slow cure time. While the Clearweld™ had a set time of five minutes and a cure time of one hour, the original formula had a set time of four to six hours, and a cure time of fifteen to twenty-four hours. This required longer wait times until the specimens could be moved out of the Looney Bin and before testing could begin. Initially, the low end of the set time was used as the time it would be safe to remove the wood support blocks from the side clevises and take the specimen out of the test setup to start gluing another specimen. However, this time turned out to be too early, causing the clevises to slowly slide down the specimen after removal, as shown in Figure 4.24. Therefore, the specimens were allowed to sit undisturbed for at least six hours prior to removal of the support blocks. The specimens were also allowed to cure at least 24 hours before being tested to maximize bond strength. No epoxy bond failures were seen after making these changes.

Figure 4.24 – Clevises that slid down cube due to premature removal of wood support blocks

Lastly, the fabrication of the clevises and plinths for the Looney Bin took a large amount of time and energy, so it was more advantageous to clean and reuse the fixtures in lieu of making new sets for each test. This was done by heating the fixtures to a temperature above the epoxy maximum temperature of 600°F using an oxygen and acetylene cutting torch. Once the epoxy was thoroughly heated, it was cleaned off the fixtures using a putty knife and steel wire brush. However, care had to be taken when heating the aluminum plinths since the risk of melting was higher due to their lower melting point of approximately 1,200°F (Figure 4.25). After the specimens were cleaned and allowed to cool, they were ready to be prepped for the next test.

Figure 4.25 – Plinth with melted corner caused by overheating with cutting torch

4.5.2. Finalizing The Test Setup

A glued specimen with fixtures attached just prior to sealing of the bin with the top plate is shown in Figure 4.26.

Figure 4.26 – Specimen just prior to testing

Once the speimens were glued and allowed to cure, they were bolted into the Looney Bin and the ball joints were attached to the clevices using steel pins. After the ball joints were attached, the top plate was bolted in place, as shown in Figure 4.27.

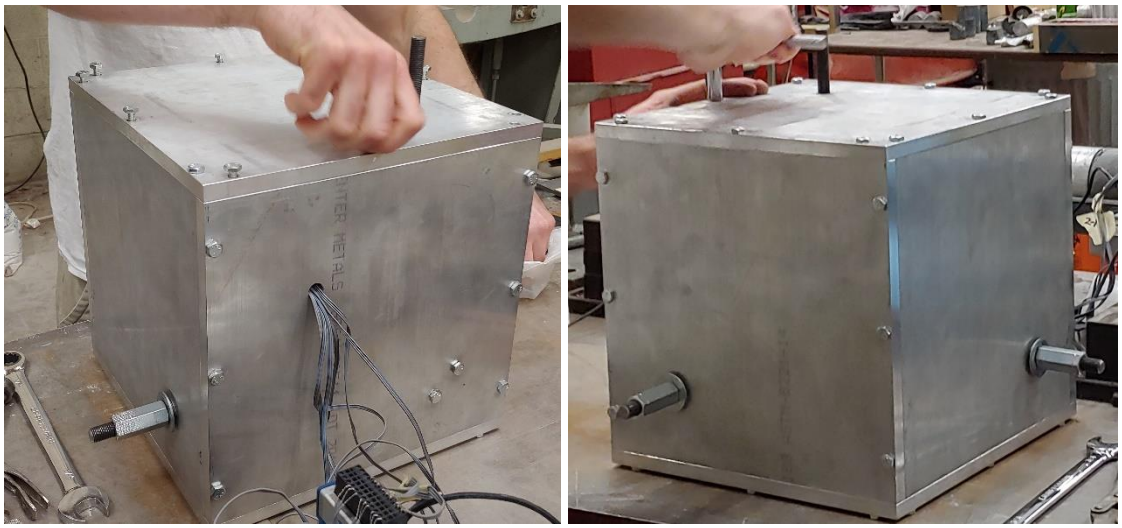

Figure 4.27 – Attachment of top plate to the Looney Bin

The bolts for the top plate were first hand tightened, then a rachet was used to tighten to snug tight. The bolts in a corner were tightened first, then the opposite side was tightened for each subsequent bolt until all of the bolts were tightened. Once the bolts were tightened, the washers were placed on the sigma one threaded rod protruding through the top plate and the nut tightened down until it just touched the washers. Before attempting any tests, concerns were raised about friction development between the nut, washer, and the Looney Bin plate wall during load application. To help reduce friction development, needle-roller thrust bearings sandwiched by equal-diameter thin washers were placed between the plate wall and larger diameter washers. These washers were

designed for slowly rotating equipment and provided a large reduction in friction. A larger washer was used between the tightening nut and the thrust bearing washer to prevent damage to the thrust bearing washers. Also, vice grips were initially used to keep the threaded rod from turning with the nut once larger tensile forces were reached, as shown in Figure 4.28. However, since attaching the vice grips to each threaded rod was time consuming and difficult, the threaded rod was greased where it contacted the nut to reduce friction between the two sets of threads. The addition of grease was sufficient to allow for smoother tightening without also rotating the threaded rod.

Figure 4.28 – Nut and washer setup with vice grips attached

Once the nuts were in place and ready to test, the entire test setup was clamped to a steel table to keep the apparatus from rotating when each nut was tightened. Also, aluminum blocks were clamped to either side of the apparatus to provide further resistance to rotation when tightening the nut for the sigma one direction. The completed test setup prior to load application is shown in Figure 4.29.

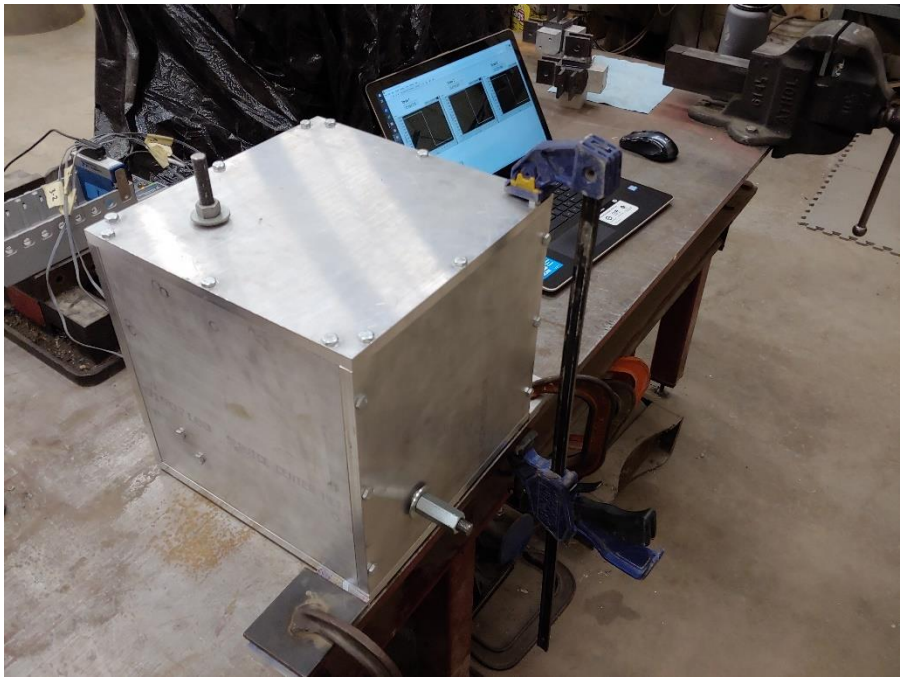

Figure 4.29 – Test setup just prior to load application

After the apparatus was fully clamped, the test was ready to start. The data collection system was first fully wired, the USB connection was made to the laptop, and the program was opened. The program was run several times to ensure the connections were adequate to properly read the data acquisition system. Once the connections were verified, the program was started and tared to zero. Since this test setup would not allow for easy proportional loading, the load was applied in the sigma two and three directions (labeled side stresses) first. Load application was started in the sigma two direction up to the specified stress first, then the sigma three direction load was applied, and lastly the load was applied in the sigma one direction until failure. In some cases, such as the fiber reinforced cubes, failure would occur in the sigma one direction and only a reduction in stress would be seen in the sigma two and three directions. This appeared to be due to the

initiation of a crack that was held together by fibers or the test fixture itself. In these cases, after failure in the sigma one direction, force was applied in the other two directions to propagate the cracks that were initiated and essentially fracture the cube apart. This was done to better highlight crack formation and expose the failed surfaces. A sample of the collected raw data for a cube with side stresses set to 800 psi (3,200 lb) and a sigma one failure load of 4,626 lb is shown in Figure 4.30.

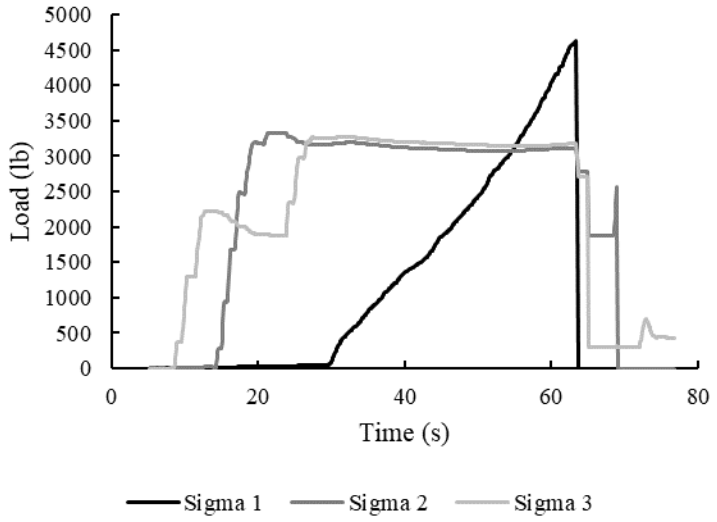

Figure 4.30 – Example of raw data collected for side stress of 800 psi (3,200 lb)

In the initial test attempts, the load in the sigma one direction was applied quickly up to failure. However, to reduce the effect of large stress rates on the failure loads, the load in the sigma one direction was applied in a relatively slow manner. Care was taken to apply the load at a rate less than 35 psi/s. However, since the load application method was manual, the load rates did vary between 15 and 35 psi/s. The loads in the sigma two

and three direction were applied quickly without regard for the load rate. The load application in the sigma three direction is shown in Figure 4.31.

Figure 4.31 – Load application in the sigma three direction

4.5.3. Troubleshooting During Data Collection

Several issues were encountered during the data collection process. One issue encountered was the fully inset plates tended to shift inward when the sigma two stress was above approximately 400 psi. This was due to that plate only being supported by the bolts and side friction with the adjacent plates. Once the side friction strength was overcome, the plate would move until the supporting bolts were in contact with the edge of the hole in the adjacent plate. This movement was enough to cause misalignment of the next specimen plinths, making it more difficult to attach the specimen in the Looney

Bin. A large amount of resistance was noted when attempting to bolt these next specimens into the Looney Bin. Also, the subsequent tests tended to fail at much lower stresses, and in some cases failure occurred before load application in the sigma one direction. This may have been due to the misalignment from the plate movement offsetting the bolts for the plinths enough to create additional stresses upon forcing the bolts in the plinths of the next specimen. These additional stresses would create premature failure of the subsequent test. Two methods were used to reduce the amount the inset plate would move during high stress applications. First, the load application order was changed to start with sigma three instead of sigma two. This would help by applying force in the plane of the inset plate to essentially clamp it and increase the frictional resistance. Second, bars of aluminum were machined to be exactly 11 in. long and were place in the bottom of the Looney Bin to brace the bottom of the plate. The locking bars are shown in Figure 4.32. These two mitigating methods were enough to reduce the likelihood of the misalignment being large enough to induce stresses when inserting the specimens. However, as a precaution, the side plates were loosened and retightened around the locking bars periodically to maintain the specified interior dimensions.

Figure 4.32 – Locking bars placed to reduce movement of inset plates

Another issue encountered early in testing was damage to a strain gauge wire, shown in Figure 4.33. This damage was caused by the wire being stuck between the top plate of the Looney Bin and the nut above the load cell following failure of the specimen. When failure occurs, the energy is released by the threaded rod jumping up at a high rate and, in some instances, bouncing off the top plate of the apparatus. When the wire was caught between the nut and the wall, it was severed. Since the wire was damaged, the load cell was no longer functional. This required the removal of the strain gauges, reapplication of new strain gauges, and recalibration of the coupling nut load cell. To help reduce the likelihood of this damage occurring again, each strain gauge wire was taped near the strain relief zip tie for protection.

Figure 4.33 – Damage to strain gauge wire in the sigma one direction

The initial size of the clevises also posed a problem upon testing UHPC containing fibers. The clevis plates were initally fabricated to be 1.875 in. x 1.875 in. to ensure there were no interferences at the corners of the specimens. However, once the applied stresses exceeded approximately 800 psi, the glued area of the clevis tended to fail by breaking the concrete right at the interface between the clevis plate and the cube surface, as shown in Figure 4.34. This type of "skin" failure would not be considered a bond failure due to there being a film of concrete on the surface of the epoxy, indicating the epoxy did bond well. However, when the clevises are undersized, the weak plane is at the interface between the epoxy and the concrete and will fail there first when the applied load is meant to apply approximately 800 psi to a four-square-inch area. To remedy this issue, a new set of clevises and plinths were constructed. The side stresses were applied through clevises that were fabricated to be 1-63/64 in. x 1-63/64 in. to maximize the contact area while still being slightly smaller than the cube faces. A total of six of this size were fabricated to allow for gluing of three cubes. Also, the clevis for the sigma one

direction was fabricated to be 2-1/64 in. x 2-1/64 in. to ensure they were slightly larger than the cube. This ensures the entire cube surface was epoxied and placed in direct tension. A total of six of this size were fabricated to allow for three of them to be used with the larger side stress clevises, as well as to replace three of the smaller clevises used in the sigma one direction with the original set.

Figure 4.34 – Specimen where concrete failed at surface due to smaller clevises

With the new set of clevises fabricated, it was then possible to glue and test six cubes during a single testing session. However, since all of the gluing was done in the Looney Bin up to that point, only two cubes could be glued a day. The entire gluing process would take a total of three days, with testing late the fourth day to allow the last glued set to cure the full 24 hours. This method of gluing was inefficient and required the cubes to sit for longer periods of time before testing. Therefore, a jig was fabricated to allow for the simultaneous gluing of two cubes, shown in Figure 4.35. The jig was machined to have the exact same dimensions as the plinth bolt holes in the Looney Bin to ensure that the bolt holes would line up properly after being glued in the jig. With the

fabrication of the jig, a total of four specimens could be glued in a single day. Two specimens would be glued on Monday morning, then, after allowing the epoxy to cure for six hours, the specimens would be removed and another set glued Monday afternoon, and the last set would be glued on Tuesday morning. Testing would then commence on Wednesday morning to allow the last glued set to cure the full 24 hours. Cleaning could then commence in the early afternoon on Wednesday and allow for gluing two cubes before the end of the day. Two more sets could be glued Thursday morning and afternoon, and the final round of testing for the week would then be completed Friday afternoon. This schedule would allow for collecting four data points a week.

Figure 4.35 – Jig constructed for gluing two cube simultaneously

5. THE LOONEY BIN TEST PROCEDURES

5.1. INTRODUCTION

This chapter will cover procedures for each of the three stress conditions evaluated using the Looney Bin. Finalized test methods and raw data processing methods will be discussed.

5.2. TRIAXIAL TENSION TEST METHOD

5.2.1. Initial Test Concept

The original intent of the Looney Bin was to evaluate the triaxial tension (TTT) strength of UHPC. The appartatus was designed in the manner outlined in Chapter 4 to create this stress condition on 2 in. x 2 in. x 2 in. cubes. The test fixtures were attached to all six faces of the cube specimen using epoxy adhesive, with the three clevises on the opposite face of a plinth with the same dimensions. After the epoxy was allowed to cure for a minimum of 24 hours, the specimen was ready for testing.

5.2.2. Finalized Test Method

The Looney Bin is shown just prior to testing in Figure 5.1. First, the Looney Bin was rotationally stabilized by clamping 0.5 in. thick aluminum plates to the table along the outside edges of the apparatus to act as rotational stops. These aluminum plates provided support to the apparatus to minimize rotation when applying force in the sigma one direction, yet still allowing for removal of the apparatus to enable specimen attachment. Then, a specimen was bolted into the apparatus by first screwing the bolts into each of the three plinths through the plate walls until just before the bolt head came into contact with the plate wall. Then, the side plinths were alternately tightened to a

hand tightened condition before being tightened to snug tight. After the side plinths were snug tight, the bottom plinth was tightened to snug tight.

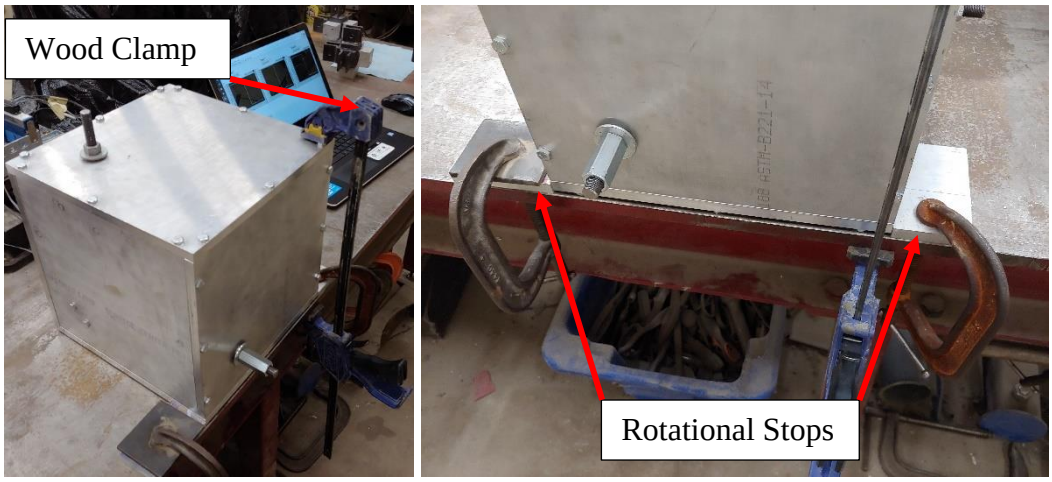

Figure 5.1 – Looney Bin apparatus just prior to start of testing

Once the plinths were bolted in, the ball joints for the sigma two and sigma three directions were attached to their respective clevises with steel shanks (Figure 5.2). Once attached, the threaded rod assembly was rotated counterclockwise until the ball joint rested against the inner side of the clevis plate wall, and the nuts were tightened after centering the threaded rod in the hole in the plate wall. At this point, the bearing, washers, and tightening nut were installed on the threaded rod outside the plate wall. The ball joint in its starting orientation is shown in Figure 5.2.

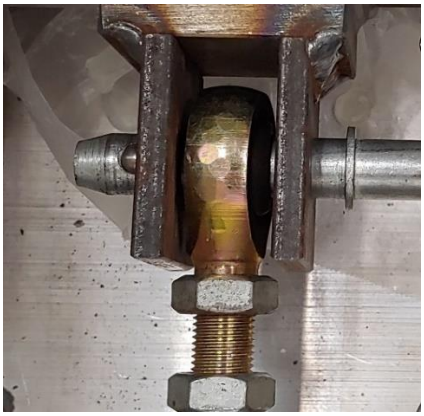

Figure 5.2 – Ball joint and clevis in original starting position

This process was completed to ensure that, once the tensile force reached a high enough level to create larger frictional forces on the threads, there was room for the ball joint to rotate clockwise with the tightening nut a short distance before coming into contact with the opposite clevis plate wall. This precaution reduced the likelihood of torsional stress application to the clevis if the threaded rod turned with the tightening nut. The grease applied to the threaded rods at the nut thread locations was sufficient in keeping the frictional forces low enough that the nut rotated independently.

After the fixtures for sigma two and sigma three were properly connected, the ball joint for sigma one was attached to the top clevis and the top plate was placed on top of the Looney Bin with the threaded rod for sigma one being fed through its designated hole. The top plate was centered on the apparatus, and then the bolts to connect the top plate to the side plates were fed through each hole location until hand tight. Once hand tight, the corner bolts were tightened to snug tight with a rachet first, then each opposite bolt was similarly tightened until all the bolts were tightened. Once tightened, a wood clamp was installed over the opposite corner of the apparatus from the sigma one

threaded rod location to provide additional support during loading (see Figure 5.1). Lastly, the bearings and washers were fed onto the sigma one threaded rod before feeding the tightening nut on. The same procedure for setting the sigma two and sigma three ball joints in the clevises was used on the sigma one threaded rod.

With the entire test setup completed, the load application could commence. Once the data collection program was opened and the wire connections verified, data collection could begin. The application of proportional loading was not feasible and would be immensely complicated for this test setup. Therefore, the tests were conducted by first setting the side stresses (sigmas two and three) to a specific stress, then applying load in the sigma one direction until failure occurred. A 12 in. long, 0.75 in. ratchet wrench was used to tighten the nuts for tensile load application. The load was first applied in the sigma three direction to the specified stress to help further clamp the inset plates in the sigma two direction. Then the load was applied in the sigma two direction to the specified stress. In the case of side stresses above 600 psi (2,400 lb), the loads were applied alternately to reduce the difference in side stresses prior to application of load in the sigma one direction. For those cases, half of the load was applied in the sigma three direction, then the entire load was applied in the sigma two direction, and lastly the remainder of the load was applied in the sigma three direction. Finally, load was applied in the sigma one direction at a rate between 15 and 35 psi/s. Care was taken to keep the load rate within that range but, since the load was manually applied using a wrench, maintaining the specified load rates was extremely difficult and slightly exceeded the limitations on several occasions. However, while load rate has the potential to affect overall strength, that normally occurs at much higher load rates (e.g., impact or blast

loading) (Kotsovos, 2015), and the slight differences in load rates for this testing will have minimal effect on overall observed strength.

In the cases where failure in the sigma one direction only caused a reduction in sigma two and sigma three stresses as opposed to complete failure (presumably due to crack initiation that was halted by the presence of fibers), the sigma two and sigma three threaded rods were tightened until breakage occurred. Example load output data where only a reduction of the side stresses occurred upon failure in the sigma one direction is shown in Figure 5.3.

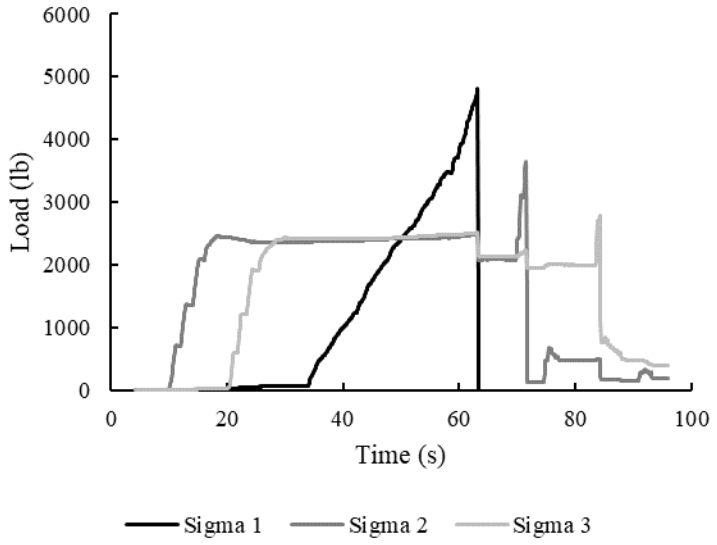

Figure 5.3 – Example plot of collected data with 2% fibers and 600 psi side stresses (2,400 lb)

5.2.3. Raw Data Processing

The data collected was sampled at a 1000 Hz frequency based on the data acquisition system requirements. However, since such a high sampling rate was not

necessary for this type of strength test (sudden failures were expected), the data was compressed to a 10 Hz frequency. This frequency was adequate to ensure the true peak was captured while keeping file sizes more reasonable. The collected data was comprised of load readings for each of the three principal directions along with the time of each data point. The data had to be reduced to show what the side stresses were and what the peak value for sigma one was at failure.

Several failure behaviors were encountered throughout testing. The most common behavior is shown in Figure 5.3. In this case, failure occurred in the sigma one direction and only a reduction in load was seen in the sigma two and three directions as opposed to complete load drop off. This appeared to be due to the initiation of a crack that was held together by fibers or the test fixture itself. In these cases, after failure in the sigma one direction, additional force was applied in the other two directions to propagate the cracks that were initiated and further break the cube apart. This was done to better highlight crack formation and expose the failed surfaces and is analogous to continuing a compression strength test post-peak to break a cylinder apart and better highlight the crack pattern. The loads applied after failure in the sigma two and sigma three directions were meaningless and not used in the data analysis.

There were small variations in the side loads during the application of the load in the sigma one direction. Therefore, the sigma two and sigma three loads were calculated as an average starting at the point at which the target load was reached and ending at a point near the sudden drop in load caused by failure in the sigma one direction. This average was determined in lieu of the peak side load or the side load at failure in the sigma one direction in order to encompass the stress history imparted on the specimen

throughout testing. The regions used in the calculated average for each side load is shown in Figure 5.4. The final step was determining the maximum load achieved in the sigma one direction.

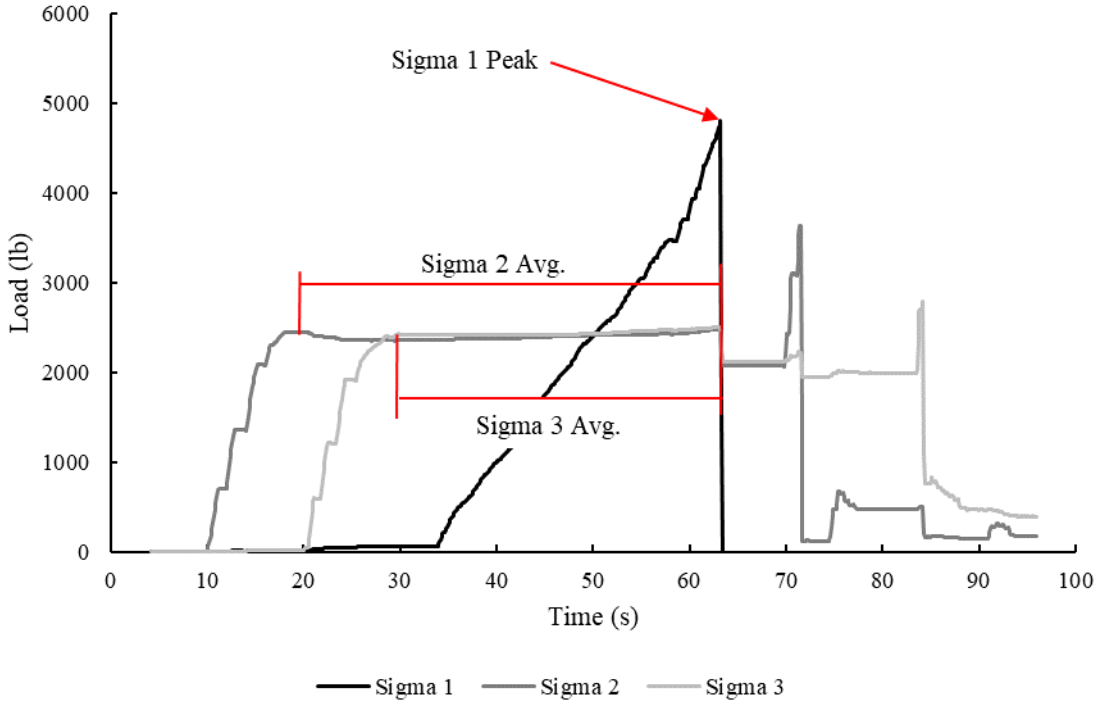

Figure 5.4 – Example plot of collected data with 2% fibers and 600 psi side stresses (2,400 lb) showing how failure loads were determined

Another common specimen behavior is shown in Figure 5.5. The side loads (sigma two and sigma three directions) in Figure 5.5 exhibited drastic reduction upon failure in the sigma one direction and, upon reapplication of load to break the cube apart, did not increase above the specified side load. This behavior appeared to occur when the failure in the sigma one direction would cause the cracks to expand further and cause fiber pullout. Then, upon attempting to apply load, the fibers were simply pulled even

further out of the concrete matrix, thus not producing a significant load increase. The failure loads for each direction were determined in the same manner as that discussed for the previous case.

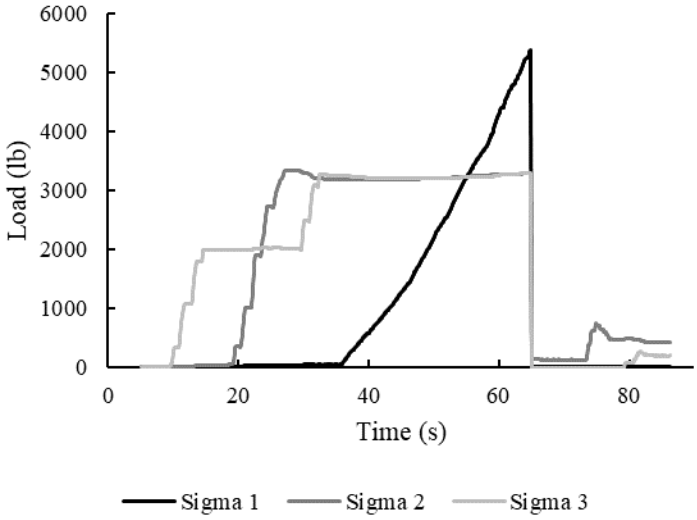

Figure 5.5 – Example plot of collected data with 1% fibers and 800 psi side stresses (3,200 lb)

The averaged side loads and the peak load in the sigma one direction were each divided by their respective areas determined from the measurements prior to gluing. The stresses were then put in the appropriate order (sigma one was greater than sigma two which was greater than sigma three). The order of the side stresses does not necessarily reflect the directions labeled on the Looney Bin. They are simply arranged in descending order to match the convention for principal stresses.

5.3. BIAXIAL TENSION TEST METHOD

5.3.1. Proportional Load Application Method

Another stress condition possible with the Looney Bin is biaxial tension testing (TT). The gluing process was very similar to the TTT testing. The gluing process differed by only gluing clevises to the sides of the cube. Since only four faces are required for TT testing, the cube was glued in the same orientation it was cast. This was done to remove the requirement to glue the as-cast top of the cube, which is inevitably the side least likely to be smooth. The specimen in the TT test setup is shown in Figure 5.6.

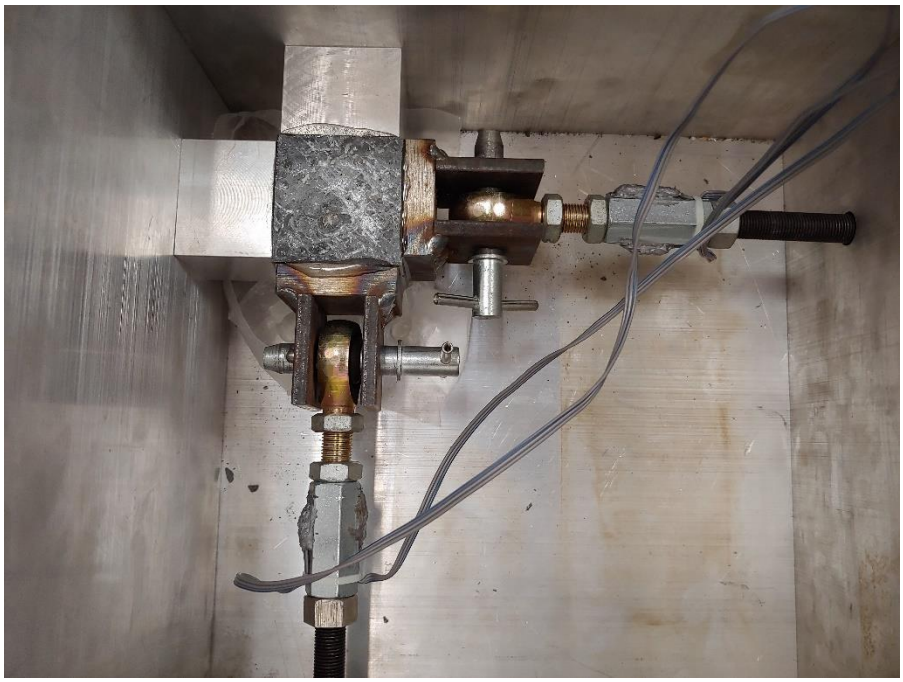

Figure 5.6 – TT test specimen in Looney Bin

The bolting method for test specimen placement in the Looney Bin and placement of the ball joints in the clevises was the same as the TTT test except no bolts were needed

for a plinth in the sigma one direction. Also, the apparatus was clamped to the table similarly to the TTT test except it was located at the corner of the table with the sigma two and sigma three threaded rods pointing out over the edge of the table. This orientation was chosen to provide 360° of access to rotate the wrenches. Testing was ready to begin once the rotational restraint plates were clamped to the table at the edges of the apparatus, the top plate was added, and the entire assembly was clamped to the table.

Proportional loading was not feasible for the TTT test due the complexity of attempting to tighten three nuts simultaneously at the same rate. However, proportional loading was possible for the TT test. The first round of TT testing was conducted using proportional loading to determine the biaxial tensile strength (sigma two and sigma three are the same stress at failure). Since the sigma two and sigma three nuts would be tightened simultaneously, a method to ensure they were increased at the same rate was required. The LabVIEW™ code was then updated to also show the difference between sigma two and sigma three during testing. Great care was taken to ensure the load rates for each direction were nearly identical and the overall load rate did not exceed 35 psi/s. A sample of the TT testing data is shown in Figure 5.7.

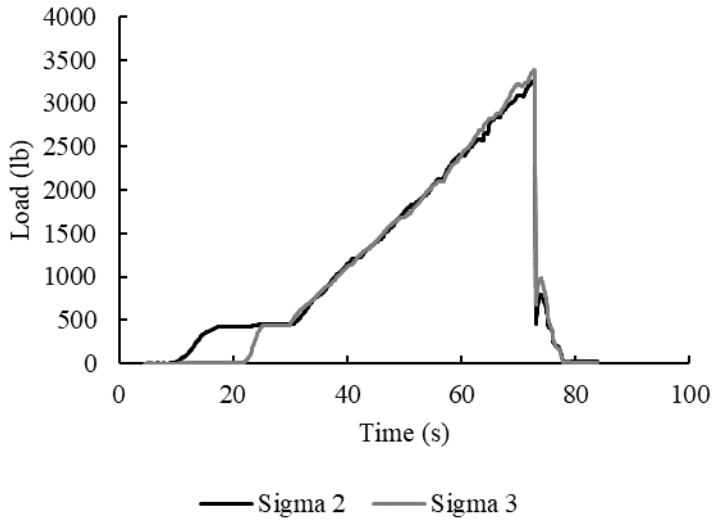

Figure 5.7 – Example plot of proportionally loaded TT test cube with 1% fibers

Once the specimen was bolted into the Looney Bin and the apparatus was clamped down, the LabVIEW™ program was started and testing could commence. The program was tared and an initial load of 500 lb was applied to both sigma two and sigma three to make it easier to maintain consistent loading in both directions for the duration of the test. A wrench was placed on both tightening nuts and, with each hand turning the two wrenches simultaneously, load was steadily applied up to the point of failure. Even loading was maintained throughout testing by monitoring the output showing the difference between sigma two and sigma three, taking care to keep the output as close to zero as possible.

5.3.2. Non-Proportional Load Application Method

While the application of equal proportional loading (i.e., identical stresses in each of the two directions) was relatively easy to carry out, unequal proportional loading (i.e., different stresses in each of the two directions) was not. Maintaining stress ratios with

uneven proportional loading would be extremely difficult. Therefore, unequal stress ratio tests were conducted similar to the TTT tests. A stress was specified for one direction, then load was applied in the other direction until failure. An example of a non-proportionally loaded TT test specimen is shown in Figure 5.8.

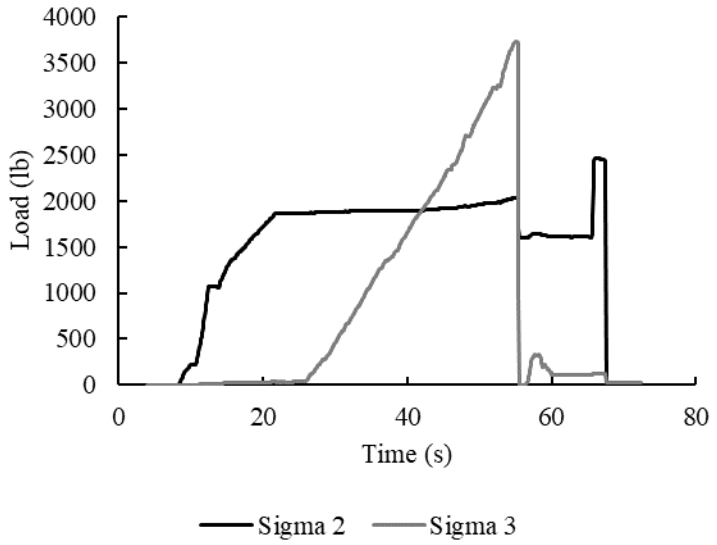

Figure 5.8 – Non-proportionally loaded TT test specimen with 450 psi (1,800 lb) in one direction for a 1% fiber specimen

Once the specimen was installed and the Looney Bin was clamped down, the program was started and tared. The specified load was applied in the sigma two direction. Then, load was applied to the sigma three direction until failure, taking care to keep the load rate less than 35 psi/s.

5.3.3. Raw Data Processing

The raw data output was in the same format as the data collected for the TTT tests. For the proportional loading case, the maximum load was extracted for both

directions and taken as the failure loads of the specimen. For the non-proportional loading case, the load in the sigma two direction was determined by averaging the load in the same manner as the side load in the TTT test data. The maximum load was then determined for the sigma three direction. Each load was then divided by their respective areas determined from the measurements prior to gluing. The stresses were then arranged in descending order for labeling of sigma one and sigma two. The value for sigma three was always zero for the TT tests since no load was applied in the third direction and tension stresses are treated as positive.

5.4. TENSION-TENSION-COMPRESSION TEST METHOD

5.4.1. Initial Test Concept

Another stress condition the Looney Bin was capable of testing was tension-tension-compression (TTC) testing. This stress condition represents a very severe case for concrete due to its brittle nature. In a uniaxial compression test, the failure is not a compression failure, but a failure caused by Poisson's effect creating tensile stresses in the lateral direction that ultimately cause fracture failure (Kotsovos, 2015). Due to this behavior, the addition of tensile loads in either of the orthogonal directions to the compression loading direction exacerbates that condition, causing failure of the specimen to occur at a much lower compression stress. This stress condition is a very important portion of the failure surface for concrete materials due to strength reduction caused by the additional tension stresses.

Since the Looney Bin had been successfully used for TT testing, the only piece left to determine was how to apply the compressive loading. The compressive loading

could easily be applied in the sigma one direction by removing the top and bottom plates of the apparatus. Fears Lab has three compression testing machines. However, for this testing, the apparatus would have to fit in the test machine and still allow room to turn the nut in the sigma two and sigma three directions for the tensile load application. The Baldwin test machine provides the necessary space with a wide table for the apparatus to sit on during compressive load application. Unfortunately, there is no mechanism to set load rates on the Baldwin test machine since the load application is through hydraulic pressure manually adjusted using dials. Therefore, the uniformity in load rates would be difficult to control throughout testing. The Looney Bin TTC setup is shown in Figure 5.9.

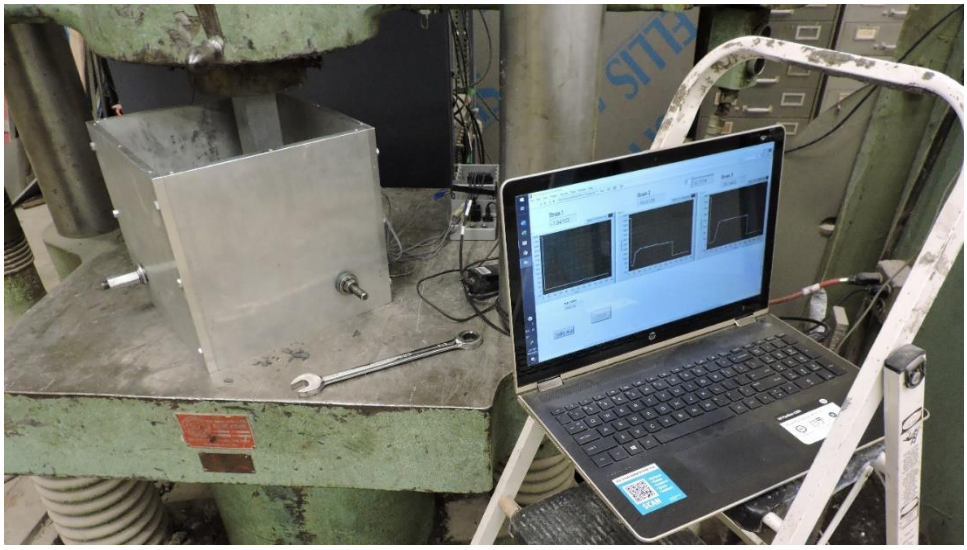

Figure 5.9 – The Looney Bin on the platform of the Baldwin during TTC testing

The gluing process also had to be altered to account for compression in the third principal direction. First, the cube orientation followed the requirements of ASTM C109 (2020b) and was rotated such that compression would be applied on formed surfaces.

Also, since there was no tensile force in the sigma one direction, the plinth that sits under the cube did not require epoxy. The top surface of the bottom plinth was instead covered with painter's tape to help protect the plinth from epoxy that may leak out from the bottoms of the side clevises, as well as to help reduce friction between the cube face and the plinth face. The compression faces were not sandblasted in order to help reduce friction. The side clevises were glued in the same manner as the TT test. Also, painter's tape was used to cover the exposed top of the cube to help keep epoxy that leaked out of the top of the side clevises from getting on the top surface. Paper towels were also used to clean any errant epoxy off the cube's top surface to eliminate potential for hardened protrusions after the epoxy cured.

5.4.2. Troubleshooting Compression Load Application

Before starting any testing, the LabVIEW™ program had to be adjusted to read loads from the pressure transducer attached to the Baldwin. The transducer was wired into an NI 9219 full bridge, 250 Ohm universal analog input module. Since this module does not have an internal power supply, the pressure transducer was also attached to a 10V power supply. The NI 9219 module was added to the eight-slot chassis, and the DAQ assist in the LabVIEW™ block diagram was reconfigured to read the output from that module in place of the sigma one threaded rod, since no data was collected from that fixture for TTC testing. Once the program was completed, the Baldwin pressure transducer was calibrated for loads up to 50,000 lb using the dial gauge on the Baldwin.

Several issues arose during the initial attempts at TTC testing. First, a method had to be devised to apply the load to the cube face directly without encountering the 11 in. tall plate walls. For this, a 10 in. long section of the same 2 in. x 2 in. aluminum bar stock

used to manufacture the plinths was used for load application. The ends were machined to be parallel to each other and perpendicular to the sides of the bar to ensure even loading on the cube. The length of the bar was sufficient to extend above the top of the Looney Bin plate walls so the Baldwin platen and crosshead would not come into contact with the plate walls during testing. The aluminum loading bar is shown on the test specimen in Figure 5.10.

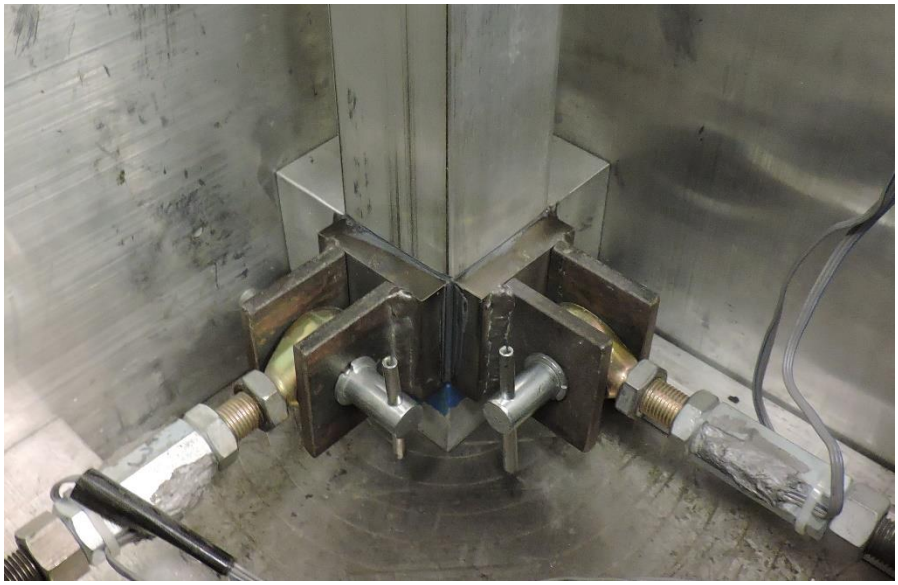

Figure 5.10 – Cube specimen with TTC fixtures in Looney Bin

Initial tests were conducted with the aluminum bar in direct contact with the cube top. However, having the bar in this condition created several issues. One issue was the potential for damage to the bar face upon failure of the cube. Aluminum is a soft metal and could therefore be damaged easily if pressed against a jagged surface caused by the failure of the cube. Also, if the top edge of a clevis protruded over the top of the cube, it could indent the end of the loading bar. Another issue was the confinement that the

aluminum bar would cause due to friction upon the application of compressive loading. This confinement could alter the observed compressive strength. Therefore, further tests were conducted using a 0.5 in. thick, 2 in. x 2 in. 70A durometer neoprene pad between the cube face and the aluminum bar to mitigate these issues. However, when compression loading was applied to the specimen with the neoprene pad, it expanded laterally around the aluminum bar, as shown in Figure 5.11. This expansion while subjected to compressive loads caused damaged to the neoprene pad, shown in Figure 5.12.

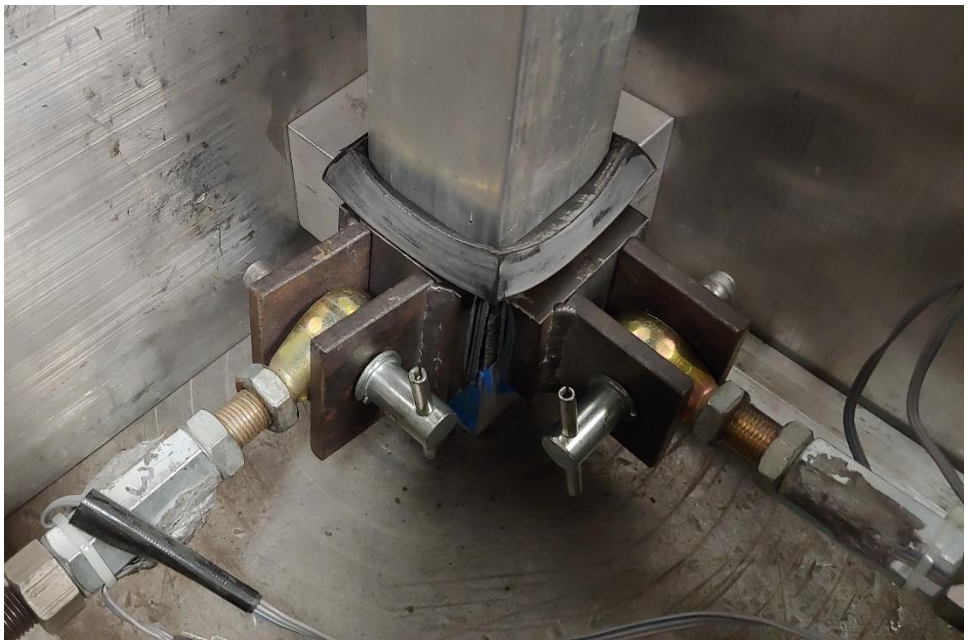

Figure 5.11 – Expansion of neoprene pad when subjected to compression

Figure 5.12 – Damaged neoprene pad after excessive expansion

This expansion created the need for a collar that would reduce the expansion of the neoprene pad under compression. A 0.5 in. thick section of HSS3x3x5/16 tube was machined to be placed around the neoprene pad to halt expansion of the neoprene pad upon loading. This type of setup is similar to that used for uniaxial compression testing of concrete cylinders. The neoprene pad collar is shown in Figure 5.13.

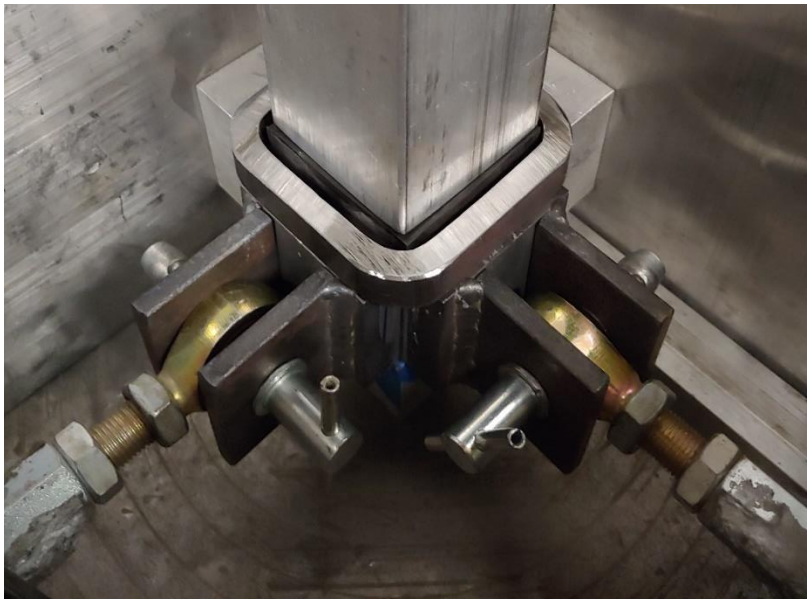

Figure 5.13 – Neoprene collar around pad prior to testing

An issue that arose with the use of the neoprene pad was found in the initial stages of compressive loading. The apparent load rate would appear small in the early stages of loading as the neoprene compresses and before the edge expansion is halted by the collar. Once the neoprene collar halts the expansion, the load rate would suddenly shoot up if the dial adjusting the hydraulic pressure was left in the same position. This required adjustment of the hydraulic pressure dial during the test and made consistent load rates difficult to obtain. However, care was taken to maintain the compression load rate lower than the 150 psi/s outlined in ASTM C1856 (2017) for UHPC specimens subjected to compression.

5.4.3. Finalized Test Method

After the TTC test setup troubleshooting was completed, data collection could commence. First, the apparatus was placed on the bottom platform of the Baldwin test machine and the glued specimen was bolted into place. The specimen was bolted into the apparatus and the ball joints attached to the clevises in the same manner as the TT test. Once the specimen was bolted in place, the neoprene pad was centered on the top cube face, the collar was placed around the neoprene pad, and aluminum loading bar was placed on the neoprene pad. Then the cross head was lowered until it was near the top of the loading bar to facilitate centering of the bar on the Baldwin platen. Once the bar was centered, the data collection program could be started. Once started and tared, the tensile load was applied in the sigma three direction first and the sigma two direction second. In the case of side stresses above 600 psi (2,400 lb), half of the applied load would be applied in the sigma three direction, then the full load would be applied in the sigma two

direction, and then the last of the sigma three load would be applied. Once the tensile loads were applied, the compression load application was started using the hydraulic pressure dial and care was taken to keep the load rate less than 150 psi/s until failure. An example plot of a TTC test is shown in Figure 5.14.

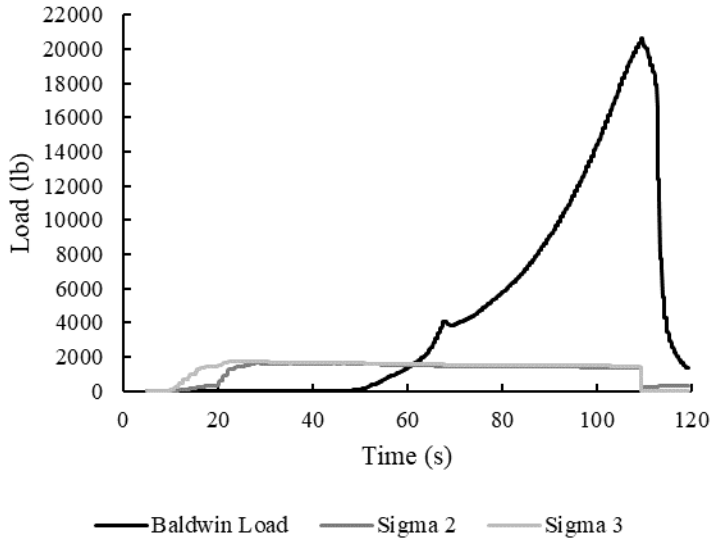

Figure 5.14 – Example plot of TTC test cube with side stresses of 400 psi (1,600 lb) with 4% fibers

5.4.4. Raw Data Processing

The raw data output was in the same format as the TTT test. The side loads were determined by averaging in the same manner as the TTT test data. Then the maximum load in the compressive loading direction was determined. However, unique specimen behavior was observed during the TTC testing of cubes with higher fiber contents (typically above 2%) and is shown in Figure 5.15.

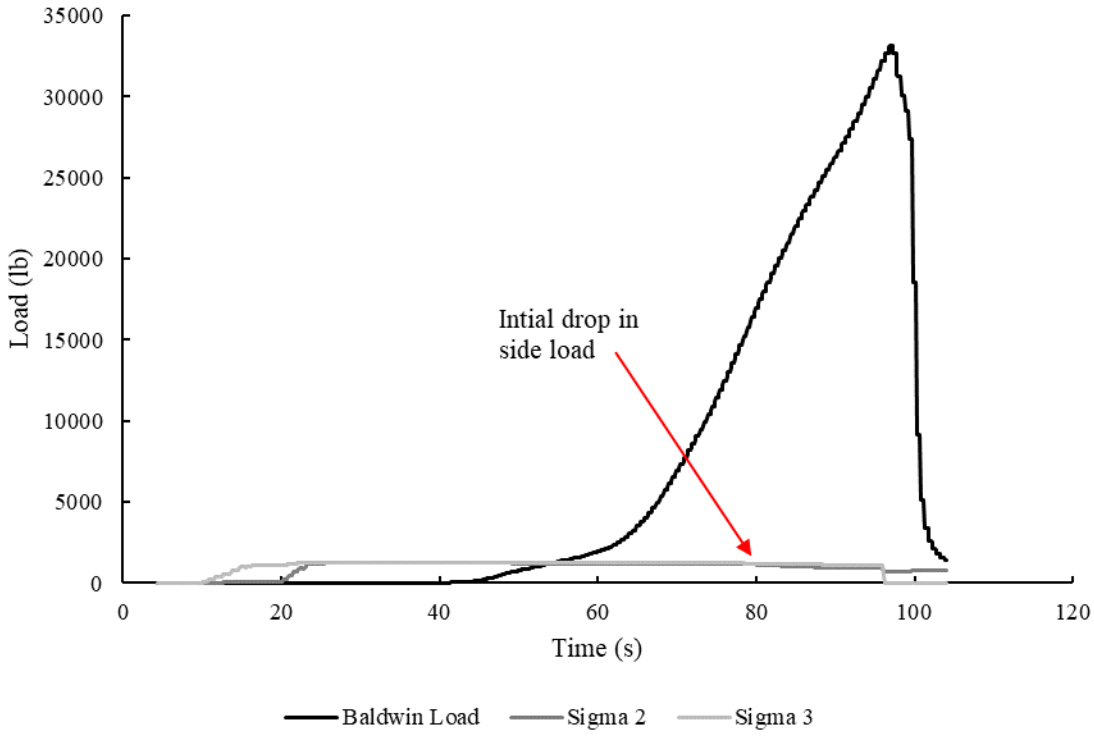

Figure 5.15 – Example plot of TTC test cube with side stresses of 300 psi (1,200 lb) with 4% fibers

During this testing, a loud pop was heard at approximately the 80 second mark, and a gradual decrease in the side load was observed thereafter. However, there was no apparent drop in the compressive load and testing was manually halted. Upon inspection of the cube, a diagonal crack was observed in the specimen, shown in Figure 5.16.

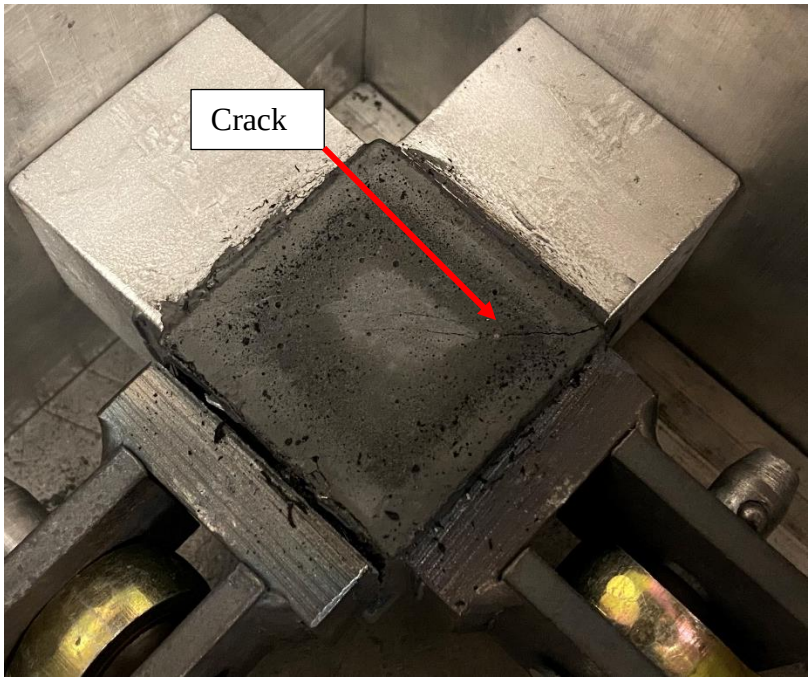

Figure 5.16 – Crack observed in specimen after halting test

This diagonal crack is indicative of failure in the direction orthogonal to the compressive load. It appears the diagonal crack occurred when the loud pop was heard, and the specimen was effectively held together by the internal fibers. Then, as the compressive load increased, the increasing lateral strains caused the fibers to slowly pull out, causing the gradual drop in the side loads. However, no apparent drop in the compressive load was observed in the data during testing. This appears to be a condition unique to TTC testing. Failure of the cube occurs by essentially cracking the cube in half, thus drastically reducing the side loads. This cracked cube can still be considered a stable specimen and will continue to withstand increasing compressive loads, presumably until extensive cracking occurs. However, failure was assumed to occur when the initial crack

was formed. In this instance, the peak compressive load was determined by finding the load at the point the side loads started to gradually decrease.

The averaged side loads and the failure compressive load were each divided by their respective areas determined from the measurements prior to gluing. The stresses were then arranged in the appropriate order. Sigmas one and two were the side tension stresses in descending order. Compression is treated as a negative stress and was therefore set as sigma three.

6. FAILURE SURFACE DATA COLLECTION AND ANALYSIS

6.1. INTRODUCTION

The purpose of this chapter is to present the collected test data, discuss statistically based adjustments to the test data, and provide explanations for the different failure mechanisms. The data collected represents individual points used to define the failure surface. Three cube specimens were tested for each data point, and the presented data points for each stress ratio represent the average of at least two cube tests. The method and rationale for determining the statistical limitations among the three replicate tests at a specified stress ratio for each test type and fiber content is also presented, as well as the final data points to be used for determining the UHPC failure surface.

6.2. ANALYSIS OF FAILURE MORPHOLOGY FOR TTT SPECIMENS

6.2.1. Failure Morphology with Equal Side Stresses

Various cracking patterns and failure morphology were observed throughout testing. Examples of near perfect TTT failures are shown in Figure 6.1 and Figure 6.2. The cracks in each cube appeared to occur within the specimen, as opposed to the exterior surface, at approximately equal angles. Each of the clevises and plinths failed with substantial sections of the cubes still attached. These failures exhibited the expected crack patterns for TTT testing.

Figure 6.1 – Failed 0% cube where cube suffered substantial damage with side stresses set to 500 psi

Figure 6.2 – Failed 0% cube with side where clevises stayed intact with side stresses set to 500 psi

Another example of a failed 0% fiber specimen is shown in Figure 6.3. The side stresses in this cube were lower than the specimens shown in Figure 6.1 and Figure 6.2. Since the side stresses were lower, the difference between sigma one at failure and the side stresses was larger, which could have caused the higher degree of cracking.

Figure 6.3 – Failed 0% cube where unusual crack patterns occurred with side stresses set to 300 psi

Cracking patterns did not appear to follow the expected patterns in all cases. Another failed 0% fiber specimen with side stresses set to 500 psi is shown in Figure 6.4. The initial crack appeared to develop into a slightly curved diagonal crack and caused a skin failure (where the cube failed right at the glued interface with a thin layer of concrete

still attached to the epoxy) in the orthogonal direction. This curved cracking is similar to the cracking patterns observed in the TT tests conducted for 0% fiber specimens.

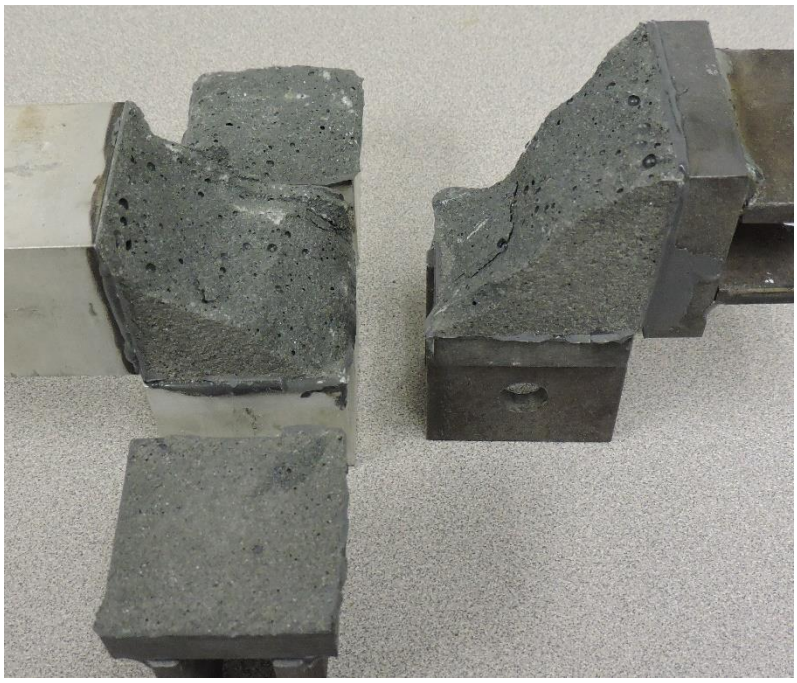

Figure 6.4 – Failed 0% fiber specimen with side stresses set to 500 psi (top clevis is in the upper right hand corner)

When fiber reinforced specimens were tested, several common behaviors were observed. For instance, a common failure in the sigma one direction involved the top clevis being pulled from the top of the cube when the concrete on the top of the cube failed in the shape of a cone, as shown in Figure 6.5 for 1% fibers and Figure 6.6 for 2% fibers. This cone type failure could be indicative of shear stresses developing due to the difference in the stresses applied in each principal direction. Also, the limited number of fibers crossing the plane of the crack suggests this was the weakest plane in the specimen.

Figure 6.5 – Top clevis from failed 1% fiber specimen with side stresses of 800 psi

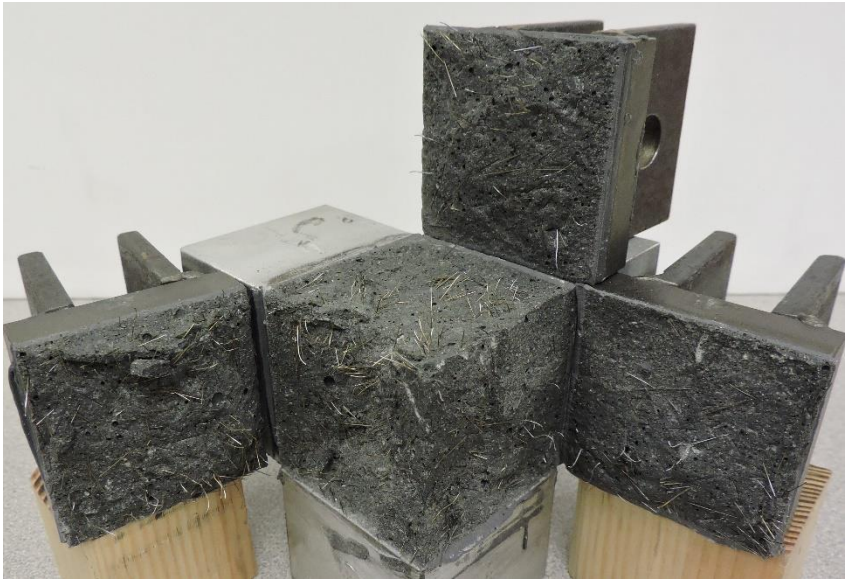

Figure 6.6 – All clevises with cone shaped concrete attached from 2% fiber specimen with side stresses set to 700 psi

Another observation regarding the testing of fiber reinforced specimens was that the specimens did not exhibit failures in the expected manner shown in Figure 6.1 and

Figure 6.2. Fiber reinforced specimens tended to fail closer to the surface of the cubes in near vertical planes, as shown in Figure 6.7. This difference in cracking pattern could be due to the ability of fibers to bridge cracks. The expected cracking pattern would create larger, angled faces in the specimen. When fibers are introduced into the specimen, the likelihood of the failures occurring along those larger faces diminishes due to the increased likelihood of a larger number of fibers crossing that angled crack plane. With a larger number of fibers crossing the crack plane, the expected capacity would increase. Due to this phenomenon, the area of the fractured faces would likely be reduced, decreasing the chance that fibers cross that crack plane. Also, the distribution of fibers in the specimen is inherently random when placing UHPC, thus ensuring the weak plane may not always be in the expected orientation. This random distribution could cause completely different crack patterns even in specimens with the same stress ratios due to the randomness of the weak planes that would develop.

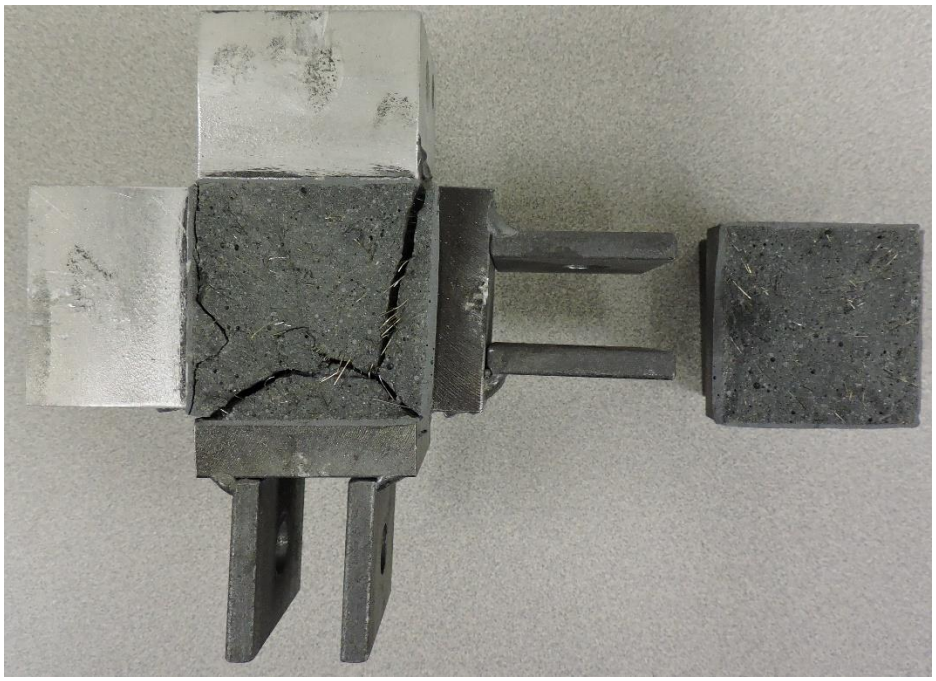

Figure 6.7 – Failed 1% specimen with cracks forming near the surface of the cube with side stresses set to 800 psi

Upon testing the 4%, 5%, and 6% fiber contents, a new behavior was observed. While skin failures were more common with the 4% fiber specimens, cracking patterns would occur that were similar to the lower fiber percentages. In those cases, a specimen would fail near the face of the cube with a short, cone-shaped portion of the cube still attached to each clevis or plinth, as shown in Figure 6.8. However, increases in failure loads were observed as fiber contents increased up to 4%, so the reduction in visible cracking was presumably due to the fiber's ability to hold cracks together more effectively at higher contents. Since the epoxy interface would fail as soon as the specimen was jolted from the volume change at failure, applying load to determine post-crack triaxial behavior was not possible.

Figure 6.8 – Failure of TTT specimen with 4% fibers and side stresses of 800 psi

Initially, the study was meant to end with 6% fiber testing. However, the increased fiber content caused a large number of fibers to be oriented parallel to the formed cube faces. This preferential orientation, coupled with the much higher content of the fibers, created a very weak plane, and caused skin failures that looked like what is shown in Figure 6.9.

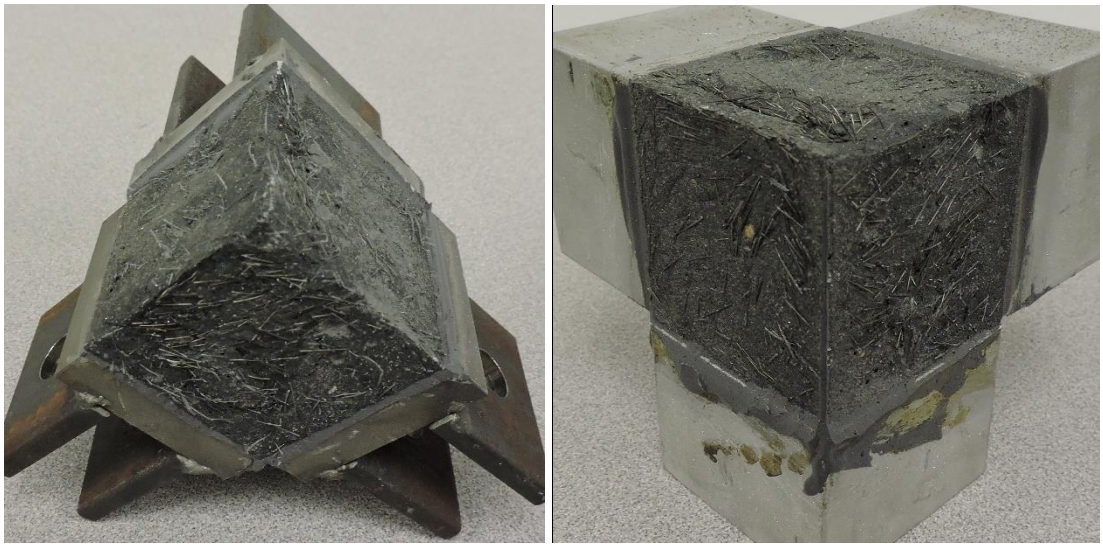

Figure 6.9 – Failed TTT specimen with 6% fibers and side stresses set to 800 psi (left) and 900 psi (right)

While similar preferential alignment was evident on the 4% cube shown in Figure 6.8, the 4% fiber specimens failed at higher loads than the lower fiber percentages and engaged more of the material within the cube compared to the 6% fiber specimens. In the case of the 6% fiber specimens, the preferential fiber alignment caused the specimens to fail at much lower loads than the 4% fiber specimens and also caused a higher difference in test results at the same side stresses. When this lower strength was observed after testing for four data points (a total of twelve specimens), the decision was made to halt testing for the 6% fiber content since that represents a fiber dosage that causes a reduction in TTT strength. This reduction in strength at this fiber content was also observed in uniaxial tests conducted by Lepissier (2020) and Campos (2021).

Since a 4% fiber content increased strength and a 6% fiber content reduced strength, the question became at what fiber content will the strengths stop increasing? This fiber dosage would represent the optimal dosage for strength. In an attempt to find

this optimal dosage, tests were conducted on specimens with a 5% fiber content. However, the same results were seen for the 5% content as the 6%. A similar reduction in strength was observed and the strength level was almost identical to the 6% fibers. An example of a failed 5% fiber content specimen is shown in Figure 6.10. Due to this reduction in strength, it was decided to halt all testing of 5% and 6% fiber dosages after collection of four TTT test data points for each. No TT or TTC testing was conducted on cubes with 5% and 6% fiber contents.

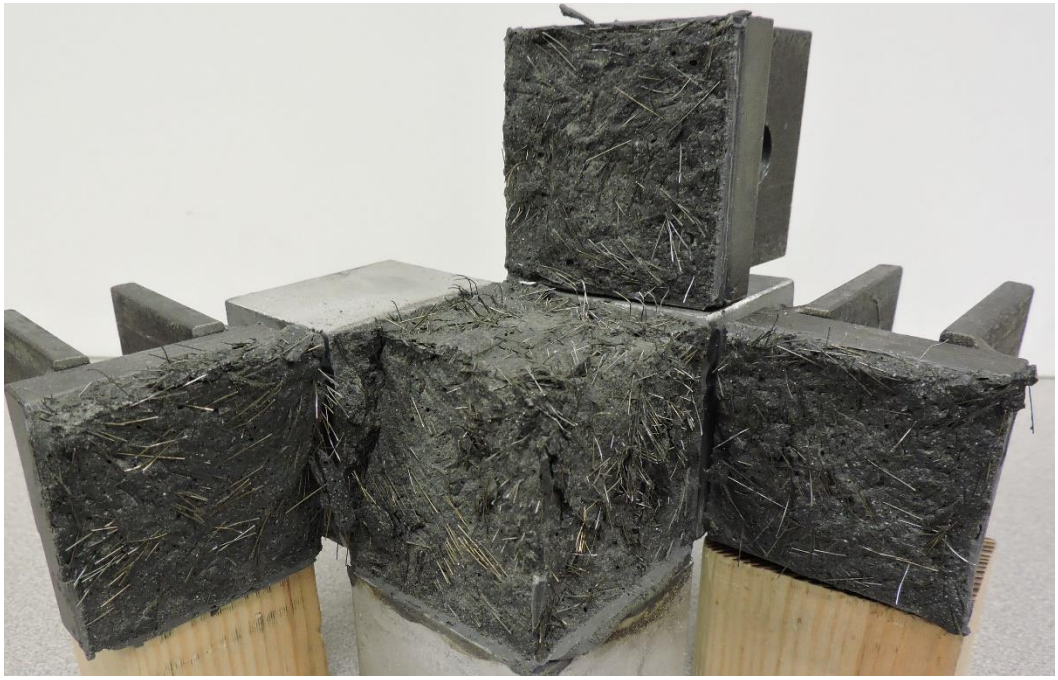

Figure 6.10 – Failed TTT specimen with 5% fibers and side stresses set to 600 psi (left side clevis) and 300 psi (right side clevis)

6.2.2. Failure Morphology with Unequal Side Stresses

When unequal side stress conditions were imposed, the crack patterns tended to be different than those with equal side stresses, as shown in Figure 6.11. When even side

stresses are present, a corner-to-corner diagonal crack would be expected. However, when the side stresses are unequal, the additional stress applied in one direction tends to interrupt the development of that corner-to-corner crack. This could result in a multitude of different variations of the corner-to-corner crack, depending on the scale of difference between the side stresses. The closer the unequal side stresses were, the more likely a corner-to-corner crack would form. Figure 6.11 is evidence of a large difference in side stresses (in this case, one side is twice as large as the other), where adjacent cracks form in multiple directions. These cracks were better highlighted in the 0% fiber specimens since the crack patterns were not interrupted by the additional reinforcement by fibers in potential weak zones.

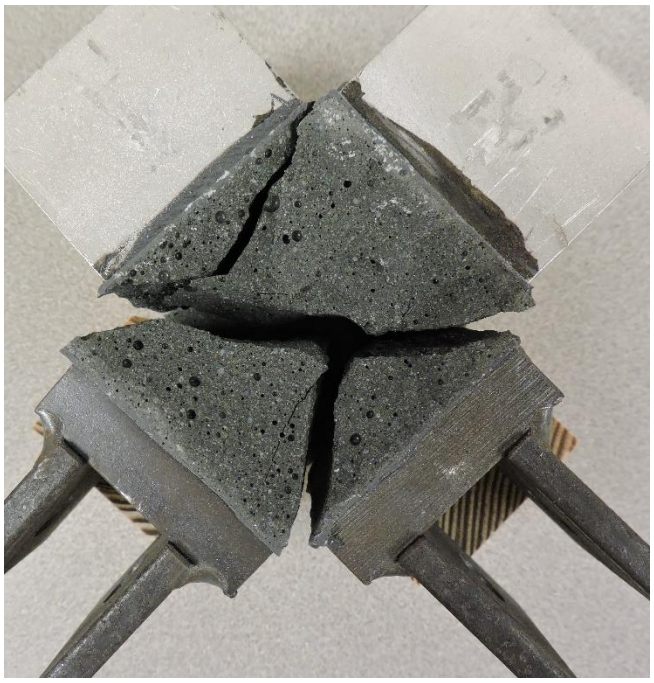

Figure 6.11 – Failed 0% cube where crack patterns occurred with side stresses set to 600 psi (lower right clevis) and 300 psi (lower left clevis)

Upon testing fiber reinforced cubes with uneven side stresses, crack patterns emerged similar to those shown in Figure 6.12 and Figure 6.13. The larger of the side stresses was applied through the clevis shown in the photos, with the other side clevis having detached upon failure. This cracking pattern would be expected in this type of loading. A gradual transition from a straight crack perpendicular to the load application direction caused by uniaxial stress to a corner-to-corner crack caused by even side stresses would be expected. This crack pattern was observed in several cases throughout testing. The adjacent side clevis appeared to detach upon development of the large crack shown. An example of this crack pattern in a cube with a 1% fiber content is shown in Figure 6.12 and 2% fiber content in Figure 6.13.

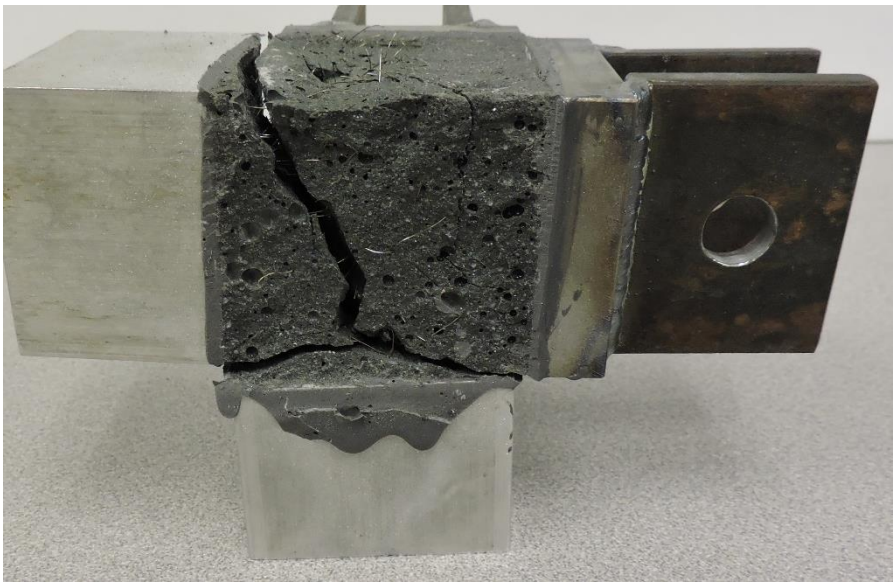

Figure 6.12 – Angled crack due to unequal side stresses with 800 psi applied through the clevis shown and 400 psi to the other clevis in 1% fiber specimen

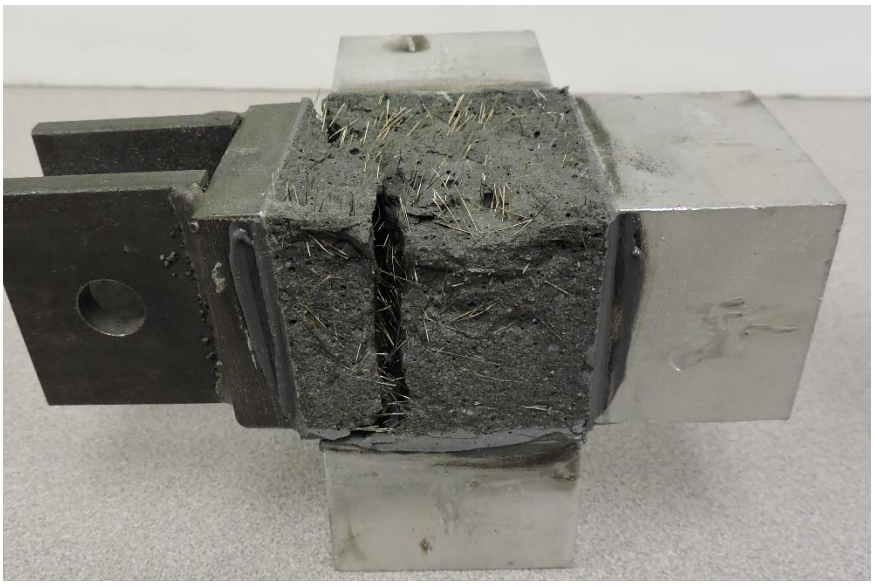

Figure 6.13 – Angled crack due to unequal side stresses with 600 psi applied through the clevis shown and 200 psi to the other clevis in 2% fiber specimen

In some cases, failure produced cracking adjacent to the concrete removed by the clevis, as shown in Figure 6.14. This phenomenon could have been caused by the creation of multiple cracks upon failure, and the portion of concrete that stayed attached to the specimen could have had a larger number of fibers crossing the crack plane. These cracks are indicative of multiple load paths being created when crack initiation occurs in multiple locations at once. This could be another mechanism by which the presence of fibers increases the tension strength of concrete.

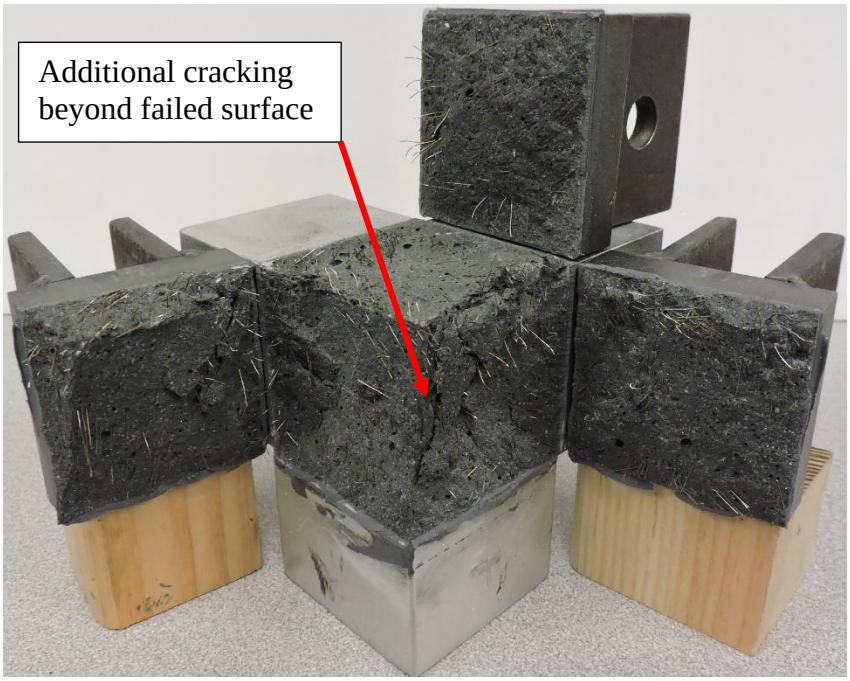

Figure 6.14 – Additional cracking formed on right side of specimen with 2% fiber content and side stress of 800 psi (left clevis) and 400 psi (right clevis)

In Chapter 4, there was discussion of the failure of the concrete at the interface of the smaller clevises and the concrete surface (skin failure). The failures in the early stages of development of the Looney Bin were mainly due to the clevis having a smaller surface than the cube and creating a weakened plane in the tensile load path. This behavior was evident in those tests, which very consistently failed at approximately 3,000 lb as measured by the coupling nut load cell. However, even after increasing the clevis size, this type of failure occurred at even higher stress levels. One example of this type of failure was seen from TTT testing for the 1% fiber content with side stresses set to 500 psi and 250 psi. For that case, failed specimen two is shown in Figure 6.15, and failed specimen three is shown in Figure 6.16. The load plots for specimen two and specimen three are also shown in Figure 6.17 and Figure 6.18, respectively.

Figure 6.15 – Specimen two for 1% fibers and side stresses of 500 psi and 250 psi

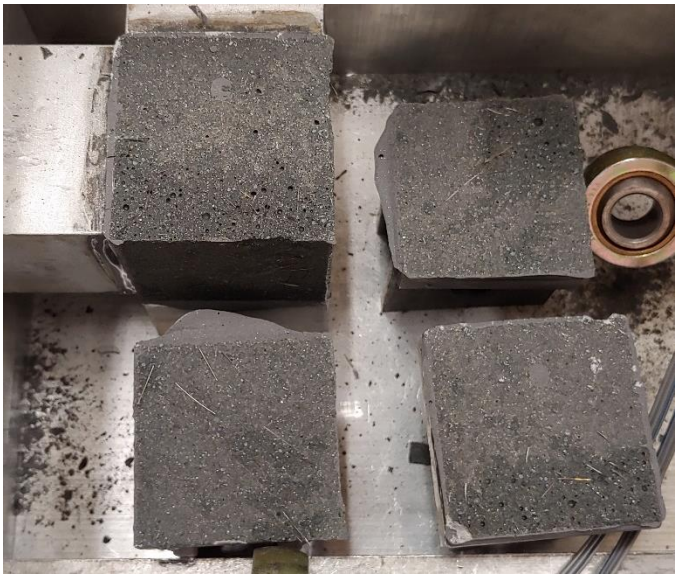

Figure 6.16 – Specimen three for 1% fibers and side stresses of 500 psi and 250 psi

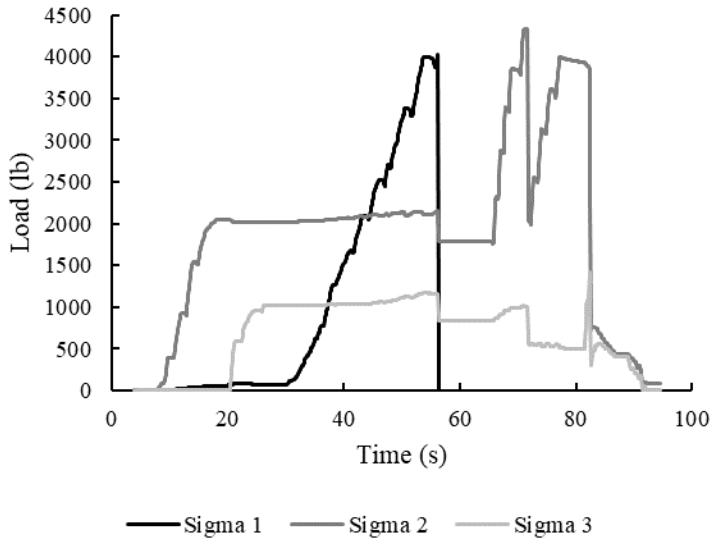

Figure 6.17 – Data collected for specimen two for 1% fibers and side stresses of 500 psi (2000 lb) and 250 psi (1000 lb)

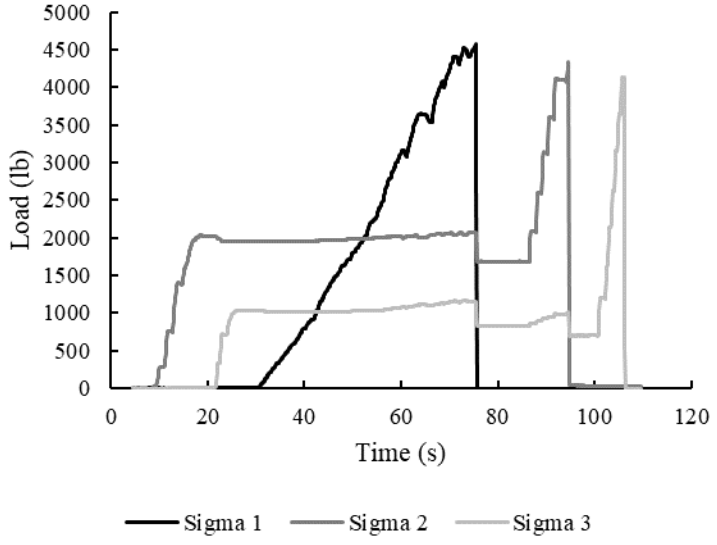

Figure 6.18 – Data collected for specimen three for 1% fibers and side stresses of 500 psi (2000 lb) and 250 psi (1000 lb)

Specimen two appeared to exhibit a skin failure in all three clevises, while also developing a very large and slightly diagonal crack. Specimen three simply appeared to

have skin failures in all three directions. In examining the failure types, the logical conclusion would be that specimen two failed at a higher failure load due to the existence of the crack. However, the failure loads for specimens two and three were 4,026 lb and 4,574 lb, respectively. Firstly, the failure loads for both cases were well above the consistent failure loads when using the smaller clevises. Also, the higher failure load from specimen three seems to indicate that the skin failure on the clevis is not indicative of a premature failure. Instead, this type of failure could be caused by jolting of the specimen due to internal cracking caused by initial failure of the specimen. Once a crack appears in the fiber reinforced specimens, the specimen undergoes a sudden volume change which can be halted almost immediately by the presence of fibers crossing the plane of the crack. In some cases, that sudden jolting of the specimen could induce a pseudo-impact load on the clevises, causing an unusual stress condition at the interface, and inducing failure at that surface.

Also, if the internal crack propagates at an angle or opens with different widths along its length, bending stresses could form on the bonded interface. The additional removal of concrete on only one portion of the right-side clevis in Figure 6.16 could be evidence of bending being applied to the clevis interface caused by uneven loading upon initiation of a crack. These apparent skin failures were more common in testing as the fiber percentages increased. This was presumably due to the larger post-cracking strengths and the ability of the fibers to immediately halt crack propagation upon failure initiation. Even though these failures occurred as fiber contents increased, the failure loads also increased with the fiber contents, indicating that higher strengths were achieved, and the apparent failures were due to specimen failure, and not caused by an

epoxy bond issue. Therefore, even if a skin failure was observed and the failure load was relatively close to the other cube specimens that did not exhibit possible skin failure, it was not immediately thrown out.

6.3. ANALYSIS OF FAILURE MORPHOLOGY FOR TT SPECIMENS

Several failure conditions were observed in the TT testing. Examples of failed TT specimens are shown in Figure 6.19 and Figure 6.20. These different failure patterns highlight the difference in weak plane locations in different concrete specimens. In Figure 6.19, there appeared to be a weak plane perpendicular to the load applied in the sigma three direction, where failure initiated first and caused a skin failure on the sigma two plinth. Figure 6.20 seems more indicative of the expected failure under proportional loading. The corner-to-corner crack is clear, with additional cracking branching off from it. Such additional cracking could have been caused by the point of crack initiation. If the crack initiated near the corner of the cube, as opposed to near the center, crack propagation could cause additional bending stresses, which could create additional cracks stemming from the original crack. While the failure patterns were drastically different, the failure loads were within 10% of the average and also met the standard deviation limit, which will be discussed later in this chapter.

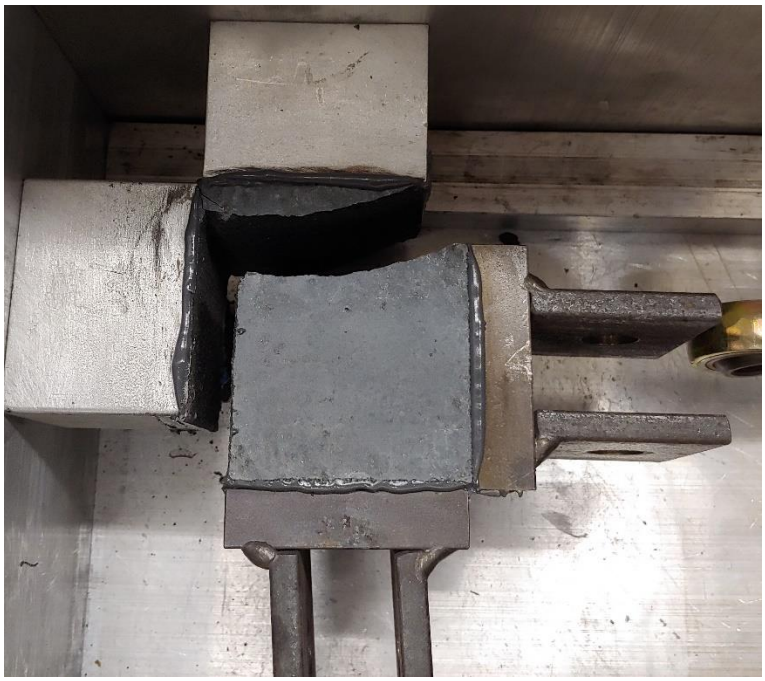

Figure 6.19 – Failed 0% fiber TT specimen subjected to proportional loading

Figure 6.20 – Failed 0% fiber TT specimen subjected to proportional loading with substantial cracking

For the 1% fiber content, specimens developed completely different cracking patterns when subjected to proportional loading. Specimens one, two, and three are shown in Figure 6.21, Figure 6.22, and Figure 6.23, respectively. Despite having three completely different fracture patterns, the failure stresses were all very close and met the standard deviation requirements, which will be discussed later in this chapter. The variability in the crack patters is also discussed later in this chapter. A similar manner of failure was observed for the 2% fiber specimens as well, and an example is shown in Figure 6.24.

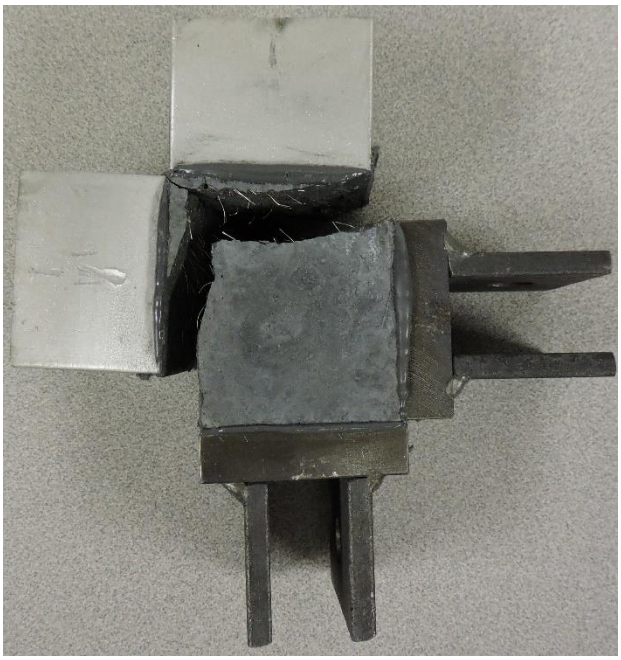

Figure 6.21 – Specimen one for 1% fibers subjected to proportional loading

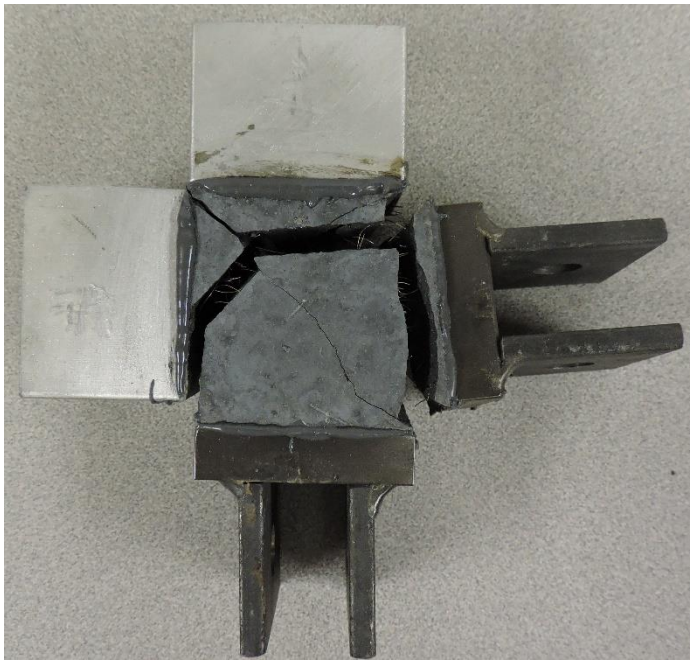

Figure 6.22 – Specimen two for 1% fibers subjected to proportional loading

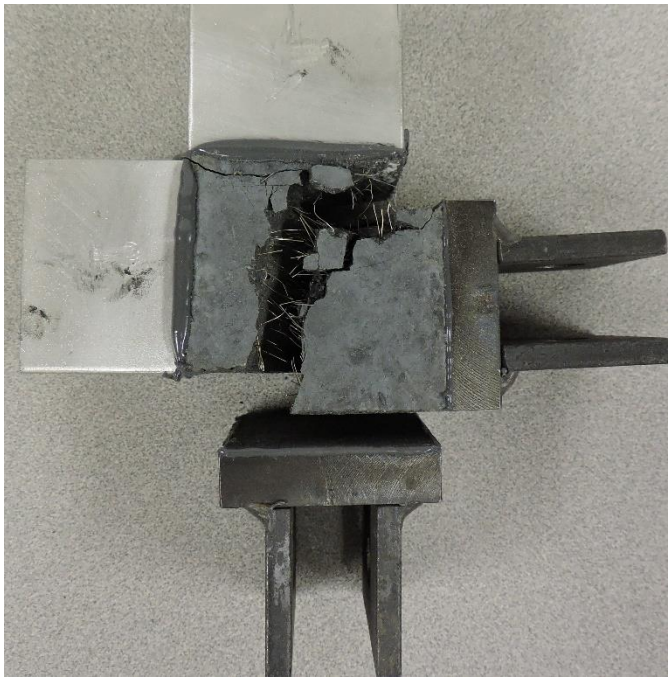

Figure 6.23 – Specimen three for 1% fibers subjected to proportional loading

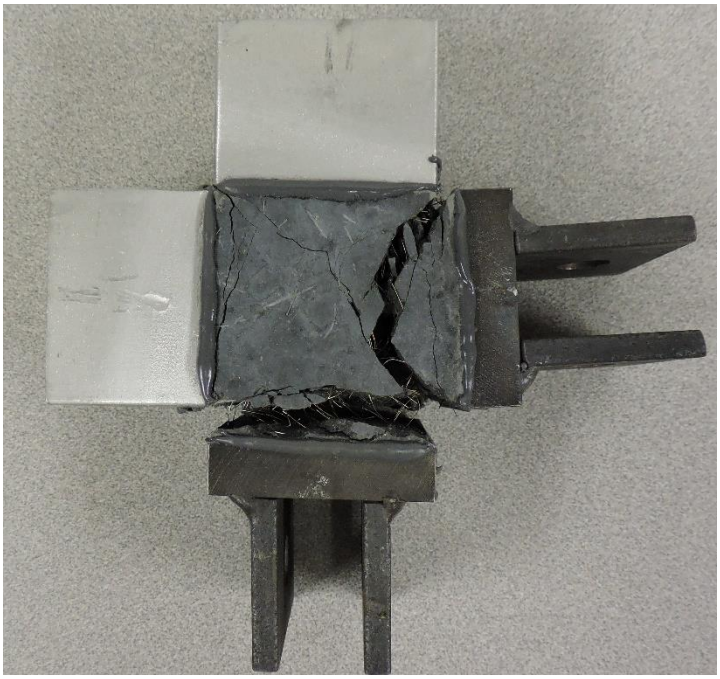

Figure 6.24 – Specimen with 2% fibers subjected to proportional loading

The TT failures in specimens with 4% fibers were less likely to cause externally visible cracks that crossed the width of the specimens. Visible cracking was more likely to form at the faces or corners of the cube, as shown in Figure 6.25 and Figure 6.26, respectively.

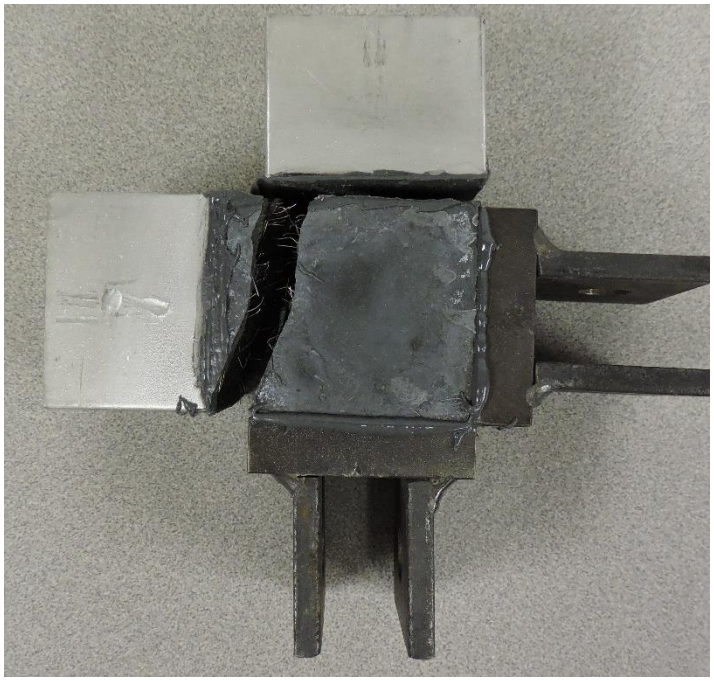

Figure 6.25 – Failed TT specimen with 4% fibers subjected to proportional loading

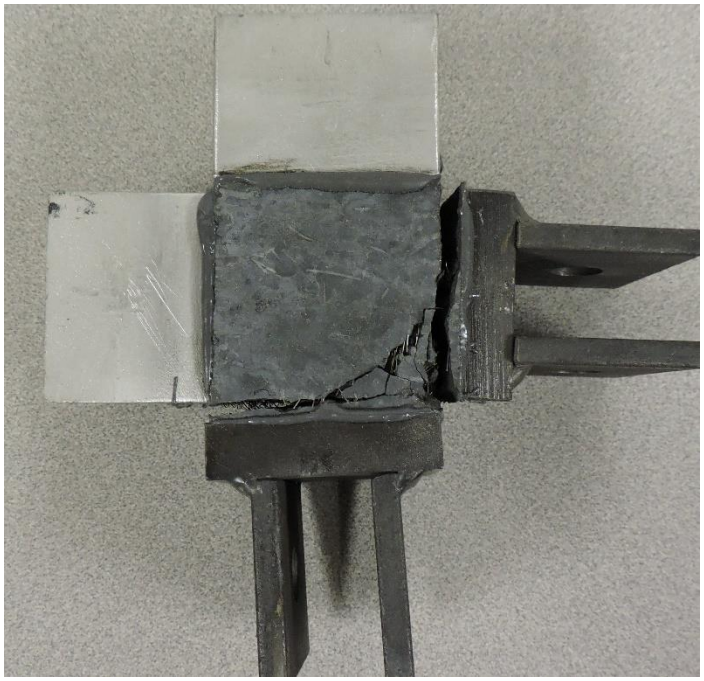

Figure 6.26 – Failed TT specimen with 4% fibers and a side stress set to 600 psi

6.4. ANALYSIS OF FAILURE MORPHOLOGY FOR TTC SPECIMENS

The TTC cracking patterns were very consistent regardless of fiber content. For equal side stresses, diagonal corner-to-corner cracking was common and is shown in Figure 6.27. For uneven side stresses, additional cracking could also form, along with the diagonal cracking, as shown in Figure 6.28. Also, a diagonal crack that was angled away from the side with the lower side stress would appear, shown in Figure 6.29. This cracking is similar to the TTT case with unequal side stresses shown in Figure 6.13. On several occasions, a clevis would detach upon failure of the specimen in a manner similar to the skin failures previously discussed. However, as was the case for the TTT testing, this occurrence did not correspond to a large reduction in strength and so was attributed to jolting of the specimen when a sudden volume change occurred.

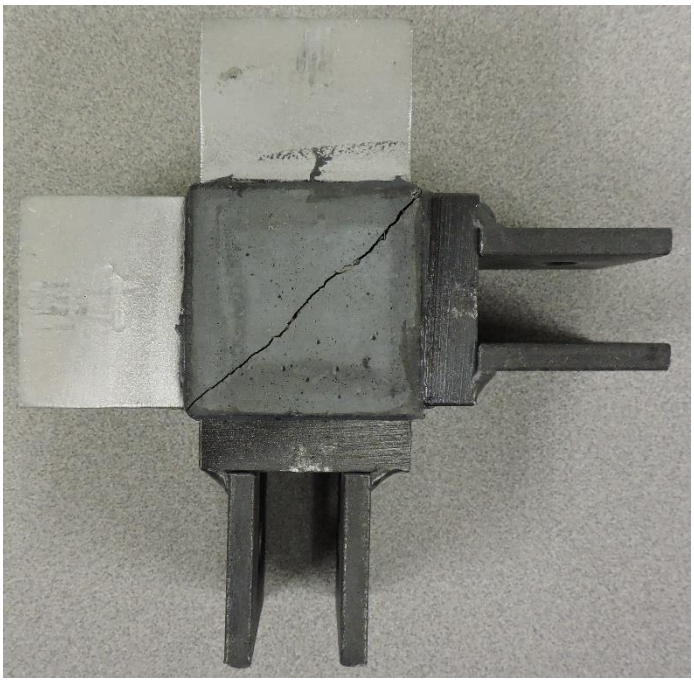

Figure 6.27 – Corner-to-corner cracking caused by TTC testing on a 1% fiber specimen with side stresses set to 450 psi

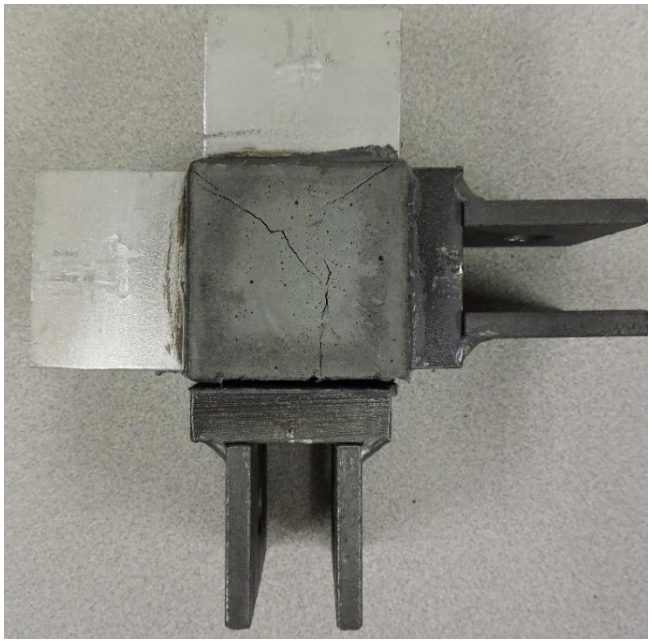

Figure 6.28 – Cracking caused by TTC testing on a 2% fiber specimen with side stresses set to 600 psi (bottom clevis) and 300 psi (right clevis)

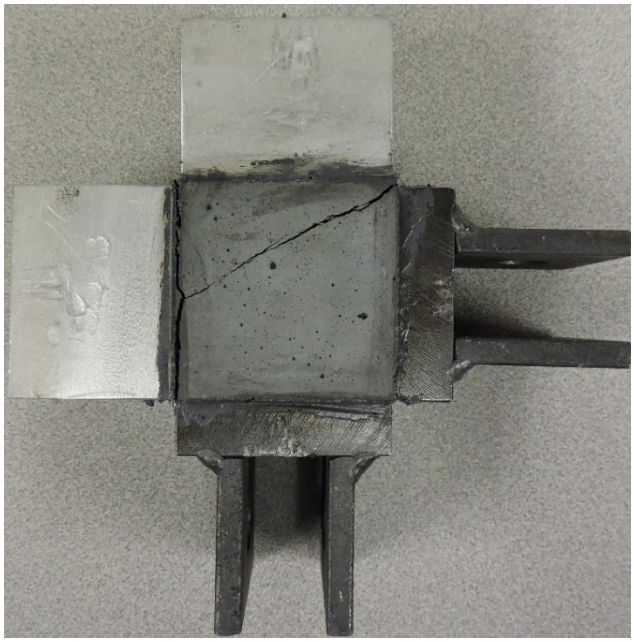

Figure 6.29 – Uneven diagonal crack caused by TTC testing on a 1% fiber specimen with side stresses set to 600 psi (bottom clevis) and 300 psi (right clevis)

6.5. PRECISION LIMITATIONS

6.5.1. Methodology Following ASTM E691

With the development of a new test method, there must be statistical limits set to determine outliers among replicate tests. For the Looney Bin testing, statistical limitations were determined following ASTM E691 Standard Practice for Conducting an Interlaboratory Study to Determine the Precision of a Test Method (2020). Separate limitations were calculated for each fiber content subjected to TTT and TTC tests. The limitations for the TTT test were also used for the TT tests since there were not enough TT tests conducted to develop their own limitations. ASTM E691 provides methods for determining standard deviations for single-operator and multi-laboratory testing. However, since all of the testing in this study was conducted by one operator (the author), the standard deviation limits were calculated for the single-operator condition.

Two different metrics for determining outliers were calculated: the sample standard deviation and the acceptable range of test results. For each test type, the values for the three tests for each individual stress ratio were collected for the calculation. First, the sample standard deviation of the three tests was determined for each stress ratio. Then, the repeatability standard deviation, s_r, was calculated from the individual test sample standard deviations using Equation 6 in ASTM E691, which is repeated as Equation 6.1.

$$\boldsymbol{s_r = \sqrt{\sum_1^p \frac{s^2}{p}}} \qquad \textbf{(6.1)}$$

Where s is the sample standard deviation of each set of replicate tests conducted for each stress ratio, and p is the number of stress ratios evaluated. Once the repeatability

standard deviation was determined, the acceptable range of test results was calculated by multiplying s_r by a factor contained in Table 1 of ASTM C670 Preparing Precision and Bias Statements for Test Methods for Construction Materials (2015). The factor associated with three replicate tests is 3.3. Therefore, each s_r value was multiplied by 3.3 to determine an acceptable difference between the high and the low tested values of the three replicate tests for each stress condition.

Once the repeatability standard deviation was determined, each set of replicate tests were evaluated for consistency using the within-laboratory consistency statistic. This process was conducted to ensure the repeatability standard deviation was not calculated using sets of data that were not consistent with the rest of the test sets. This value is a way to determine an outlier among the individual sample standard deviations for each stress ratio. The within-laboratory consistency statistic was determined using Equation 10 in ASTM E691 and is repeated as Equation 6.2. Once the consistency statistic was calculated, it was compared to a critical value contained in Table 5 in ASTM E691 to determine if the replicate tests for each stress ratio were consistent enough to be used in the determination of the repeatability standard deviation. The critical *k* value for three replicate tests is listed as 1.67.

$$\boldsymbol{k = \frac{s}{s_r}} \qquad \textbf{(6.2)}$$

6.5.2. Statistical Limitations for Each Test and Fiber Content

Using the equations discussed in Section 6.5.1, Table 6.1 through Table 6.8 present the calculations conducted to determine the repeatability standard deviation and

acceptable range of test results for each test type and fiber content. Only the peak load from sigma one was used for determining the repeatability standard deviation since the other two stresses were essentially the same for each of the three tests, and sigma one was the stress of interest in each test. The test results in red were determined to be outside of the consistency standard and were not used in the repeatability standard deviation.

Table 6.1 – Statistical limitation calculation for TTT tests with 0% fiber content

Test Results (psi)				
1	2	3	s (psi)	k
801.3	970.9	1019.8	114.67	1.22
947.9	932.6	842.4	57.02	0.61
734.9	795.3	918.7	93.69	1.00
822.0	857.0	903.1	40.67	0.43
480.5	621.4	-	99.60	1.06
1242.3	1029.2	1259.4	128.27	1.37
1047.6	885.7	1005.2	83.99	0.90
1088.7	1050.0	1260.1	111.85	1.19
1017.4	833.6	829.0	107.47	1.15
1039.9	920.0	970.8	60.14	0.64
Repeatability Standard (psi)				93.77
Acceptable Range of Results (psi)				309.46

Table 6.2 – Statistical limitation calculation for TTT tests with 1% fiber content

Test Results (psi)				
1	2	3	s (psi)	k
919.9	1196.2	975.7	146.07	1.20
1086.5	755.8	897.0	165.93	1.36
1216.1	997.9	1130.8	109.97	0.90
1231.3	1193.8	1153.7	38.81	0.32
1257.8	1072.8	1085.8	103.22	0.85
1237.6	1080.9	-	110.76	0.91
1026.5	1262.0	975.5	152.84	1.25
1316.6	1341.6	1152.3	102.80	0.84
Repeatability Standard (psi)				122.13
Acceptable Range of Results (psi)				403.02

Table 6.3 – Statistical limitation calculation for TTT tests with 2% fiber content

Test Results (psi)				
1	2	3	s (psi)	k
1343.7	1249.7	1222.1	63.75	0.69
1092.8	933.2	878.5	111.36	1.21
1017.8	1149.4	1096.7	66.22	0.72
1090.9	1198.4	1134.5	54.04	0.59
1340.5	1295.7	1193.5	75.33	0.82
1105.5	1329.2	1055.8	145.62	1.59
1262.1	1048.6	1271.2	125.96	1.37
1072.6	1215.7	1218.8	83.53	0.91
1273.3	1196.2	1182.0	49.16	0.54
Repeatability Standard (psi)				91.84
Acceptable Range of Results (psi)				303.07

Table 6.4 – Statistical limitation calculation for TTT tests with 4% fiber content

Test Results (psi)				
1	2	3	s (psi)	k
1180.5	1303.5	1139.5	85.35	0.95
1401.2	1389.1	1341.5	31.56	0.35
1403.1	1305.5	1351.2	48.81	0.54
1314.5	1442.1	-	90.17	1.00
1455.5	1307.8	1213.1	122.15	1.36
1119.1	991.2	1130.7	77.42	0.86
1346.2	1319.1	1100.1	134.93	1.50
1200.1	1209.1	1353.5	86.07	0.96
1260.3	1217.5	1094.2	86.23	0.96
1195.6	886.0	-	218.95	2.44
Repeatability Standard (psi)				89.91
Acceptable Range of Results (psi)				296.71

Table 6.5 – Statistical limitation calculation for TTC tests with 0% fiber content

Test Results (psi)				
1	2	3	s (psi)	k
4033.2	2498.9	2217.7	977.16	1.14
2707.8	4119.5	3117.2	726.28	0.85
2273.7	4136.0	4091.0	1062.48	1.24
1553.2	2868.0	3209.9	874.66	1.02
3349.7	6432.8	2290.5	2151.99	2.52
2500.07	1757.63	-	524.98	0.61
Repeatability Standard (psi)				854.61
Acceptable Range of Results (psi)				2820.23

Table 6.6 – Statistical limitation calculation for TTC tests with 1% fiber contents

Test Results (psi)				
1	2	3	s (psi)	k
4266.7	4890.3	5457.4	595.56	0.68
5081.8	5715.8	5829.1	402.77	0.46
5868.7	4138.0	6737.7	1323.41	1.51
2682.0	3935.1	2445.3	800.60	0.91
2323.3	2284.0	3382.6	623.23	0.71
2184.6	3479.8	3732.2	830.27	0.95
969.4	-	2448.5	1045.90	1.19
2733.4	2964.0	1057.6	1040.46	1.19
Repeatability Standard (psi)				877.75
Acceptable Range of Results (psi)				2896.57

Table 6.7 – Statistical limitation calculation for TTC tests with 2% fiber contents

Test Results (psi)				
1	2	3	s (psi)	k
3431.0	2528.8	3011.7	451.49	0.76
3040.7	2541.1	2806.7	249.96	0.42
2218.7	1762.5	1801.5	252.85	0.42
4556.5	5069.7	5018.6	282.69	0.47
3869.7	3778.6	4794.8	562.26	0.94
2363.6	2537.1	4377.6	1116.11	1.87
1633.8	2701.0	3246.2	820.17	1.37
1956.6	2543.2	-	414.78	0.69
1833.2	591.8	1627.1	665.27	1.11
3960.1	3074.2	-	626.44	1.05
1092.8	1832.8	-	523.26	0.88
Repeatability Standard (psi)				597.38
Acceptable Range of Results (psi)				1971.37

Table 6.8 – Statistical limitation calculation for TTC tests with 4% fiber contents

Test Results (psi)				
1	2	3	s (psi)	k
4793.9	8805.0	4950.3	2272.01	2.52
5871.2	2722.5	7199.1	2299.19	2.55
4669.8	4274.2	3271.6	720.71	0.80
5508.4	5171.7	2400.1	1705.69	1.89
2439.0	2275.4	4044.2	977.36	1.08
2370.3	543.3	-	1291.86	1.43
1803.8	1266.2	1221.5	324.03	0.36
Repeatability Standard (psi)				901.19
Acceptable Range of Results (psi)				2973.92

Some sets only show two individual test results listed instead of three. This was the case when an individual test experienced a premature failure and was unusable. For instance, on several occasions, the side clevises failed prior to application of load in the sigma one direction. This type of failure occurred due to a number of reasons, such as misalignments in the apparatus. However, if at least two data points were collected that appeared to be similar, they were kept for statistical evaluation.

In some cases, there are several datasets that were tests conducted with the same side stresses. Multiple tests for stress ratios were conducted in some cases for repeatability checks, as well as to replace data points that initially appeared to be outliers. While these tests were used for the statistical limitation determination, not all sets of data were used for the failure surface calculations.

After conducting the statistical limitations for each of the test types and fiber percentages, the finalized limits were listed for comparison and are shown in Table 6.9. When compiled together, trends in the limits for each of the test types was evident as the fiber percentages changed.

Table 6.9 – Statistical limitations for each test type and fiber percentage

Fiber Content	Repeatability Standard Deviation (psi)		Acceptable Range of Results (psi)	
	TTT	TTC	TTT	TTC
0%	93.77	854.61	309.46	2820.23
1%	122.13	877.75	403.02	2896.57
2%	91.84	597.38	303.07	1971.37
4%	89.91	901.19	296.71	2973.92

A noteworthy aspect of the statistical analysis is that the limitations for the TTT test are much lower than the TTC testing, as shown in Table 6.9, suggesting a much lower degree of variability for the TTT results. This could be due to the complex stress state created by the TTC testing. The tension stresses applied to the sides were exacerbated by tension strains caused by the compressive load and Poisson's effect, which is inherently variable due to the non-homogenous nature of concrete.

Overall, as shown in Table 6.9, variability from the 1% fiber specimens in the TTT tests and the 2% fiber specimens in the TTC test appear to be different than the overall trends. The variability in the 1% fiber content could be due to fiber distribution issues. With a lower content of fibers, the likelihood of developing a weak plane where very few, if any, fibers cross is higher. This condition would cause a higher variability in replicate tests due to the likelihood of one or more of the tests having such weak planes. Otherwise, the repeatability standard deviation for the TTT test showed continuous, if small, decreases as the fiber percentages increased. This change is consistent with the degree of variability expected from test results of steel fibers when compared to the cementitious matrix. Due to this behavioral difference, as the fiber content increases, the failure mechanism of the composite material should become more consistent.

However, for the TTC test, the repeatability standard deviation exhibited a gradual increase with fiber percentage. The low TTC repeatability standard deviation for 2% fiber specimens could simply be due to having a larger data pool for developing the repeatability standard deviation. This was only due to the fact that 2% fiber specimens were tested early on in the TTC testing phase and more tests were conducted to establish expected trends for the subsequent tests.

6.6. COLLECTED DATA

6.6.1. Method for Determining Outliers Among Replicate Datasets

With the statistical limitations set, the individual data points for each stress ratio could be determined by applying those limits to each replicate dataset to determine if any of the three tests were outliers. This process was conducted on every set of test data, and the results are provided in Appendix A. Each data point determined was the average of at least two replicate tests. If the statistical limitations could not be met with at least two replicate tests, that data point was discarded. The following tables show examples of the statistical limit check for a dataset with three statistically valid tests (Table 6.10), a dataset with only two statistically valid tests (Table 6.11), and a dataset that did not meet the statistical limit check and was subsequently discarded (Table 6.12). The red text indicates a test that was removed from the set upon determining the three replicate tests did not meet the statistical requirements. The red highlight cell indicates a standard deviation that does not meet the statistical requirements.

Table 6.10 – Example data table for stress ratio where all tests meet statistical limits for TTT tests (2% fiber content)

Stress Ratio: 800-800			
	Specimen Failure Stresses (psi)		
Specimen #	Sigma 1	Sigma 2	Sigma 3
1	1273.3	787.2	810.4
2	1196.2	796.2	815.4
3	1182.0	797.2	816.8
Avg. (psi)	**1217.2**	**793.5**	**814.2**
Stdev. (psi)	49.16		
Max Diff. (psi)	91.38		

Table 6.11 – Example data table for stress ratio where two tests meet statistical limits for TTT tests (0% fiber content)

Stress Ratio: 200-200			
	Specimen Failure Stresses (psi)		
Specimen #	Sigma 1	Sigma 2	Sigma 3
1	801.3	212.0	212.8
2	970.9	213.1	221.5
3	1019.8	212.5	214.5
Avg. (psi)	**995.3**	**212.8**	**218.0**
Stdev. (psi)	34.57		
Max Diff. (psi)	48.88		

Table 6.12 – Example data table for stress ratio where the standard deviation limit is not met for TTC tests (4% fiber content)

Stress Ratio: 300-300			
	Specimen Failure Stresses (psi)		
Specimen #	Baldwin	Sigma 2	Sigma 3
1	-5871.2	285.7	306.2
2	-2722.5	298.2	307.7
3	-7199.1	302.0	313.3
Avg. (psi)	**-6535.1**	**293.9**	**309.8**
Stdev. (psi)	938.98		
Max Diff. (psi)	-1327.92		

The top of every table shows what the sigma two and sigma three stresses were set to for those tests and are labeled as the stress ratio. The numbers for the stress ratio are ordered to match standard principal stress notation and are in descending order. Those values do not necessarily correspond to the sigma two and sigma three stresses listed in the table. The sigma one, sigma two, and sigma three stresses listed in the table correspond to the label of the threaded rod in the Looney Bin and do not necessarily relate to standard stress notation. The individual tests highlighted in red were discarded for not meeting the statistical limitations. Once the test was discarded, the standard deviation and maximum difference calculations were completed with the two remaining tests. If those two remaining tests met the statistical limit checks, the data point was kept. If not, the data point was discarded.

The averages and standard deviations shown are for the replicate tests that met the statistical limitations and do not include the outliers highlighted in red. The cells calculating the standard deviation and maximum difference between results were formatted to be filled with different colors depending on if the limit was met. If the statistical limit was met, the cell is highlighted in green, and if the limit was not met, the cell is highlighted in red.

6.6.2. Final Data Points to be Used in Calculating the Failure Surface

After the statistical checks were conducted on each set of tests, the data points that did not meet the limits were discarded from the data pool. The final sets of data points used to determine the failure surface for each fiber content evaluated are shown in Table 6.13 through Table 6.18, along with their respective uniaxial compressive strengths. The uniaxial compressive strengths were determined using 3 in. x 6 in.

cylinders and represent the average of three tests. The data was also converted to Haigh-Westergaard coordinates to facilitate two-dimensional plotting using Equations 6.3, 6.4, and 6.5, and the calculated coordinates are shown in the data tables. The data is plotted in Figure 6.30 through Figure 6.35.

$$\boldsymbol{\xi = \frac{1}{\sqrt{3}} I_1} \tag{6.3}$$

$$\boldsymbol{\rho = \sqrt{2J_2}} \tag{6.4}$$

$$\boldsymbol{\cos\ 3\theta = \frac{3\sqrt{3}}{2}\frac{J_3}{J_2^{3/2}}} \tag{6.5}$$

Table 6.13 – Finalized data points for 0% fiber content

0%	Stress Ratio	(psi)						
		σ_1	σ_2	σ_3	f_c	ξ	ρ	$\theta°$
TTT	0-0	1233	0	0	16200	712	1007	0.00
	200-200	995	218	213	17580	823	637	0.33
	300-300	908	312	306	16110	881	489	0.49
	400-400	765	408	393	16790	904	298	1.95
	500-250	861	482	266	16320	929	425	21.03
	500-500	1251	496	494	15620	1294	617	0.14
	500-500	980	496	488	15620	1134	398	0.91
	500-500	1069	510	497	18330	1199	462	1.16
	600-300	831	590	306	14380	998	372	32.72
	600-600	977	594	593	18330	1250	313	0.12
TT	Prop.	676	681	0	16040	783	554	59.67
	350	670	367	0	16040	599	475	33.18
TTC	200-200	195	193	-2358	17420	-1138	2084	59.95
	200-200	199	198	-3315	16500	-1685	2868	59.99
	300-300	296	290	-4114	16220	-2037	3598	59.94
	300-300	306	294	-3039	16500	-1408	2726	59.83
	400-200	391	198	-2820	16220	-1288	2547	56.93
	400-400	403	387	-2129	17420	-773	2061	59.68

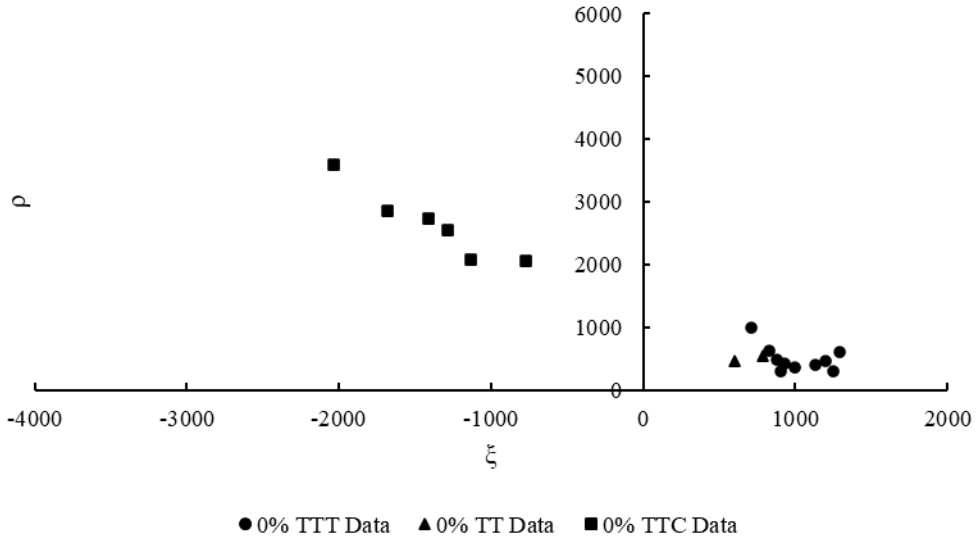

Figure 6.30 – 0% fiber content data plotted using Haigh-Westergaard coordinates

Table 6.14 – Finalized data points for 1% fiber content

1%	Stress Ratio	(psi)						
		σ_1	σ_2	σ_3	f_c	ξ	ρ	$\theta°$
TTT	300-300	948	311	309	16920	906	520	0.15
	500-250	1115	501	263	17330	1085	622	15.72
	600-600	1193	615	613	16570	1397	473	0.18
	700-700	1159	705	689	17620	1474	378	1.65
	800-400	1001	811	416	17560	1286	422	41.51
	800-800	1045	814	808	17320	1540	191	1.32
	800-800	1270	806	776	16430	1647	392	3.10
TT	Prop.	776	767	0	17990	890	630	59.42
	450	1157	459	0	17990	933	824	23.18
TTC	200-200	199	195	-4871	18190	-2585	4139	59.96
	300-300	291	277	-6303	17770	-3311	5378	59.90
	450-450	451	446	-2663	18420	-1019	2541	59.92
	600-300	576	296	-3132	18420	-1305	2920	56.12
	600-600	614	605	-2849	18190	-941	2824	59.86

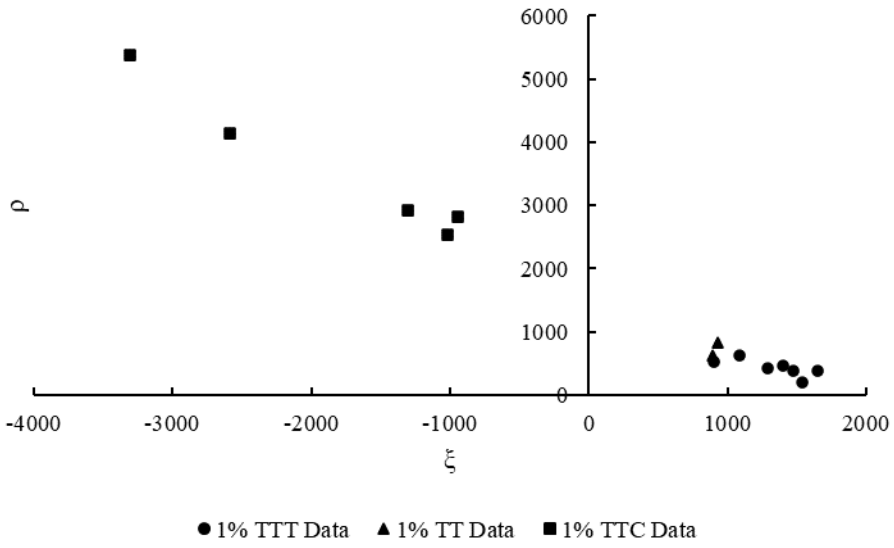

Figure 6.31 – 1% fiber content data plotted using Haigh-Westergaard coordinates

Table 6.15 – Finalized data points for 2% fiber content

2%	Stress Ratio	(psi)						
		σ_1	σ_2	σ_3	f_c	ξ	ρ	$\theta°$
TTT	300-300	1272	327	304	18720	1098	781	1
	500-250	1088	498	263	19170	1068	601	16
	600-200	1141	587	228	18950	1129	651	23
	600-600	1277	608	603	18810	1436	548	0
	700-700	1267	690	665	18950	1514	481	2
	800-400	1169	775	397	18720	1352	546	29
	800-800	1217	814	794	18810	1631	338	2
TT	Prop.	842	838	0	18710	970	686	60
	500	1044	509	0	18710	897	738	29
TTC	300-300	308	304	-2990	16630	-1373	2692	60
	300-300	311	299	-2796	19180	-1262	2532	60
	450-450	456	441	-4148	19500	-1877	3753	60
	600-300	588	307	-2450	18270	-898	2375	55
	600-600	596	593	-2974	16630	-1030	2913	60
	600-600	609	588	-2250	19180	-608	2326	60
	700-700	705	705	-1463	18270	-31	1770	60

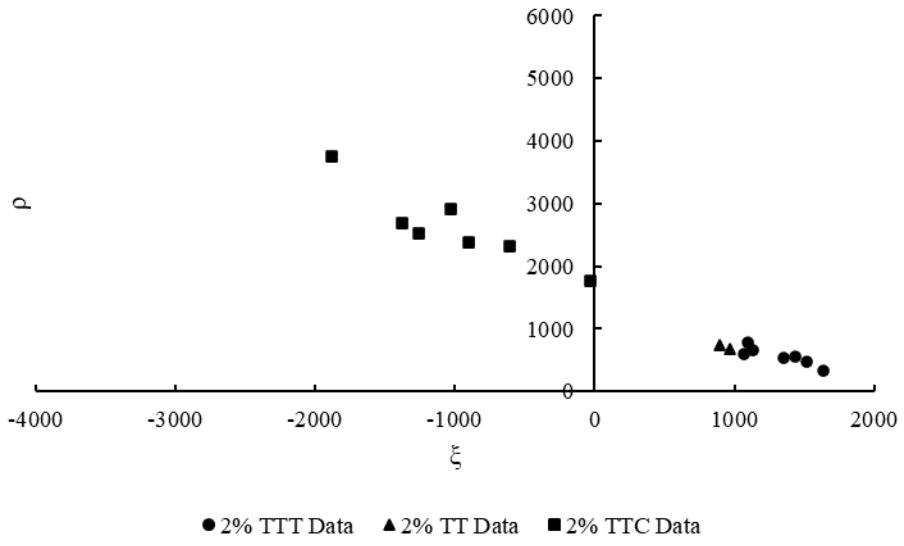

Figure 6.32 – 2% fiber content data plotted using Haigh-Westergaard coordinates

Table 6.16 – Finalized data points for 4% fiber content

4%	Stress Ratio	(psi)						
		σ_1	σ_2	σ_3	f_c	ξ	ρ	$\theta°$
TTT	200-200	1208	218	205	19650	941	814	0.65
	400-400	1260	427	405	19870	1208	690	1.33
	500-200	1377	500	224	20330	1213	852	13.26
	600-300	1353	596	331	20230	1316	751	14.47
	800-500	1254	800	520	20330	1486	524	22.19
	800-800	1191	789	770	20380	1587	336	2.34
TT	Prop.	952	928	0	19430	1085	768	58.71
	600	1173	601	0	19430	1024	830	30.79
TTC	300-300	303	301	-4872	19520	-2465	4224	59.98
	400-400	386	381	-5340	19050	-2641	4673	59.96
	700-350	698	347	-2357	19520	-758	2364	53.99

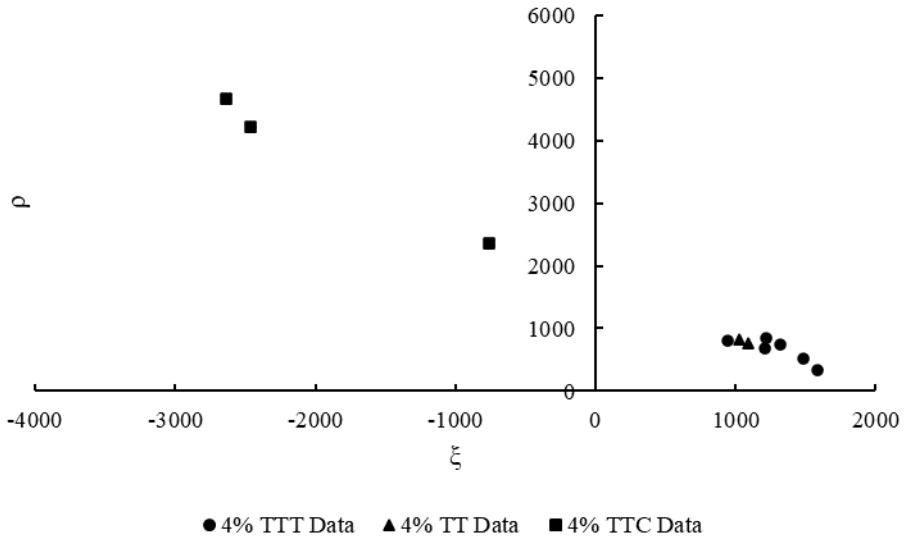

Figure 6.33 – 4% fiber content data plotted using Haigh-Westergaard coordinates

Table 6.17 – Finalized data points for 5% fiber content

5%	Stress Ratio	(psi)						
		σ_1	σ_2	σ_3	f_c	ξ	ρ	$\theta°$
TTT	600-300	1070	597	323	20760	1149	535	21.26
	600-600	1106	606	599	21050	1335	411	0.65
	800-800	1080	812	804	21050	1557	222	1.43

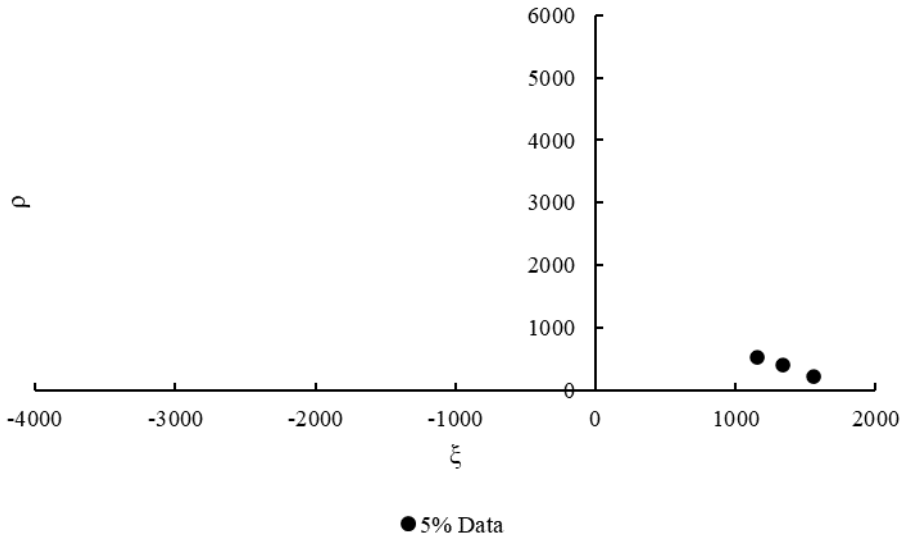

Figure 6.34 – 5% fiber content data plotted using Haigh-Westergaard coordinates

Table 6.18 – Finalized data points for 6% fiber content

6%	Stress Ratio	(psi)						
		σ_1	σ_2	σ_3	f_c	ξ	ρ	$\theta°$
TTT	400-400	1202	412	408	21570	1167	646	0.28
	600-300	1144	592	322	20880	1188	592	18.76
	800-800	1025	820	805	21570	1530	174	3.63
	900-900	1192	887	909	20880	1725	241	3.69

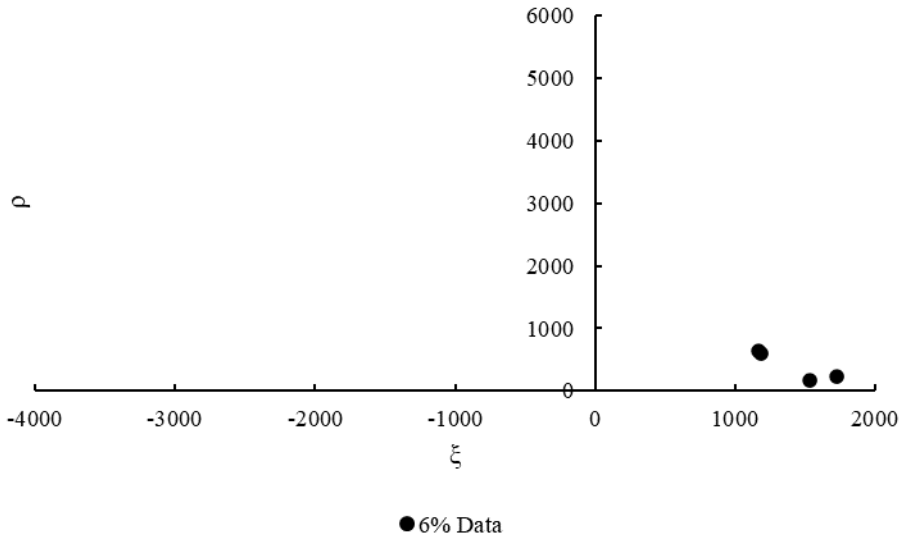

Figure 6.35 – 6% fiber content data plotted using Haigh-Westergaard coordinates

6.7. COMPARISON TO DIFFERENT FIBER MANUFACTURER

6.7.1. Alternative Fiber Selection and Comparison to Dramix® Fiber

During the time this research project was conducted, the manufacturer of the Dramix® OL 0.2/13 fibers announced a halt in production. Therefore, since that fiber brand would not be available in the future, the decision was made to conduct proof testing using a similar fiber from another manufacturer to establish a correlation between the new fibers and the Dramix® fibers. This change also provided the opportunity to demonstrate the applicability of the developed failure surface to different UHPC formulations including the type of fiber. After reviewing available products, the new fiber chosen for the correlation testing was the Type A: Straight Steel Fibers, manufactured by HiPer Fiber, LLC. The properties of both types of fibers are shown in Table 6.19. Also, a photo comparing the fibers is shown in Figure 6.36.

Table 6.19 – Comparison of physical properties of fiber brands

	HiPer Fiber	Dramix®
Diameter (in.)	0.008	0.008
Length (in.)	0.5	0.5
Youngs Modulus (ksi)	30,450	30,450
Tensile Strength (ksi)	413	313

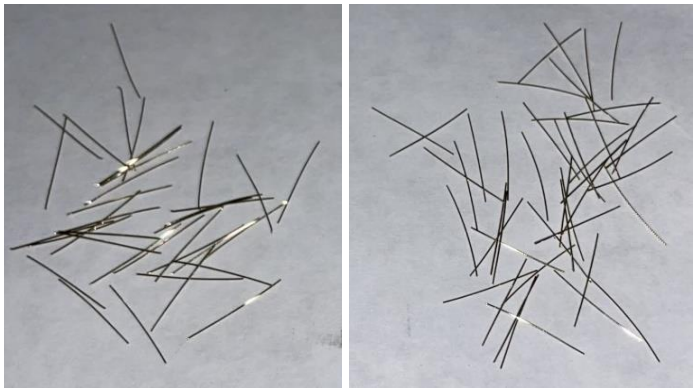

Figure 6.36 – Dramix® fibers (left) and HiPer Fibers (right)

Both fiber types are nearly identical in size and stiffness. The HiPer Fibers have a slightly higher tensile strength. The difference in strength was not expected to cause a noticeable difference in behavior since the fibers typically fail due to pullout and not fracture. Fiber fracture with smooth fibers in UHPC was never observed throughout testing. Since the material stiffnesses are identical, the overall behavior of the fibers in the UHPC matrix was expected to be the same. The only difference between the two fiber brands appeared to be in surface texture. Upon close inspection, a slight indentation was observed on the HiPer Fibers that could have been caused by the equipment used by the manufacturer during extrusion and cutting.

6.7.2. Comparison to Original Fibers

The data collected using the HiPer Fiber fibers were analyzed in the same manner as the previous tests. The statistical analysis results are provided in Appendix A. The final HiPer Fiber data points are shown in the Table 6.20, Table 6.21 and Table 6.22. Comparisons were made to the data collected using the Dramix® fibers and are shown in Figure 6.37, Figure 6.38, and Figure 6.39. These comparisons were only made for 1%, 2%, and 4% fiber contents since the decision was made to halt testing with the 5% and 6% fiber contents. Generally, the HiPer Fibers appeared to have the same trends as the data collected using the Dramix® fibers. The collected data appear to show no difference in behavior between the two fiber types, so no correlation factor was necessary for the different fiber brand. The subsequent failure models were created using a combination of both sets of data since no discernible difference in behavior was observed.

Table 6.20 – Finalized data points for 1% fiber content using HiPer Fibers

1%	Stress Ratio	(psi)						
		σ_1	σ_2	σ_3	f_c	ξ	ρ	$\theta°$
TTT	300-300	826	308	306	17950	832	424	0
	600-600	1139	586	577	17950	1329	455	1
TTC	200-200	197	193	-5542	18360	-2975	4684	60
	400-400	397	393	-3021	18360	-1288	2789	60

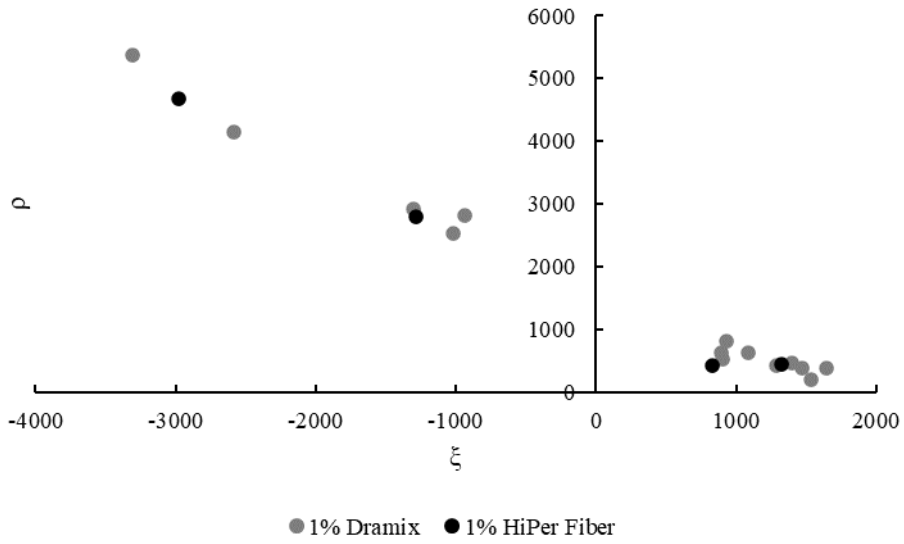

Figure 6.37 – Comparison plot of Dramix® and HiPer Fiber at 1% fiber content

Table 6.21 – Finalized data points for 2% fiber content using HiPer Fibers

2%	Stress Ratio	(psi)						
		σ_1	σ_2	σ_3	f_c	ξ	ρ	$\theta°$
TTT	300-300	906	309	299	18340	874	492	1
	600-600	1081	583	581	18340	1296	407	0
TTC	300-300	302	296	-1928	17770	-768	1818	60
	300-300	301	296	-4882	18940	-2474	4230	60
	600-600	598	597	-1730	17770	-309	1900	60

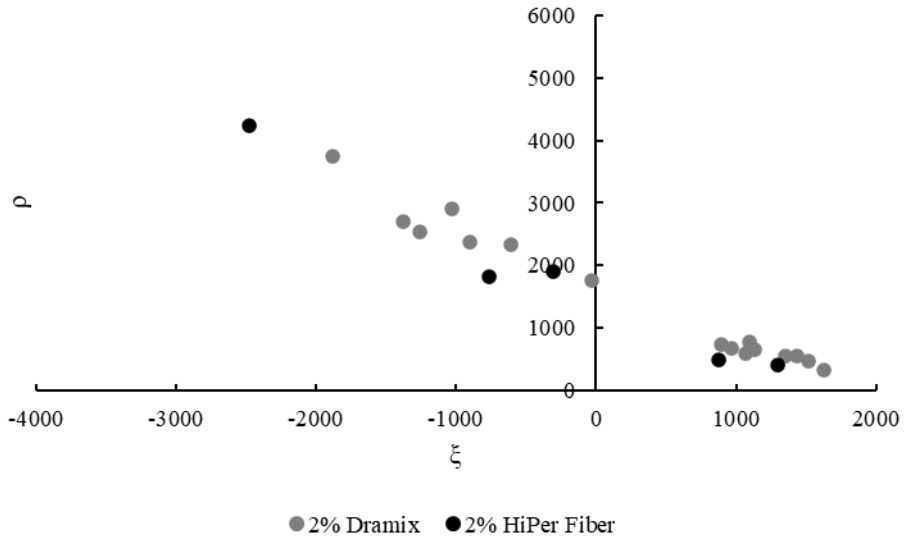

Figure 6.38 – Comparison plot of Dramix® and HiPer Fiber at 2% fiber content

Table 6.22 – Finalized data points for 4% fiber content using HiPer Fibers

4%	Stress Ratio	(psi)						
		σ_1	σ_2	σ_3	f_c	ξ	ρ	$\theta°$
TTT	400-400	1080	422	397	20520	1096	548	2
	700-700	1333	697	696	20520	1574	519	0
TTC	300-300	307	300	-4072	20050	-2001	3572	60
	700-700	705	701	-1430	20050	-14	1742	60

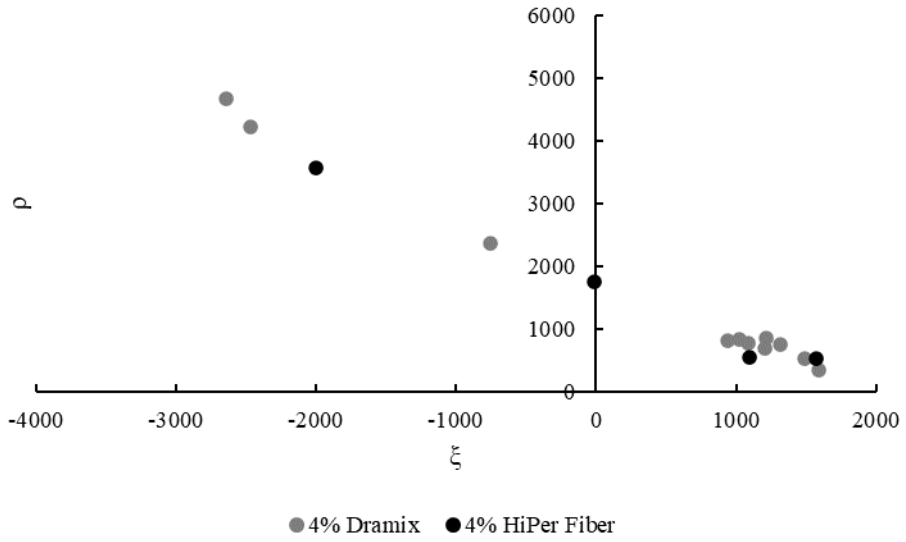

Figure 6.39 – Comparison plot of Dramix® and HiPer Fiber at 4% fiber content

7. FAILURE SURFACE DEVELOPMENT

7.1. INTRODUCTION

In this chapter, the collected data will first be evaluated for trends, with each fiber percentage being compared to determine the effect of increasing fiber percentage on multiaxial tension behavior. Then, a dataset from previous research will be added to the collected data for the purpose of determining the three-dimensional failure surface. A nonlinear regression analysis was conducted to determine the arbitrary parameters of each evaluated failure surface equation that produced the best fit. The best fit was determined by comparing the total error between each data point and the proposed failure model of each set of parameters evaluated in order to arrive at the final failure surface equations. The finalized Looney Bin data used for all subsequent calculations is shown in Table 7.1 through Table 7.4, which includes specimens with Dramix® and HiPer Fibers.

Table 7.1 – Finalized 0% data points

0%	Stress Ratio	(psi)						
		σ_1	σ_2	σ_3	f_c	ξ	ρ	$\theta°$
TTT	0-0	1233	0	0	16200	712	1007	0.0
	200-200	995	218	213	17580	823	637	0.3
	300-300	908	312	306	16110	881	489	0.5
	400-400	765	408	393	16790	904	298	1.9
	500-250	861	482	266	16320	929	425	21.0
	500-500	1251	496	494	15620	1294	617	0.1
	500-500	980	496	488	15620	1134	398	0.9
	500-500	1069	510	497	18330	1199	462	1.2
	600-300	831	590	306	14380	998	372	32.7
	600-600	977	594	593	18330	1250	313	0.1
TT	Prop.	676	681	0	16040	783	554	59.7
	350	670	367	0	16040	599	475	33.2
TTC	200-200	195	193	-2358	17420	-1138	2084	59.9
	200-200	199	198	-3315	16500	-1685	2868	60.0
	300-300	296	290	-4114	16220	-2037	3598	59.9
	300-300	306	294	-3039	16500	-1408	2726	59.8
	400-200	391	198	-2820	16220	-1288	2547	56.9
	400-400	403	387	-2129	17420	-773	2061	59.7

Table 7.2 – Finalized 1% data points

1%	Stress Ratio	(psi)						
		σ_1	σ_2	σ_3	f_c	ξ	ρ	$\theta°$
TTT	300-300	948	311	309	16920	906	520	0.1
	300-300	826	308	306	17950	832	424	0.3
	500-250	1115	501	263	17330	1085	622	15.7
	600-600	1193	615	613	16570	1397	473	0.2
	600-600	1139	586	577	17950	1329	455	0.8
	700-700	1159	705	689	17620	1474	378	1.7
	800-400	1001	811	416	17560	1286	422	41.5
	800-800	1045	814	808	17320	1540	191	1.3
	800-800	1270	806	776	16430	1647	392	3.1
TT	Prop.	776	767	0	17990	890	630	59.4
	450	1157	459	0	17990	933	824	23.2
TTC	200-200	199	195	-4871	18190	-2585	4139	60.0
	200-200	197	193	-5542	18360	-2975	4684	60.0
	300-300	291	277	-6303	17770	-3311	5378	59.9
	400-400	397	393	-3021	18360	-1288	2789	59.9
	450-450	451	446	-2663	18420	-1019	2541	59.9
	600-300	576	296	-3132	18420	-1305	2920	56.1
	600-600	614	605	-2849	18190	-941	2824	59.9

Table 7.3 – Finalized 2% data points

2%	Stress Ratio	(psi)						
		σ_1	σ_2	σ_3	f_c	ξ	ρ	$\theta°$
TTT	300-300	1272	327	304	18720	1098	781	1.2
	300-300	906	309	299	18340	874	492	0.8
	500-250	1088	498	263	19170	1068	601	16.0
	600-200	1141	587	228	18950	1129	651	23.0
	600-600	1277	608	603	18810	1436	548	0.4
	600-600	1081	583	581	18340	1296	407	0.2
	700-700	1267	690	665	18950	1514	481	2.2
	800-400	1169	775	397	18720	1352	546	29.3
	800-800	1217	814	794	18810	1631	338	2.5
TT	Prop.	842	838	0	18710	970	686	59.8
	500	1044	509	0	18710	897	738	29.2
TTC	300-300	308	304	-2990	16630	-1373	2692	59.9
	300-300	311	299	-2796	19180	-1262	2532	59.8
	300-300	302	296	-1928	17770	-768	1818	59.9
	300-300	301	296	-4882	18940	-2474	4230	59.9
	450-450	456	441	-4148	19500	-1877	3753	59.8
	600-300	588	307	-2450	18270	-898	2375	55.2
	600-600	596	593	-2974	16630	-1030	2913	60.0
	600-600	598	597	-1730	17770	-309	1900	60.0
	600-600	609	588	-2250	19180	-608	2326	59.6
	700-700	705	705	-1463	18270	-31	1770	60.0

Table 7.4 – Finalized 4% data points

4%	Stress Ratio	(psi)						
		σ_1	σ_2	σ_3	f_c	ξ	ρ	$\theta°$
TTT	200-200	1208	218	205	19650	941	814	0.7
	400-400	1260	427	405	19870	1208	690	1.3
	400-400	1080	422	397	20520	1096	548	1.9
	500-200	1377	500	224	20330	1213	852	13.3
	600-300	1353	596	331	20230	1316	751	14.5
	700-700	1333	697	696	20520	1574	519	0.1
	800-500	1254	800	520	20330	1486	524	22.2
	800-800	1191	789	770	20380	1587	336	2.3
TT	Prop.	952	928	0	19430	1085	768	58.7
	600	1173	601	0	19430	1024	830	30.8
TTC	300-300	303	301	-4872	19520	-2465	4224	60.0
	300-300	307	300	-4072	20050	-2001	3572	59.9
	400-400	386	381	-5340	19050	-2641	4673	60.0
	700-350	698	347	-2357	19520	-758	2364	54.0
	700-700	705	701	-1430	20050	-14	1742	59.9

7.2. ANALYSIS OF DATA TRENDS

7.2.1. TTT Data Trends

Upon initial inspection of the TTT data, one obvious trend was observed in the sigma one data. Each of the sigma one values were very close in magnitude, regardless of the side stress levels. In order to evaluate this apparent trend, each of the sigma one values were collected for each fiber percentage and averaged. Since the value did not appear to be drastically different than each individual test, the average would represent the theoretical TTT strength. The averaged sigma one values were then compared to the average compressive strengths of their respective fiber percentage. The collected data is shown in Table 7.5.

Table 7.5 – Sigma one for each TTT data point with average compressive strength

	0%	1%	2%	4%
σ_1, Each TTT Test (psi)	995	948	1272	1208
	908	1115	1088	1260
	765	1193	1141	1377
	861	1159	1277	1353
	1251	1001	1267	1254
	980	1045	1169	1191
	1069	1270	1217	1080
	831	826	906	1333
	977	1139	1081	-
Avg. σ_1 (psi)	960	1077	1157	1257
Avg. f_c (psi)	16530	17290	18760	20230
Avg. σ_1/Avg. f_c	5.81%	6.23%	6.17%	6.21%

A gradual increase in both the average of sigma one and the average of the compressive strength was observed as the fiber percentage increases. The average sigma one for each fiber content was divided by their respective average compressive strengths and converted to a percentage. The sigma one/compressive strength percentages for each fiber content are relatively close, ranging from 6.17% to 6.23%, showing a clear relationship between the TTT strength and the compressive strength for specimens with fibers. Also, there is a clear drop in the sigma one/compressive strength percentage for specimens without any fibers. This result makes sense since the addition of fibers to UHPC should increase the relative tension strength. The lower percentage for the specimens without fibers indicates a drop in relative tension strength when compared to fiber reinforced specimens. This data appears to show that the TTT strength is approximately 6.2% of the compressive strength for fiber reinforced specimens up to 4%. When fibers are not present, that percentage drops to 5.8%.

The increase in both TTT and compressive strength makes sense when considering the failure mechanisms of concrete in tension. Upon curing of concrete specimens, internal shrinkage tends to create microcracks randomly spaced in the cementitious matrix. Upon application of loading, these microcracks tend to develop stress concentrations at their tips. These stress concentrations will develop until the point at which the crack widens and/or extends, which causes a microcrack to develop into a macrocrack (Kotsovos, 2015). This process, which proceeds up to the development of excessive macrocracks, is essentially the failure mechanism for both compression elements indirectly (due to Poisson's effect) and tension elements directly (due to the direct application of tension). The addition of steel fibers to UHPC provides additional support to the microcracks that develop during curing and, upon the stress concentrations at the crack tips reaching fracture levels, provides an alternate load path for the stress, allowing the stress to be better distributed throughout the cementitious matrix. This level of support would tend to increase with an increase in fiber percentage, which would explain how there was a gradual increase in both the compressive strength and TTT strength with increasing fiber percentages.

However, there was a fiber saturation point realized during this testing, which was found to be somewhere between 4 and 5% fibers by volume. This point was determined by a noticeable reduction in the TTT strength. At this saturation dosage, there is overcrowding of the fibers in the cementitious matrix, reducing its continuous volume. While, theoretically, the higher fiber contents would still provide increased strength by reducing the extent to which microcracks would expand into macrocracks, this increase in strength was countered by a reduction in strength caused by a reduced cementitious

cross section at the weak planes due to excessive fiber content. This reduction in strength is analogous to a reduction in conventional concrete strength caused by excessive coarse aggregate. A reduction in the binding material would eventually cause a reduction in strength due to its inability to successfully bond the stronger particles together (coarse aggregate particles in the case of conventional concrete and fibers in the case of the UHPC).

Another observation for the TTT data was how, when the stress states were converted to Hiagh-Westergaard coordinates, as shown in Table 7.1 through Table 7.4, the angle, θ, appeared to change with the changing stress ratios while the sigma one failure loads stayed the same. The Haigh-Westergaard coordinates convert the principal stresses to polar coordinates that can reduce the three-dimensional failure surface to a series of two-dimensional lines. The ξ term is the hydrostatic axis of the failure surface, meaning all points on that axis represent coordinates in stress space when the principal stresses are equal. The ρ term represents the distance between the hydrostatic axis and the exterior edge of the failure surface, which encompasses the deviatoric plane. The θ term locates the plane of the failure surface where ρ is calculated and ranges from zero degrees to sixty degrees. The failure surface is envisioned to be symmetrical about three axes, so the deviatoric plane term, ρ, would only need to be calculated for those angles. A graphic describing this coordinate transformation is shown in Figure 7.1.

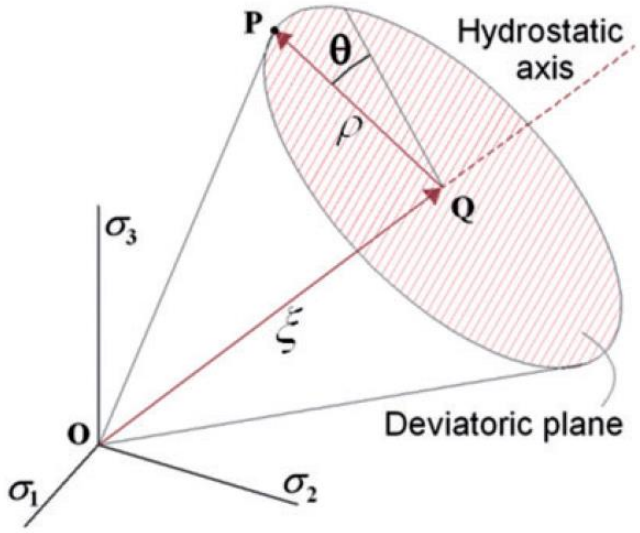

Figure 7.1 – Description of conversion from stress coordinates to Haigh-Westergaard coordinates (Cortese et al., 2015)

The data collected revealed a trend in the sigma one failure stresses between stress ratios for each fiber percentage. However, while the sigma one values tended to be close in magnitude, the angles changed with different stress ratios. This would indicate that the failure surface has a near-circular deviator plane similar to that shown in Figure 7.1 at the tension region.

7.2.2. TTC Data Trends

One apparent trend in the TTC data was a reduction in the compressive strength as the side tension stresses were increased. This result is consistent with the fact that concrete failure in compression is due to the development of perpendicular tensile strains caused by Poisson's effect. The applied side tension stresses would exacerbate these developing strains and ultimately reduce the compressive capacity. An attempt was made to determine a trend in this compressive strength reduction as the side stresses increased.

To do this, the data was first reduced to a two-dimensional format by averaging the side stresses and normalizing the data by dividing by the respective cylinder uniaxial compressive strengths. The data was then plotted with the normalized average side stress on the x-axis and the normalized TTC compressive stress on the y-axis. The point that represents zero side stresses would be equivalent to the uniaxial compressive strength and was set to negative one. The plots for each fiber percentage are shown in Figure 7.2 through Figure 7.5.

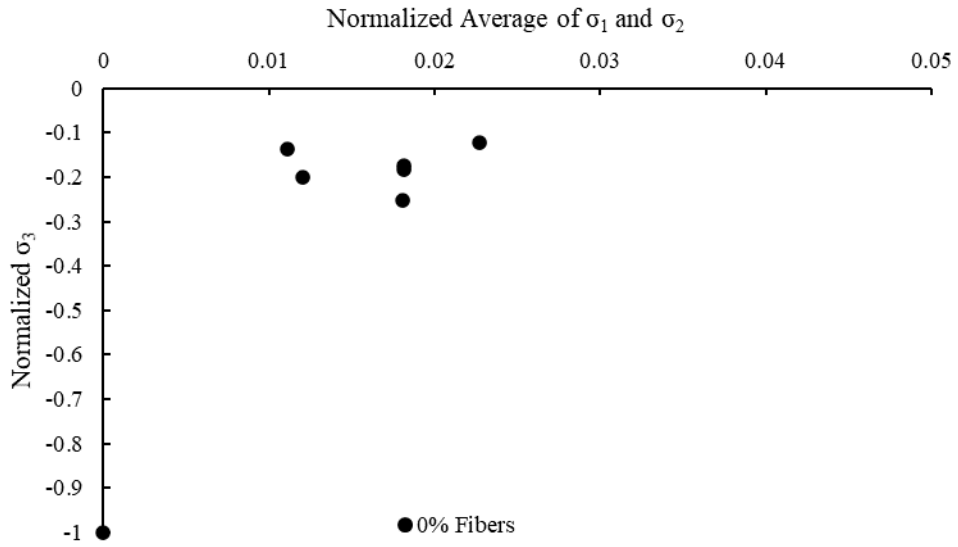

Figure 7.2 – TTC compressive strength plot as a function of the averaged side stresses for 0% fibers

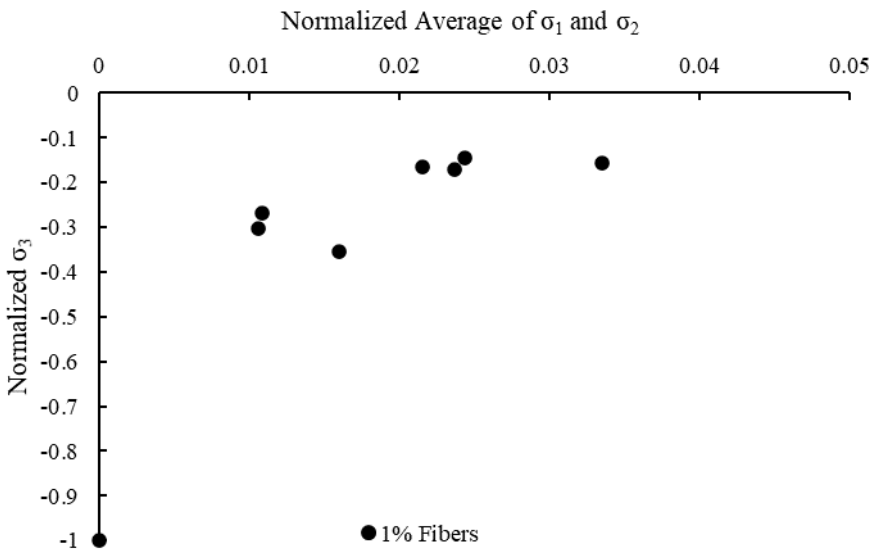

Figure 7.3 – TTC compressive strength plot as a function of the averaged side stresses for 1% fibers

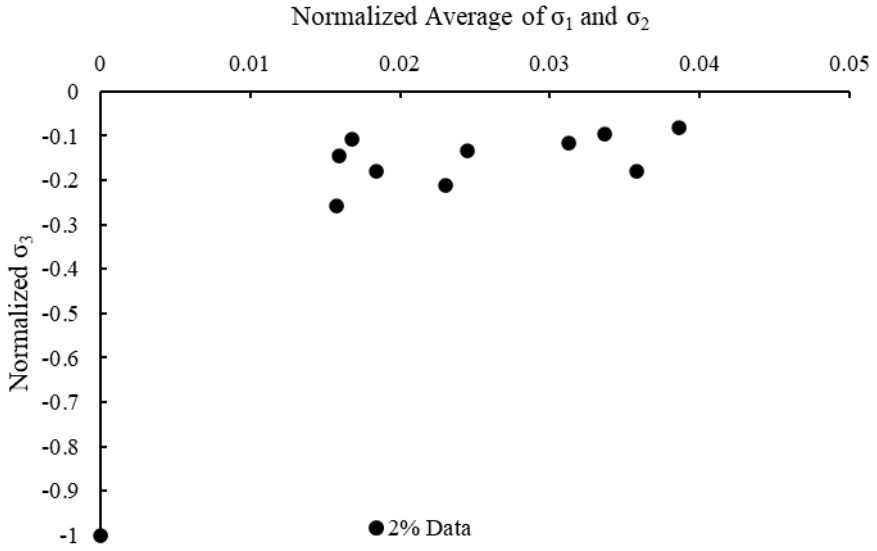

Figure 7.4 – TTC compressive strength plot as a function of the averaged side stresses for 2% fibers

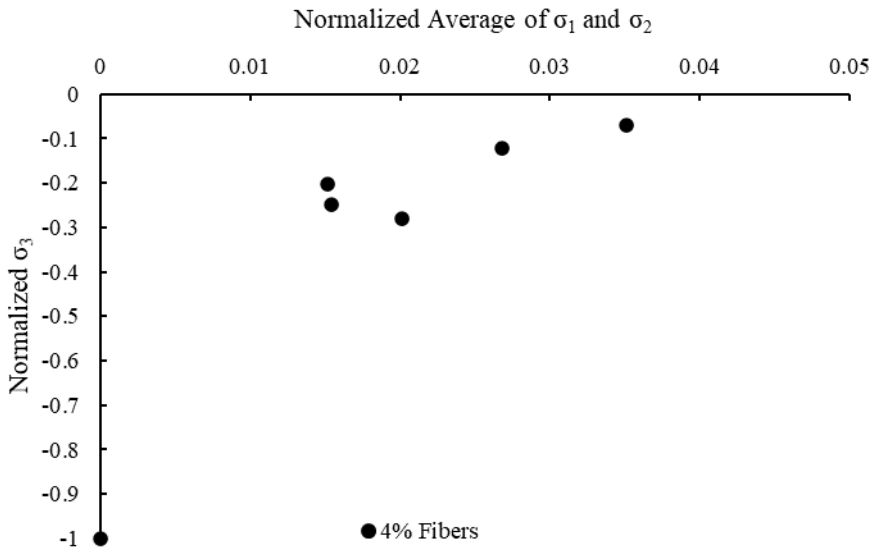

Figure 7.5 – TTC compressive strength plot as a function of the averaged side stresses for 4% fibers

A gradual decrease in strength was observed as the side stresses increased. The data also appeared to be nonlinear. With a trend visually established, the MathWorks© software MATLAB was used to establish a general equation for the decay of compressive strength as a function of the side stresses. The general decay function was in the form of Equation 7.1.

$$\boldsymbol{y = -e^{ax}} \qquad \textbf{(7.1)}$$

In Equation 7.1, *a* is an arbitrary parameter used to fit the decay function to the data. The exponential term was multiplied by negative one to ensure the y-intercept was set to negative one. Logically, this will always be the case since the data was normalized by the cylinder uniaxial compressive strength and, at the y-intercept, the side stress are zero, which equates to the uniaxial compressive strength.

The data for each fiber percentage was collected into a CSV file to be read into the MATLAB program and a nonlinear regression analysis was conducted using the Levenberg-Marquardt nonlinear least squares regression analysis method. This method is a combination of the gradient descent and the Gauss-Newton algorithms. The Levenberg-Marquardt algorithm works more like the gradient descent algorithm when the initial value is far from the ideal value and more like the Gauss-Newton algorithm when the initial value is near the ideal value (Gavin, 2020). The normalized TTC data used for the regression analysis for each fiber percentage is shown in Table 7.6 through 7.9. The MATLAB code used to determine the arbitrary parameter, *a*, in Equation 7.1 is shown in Figure 7.6.

Table 7.6 – Normalized 0% TTC data for curve fitting

	$\frac{\frac{\sum \sigma_1 + \sigma_2}{2}}{f_c}$	$\frac{\sigma_3}{f_c}$
0%	0.011	-0.135
	0.012	-0.201
	0.018	-0.254
	0.018	-0.184
	0.018	-0.174
	0.023	-0.122
	0.000	-1.000

Table 7.7 – Normalized 1% TTC data for curve fitting

	$\frac{\frac{\sum \sigma_1 + \sigma_2}{2}}{f_c}$	$\frac{\sigma_3}{f_c}$
1%	0.011	-0.268
	0.016	-0.355
	0.024	-0.145
	0.024	-0.170
	0.034	-0.157
	0.011	-0.302
	0.022	-0.165
	0.000	-1.000

Table 7.8 – Normalized 2% TTC data for curve fitting

	$\frac{\frac{\sum \sigma_1 + \sigma_2}{2}}{f_c}$	$\frac{\sigma_3}{f_c}$
2%	0.018	-0.180
	0.016	-0.146
	0.023	-0.213
	0.025	-0.134
	0.036	-0.179
	0.031	-0.117
	0.039	-0.080
	0.017	-0.108
	0.016	-0.258
	0.034	-0.097
	0.000	-1.000

Table 7.9 – Normalized 4% TTC data for curve fitting

	$\frac{\frac{\sum \sigma_1 + \sigma_2}{2}}{f_c}$	$\frac{\sigma_3}{f_c}$
4%	0.015	-0.250
	0.020	-0.280
	0.027	-0.121
	0.015	-0.203
	0.035	-0.071
	0.000	-1.000

```
%% 0% Data

 load TTC0.csv;
 xdata = TTC0(:,1);
 ydata = TTC0(:,2);

 fun = @(x,xdata)-1*exp(x(1)*xdata);

 x0 = [-50];

 options = optimoptions('lsqcurvefit','Algorithm','levenberg-marquardt');

 lb = [-500];
 ub = [1];

 x = lsqcurvefit(fun,x0,xdata,ydata,lb,ub,options)
```

Figure 7.6 – Example MATLAB code used for TTC curve fitting for 0% fiber data

The MATLAB code first loads in a .CSV file containing the data for each fiber percentage. Then, the generalized decay function shown in Equation 7.1 was defined and was labeled *fun*. The arbitrary parameter, *a*, was labeled *x(1)* in the code. Next, a start point was set for the iterative process of determining the arbitrary parameter. Then, the option for using the Levenberg-Marquardt algorithm was applied. The *lb* and *ub* represent lower and upper bounds for the arbitrary parameter, respectively. Lastly, the

lsqcurvefit function was defined with the above inputs defined in the function. The program was then executed to determine the arbitrary parameter that provides the best fit. After conducting the first run, the start point was changed to be closer to the first answer, then rerun to ensure the program converges on the same value. The arbitrary parameters determined for each fiber percentage are shown in Table 7.10. The decay function plotted with the original data is shown in Figure 7.7 through Figure 7.10 for each fiber percentage.

Table 7.10 – Arbitrary parameters in decay function for each fiber percentage

	a
0%	-114.18
1%	-88.8
2%	-89.8
4%	-83.9

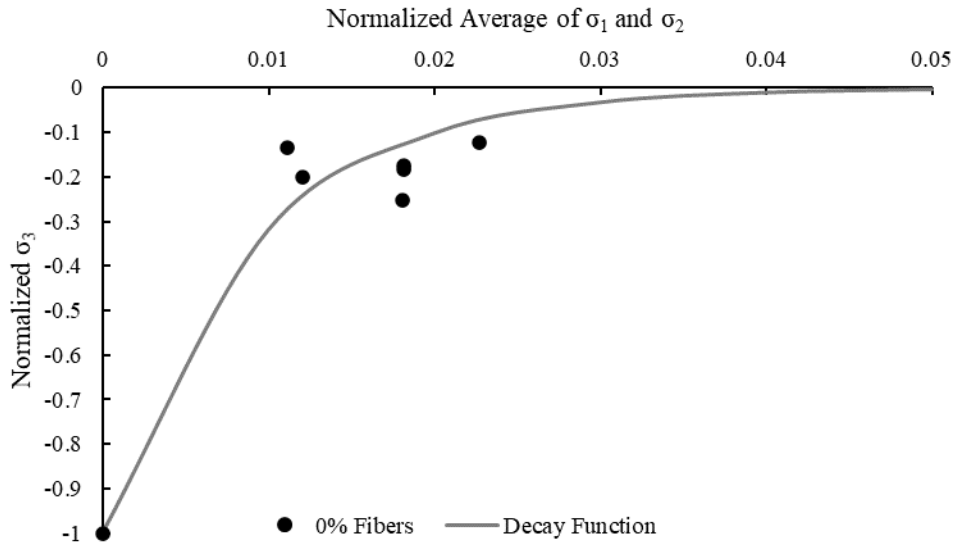

Figure 7.7 – TTC compressive strength plot along with fitted decay function for 0% fibers

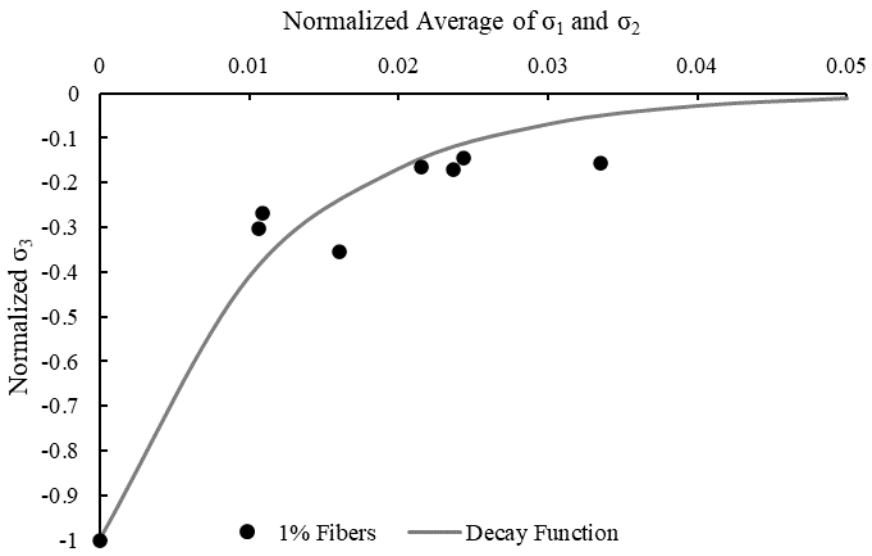

Figure 7.8 – TTC compressive strength plot along with fitted decay function for 1% fibers

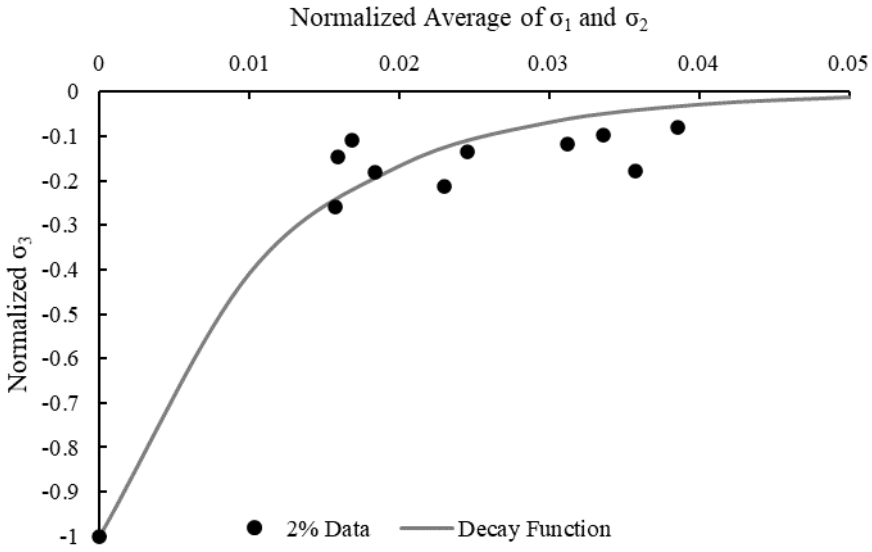

Figure 7.9 – TTC compressive strength plot along with fitted decay function for 2% fibers

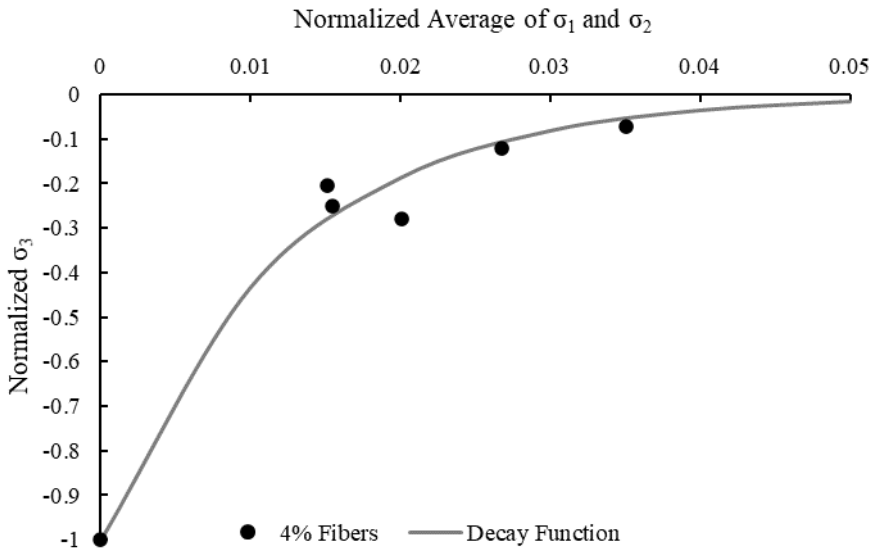

Figure 7.10 – TTC compressive strength plot along with fitted decay function for 4% fibers

The 0% parameter was much higher than the fiber reinforced specimens, which implies a much sharper decrease in compressive strength as the applied tension stresses increase in the other two directions. This behavior makes sense since the presence of the fibers would provide alternate load paths when the microcracks expanded as Poisson's effect increased with increasing compressive stress, thus providing additional capacity. The parameter values for both 1% and 2% were nearly identical, while the 4% parameter was slightly lower. The slightly lower value could imply an increase in TTC capacity with the additional fibers. However, additional data would be needed to fully understand behavioral differences in the fiber reinforced specimens.

7.2.3. Comparison of All Normalized Data

After observing the behavior associated with the different stress conditions, the full datasets were then compared to each other. First, the data was converted to Haigh-

Westergaard coordinates. Then, the terms ξ and ρ were normalized by dividing each data point by their respective cylinder uniaxial compressive strengths. This normalization technique was used to match previous research (e.g., Menétrey and Willam, 1995; Ritter and Curbach, 2016). After plotting each set of data, polynomial and linear trend lines were fit to the data to evaluate the general trend of the data. The normalized plotted data with their associated trend lines are shown in Figure 7.11 through Figure 7.14. The R^2 values associated with each trend line equation for each fiber percentage is tabulated in Table 7.11 for comparison. The parameters for both fit types are shown in Table 7.12.

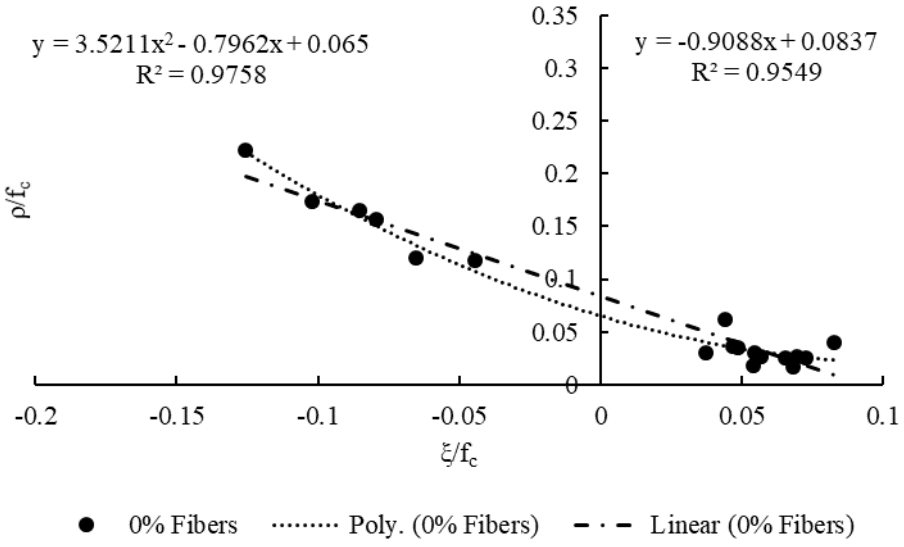

Figure 7.11 – Normalized 0% fiber data with trend lines

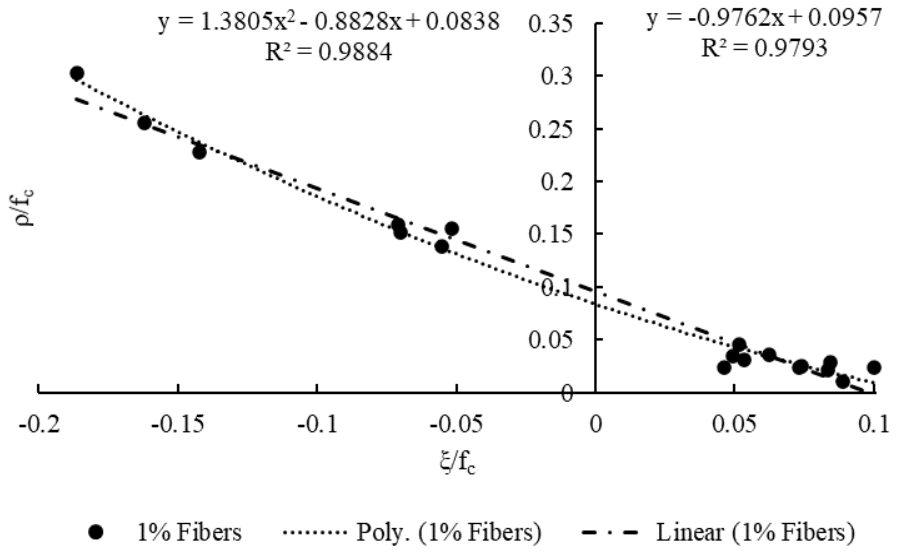

Figure 7.12 – Normalized 1% fiber data with trend lines

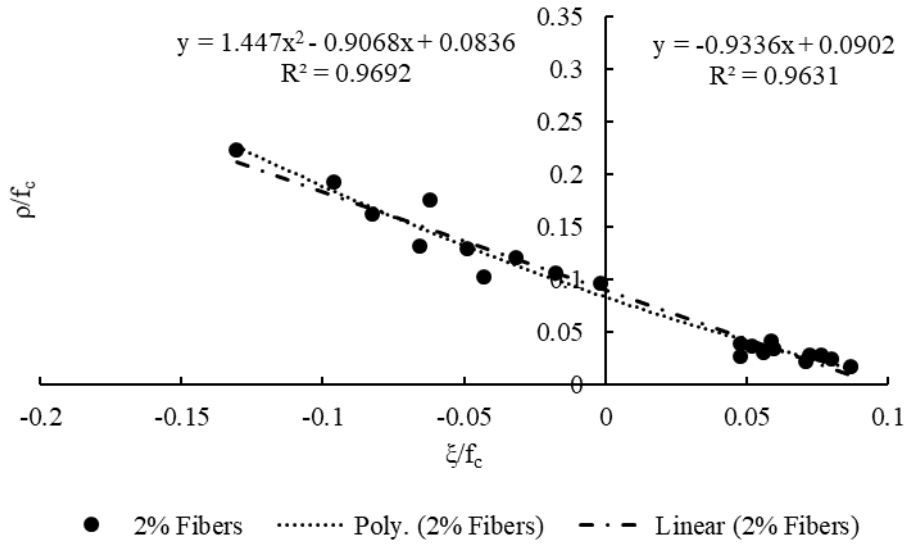

Figure 7.13 – Normalized 2% fiber data with trend lines

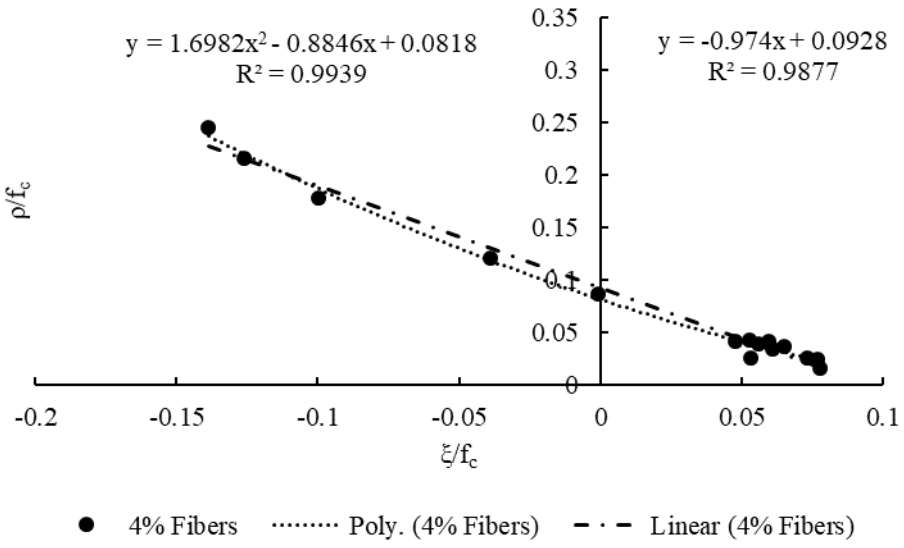

Figure 7.14 – Normalized 4% fiber data with trend lines

Table 7.11 – R^2 values for each fiber percentage and trend type

	R^2	
	Linear	Polynomial
0%	0.9549	0.9758
1%	0.9793	0.9884
2%	0.9631	0.9692
4%	0.9877	0.9939

Table 7.12 – Fit parameters for each fit type

	Linear		Polynomial		
	Slope	Intercept	x^2	x	Intercept
0%	-0.9088	0.0837	3.5211	-0.7962	0.065
1%	-0.9762	0.0957	1.3805	-0.8828	0.0838
2%	-0.9336	0.0902	1.447	-0.9068	0.0836
4%	-0.974	0.0928	1.698	-0.8846	0.0818

The R^2 value was higher when using a polynomial fit for each set of data. This implies that the data tends to take the shape of a parabola in the tension regions of the failure surface. However, the parameters appear to be significantly different between the specimens with and without fibers. The parameters for the fiber reinforced specimens all appear to be very close, implying that the behavior of fiber reinforced UHPC in the tension region of the failure surface is proportional to its relationship to the uniaxial compressive strength. This relationship was also apparent in the TTT data, shown in Table 7.1 This also implies that a single, normalized failure model can be developed for fiber reinforced UHPC for fiber contents up to 4%. This is an important relationship because it simplifies modeling techniques for various fiber percentages by only requiring one, normalized model. A different failure model would be required for UHPC without fibers.

7.3. INCORPORATION OF RITTER AND CURBACH TRIAXIAL TESTING DATA (2016)

The data collected from the Looney Bin represents a relatively small portion of the entire failure surface owing to fact that concrete has a relatively low tensile strength when compared to its compressive strength. For this reason, additional data was needed from other portions of the failure surface to develop the equation in its entirety. Ritter and Curbach (2016) conducted triaxial testing on UHPC using 4 in. cube specimens for a large portion of the failure surface. This data consisted of triaxial compression, compression-compression, tension-compression, and tension-compression-compression stress conditions. The authors did not publish uniaxial compressive strengths for each

data point but published average compressive and tensile strength values. The average cylinder uniaxial compressive strength was used to normalize each data point. The published stresses were converted to Haigh-Westergaard coordinates and normalized by dividing ξ and ρ by the uniaxial compressive strength. This set of data was then combined with the Looney Bin data and used for the regression analysis. The published data from Ritter and Curbach (2016) is shown in Table 7.13. The data points are plotted by angle, θ, in Figure 7.15.

Table 7.13 – Published data from Ritter and Curbach (2016)

(psi)						
σ_1	σ_2	σ_3	f_c	ξ/f_c	ρ/f_c	$\theta°$
1150	0	0	25250	0.026	0.037	0.0
1150	-210	-210	25250	0.017	0.044	0.0
1080	-540	-540	25250	0.000	0.052	0.0
880	-880	-880	25250	-0.020	0.057	0.0
880	-1200	-1200	25250	-0.035	0.067	0.0
780	-2250	-2250	25250	-0.085	0.098	0.0
560	-5090	-5090	25250	-0.220	0.183	0.0
660	-13190	-13190	25250	-0.588	0.448	0.0
530	-21330	-21330	25250	-0.963	0.707	0.0
0	-25030	-25030	25250	-1.145	0.809	0.0
-1380	-35480	-35480	25250	-1.654	1.103	0.0
1100	0	-400	25250	0.016	0.044	14.9
1160	-310	-850	25250	0.000	0.058	15.0
430	-1030	-1570	25250	-0.050	0.058	15.1
750	-10840	-15080	25250	-0.576	0.459	15.0
920	-7280	-10290	25250	-0.381	0.325	15.0
500	-18170	-24990	25250	-0.975	0.739	15.0
0	-19170	-26180	25250	-1.037	0.759	15.0
-950	-26010	-35020	25250	-1.417	0.989	14.8
1100	0	-1100	25250	0.000	0.062	30.0
1030	-380	-1790	25250	-0.026	0.079	30.0
850	-850	-2540	25250	-0.058	0.095	29.9
580	-1000	-2570	25250	-0.068	0.088	29.9

Table 7.13 – Published data from Ritter and Curbach (2016) (continued)

(psi)						
σ_1	σ_2	σ_3	f_c	ξ/f_c	ρ/f_c	$\theta°$
820	-5090	-10990	25250	-0.349	0.331	30.0
710	-8510	-17730	25250	-0.584	0.516	30.0
290	-14350	-28980	25250	-0.984	0.820	30.0
0	-13730	-27460	25250	-0.942	0.769	30.0
-1120	-19820	-38570	25250	-1.361	1.049	30.0
920	0	-2500	25250	-0.036	0.099	44.9
610	-550	-3730	25250	-0.084	0.126	45.0
1000	-1000	-6480	25250	-0.148	0.217	45.0
760	-3510	-15220	25250	-0.411	0.463	45.0
600	-5960	-23850	25250	-0.668	0.709	45.0
0	-7510	-28010	25250	-0.812	0.812	45.0
-1000	-10590	-36900	25250	-1.109	1.041	45.1
0	0	-23370	25250	-0.534	0.756	60.0
-1380	-1380	-34410	25250	-0.850	1.068	60.0
-4650	-4650	-46500	25250	-1.276	1.353	60.0

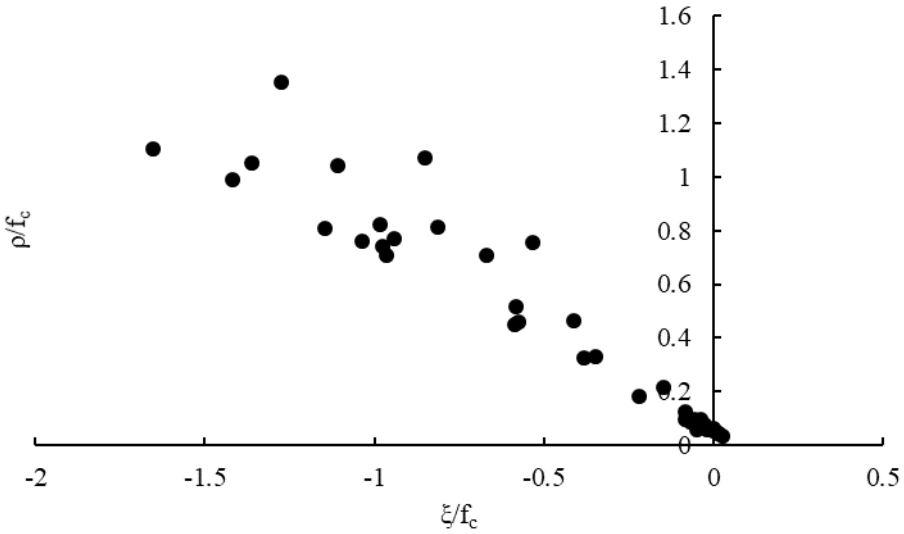

Figure 7.15 – Ritter and Curbach (2016) data points plotted in Haigh-Westergaard coordinates

7.4. MENÉTREY AND WILLAM EQUATION (1995) NONLINEAR REGRESSION ANALYSIS WITH COMBINED DATASET

7.4.1. MATLAB Code for Regression Analysis

The first equation that was fit to the compiled data was the generalized equation developed by Menétrey and Willam (1995). The generalized equation is outlined below in Equations 7.2, 7.3, and 7.4.

$$\boldsymbol{F(\xi,\rho,\theta) = \left[A_f \rho\right]^2 + m\left[B_f \rho r(\theta,e) + C_f \xi\right] - c = 0} \quad \textbf{(7.2)}$$

$$\boldsymbol{m = 3\frac{f_c'^2 - f_t'^2}{f_c' f_t'}\frac{e}{e+1}} \quad \textbf{(7.3)}$$

$$\boldsymbol{r(\theta,e) = \frac{4(1-e^2)cos^2\theta + (2e-1)^2}{2(1-e^2)cos\theta + (2e-1)[4(1-e^2)cos^2\theta + 5e^2 - 4e]^{1/2}}} \quad \textbf{(7.4)}$$

The arbitrary parameters meant to alter the shape of the curves for this equation are *A*, *B*, and *C*. The parameter *e* adjusts the out-of-roundness of the failure surface and ranges from 0.5 to 1 with 0.5 creating a near-triangular deviatoric plane shape and 1 creating a circular deviatoric plane shape. The equation *m* is considered the friction coefficient and adjusts the shape of the curve by associating the failure surface with the relationship between the compressive and tensile strengths.

First, the general equation for the shape of the failure surface was rearranged to solve for ρ as a function of ξ. The rearranged equation is shown as Equation 7.5. The MATLAB code used for the regression analysis is shown in Figure 7.16, and the code for the general equation is shown in Figure 7.17.

$$\rho = \sqrt{\frac{c}{A^2} - \frac{Cm\xi}{A^2} + \frac{m^2B^2r^2}{4A^4}} - \frac{mBr}{2A^2} \qquad (7.5)$$

```
%% Nonlinear Curve Fitting
% Menetrey and Willam (1995)

 load combineddata.csv;
 xi = combineddata(:,1);
 rho = combineddata(:,2);
 thetad = combineddata(:,3);
 theta = thetad*pi./180;
 fc = 1;

 data = [xi,theta];

 x0 = [1 1 1 1 1]; %A, B, C, e, %fc for ft

 options = optimoptions('lsqcurvefit','Algorithm','levenberg-marquardt');

 lb = [-inf -inf -inf 0.5 -inf];
 ub = [inf inf inf 1 inf];

 [y,resnorm,~,exitflag,output] = lsqcurvefit(@(x,data)solverho(x,data),x0,data,rho,
lb,ub,options)
```

Figure 7.16 – MATLAB regression analysis code for the Menétrey and Willam equation (1995)

```
function rho = equ7(x,data)

 xi = data(:,1);
 theta = data(:,2);

fc=1;

A=x(1);
B=x(2);
C=x(3);
e=x(4);
z=x(5);

m = (3*((fc^2-(fc*z)^2)/(fc^2*z))*(e/(e+1)));
r=(4*(1-e^2)*cos(theta).^2+(2*e-1)^2)./(2*(1-e^2)*cos(theta)+(2*e-1)*(4*(1-e^2)*cos
(theta).^2+5*e^2-4*e).^(0.5));


rho = sqrt(1/A^2-(C*m*xi)/A^2+(m^2*B^2.*r.^2)/(4*A^4))-(m*B.*r)/(2*A^2);
```

Figure 7.17 – MATLAB code forming the equation to solve for ρ

The compiled dataset was converted to Haigh-Westergaard coordinates, normalized by dividing by the cylinder uniaxial compressive strengths for each data point, and compiled in a CSV file to be read in by the MATLAB code. The two independent variables were combined into one matrix so it could be read into the ρ equation outlined in a separate file. The equation was coded in a separate file due to its complexity. Creating a separate function file made it easier to adjust the equation if any problems in the code arose. The term x_0 outlined the starting point for the parameters to be determined. The arbitrary parameters in the equation are *A*, *B*, and *C*. However, since the eccentricity, *e*, was not known, it was also set as a parameter to determine. The last parameter to be determined was the percentage adjustment to the compressive strength to estimate tensile strength. This value would ordinarily be independently determined using uniaxial compression and tension testing. However, since the uniaxial tensile strength was not determined for the fiber reinforced specimens, it was set as an adjustable parameter to see if a reasonable value could be estimated through the regression analysis.

7.4.2. Solving for the Arbitrary Parameters

Once the starting points were set, the upper and lower bounds were adjusted. For the initial run, the bounds were set to infinity (*inf* in the code) for all of the arbitrary values except *e*. The eccentricity term was given a lower bound of 0.5 and an upper bound of 1 based on the requirements of the equation outlined by Menétrey and Willam (1995). After the initial run, the bounds and starting points of the variables were incrementally adjusted to test the fit assuming no bounds to the parameters. The fit was evaluated by comparing the output, *resnorm*, of the different runs. This term represents

the sum of the squared difference between the calculated value of ρ and the tested value of the individual data points. The equation for *resnorm* is shown as Equation 7.6. The arbitrary parameters determined from each iteration of the regression analysis are shown in Table 7.14.

$$\boldsymbol{resnorm = \sum_{1}^{\#\ of\ points}\left(\frac{\rho_{test}}{f_c} - \frac{\rho_{model}}{f_c}\right)^2} \qquad \textbf{(7.6)}$$

Table 7.14 – Parameters determined for Menétrey and Willam equation (1995)

Iteration #	A	B	C	e	% fc for ft	Resnorm
1	0.9108	1.2892	1.4858	0.5932	13.69%	0.0434
2	0.8499	1.0411	1.1815	0.6	11.20%	0.0436
3	0.8498	0.4601	0.522	0.6	5.00%	0.0436
4	0.8499	0.739	0.8388	0.6	8.00%	0.0436
5	0.911	0.4633	0.534	0.5932	5.00%	0.0434
6	0.9108	0.7441	0.8576	0.5932	8.00%	0.0434
7	0.0002	1.4248	1.2496	0.8	17.06%	0.1918

Iteration 1 represents the first run of the regression analysis using the bounds and starting points shown in the MATLAB code. Then, several iterations were conducted to see how setting certain parameters affects the fit. Iteration 2 was meant to see the effect of setting the eccentricity parameter to an even number for ease of modeling. This small change had a small impact on the *resnorm* value but appeared to alter the parameters to a greater extent. The percent adjustment to the compressive strength to determine tensile strength appeared higher in both iterations than what was measured in the case of 0% fibers. Also, previous researchers determined different values. Graybeal and Baby (2013)

found the percentage to be approximately 5%, Wille et al. (2014) to be approximately 6%, Savino et al. to be approximately 8%, Campos (2020) to be approximately 6%, and Lepissier (2019) to be approximately 5%. Therefore, iterations were conducted setting the percentage to 5% and 8% to evaluate how the fit changes. No change was observed in the *resnorm* value or the *A* parameter by changing the percentage. However, the *B* and *C* values changed with those adjustments. Then, those same iterations were conducted for iteration 5 and 6 but the eccentricity was reset to the original range. The *resnorm* dropped back to the value in the initial iteration, with changes to the parameters. This implies that the eccentricity has a much larger impact on the fit than the percentage for tensile strength. This was tested in iteration 7, where the eccentricity was set to 0.8, resulting in a much larger *resnorm*. However, since no reduction in *resnorm* was seen with any additional iteration, iteration 1 was used for the final equation.

7.4.3. Evaluation of Fit Using Parameters with Lowest *Resnorm* Value

A plot with the combined dataset with the Menétrey and Willam equation (1995) and the fitted parameters from iteration 1 is shown in Figure 7.18. The plot was constructed using Haigh-Westergaard coordinates using normalized data. Each dashed line of the equation represents the outer edge of the failure surface at their respective angles. The angles plotted match those set for the Ritter and Curbach data (2016).

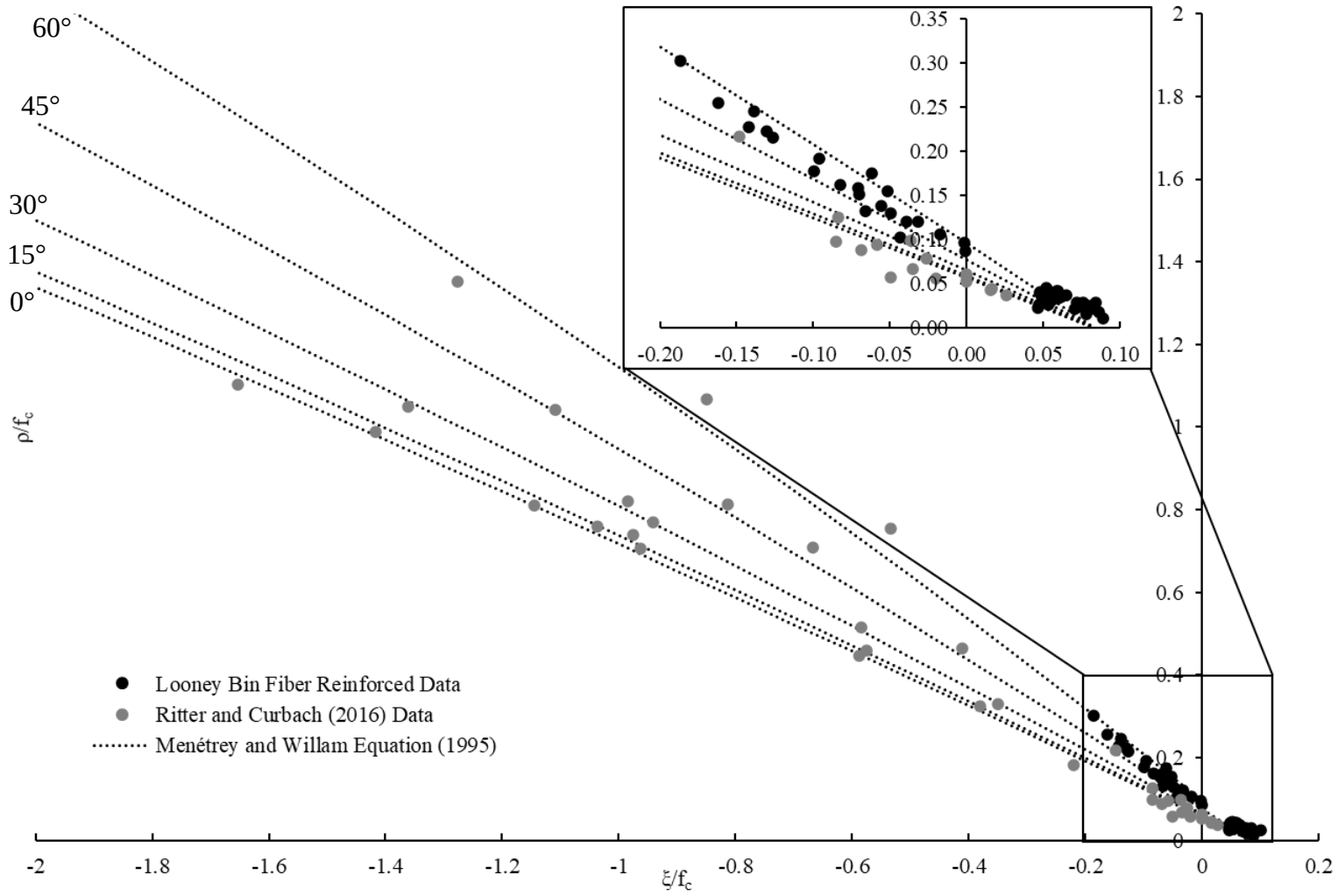

Figure 7.18 – Combined dataset with fitted Menétrey and Willam equation

The equation appears to fit the data well on the compression end of the failure surface. However, there appears to be a poor fit to the Looney Bin data. This could be due to the fact that the equation is parabolic with curvature in the opposite direction of the Looney Bin data. The equation would have to take the form of a cubic function to follow the trend in the tension region of the surface while maintaining the trend in the compression side of the failure surface.

7.5. RITTER AND CURBACH (2016) EQUATION NONLINEAR REGRESSION ANALYSIS WITH COMBINED DATASET

7.5.1. MATLAB Code for Regression analysis

The regression analysis on the Menétrey and Willam equation (1995) highlighted the shortcomings of trying to fit a parabolic equation to what appears to be a cubic shape. The equation could not be fit to the reverse curvature in the Looney Bin data. Therefore, the Ritter and Curbach equation (2016) was also chosen for evaluation due to its increased ability to adjust to various shapes. This equation does not use the Haigh-Westergaard coordinates. Instead, a coordinate rotation was developed by Ritter and Curbach (2016) to plot principal stress data in the same manner as Haigh-Westergaard coordinates. The stress transformation equations are shown as Equations 7.7 through 7.10.

$$x' = \frac{x-y}{\sqrt{2}} \tag{7.7}$$

$$y' = \frac{x+y-2z}{\sqrt{6}} \tag{7.8}$$

$$z' = \frac{x+y+z}{\sqrt{3}} \tag{7.9}$$

$$\varphi = 60° - \arctan\left(\frac{x'}{y'}\right) = 60° - arctan\left(\frac{\sqrt{3}(x-y)}{(x+y-2z}\right) \tag{7.10}$$

The axis rotation works in a similar manner as the Haigh-Westergaard coordinates. The *z'* axis becomes the horizontal axis, the *y'* axis becomes the vertical axis, and a line is plotted that represents the exterior edge of the failure surface. The changes in the outer surface caused by the shape of the deviatoric plane are shown by changing the angle, φ, between zero and sixty degrees. This relationship is highlighted in Figure 7.19.

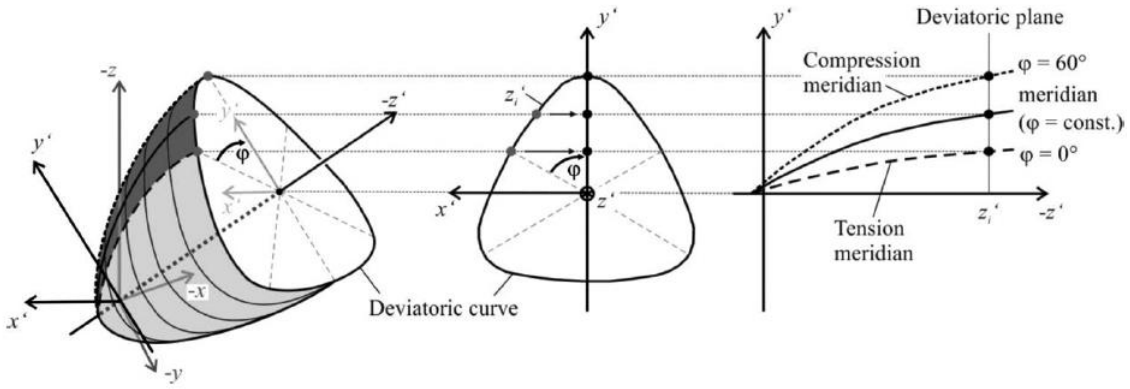

Figure 7.19 – Coordinate rotation by Ritter and Curbach (2016) to convert to a two dimensional plot

Once the principal stresses were converted to the new coordinates, the failure surface would be formed by Equations 7.11 and 7.12.

$$\boldsymbol{y'(z^*, \varphi) = \left[\frac{\sqrt{3}}{2}\tan(\varphi) + \frac{1}{2}\right] k(z^*, \varphi) y'_{tm} z^*} \quad \textbf{(7.11)}$$

$$\boldsymbol{z^* = \frac{-z'}{|f_c|} + \frac{f_{ttt}}{|f_c|}} \quad \textbf{(7.12)}$$

The values of *z'* were transformed into z^* to ensure that compression values were positive and to also normalize the data by the cylinder uniaxial compressive strength. The term f_{ttt} is the hydrostatic tension strength. To make the equation more generalized and allow for multiple deviatoric plane shapes and trends from hydrostatic tension to hydrostatic compression, the authors provide multiple equations. The deviatoric shape is determined by the term $k(z^*, \varphi)$. The equation for $k(z^*, \varphi)$ is shown as Equation 7.13.

$$\boldsymbol{k(z^*, \varphi) = 10.539 - \left(5.27 - r(z^*)\right)\left(\frac{\varphi^\circ}{60^\circ}\right)^2 - \left(\frac{\varphi^\circ}{60^\circ}\right)^{3.8138 r(z^*) - 2.8138}} \quad \textbf{(7.13)}$$

$$\boldsymbol{r(z^*) = \frac{r_1}{1 + exp[r_2 z^*]} + r_4} \quad \textbf{(7.14)}$$

$$\boldsymbol{r(z^*) = \frac{r_1}{1 + exp[r_2 z^*]} \frac{1}{1 + exp[r_3 z^*]} + r_4} \quad \textbf{(7.15)}$$

If the value of $r(z^*) = 1$, the deviatoric plane is circular, if $r(z^*) = 5.27$, the deviatoric plane is triangular, and if $r(z^*) > 5.27$, the deviatoric plane is a non-convex triangular shape. Two different equations for $r(z^*)$, Equations 7.14 and 7.15, were provided for further customization. The various *r* terms can be used to adjust the

deviatoric plane shape as the surface transitions from hydrostatic tension to hydrostatic compression.

The final term in the general equation, y'_{tm}, defines the trend of the tension meridian (the line of the failure surface when $\varphi = 0°$). Five equations were provided that can be used in the general equation to describe various shapes, shown as Equations 7.16 through 7.20.

$$\boldsymbol{y'_{tm}(z^*) = a_1(z^*)^{b_1}} \quad \textbf{(7.16)}$$

$$\boldsymbol{y'_{tm}(z^*) = a_1(1 - b_2{}^{z^*})} \quad \textbf{(7.17)}$$

$$\boldsymbol{y'_{tm}(z^*) = a_3(z^*)^2 + b_3 z^*} \quad \textbf{(7.18)}$$

$$\boldsymbol{y'_{tm,mod,1}(z^*) = (1 + c^{z^*})^d y'_{tm}(z^*)} \quad \textbf{(7.19)}$$

$$\boldsymbol{y'_{tm,mod,2}(z^*) = y'_{tm}(z^*)\left(\frac{-f_{ccc}}{|f_c|} - z^*\right)^f} \quad \textbf{(7.20)}$$

The last two equations are modified versions of the y'_{tm} equation for small values of z^*., which is the tension region of the failure surface. The various equations for y'_{tm} can be used to describe both an open ended and closed ended shape in the hydrostatic compression direction by adjusting the *a* and *b* terms. The limits to the *a* and *b* terms are shown in Table 7.15. While Ritter and Curbach set limitations for each equation based on

the anticipated behavior of the compression end of the failure surface (2016), these anticipated behaviors and coefficient limitations were ignored in some iterations of the regression analysis to completely evaluate all possible combinations.

Table 7.15 – Limits for *a* and *b* terms in y'_{tm} equation based on trend of compression end of surface (Ritter and Curbach, 2016)

Eq. 7.16 (Opening)	Eq. 7.17 (Asymptotic)	Eq. 7.18 (Closing)
$a_1 > 0$	$a_2 > 0$	$a_3 < 0$
$0 < b_1 < 1$	$0 < b_2 < 1$	$b_3 > 0$

With all of the equations set, the MATLAB code was written to conduct the regression analysis. A separate file was created to form the failure surface functions due to their complexity and ability to incorporate different versions of each equation for different shapes. Each of the $r(z^*)$ and y'_{tm} equations were input into the function file and were incrementally commented out to make it easier to alter the failure surface function. The MATLAB code used for the regression analysis is shown in Figure 7.20, and the code for the equations is shown in Figure 7.21.

```
% Nonlinear Curve Fitting
% Ritter and Curbach 2016

 load combineddata2.csv;
 xp = combineddata2(:,1);
 yp = combineddata2(:,2);
 zp = combineddata2(:,3);
 thetad = combineddata2(:,4);
 theta = thetad*pi./180;

 data = [zp,theta];

 x0 = [1 1 1 1 1 1 1 1 1]; %fttt, r1, r2, r3, r4, a, b, c, d

 options = optimoptions('lsqcurvefit','Algorithm','levenberg-marquardt');

 lb = [-inf -inf -inf -inf -inf -inf -inf -inf -inf];
 ub = [inf inf inf inf inf inf inf inf inf];
 [y,resnorm,~,exitflag,output] = lsqcurvefit(@(x,data)eq6(x,data),x0,data,yp,lb,ub, ↙
options)
```

Figure 7.20 – MATLAB regression analysis code for the Ritter and Curbach (2016)

```
function yp = eq6(x,data)

zp = data(:,1);
phi = data(:,2);

A = 0.5*sqrt(3)*tan(phi)+0.5;

fttt = x(1);
r1 = x(2);
r2 = x(3);
r3 = x(4);
r4 = x(5);
a = x(6);
b = x(7);
c = x(8);
d = x(9);
% fccc = x(10);
% f = x(11);

zstar = -zp+fttt; % eq. (7)
r = (r1*(1+exp(r2*zstar)).^-1).*(1*(1+exp(r3*zstar)).^-1)+r4; % eq. (10)
k = 10.539 - (5.27-r).*((phi*180/pi)/60).^2 - ((phi*180/pi)/60).^(3.8138*r-2.8138); %↙
eq. (8)
% r = (r1/(1+exp(r2*zs)))+r4; % eq. (9)

% yptm = a*(zstar).^b; % eq. (11)
yptm = a*(1-b.^zstar); % eq. (12)
% yptm = a*(zstart).^2+b*zstar; % eq. (13)
yptmmod1 = ((1+c.^zstar).^d).*yptm; % eq. (14)
% yptmmod2 = yptm.*(-fccc-zstar)^f; % eq. (15)

yp = A.*k.*yptmmod1;
```

Figure 7.21 – MATLAB code forming the equation to solve for *y'*

The MATLAB code for the regression analysis works in the same manner as for the Menétrey and Willam equation (1995). However, in lieu of ξ/f_c, ρ/f_c, and θ, the loaded parameters were x'/f_c, y'/f_c, z'/f_c, and φ. Another difference in this code was the number of parameters. In the Menétrey and Willam equation (1995), five parameters were initially set to be determined by the regression. In the Ritter and Curbach equation (2016), there were up to nine parameters used to adjust the failure surface, depending on the equations being evaluated. The parameters being determined and the different $r(z^*)$ and y'_{tm} equations were adjusted together to evaluate different potential failure surface shapes. Several combinations of equations were evaluated, including evaluating the effect of assuming both an open and closed compression end of the failure surface. The data used for the regression analysis after transformation to the new coordinates is shown in Table 7.16 through Table 7.20.

Table 7.16 – 0% data converted for Ritter and Curbach equation (2016)

	(psi)							
	σ_1	σ_2	σ_3	f_c	x'/f_c	y'/f_c	z'/f_c	ϕ^o
0%	1233	0	0	16200	0.054	0.031	0.044	0.0
	995	218	213	17580	0.031	0.018	0.047	0.3
	908	312	306	16110	0.026	0.015	0.055	0.5
	765	408	393	16790	0.015	0.009	0.054	1.9
	861	482	266	16320	0.016	0.020	0.057	21.0
	1251	496	494	15620	0.034	0.020	0.083	0.1
	980	496	488	15620	0.022	0.013	0.073	0.9
	1069	510	497	18330	0.022	0.013	0.065	1.2
	831	590	306	14380	0.012	0.023	0.069	32.7
	977	594	593	18330	0.015	0.009	0.068	0.1
	676	681	0	16040	0.000	0.035	0.049	60.3
	670	367	0	16040	0.013	0.026	0.037	33.2
	195	193	-2358	17420	0.000	0.120	-0.065	59.9
	199	198	-3315	16500	0.000	0.174	-0.102	60.0
	296	290	-4114	16220	0.000	0.222	-0.126	59.9
	306	294	-3039	16500	0.000	0.165	-0.085	59.8
	391	198	-2820	16220	0.008	0.157	-0.079	56.9
	403	387	-2129	17420	0.001	0.118	-0.044	59.7

Table 7.17 – 1% data converted for Ritter and Curbach equation (2016)

	(psi)							
	σ_1	σ_2	σ_3	f_c	x'/f_c	y'/f_c	z'/f_c	ϕ^o
1%	948	311	309	16920	0.027	0.015	0.054	0.1
	826	308	306	17950	0.020	0.012	0.046	0.3
	1115	501	263	17330	0.025	0.026	0.063	15.7
	1193	615	613	16570	0.025	0.014	0.084	0.2
	1139	586	577	17950	0.022	0.013	0.074	0.8
	1159	705	689	17620	0.018	0.011	0.084	1.7
	1001	811	416	17560	0.008	0.023	0.073	41.5
	1045	814	808	17320	0.009	0.006	0.089	1.3
	1270	806	776	16430	0.020	0.013	0.100	3.1
	776	767	0	17990	0.000	0.035	0.049	59.4
	1157	459	0	17990	0.027	0.037	0.052	23.2
	199	195	-4871	18190	0.000	0.228	-0.142	60.0
	197	193	-5542	18360	0.000	0.255	-0.162	60.0
	291	277	-6303	17770	0.001	0.303	-0.186	59.9
	397	393	-3021	18360	0.000	0.152	-0.070	59.9
	451	446	-2663	18420	0.000	0.138	-0.055	59.9
	576	296	-3132	18420	0.011	0.158	-0.071	56.1
	614	605	-2849	18190	0.000	0.155	-0.052	59.9

Table 7.18 – 2% data converted for Ritter and Curbach equation (2016)

	(psi)							
	σ_1	σ_2	σ_3	f_c	x'/f_c	y'/f_c	z'/f_c	ϕ^o
	1272	327	304	18720	0.036	0.022	0.059	1.2
	906	309	299	18340	0.023	0.014	0.048	0.8
	1088	498	263	19170	0.022	0.023	0.056	16.0
	1141	587	228	18950	0.021	0.027	0.060	23.0
	1277	608	603	18810	0.025	0.015	0.076	0.4
	1081	583	581	18340	0.019	0.011	0.071	0.2
	1267	690	665	18950	0.022	0.014	0.080	2.2
	1169	775	397	18720	0.015	0.025	0.072	29.3
	1217	814	794	18810	0.015	0.010	0.087	2.5
	842	838	0	18710	0.000	0.037	0.052	59.8
2%	1044	509	0	18710	0.020	0.034	0.048	29.2
	308	304	-2990	16630	0.000	0.162	-0.083	59.9
	311	299	-2796	19180	0.000	0.132	-0.066	59.8
	302	296	-1928	17770	0.000	0.102	-0.043	59.9
	301	296	-4882	18940	0.000	0.223	-0.131	59.9
	456	441	-4148	19500	0.001	0.192	-0.096	59.8
	588	307	-2450	18270	0.011	0.130	-0.049	55.2
	596	593	-2974	16630	0.000	0.175	-0.062	60.0
	598	597	-1730	17770	0.000	0.107	-0.017	60.0
	609	588	-2250	19180	0.001	0.121	-0.032	59.6
	705	705	-1463	18270	0.000	0.097	-0.002	60.0

Table 7.19 – 4% data converted for Ritter and Curbach equation (2016)

	(psi)							
	σ_1	σ_2	σ_3	f_c	x'/f_c	y'/f_c	z'/f_c	ϕ^o
4%	1208	218	205	19650	0.036	0.021	0.048	0.7
	1260	427	405	19870	0.030	0.018	0.061	1.3
	1080	422	397	20520	0.023	0.014	0.053	1.9
	1377	500	224	20330	0.030	0.029	0.060	13.3
	1353	596	331	20230	0.026	0.026	0.065	14.5
	1333	697	696	20520	0.022	0.013	0.077	0.1
	1254	800	520	20330	0.016	0.020	0.073	22.2
	1191	789	770	20380	0.014	0.009	0.078	2.3
	952	928	0	19430	0.001	0.039	0.056	58.7
	1173	601	0	19430	0.021	0.037	0.053	30.8
	303	301	-4872	19520	0.000	0.216	-0.126	60.0
	307	300	-4072	20050	0.000	0.178	-0.100	59.9
	386	381	-5340	19050	0.000	0.245	-0.139	60.0
	698	347	-2357	19520	0.013	0.120	-0.039	54.0
	705	701	-1430	20050	0.000	0.087	-0.001	59.9

Table 7.20 – Ritter and Curbach data converted for Ritter and Curbach equation (2016)

	(psi)							
	σ_1	σ_2	σ_3	f_c	x'/f_c	y'/f_c	z'/f_c	ϕ^o
Ritter and Curbach (2016)	1150	0	0	25250	0.032	0.019	0.026	0.0
	1150	-210	-210	25250	0.038	0.022	0.017	0.0
	1080	-540	-540	25250	0.045	0.026	0.000	0.0
	880	-880	-880	25250	0.049	0.028	-0.020	0.0
	880	-1200	-1200	25250	0.058	0.034	-0.035	0.0
	780	-2250	-2250	25250	0.085	0.049	-0.085	0.0
	560	-5090	-5090	25250	0.158	0.091	-0.220	0.0
	660	-13190	-13190	25250	0.388	0.224	-0.588	0.0
	530	-21330	-21330	25250	0.612	0.353	-0.963	0.0
	0	-25030	-25030	25250	0.701	0.405	-1.145	0.0
	-1380	-35480	-35480	25250	0.955	0.551	-1.654	0.0
	1100	0	-400	25250	0.031	0.031	0.016	14.9
	1160	-310	-850	25250	0.041	0.041	0.000	15.0
	430	-1030	-1570	25250	0.041	0.041	-0.050	15.1

Table 7.20 – Ritter and Curbach data converted for Ritter and Curbach equation (2016) (continued)

	(psi)							
	σ_1	σ_2	σ_3	f_c	x'/f_c	y'/f_c	z'/f_c	ϕ^o
Ritter and Curbach (2016)	750	-10840	-15080	25250	0.325	0.324	-0.576	15.0
	920	-7280	-10290	25250	0.230	0.230	-0.381	15.0
	500	-18170	-24990	25250	0.523	0.522	-0.975	15.0
	0	-19170	-26180	25250	0.537	0.537	-1.037	15.0
	-950	-26010	-35020	25250	0.702	0.697	-1.417	14.8
	1100	0	-1100	25250	0.031	0.053	0.000	30.0
	1030	-380	-1790	25250	0.039	0.068	-0.026	30.0
	850	-850	-2540	25250	0.048	0.082	-0.058	29.9
	580	-1000	-2570	25250	0.044	0.076	-0.068	29.9
	820	-5090	-10990	25250	0.166	0.286	-0.349	30.0
	710	-8510	-17730	25250	0.258	0.447	-0.584	30.0
	290	-14350	-28980	25250	0.410	0.710	-0.984	30.0
	0	-13730	-27460	25250	0.384	0.666	-0.942	30.0
	-1120	-19820	-38570	25250	0.524	0.909	-1.361	30.0
	920	0	-2500	25250	0.026	0.096	-0.036	44.9
	610	-550	-3730	25250	0.032	0.122	-0.084	45.0
	1000	-1000	-6480	25250	0.056	0.210	-0.148	45.0
	760	-3510	-15220	25250	0.120	0.448	-0.411	45.0
	600	-5960	-23850	25250	0.184	0.685	-0.668	45.0
	0	-7510	-28010	25250	0.210	0.784	-0.812	45.0
	-1000	-10590	-36900	25250	0.269	1.006	-1.109	45.1
	0	0	-23370	25250	0.000	0.756	-0.534	60.0
	-1380	-1380	-34410	25250	0.000	1.068	-0.850	60.0
	-4650	-4650	-46500	25250	0.000	1.353	-1.276	60.0

7.5.2. Regression After Determining Optimal Combinations of $r(z^*)$ and y'_{tm} Using y'_{tmod1} for an Open Compression End

Initial attempts were meant to determine which combinations of $r(z^*)$ and y'_{tm} equations would best fit the dataset. The modification, y'_{tmod1}, was used for all iterations for the open compression end since there appeared to be changes in curvature in the Looney Bin data at small values of z^*, and this modification was created to address that

area of the curve. The first set of iterations and their respective parameters are shown in Table 7.21.

Table 7.21 – Regression analyses evaluating $r(z^*)$ and y'_{tm} equations

	Iteration					
	1	2	3	4	5	6
f_{ttt}	-	0.074	0.242	-	0.074	0.118
r_1	-	1.839	4.018	-	1.036	-8.106
r_2	-	0.263	-7.056	-	0.134	-0.822
r_3	-	-	-	-	0.134	-0.822
r_4	-	3.278	0.162	-	3.842	8.338
a	-	0.262	0.700	-	0.234	3.368
b	-	0.889	0.000	-	0.883	0.999
c	-	0.962	1.685	-	0.960	1.287
d	-	1.176	-2.547	-	1.276	-5.126
Resnorm	-	0.0365	0.0304	-	0.0366	0.0148

Iterations 1 through 3 are using Equation 7.14 and iterations 4 through 6 are using Equation 7.15, each combined with the three y'_{tm}, which are Equations 7.16, 7.17, and 7.18. In several cases, the regression analysis returned imaginary numbers, which was taken to show that the program could not effectively match the data to the trends of the equations used. In those cases, dashes were placed in the table for that iteration to show no useable function was developed. This instance occurred while trying to use the Equation 7.16 version of y'_{tm} to the data with both $r(z^*)$ equations, showing that that form of this equation could not create a good fit. The *resnorm* values did not change substantially when using Equation 7.17 between the two $r(z^*)$ equations. However, there was a drastic improvement in *resnorm* when Equation 7.15 for $r(z^*)$ was used with Equation 7.18 for y'_{tm}. Therefore, iterations after 6 were conducted using Equation 7.15

for $r(z^*)$ with Equation 7.18 for y'_{tm}. Once the equations were set, the individual parameters were evaluated. The iterations using those equations are shown in Table 7.22.

Table 7.22 – Regression analyses with $r(z^*)$ and y'_{tm} equations set

	Iteration						
	7	8	9	10	11	12	13
f_{ttt}	0.123	0.123	0.112	0.112	0.112	0.112	0.112
r_1	3.658	3.658	10.000	10.000	10.000	10.000	10.000
r_2	0.508	0.508	0.936	0.936	0.936	0.936	0.936
r_3	0.508	0.508	-5.343	-5.343	-5.343	-5.343	-5.343
r_4	1.818	1.818	1.592	1.592	1.592	1.592	1.592
a	0.000	0.000	1.940	1.940	1.940	1.907	1.907
b	0.000	0.000	0.915	0.915	0.915	0.901	0.901
c	-1.698	-1.698	1.293	1.293	1.293	1.294	1.294
d	2.877	2.877	-4.596	-4.596	-4.596	-4.572	-4.572
Resnorm	10.7136	10.7136	0.0120	0.0120	0.0120	0.0120	0.0120

It became evident that, with so many parameters available to alter the shape of the failure surface, the regression analysis was exponentially more complicated, and the most effective set of parameters was not initially found with open-ended limits on each parameter. The next set of iterations were conducted with changes in the upper and lower bounds such that previous iterations fit within those bounds. Iteration 7 set bounds for the f_{ttt} value to 0 to 0.15, iteration 8 added bounds to r_1 of -10 to 10, iteration 9 added bounds to r_2 of 0 to 1, iteration 10 added bounds to r_3 of -10 to 10, iteration 11 added bounds to r_4 of -2 to 2, iteration 12 added bounds to *c* of -2 to 2, and iteration 13 added bounds to *d* of -10 to 5. The bounds for *a* and *b* were initially kept at the limits set by Ritter and Curbach (2016) for an open compression end.

The *rensorm* values changed substantially as the bounds were set for each element. This behavior highlights the complexity of the regression analysis with so many arbitrary parameters. Even though the bounds set on each parameter were wide enough to fit most of the values from the previous iterations, drastic changes in the fit still occurred. However, a much lower *resnorm* value was achieved from iteration 9 and on, with only slight changes in the parameter values. The largest drop in the *resnorm* value occurred when there was a large change in r_1, r_2, and r_3. Also, bounds were systematically adjusted to address the fact that r_1 was at its upper bound. These iterations are shown in Table 7.23.

Table 7.23 – Regression analyses where bounds adjustments were established

	Iteration					
	14	15	16	17	18	19
f_{ttt}	0.113	0.114	0.115	0.116	0.118	0.082
r_1	18.756	20.000	21.656	22.895	24.828	7.364
r_2	0.601	0.529	0.503	0.492	0.451	0.238
r_3	-5.113	-4.457	-5.520	-5.479	-5.748	-2.732
r_4	-2.000	-2.794	-3.509	-4.000	-4.963	1.000
a	1.351	1.432	1.392	1.679	1.902	0.000
b	0.885	0.997	1.000	1.243	1.432	0.028
c	1.261	1.249	1.243	1.223	1.211	0.834
d	-4.394	-4.526	-4.524	-4.830	-5.033	1.368
Resnorm	0.0094	0.0092	0.0089	0.0088	0.0086	0.0290

The r_1 parameter was unique since it reached the upper bound and stayed there for all of the iterations with the lowest *resnorm*. Iteration 14 changed the upper bound for that value to 20. This change resulted in another large drop in the *resnorm* value, while putting the r_4 parameter at its lower bound. Therefore, iteration 15 change the lower

bound of the r_4 parameter to -4. This caused a slight drop in *resnorm*, with r_1 again reaching its upper bound. Iteration 16 increased the upper bound for r_1 to 25, which caused another slight drop in the *resnorm* value while putting the *b* value to its upper bound. This upper bound was set by Ritter and Curbach (2016) for the opening and asymptotic compression end behaviors. However, iteration 17 increased the upper bound to 2 in order to continue to reduce *resnorm*. After causing another slight drop in *resnorm*, the lower bound for r_4 was reached, so this lower bound was dropped to -5 in iteration 18. This adjustment caused another slight drop in the *resnorm* value, while keeping the other parameters within the bounds set. Iteration 18 had the lowest value for *resnorm* determined thus far.

After adjusting the parameters to achieve the lowest *resnorm* value, the optimized factors were input into the equation and plotted with the data to visually evaluate the fit. An issue was immediately apparent upon inspection of the compression end of the failure surface. The parameters producing the lowest *resnorm* value (iteration 18) caused the equation to compute a reduction in the y' value after z' reaches a high value, as shown in Figure 7.22. This occurs at increasing compressive stress ratios. Also, when φ was set to zero, the *k* equation divides by zero when z^* is above 2.6. This represents an unstable equation and would be inadequate for a full failure model, despite matching the datasets well.

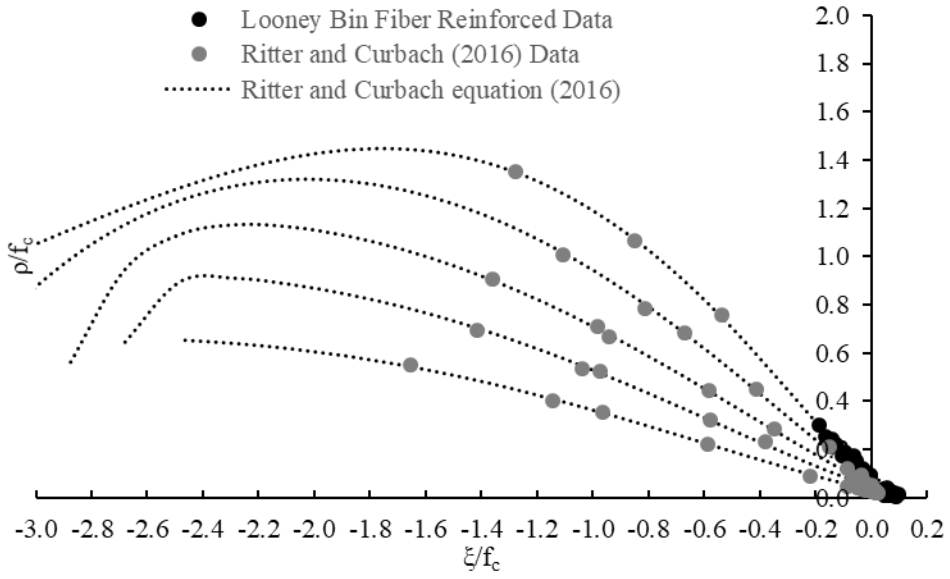

Figure 7.22 – Iteration 18 parameters exhibiting closing of failure surface at compression end

Manual adjustments were then made to each parameter to determine which individual parameter, or combination of parameters, were causing these issues. It was determined that the issue was caused by setting r_4 to a value below 1. Ritter and Curbach (2016) also referenced setting r_4 to 1 for their iterations for open compression ends but did not explain the reason. Therefore, one final iteration was conducted where r_4 was set to 1. This produced a relatively high *resnorm* value, but the function does not close the failure surface at high *z'* values. Iteration 19 represented the best fit with the combination of Equation 7.15 for *r(z*)* and Equation 7.18 for y'_{tm}. The final boundaries for iteration 19 are shown in Table 7.24. The equation with parameters from Iteration 19 is plotted with the two datasets in Figure 7.23.

Table 7.24 – Upper and lower bound settings for iteration 19

	Lower	Upper
f_{ttt}	0	0.15
r_1	-10	25
r_2	0	1
r_3	-10	10
r_4	1	1
a	0	inf
b	0	2
c	-2	2
d	-10	5

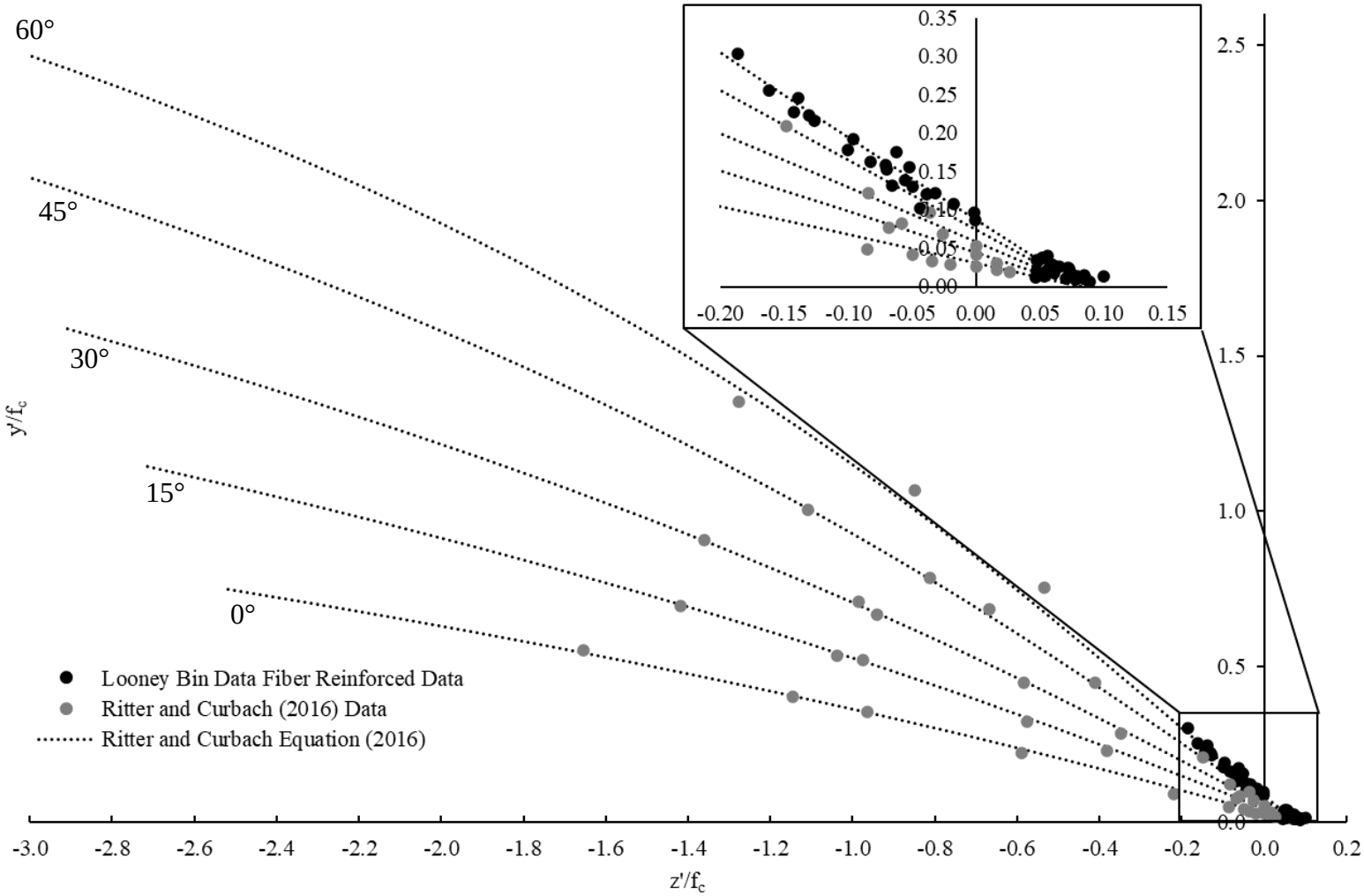

Figure 7.23 – Best fit using Equation 7.15 and 7.18 for *r(z*)* and *y'tm*, respectively

7.5.3. Evaluating Ritter and Curbach Hyperbolic Fit Parameters (2016)

After systematically checking combinations starting with infinite bounds, an iteration conducted by Ritter and Curbach (2016) was evaluated. The authors highlighted two different sets of equations which fit their data best; one was a parabolic shape and one was a hyperbolic shape. Since the Looney Bin data appears to create a hyperbolic shape, and the fit established in the previous section using a hyperbolic curve had a lower *resnorm* value than the fit for a parabolic curve, the hyperbolic shape was chosen for further optimization. The following iterations use Equation 7.15 for $r(z^*)$ and Equation 7.17 for y'_{tm}. The $y'_{tm,mod,}$ equation was also used. The initial and final iterations conducted using this set of equations is shown in Table 7.25.

Table 7.25 – Iterations using established equations from Ritter and Curbach (2016)

	Iteration	
	20	29
f_{ttt}	0.132	0.164
r_1	20.815	12.456
r_2	1.131	0.861
r_3	-0.996	-3.942
r_4	1.000	1.000
a	0.605	0.755
b	0.899	0.921
c	0.010	0.006
d	-1.379	-2.116
Resnorm	0.0158	0.0081

A similar method for iterations was conducted for this set of equations. Iteration 20 set the parameters to the same values as reported by Ritter and Curbach (2016). Then, each parameter was given wider upper and lower bounds, starting from the f_{ttt} value, until

resnorm was minimized. The only parameters where upper and lower bounds were not adjusted was *a*, *b*, and r_4. The *a* and *b* terms were given the upper and lower bounds set in Table 7.15, and r_4 was set to one for every iteration. The final iteration (iteration 29) represented the lowest value of *resnorm* determined thus far, indicating progressively closer fits to the dataset.

One optimized parameter that stood from the final iteration was the value for f_{ttt}. This value was presumed to mean that the TTT strength for this model would be 0.164 times the compressive strength of the concrete. However, when the values of the transformed coordinates were converted back to principal stresses, the TTT strength calculated was determined to be 0.095 times the compressive strength. This is also approximately 57.7% lower than the parameter determined through the regression analysis. This same relationship was determined for fit equation set in the previous section. This means that the f_{ttt} parameter does not actually represent the TTT strength for the failure model. The final boundaries for iteration 29 are shown in Table 7.26. The equation with parameters from Iteration 29 is plotted with the two datasets in Figure 7.24.

Table 7.26 – Upper and lower bound settings for iteration 29

	Lower	Upper
f_{ttt}	0	0.4
r_1	-10	30
r_2	0	2
r_3	-5	5
r_4	1	1
a	0	inf
b	0	1
c	0.005	0.0105
d	-3	3

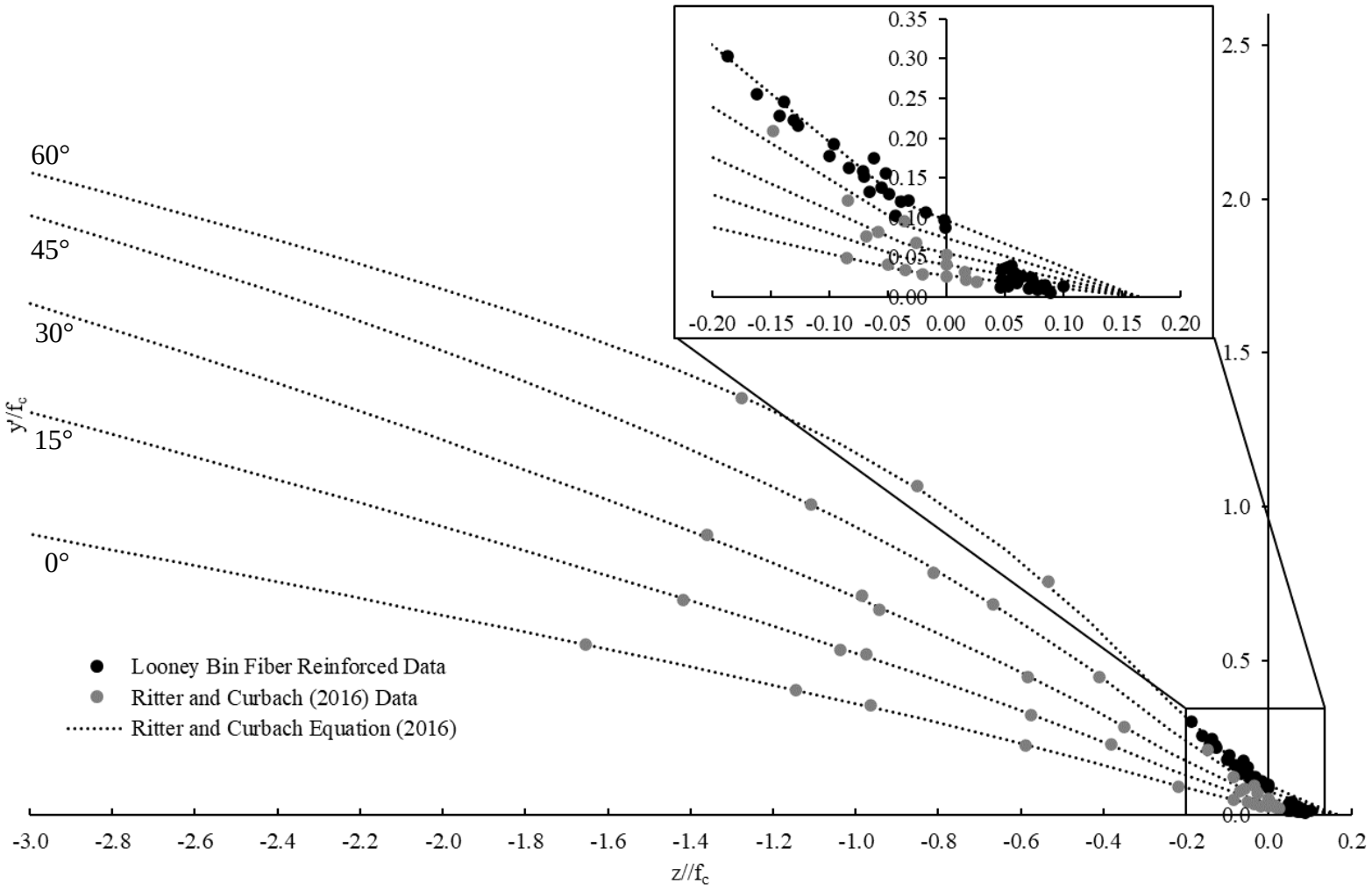

Figure 7.24 – Best fit using Equation 7.15 and 7.17 for *r(z*)* and *y'$_{tm}$*, respectively

7.5.4. Setting f_{ttt} to Coefficient Determined from TTT Data

While the previous regression analysis using the parameters from Ritter and Curbach (2016) as a starting point established the closest fit thus far, the TTT strength calculated using those parameters was approximately 50% larger than the values determined from TTT testing (shown in Table 7.5). Due to this large difference, the next iterations were conducted setting the TTT strength of the optimized model to the percentage of the compressive strength determined from the Looney Bin data. The average percentage of the compressive strength to estimate the TTT strength determined from the data shown in Table 7.5 was 6.2%. Therefore, the f_{ttt} value was set to 0.107 (0.062 divided by 0.577) for the following iterations. The iterations are shown in Table 7.27.

Table 7.27 – Iterations while setting f_{ttt} to 0.107

	Iteration	
	30	31
f_{ttt}	0.107	0.107
r_1	12.261	12.193
r_2	0.882	0.882
r_3	-3.873	-4.092
r_4	1.000	1.000
a	0.412	0.364
b	0.847	0.826
c	0.011	0.016
d	-0.894	-0.885
Resnorm	0.0095	0.0095

After setting the f_{ttt} value to 0.107, the upper and lower bounds used for iteration 29 were again used for the remaining parameters. After the initial run, the *resnorm* value

determined was only slightly higher than the value from iteration 29. Another iteration was conducted where the upper bound for *c* was increased to address the fact that iteration 30 was stopped at the previous upper bound. Iteration 31 was run with that upper bound set to 0.02. This final iteration showed no reduction in the *resnorm* and all variables were within the bounds set. Therefore, iteration 31 was determined to be the optimized model when setting f_{ttt} to 0.107. The final boundaries for iteration 31 are shown in Table 7.28. The equation with parameters from iteration 31 is plotted with the two datasets in Figure 7.25.

Table 7.28 – Upper and lower bound settings for iteration 31

	Lower	Upper
f_{ttt}	0.108	0.108
r_1	-10	30
r_2	0	2
r_3	-5	5
r_4	1	1
a	0	inf
b	0	1
c	0	0.0
d	-3	3

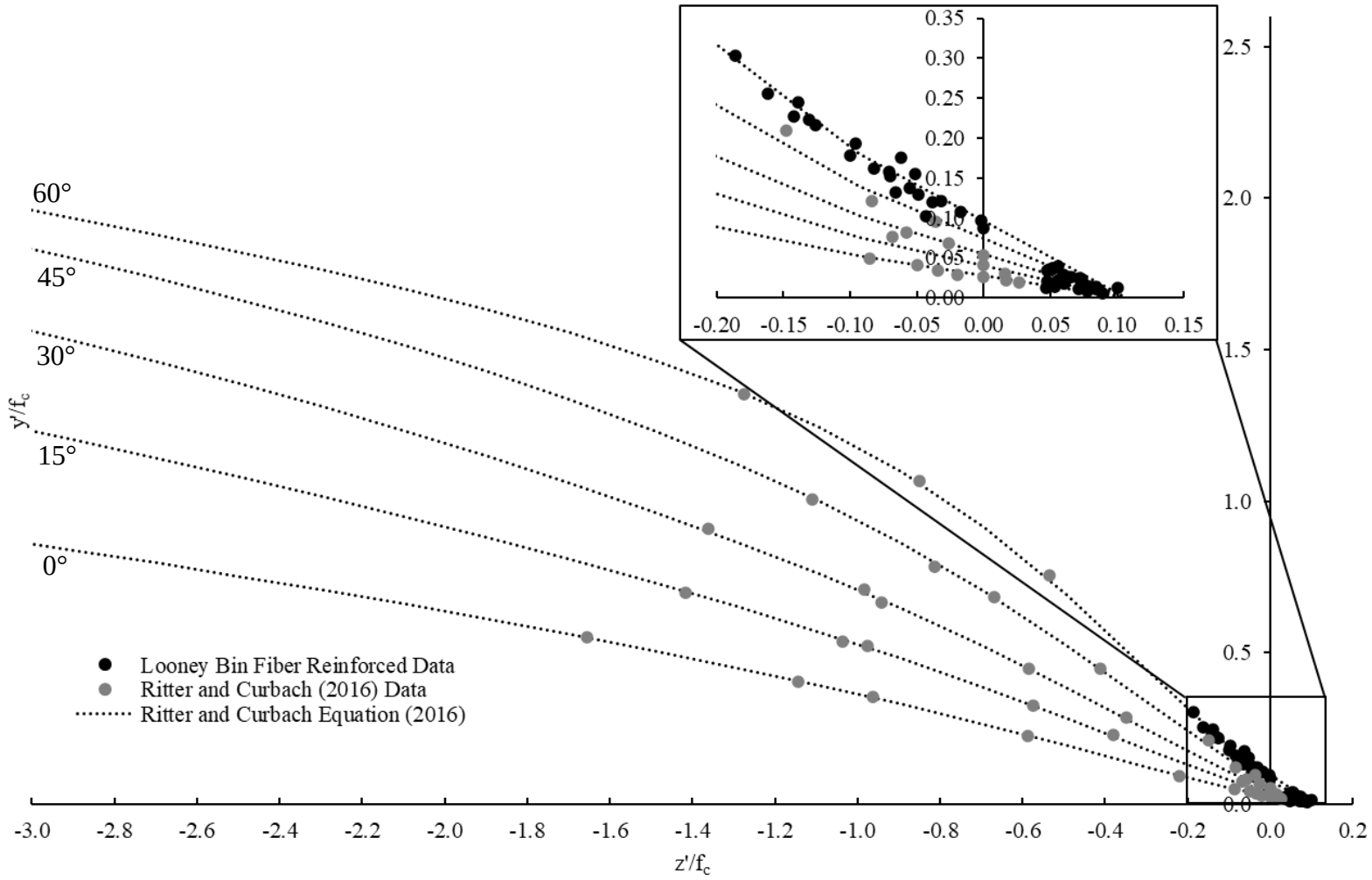

Figure 7.25 – Best fit setting f_{ttt} to 0.107 and using Equation 7.15 and 7.17 for $r(z^*)$ and y'_{tm}, respectively

7.5.5. Regression Assuming Closed Compression End

After determining the parameters for a failure surface that has an opened compression end, an attempt was made to utilize the $y'_{tm,mod,2}$ equation, which was tailored to cause the compression end to close. This equation introduces two new terms, f and f_{ccc}. The term f_{ccc} represents the multiplier to the uniaxial compressive strength to determine the triaxial compressive strength. The term f is an arbitrary parameter used to establish the slope of the closed compressive end.

Iterations were conducted attempting all possible combinations of $r(z^*)$ and y'_{tm} with the $y'_{tm,mod,2}$ equation. Each combination of equations returned imaginary numbers in the solution, indicating that there was no reasonable combination of factors to fit the data. This makes sense since the data does not appear to follow the trend of closing at the compression end.

7.6. FINALALIZED MULTIAXIAL FAILURE MODELS

7.6.1. Menétrey and Willam Equation (1995)

The final parameters for the failure surface equation developed by Menétrey and Willam (1995) and fitted using the combined dataset are shown in Table 7.29, and their associated equation is repeated in Equations 7.21 through 7.23. The deviatoric plane at various values of ξ/f_c is shown in Figure 7.26.

Table 7.29 – Final parameters for the Menétrey and Willam equation

A	B	C	e	% fc for ft
0.9108	1.2892	1.4858	0.5932	13.69%

$$F(\xi,\rho,\theta) = \left[A_f\rho\right]^2 + m\left[B_f\rho r(\theta,e) + C_f\xi\right] - c = 0 \qquad (7.21)$$

$$m = 3\frac{f'^2_c - f'^2_t}{f'_c f'_t}\frac{e}{e+1} \qquad (7.22)$$

$$r(\theta,e) = \frac{4(1-e^2)cos^2\theta+(2e-1)^2}{2(1-e^2)cos\theta+(2e-1)[4(1-e^2)cos^2\theta+5e^2-4e]^{1/2}} \qquad (7.23)$$

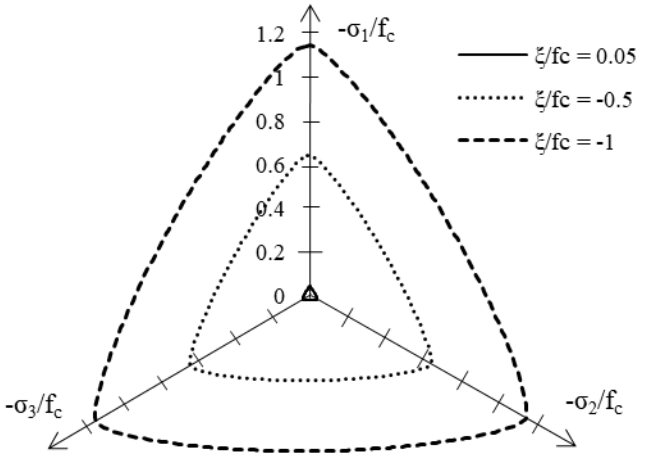

Figure 7.26 – Deviatoric plane shape at various points along ξ axis

The ξ/f_c sections plotted represent different portions of the failure surface. The ξ/f_c value of 0.05 is the tension region of the surface, near the TTT strength point where all the surface sides meet. The ξ/f_c value of -0.5 is near the end of the region where at least one of the principal stresses is in tension. The ξ/f_c value of -1 is where all the principal stresses are in compression and is near where the uniaxial compressive strength is located. The deviatoric plane shape more closely resembles a triangle at each of the sections plotted. There is very little change in the deviatoric plane shape at the sections plotted, and this shape would continue with only small increases in roundness as the ξ/f_c

value decreases while continuously expanding outward, indicating an open compression end. Such steep angled sides suggests that large differences between principal stresses heavily influenced the failure strengths. This means the material failure is more influenced by shear stresses.

This model would predict a uniaxial tension strength of 4.74% of the uniaxial compressive strength. This value does not match the value associated with the friction parameter *m*. This indicates that the equation for *m* does not actually use the tensile strength, making the parameter arbitrary. The TTT strength predicted by this model was 4.85% of the uniaxial compressive strength. This percentage is lower than determined from the test data shown in Table 7.5. A full, three-dimensional plot of the failure surface is shown in Figure 7.27. The data used to determine the parameters are shown as black spheres in the plot. The region of the failure surface where the Looney Bin data is encompassed is shown in Figure 7.28. The dashed line in each plot represents the hydrostatic axis (where all three principal stresses are equal).

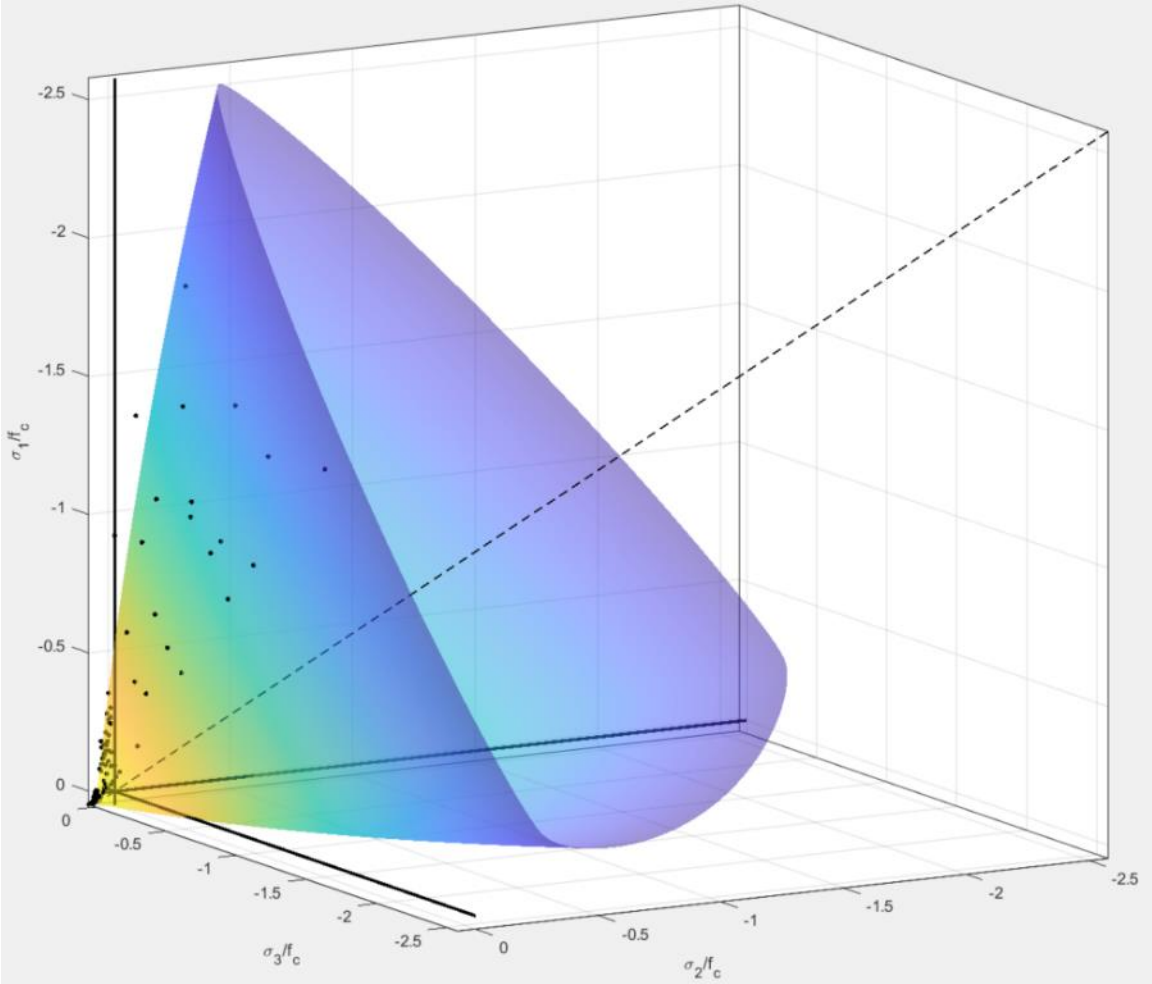

Figure 7.27 – Full failure surface of Menétrey and Willam equation with data

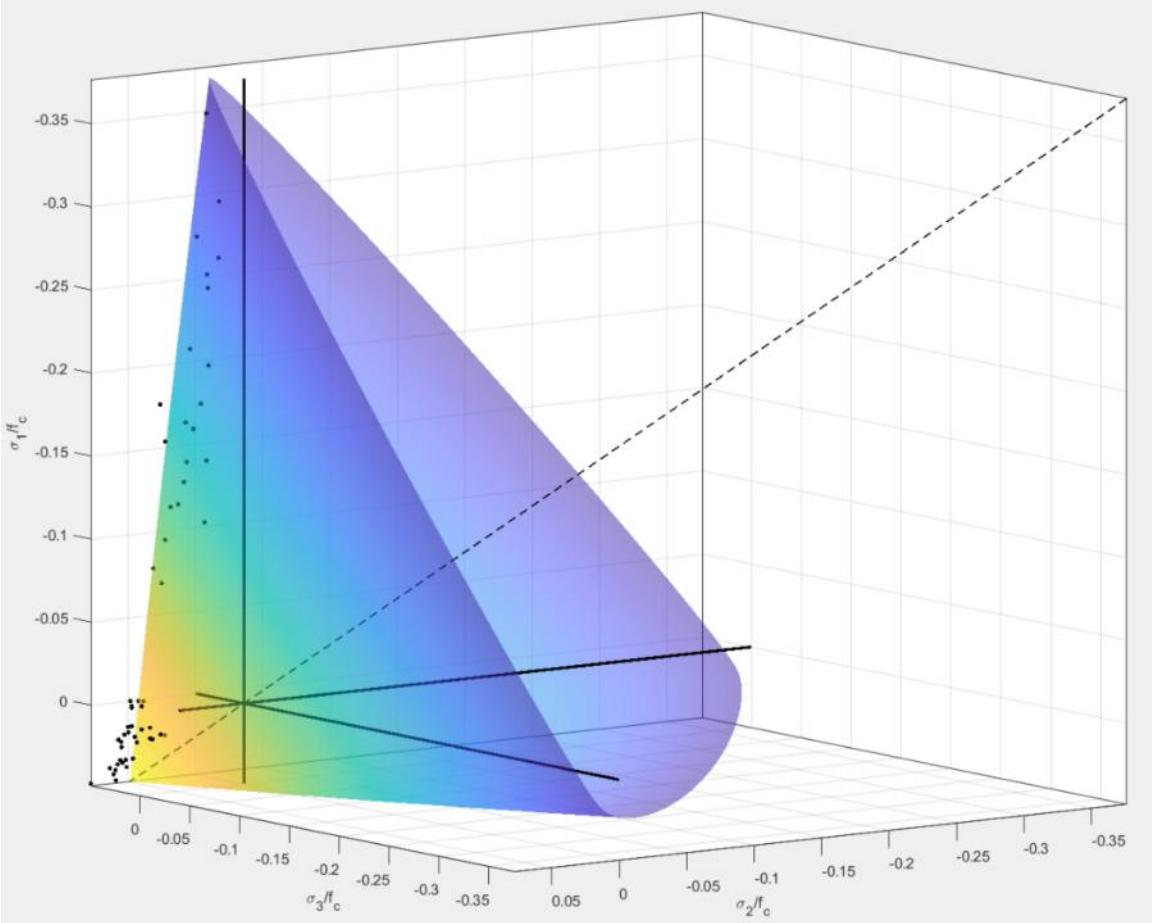

Figure 7.28 – Tension region of the Menétrey and Willam equation failure surface with Looney Bin data

7.6.2. Ritter and Curbach Equation (2016)

The final parameters for the failure surface equation developed by Ritter and Curbach (2016) and fitted using the combined dataset are shown in Table 7.30, and their associated equation is repeated in Equations 7.24 through 7.29. The deviatoric plane at various values of z'/f_c is shown in Figure 7.29.

Table 7.30 – Final parameters for the Ritter and Curbach equation

f_{ttt}	r_1	r_2	r_3	r_4	a	b	c	d
0.107	12.193	0.882	-4.092	1.000	0.364	0.826	0.016	-0.885

$$y'(z^*, \varphi) = \left[\frac{\sqrt{3}}{2}\tan(\varphi) + \frac{1}{2}\right] k(z^*, \varphi) y'_{tm} z^* \quad (7.24)$$

$$z^* = \frac{-z'}{|f_c|} + \frac{f_{ttt}}{|f_c|} \quad (7.25)$$

$$k(z^*, \varphi) = 10.539 - \left(5.27 - r(z^*)\right)\left(\frac{\varphi^\circ}{60^\circ}\right)^2 - \left(\frac{\varphi^\circ}{60^\circ}\right)^{3.8138 r(z^*) - 2.8138} \quad (7.26)$$

$$r(z^*) = \frac{r_1}{1+exp[r_2 z^*]} \frac{1}{1+exp[r_3 z^*]} + r_4 \quad (7.27)$$

$$y'_{tm}(z^*) = a_1(1 - b_2{}^{z^*}) \quad (7.28)$$

$$y'_{tm,mod,1}(z^*) = (1 + c^{z^*})^d y'_{tm}(z^*) \quad (7.29)$$

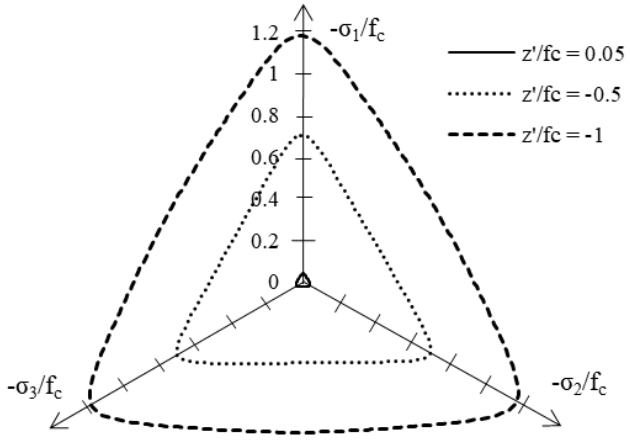

Figure 7.29 – Deviatoric plane shape at various points along *z'* axis

The deviatoric planes are plotted at the same locations in Figure 7.29 along the hydrostatic axis as Figure 7.26 for the Menétrey and Willam equation. The deviatoric plane shape is very similar to the Menétrey and Willam equation at smaller values of z'/f_c. However, as z'/f_c increases, there appears to be more rounding of the deviatoric plane. This rounding at larger z'/f_c values is further highlighted in Figure 7.30.

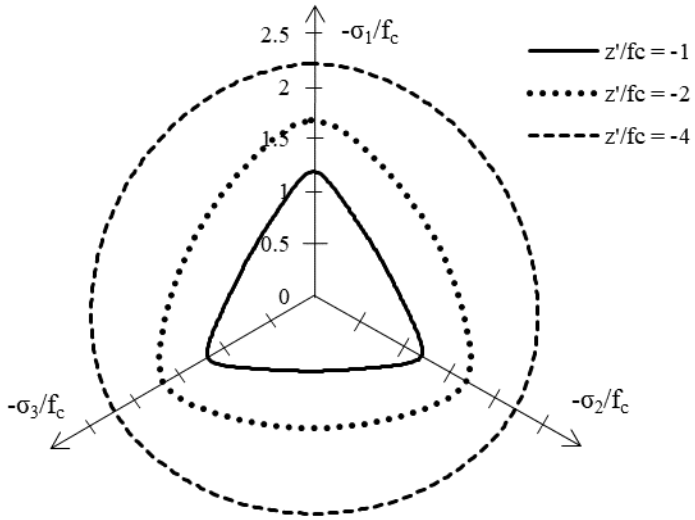

Figure 7.30 – Rounding of deviatoric plane at larger values of z'/f_c

As z'/f_c approaches negative infinity, the deviatoric shape remains a circle. This gradual increase in roundness implies that, as the compressive confinement increases, the effect of shear stresses on failure is reduced. This behavior seems more realistic to observed compressive behavior. Unfortunately, test equipment able to reach confinement stresses to the level necessary to test concrete at the deviatoric plane locations shown in Figure 7.30 has not been developed, making it impossible to obtain test data at these locations to verify behavior.

This model would predict a uniaxial tension strength of 4.49% of the uniaxial compressive strength, nearly identical to the Menétrey and Willam equation. The TTT strength predicted by this model was 6.18% of the uniaxial compressive strength. This shows that, by setting the f_{ttt} value to 0.107 during the fitting process, the model was able to predict a TTT strength percentage of the uniaxial compressive strength similar to what was found in the Looney Bin data, shown in Table 7.5. A full, three-dimensional plot of the failure surface is shown in Figure 7.31. The data used to determine the parameters are shown as black spheres in the plot. The region of the failure surface where the Looney Bin data is encompassed is shown in Figure 7.32. The dashed line in each plot represents the hydrostatic axis (where all three principal stresses are equal).

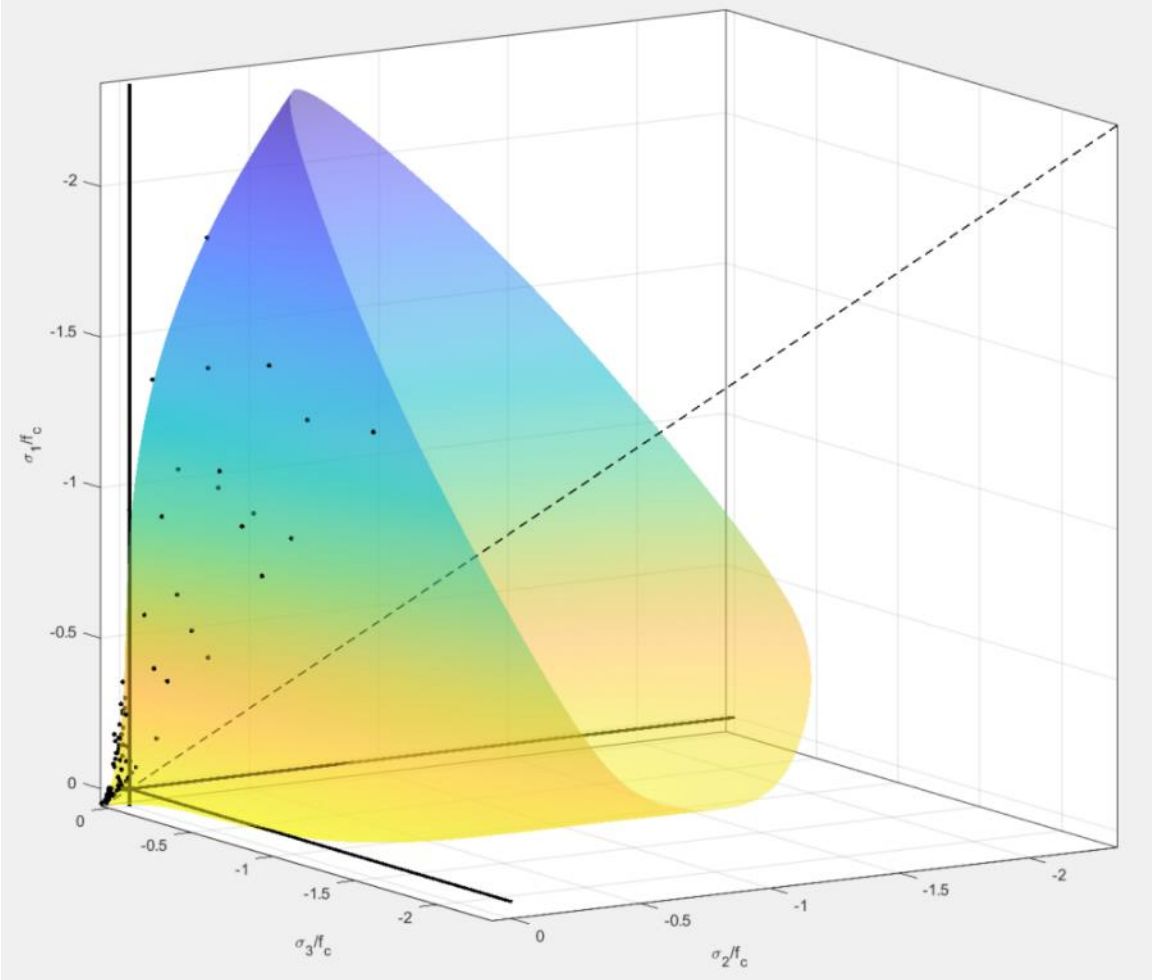

Figure 7.31 – Full failure surface of Ritter and Curbach equation with data

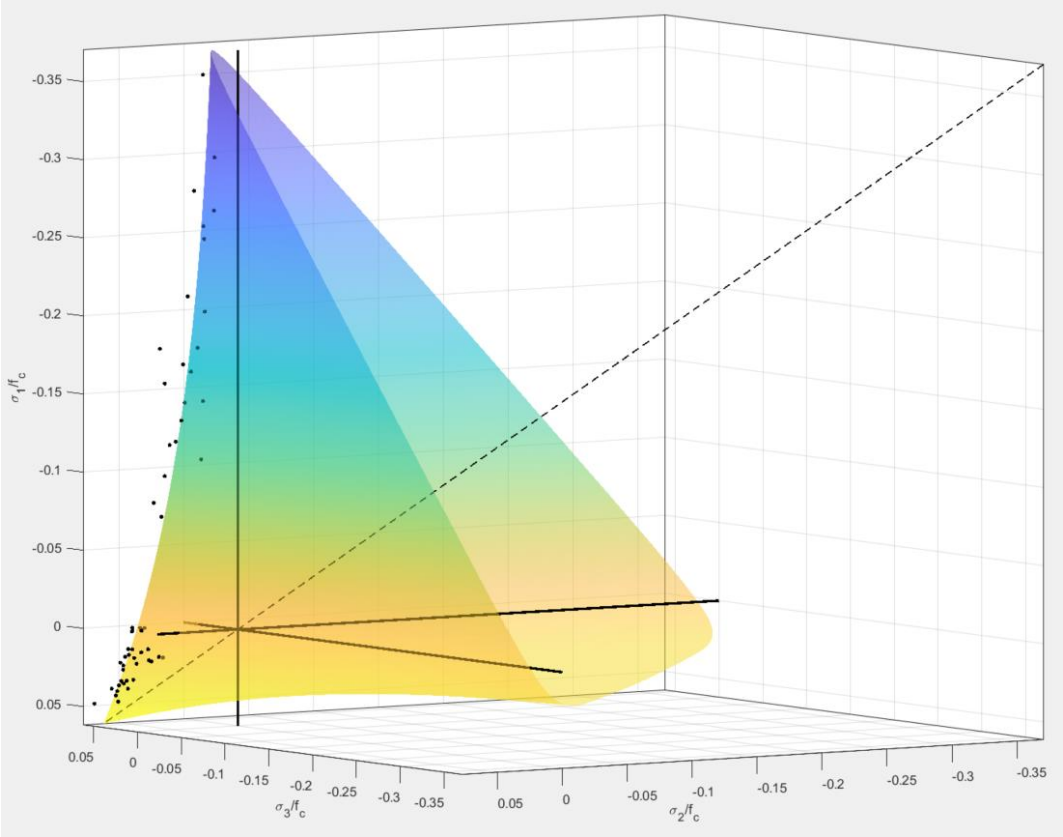

Figure 7.32 – Tension region of the Ritter and Curbach failure surface with Looney Bin data

The change in deviatoric plane shape as the surface moves farther along the hydrostatic axis in the compression direction is clearly shown in the plots above. Also, the reverse curvature of the Ritter and Curbach fitted equation is very apparent in Figure 7.32. When comparing the tension regions of the Menétrey and Willam equation and the Ritter and Curbach equations, it is very clear that the latter fits the Looney Bin data much better than the former. This provides more evidence of the reverse curvature nature of the failure surface as it transitions from the compression end to the tension end.

8. FINDINGS, CONCLUSIONS AND RECOMMENDATIONS

8.1. OVERVIEW OF RESEARCH STUDY

The purpose of this study was to develop a multiaxial tension testing apparatus capable of conducting tests on UHPC with TTT, TT, and TTC stress conditions to provide data points for portions of the failure surface that have scarce data. A test apparatus called the Looney Bin was designed that was easily maneuvered by a single individual, easily deconstructed to facilitate ease of testing, and was able to test UHPC specimens in all three stress conditions targeted. After fabrication of the apparatus, the test method was finalized for each test type through various trial testing.

Once the test method was finalized, testing was conducted on a non-proprietary UHPC with fiber contents of 0%, 1%, 2%, 4%, 5%, and 6% by volume. The data collected for all fiber contents consisted of TTT, TT, and TTC data points. Replicate tests were conducted for each ratio of stresses, and statistical limitations were determined to find outliers in the replicate tests. Each data point represented the average of at least two replicate tests that met the determined statistical limitations. Also, limited testing was conducted on another fiber brand with similar properties to the original fiber brand for comparison.

Lastly, the finalized multiaxial dataset was evaluated for trends and comparison to their associated compressive strengths. Data encompassing the compression end of the failure surface from the literature was added to the Looney Bin data for curve fitting. Nonlinear regression analyses were then used to fit two separate failure surface functions to the combined dataset.

8.2. FINDINGS

The findings associated with this study are as follows:

- The Looney Bin was required to be 12 in. x 12 in. x 12 in. in order to fit all of the associated fixtures inside of the apparatus while providing enough room to facilitate specimen attachment.
- A minimum thickness of 0.5 in. was required for aluminum plates with the exterior dimensions required assuming a max tensile force of 5,000 lb and reducing the level of yielding in the plate walls.
- A more viscous epoxy was more advantageous since it was less likely to leak out during curing.
- When minimizing the time the specimens were left in the Looney Bin for curing, it was best to not move the glued specimens until at least six hours after gluing for the epoxy utilized to ensure it was cured enough to stay in place for the remainder of the curing time.
- When applying load in the sigma one direction, rotational stops were necessary to ensure the Looney Bin remained stabilized throughout testing.
- Grease was needed on the threaded rod at the tightening nut to reduce friction between the nut and the threads caused by high tensile loads and facilitate independently turning the nut while the threaded rod remained stationary.
- The original clevis size of 1.875 in. x 1.875 in. was too small for stress application above approximately 800 psi due to failure caused by a thin skin of UHPC being removed from the cube surface before cube failure. Larger clevis and plinth sizes were required for higher stress application but were sized to be

1/64 in. smaller than the cube face to ensure no corner interference with the other fixtures.

- Locking bars were required to brace the inset plates of the Looney Bin due to them slipping inward during high load application. The movement in the walls caused misalignment of the following test specimen, which created additional stresses upon placement into the apparatus, ultimately reducing its capacity.
- Due to the way the coupling nut load cell was constructed, the strain gauge wire required protective sheathing to ensure it was not damaged upon failure of the specimen.
- When compressive loading was applied, a steel collar was required to contain the expanding neoprene and ensure a more even stress application.
- HRWR admixture dosage needed to be adjusted based on the fiber content of the UHPC mix.
- At fiber contents of 4% and higher, the fibers would become tangled during the flow test, creating a mound of fibers that became increasingly larger as the fiber content increased.
- The multiplier to 2 in. x 2 in. x 2 in. cube uniaxial compressive strength to estimate the 3 in. x 6 in. cylinder uniaxial compressive strength was determined to be 1.27 for 0% fibers, 0.99 for 1% fibers, 0.93 for 2% fibers, 0.89 for 4% fibers, 0.91 for 5% fibers, and 0.89 for 6% fibers. However, the 5% and 6% multipliers were based on only two sets of tests so further tests are needed to verify the results.

- Failures commonly caused the sigma one clevis to remove a cone-shaped portion of the cube.
- Large differences between the sigma one stress and the side stresses appeared to cause a higher degree of cracking in 0% fiber specimens.
- Fiber reinforced specimens tended to fail closer to the surface of the cubes in planes nearly parallel with the clevis attachments.
- Skin failures were more likely to occur on fiber reinforced specimens even with the larger clevises. However, these failures occurred at loads that steadily increased with an increase in the fiber percentage, and were near failure loads of other similar tests that more clearly fractured the specimens.
- A gradual increase in TTT strength was observed as the fiber content increased up to 4% fibers.
- For the 5% and 6% fiber contents, preferential fiber orientation, coupled with the much larger volume of fibers, created very weak failure planes, causing the ultimate failure loads to be lower than the 4% fiber specimens.
- Different crack morphology was observed between specimens subjected to equal and unequal side stresses.
- Corner-to-corner cracking (i.e., 45 degrees) was commonly observed in the TT and TTC testing when the side stresses were equal. That cracking tended to be angled slightly away from the corner -to-corner direction when the side stresses were unequal.

- The data collected using the Type A: Straight Steel Fibers manufactured by HiPer Fiber, LLC was within the acceptable range of results when compared to the Dramix® OL 0.2/13 data point with the same side stresses.
- The statistical analysis showed that the limitations for the TTT test were much lower than the TTC testing.
- For the TTC test, the repeatability standard deviation exhibited a gradual increase with fiber percentage. The opposite trend was observed in the TTT standard deviations.
- The 1% fiber specimen standard deviation was the largest TTT standard deviation when compared to the other fiber contents. The 4% fiber specimen standard deviation was the largest TTC standard deviation when compared to the other fiber contents.
- A clear trend was observed between the sigma one failure stress in TTT testing and the uniaxial compressive strength. As the fiber content increased, the sigma one failure stress increased proportionally to the increase in the uniaxial compressive strength.
- The TTC sigma one data appeared to follow an exponential decay trend. As the side stress increased, the compressive strength decreased.
- The collected Looney Bin Data appeared to follow a parabolic trend more closely than a linear trend. This parabolic trend was in reverse curvature when compared to the compression end of the previously published failure data.
- The fitted Menétrey and Willam equation had a *resnorm* of 0.0434, estimated a uniaxial tension strength of 4.74% of the uniaxial compressive strength, and

estimated a TTT strength of 4.85% of the uniaxial compressive strength. The deviatoric plane appeared more triangular until at very high compressive confining stresses, where it became slightly rounded.

- The fitted Ritter and Curbach equation had a *resnorm* of 0.0095, estimated a uniaxial tensile strength of 4.49 % of the uniaxial compressive strength, and estimated a TTT strength of 6.18% of the uniaxial compressive strength. The deviatoric plane appeared as a slightly rounded triangle in the tension region, was less rounded in the TTC region, and then transitioned to a circle from the TTC region to the region encompassing very high compressive confining stresses.

8.3. CONCLUSIONS

The findings of this study led to the following conclusions:

- The design and fabrication of an apparatus that was able to test TTT, TT, and TTC stress conditions was successful.
- The random orientation of fibers in UHPC caused variations in the crack morphology between the specimens with and without fibers. The weak planes were less likely to fall in the same angles and portions of the curve due to the shifting nature of the fiber orientation from specimen to specimen. For this reason, the “perfect” triaxial crack pattern was significantly less likely to occur as the fiber contents increased.
- Even though skin failures occurred more commonly as the fiber content increased, the magnitudes of the failure loads indicated that those specimens failed near the same levels as specimens that fractured more completely. This could indicate that

the cracking occurred internally and the fibers bridging the cracks were able to halt rapid crack expansion. However, this sudden volume change caused the specimen to jolt, potentially inducing bending stresses in the interface between the fixtures and the cube, causing the skin failures. Due to this, the data collected from specimens exhibiting skin failure was still considered in the analysis as long as the result was within reason when compared to the other replicate tests.

- There was no apparent difference in strength between the Dramix® OL 0.2/13 fiber and the Type A: Straight Steel Fibers manufactured by HiPer Fiber, LLC.
- A much higher degree of variability occurred with the TTC tests than the TTT tests.
- The 1% fiber specimens exhibited a higher degree of variability due to the higher likelihood of weak planes developing with few, if any, fibers crossing those planes due to the lower total number of fibers.
- The fitted Ritter and Curbach equation appeared to be a better fit to the dataset including the Looney Bin data and the data collected by Ritter and Curbach (2016) due to its ability to develop reverse curvature at the transition from the tension to the compression region of the failure surface.

8.4. RECOMMENDATIONS

The following recommendations are provided for future work on multiaxial tension testing:

- Alter the Looney Bin design to have interlocking wall panels to inhibit slip during load application.

- Design a mechanism to apply proportional loading in all three directions at different ratios to determine the difference between proportional and non-proportional loading.
- Investigate the use of a more flexible epoxy to reduce the likelihood of skin failures.
- Conduct TTT, TT, and TTC testing on UHPC blends with various compressive strengths in order to verify the applicability of the failure surface to those materials.
- Investigate the fiber content at which a reduction in triaxial tensile strength is observed.
- Conduct TTT, TT, and TTC testing on different fiber materials, types, and sizes in order to verify the applicability of the failure surface to those materials.
- Conduct TTT, TT, and TTC testing on conventional concretes, particularly high strength concretes, in order to verify the applicability of the Looney Bin on different concrete classes.
- Investigate the effect of end confinement on tensile strength test data.

APPENDIX – STATISTICAL ANALYSIS OF DATA COLLECTED IN THIS STUDY

Table A.1 – 0% fiber content data for TTT and TT testing

Stress Ratio: 0-0

	Specimen Failure Stresses (psi)		
Specimen #	Sigma 1	Sigma 2	Sigma 3
1	1214.6	0.0	0.0
2	1171.2	0.0	0.0
3	1312.4	0.0	0.0
Avg. (psi)	**1232.7**	**0.0**	**0.0**
Stdev. (psi)	72.31		
Max Diff. (psi)	97.71		

Stress Ratio: 200-200

	Specimen Failure Stresses (psi)		
Specimen #	Sigma 1	Sigma 2	Sigma 3
1	801.3	212.0	212.8
2	970.9	213.1	221.5
3	1019.8	212.5	214.5
Avg. (psi)	**995.3**	**212.8**	**218.0**
Stdev. (psi)	34.57		
Max Diff. (psi)	48.88		

Stress Ratio: 300-300

	Specimen Failure Stresses (psi)		
Specimen #	Sigma 1	Sigma 2	Sigma 3
1	947.9	294.2	303.7
2	932.6	308.0	318.5
3	842.4	315.3	313.1
Avg. (psi)	**907.6**	**305.9**	**311.7**
Stdev. (psi)	57.02		
Max Diff. (psi)	105.50		

Stress Ratio: 400-400

	Specimen Failure Stresses (psi)		
Specimen #	Sigma 1	Sigma 2	Sigma 3
1	734.9	389.1	407.2
2	795.3	397.6	408.1
3	918.7	399.3	411.9
Avg. (psi)	**765.1**	**393.3**	**407.7**
Stdev. (psi)	42.75		
Max Diff. (psi)	60.46		

Stress Ratio: 500-250

	Specimen Failure Stresses (psi)		
Specimen #	Sigma 1	Sigma 2	Sigma 3
1	822.0	486.1	272.4
2	857.0	480.5	260.3
3	903.1	480.4	266.7
Avg. (psi)	**860.7**	**482.3**	**266.5**
Stdev. (psi)	40.67		
Max Diff. (psi)	81.08		

Stress Ratio: 500-500

	Specimen Failure Stresses (psi)		
Specimen #	Sigma 1	Sigma 2	Sigma 3
1	480.5	480.5	502.6
2	621.4	502.3	495.4
3	-	-	-
Avg. (psi)	**550.9**	**491.4**	**499.0**
Stdev. (psi)	99.60		
Max Diff. (psi)	140.85		

Stress Ratio: 500-500 2

	Specimen Failure Stresses (psi)		
Specimen #	Sigma 1	Sigma 2	Sigma 3
1	1242.3	487.6	486.1
2	1029.2	470.4	502.8
3	1259.4	504.1	501.3
Avg. (psi)	**1250.8**	**495.9**	**493.7**
Stdev. (psi)	12.06		
Max Diff. (psi)	17.06		

Stress Ratio: 500-500 3

	Specimen Failure Stresses (psi)		
Specimen #	Sigma 1	Sigma 2	Sigma 3
1	1047.6	493.6	483.1
2	885.7	492.6	486.9
3	1005.2	503.2	492.5
Avg. (psi)	**979.5**	**496.5**	**487.5**
Stdev. (psi)	83.99		
Max Diff. (psi)	119.54		

Stress Ratio: 500-500 4

	Specimen Failure Stresses (psi)		
Specimen #	Sigma 1	Sigma 2	Sigma 3
1	1088.7	514.6	497.2
2	1050.0	505.7	496.5
3	1260.1	496.5	508.0
Avg. (psi)	**1069.3**	**510.1**	**496.9**
Stdev. (psi)	27.36		
Max Diff. (psi)	38.69		

Stress Ratio: 600-300

	Specimen Failure Stresses (psi)		
Specimen #	Sigma 1	Sigma 2	Sigma 3
1	1017.4	574.7	311.9
2	833.6	592.1	317.5
3	829.0	588.7	295.0
Avg. (psi)	**831.3**	**590.4**	**306.3**
Stdev. (psi)	3.27		
Max Diff. (psi)	4.62		

Stress Ratio: 600-600

	Specimen Failure Stresses (psi)		
Specimen #	Sigma 1	Sigma 2	Sigma 3
1	1039.9	584.1	587.2
2	920.0	586.0	595.1
3	970.8	612.7	597.9
Avg. (psi)	**976.9**	**594.3**	**593.4**
Stdev. (psi)	60.14		
Max Diff. (psi)	69.11		

Stress Ratio: TT, Proportional Loading

	Specimen Failure Stresses (psi)		
Specimen #	Sigma 1	Sigma 2	Sigma 3
1	-	595.1	609.0
2	-	709.2	703.3
3	-	724.5	729.9
Avg. (psi)		**676.3**	**680.8**
Stdev. (psi)		70.70	63.52
Max Diff. (psi)		129.37	120.90

Stress Ratio: TT, 350

	Specimen Failure Stresses (psi)		
Specimen #	Sigma 1	Sigma 2	Sigma 3
1		369.2	673.7
2		365.7	667.0
3		363.2	889.5
Avg. (psi)		**367.4**	**670.3**
Stdev. (psi)			4.80
Max Diff. (psi)			6.78

Table A.2 – 0% fiber content data for TTC testing

Stress Ratio: 200-200

	Specimen Failure Stresses (psi)		
Specimen #	Baldwin	Sigma 2	Sigma 3
1	-4033.2	178.4	202.1
2	-2498.9	206.5	195.1
3	-2217.7	184.2	190.1
Avg. (psi)	**-2358.3**	**195.4**	**192.6**
Stdev. (psi)	198.79		
Max Diff. (psi)	-281.14		

Stress Ratio: 200-200 2

	Specimen Failure Stresses (psi)		
Specimen #	Baldwin	Sigma 2	Sigma 3
1	-2707.8	202.8	211.2
2	-4119.5	187.0	188.7
3	-3117.2	203.6	196.4
Avg. (psi)	**-3314.8**	**197.8**	**198.8**
Stdev. (psi)	726.28		
Max Diff. (psi)	-1411.64		

Stress Ratio: 300-300

	Specimen Failure Stresses (psi)		
Specimen #	Baldwin	Sigma 2	Sigma 3
1	-2273.7	301.1	308.7
2	-4136.0	282.2	279.3
3	-4091.0	297.4	311.7
Avg. (psi)	**-4113.5**	**289.8**	**295.5**
Stdev. (psi)	31.84		
Max Diff. (psi)	-45.02		

Stress Ratio: 300-300 2

	Specimen Failure Stresses (psi)		
Specimen #	Baldwin	Sigma 2	Sigma 3
1	-1553.2	288.4	298.8
2	-2868.0	307.8	302.9
3	-3209.9	303.2	285.8
Avg. (psi)	**-3039.0**	**305.5**	**294.3**
Stdev. (psi)	241.76		
Max Diff. (psi)	-341.90		

Stress Ratio: 400-200

	Specimen Failure Stresses (psi)		
Specimen #	Baldwin	Sigma 2	Sigma 3
1	-3349.7	198.9	382.7
2	-6432.8	181.5	391.5
3	-2290.5	197.6	400.0
Avg. (psi)	**-2820.1**	**198.3**	**391.3**
Stdev. (psi)	748.99		
Max Diff. (psi)	-1059.23		

Stress Ratio: 400-400

	Specimen Failure Stresses (psi)		
Specimen #	Baldwin	Sigma 2	Sigma 3
1	-	-	-
2	-2500.1	396.5	383.6
3	-1757.6	410.1	390.6
Avg. (psi)	**-2128.8**	**403.3**	**387.1**
Stdev. (psi)	524.98		
Max Diff. (psi)	-742.44		

Table A.3 – 1% fiber content data for TTT and TT testing with HiPer Fiber specimens labeled with the letters HP next to the stress ratio

Stress Ratio: 300-300

	Specimen Failure Stresses (psi)		
Specimen #	Sigma 1	Sigma 2	Sigma 3
1	919.9	308.5	311.8
2	1196.2	321.2	329.6
3	975.7	314.1	306.9
Avg. (psi)	**947.8**	**311.3**	**309.4**
Stdev. (psi)	39.41		
Max Diff. (psi)	55.74		

Stress Ratio: 300-300 HP

	Specimen Failure Stresses (psi)		
Specimen #	Sigma 1	Sigma 2	Sigma 3
1	1086.5	299.0	309.4
2	755.8	303.9	307.9
3	897.0	312.7	303.3
Avg. (psi)	**826.4**	**308.3**	**305.6**
Stdev. (psi)	99.81		
Max Diff. (psi)	141.16		

Stress Ratio: 500-250

	Specimen Failure Stresses (psi)		
Specimen #	Sigma 1	Sigma 2	Sigma 3
1	1216.1	499.7	258.9
2	997.9	511.7	265.7
3	1130.8	491.8	264.1
Avg. (psi)	**1114.9**	**501.1**	**262.9**
Stdev. (psi)	109.97		
Max Diff. (psi)	218.22		

Stress Ratio: 600-600

	Specimen Failure Stresses (psi)		
Specimen #	Sigma 1	Sigma 2	Sigma 3
1	1231.3	619.4	608.8
2	1193.8	618.5	620.1
3	1153.7	606.2	608.9
Avg. (psi)	**1193.0**	**614.7**	**612.6**
Stdev. (psi)	38.81		
Max Diff. (psi)	77.60		

Stress Ratio: 600-600 HP

	Specimen Failure Stresses (psi)		
Specimen #	Sigma 1	Sigma 2	Sigma 3
1	1257.8	578.5	569.7
2	1072.8	588.7	589.5
3	1085.8	564.9	598.6
Avg. (psi)	**1138.8**	**577.4**	**585.9**
Stdev. (psi)	103.22		
Max Diff. (psi)	171.97		

Stress Ratio: 700-700

	Specimen Failure Stresses (psi)		
Specimen #	Sigma 1	Sigma 2	Sigma 3
1	1237.6	702.4	681.9
2	-	-	-
3	1080.9	707.1	696.7
Avg. (psi)	**1159.2**	**704.7**	**689.3**
Stdev. (psi)	110.76		
Max Diff. (psi)	156.64		

Stress Ratio: 800-400

	Specimen Failure Stresses (psi)		
Specimen #	Sigma 1	Sigma 2	Sigma 3
1	1026.5	818.8	402.6
2	1262.0	808.3	430.3
3	975.5	804.1	428.5
Avg. (psi)	**1001.0**	**811.5**	**415.5**
Stdev. (psi)	36.06		
Max Diff. (psi)	51.00		

Stress Ratio: 800-800

	Specimen Failure Stresses (psi)		
Specimen #	Sigma 1	Sigma 2	Sigma 3
1	1316.6	755.6	808.1
2	1341.6	799.3	810.4
3	1152.3	773.7	800.1
Avg. (psi)	**1270.2**	**776.2**	**806.2**
Stdev. (psi)	102.80		
Max Diff. (psi)	189.23		

Stress Ratio: TT, Proportional

	Specimen Failure Stresses (psi)		
Specimen #	Sigma 1	Sigma 2	Sigma 3
1	-	807.7	838.9
2	-	669.6	669.0
3	-	822.5	818.8
Avg. (psi)		**766.6**	**775.6**
Stdev. (psi)		84.33	92.84
Max Diff. (psi)		152.91	169.92

Stress Ratio: TT, 450

	Specimen Failure Stresses (psi)		
Specimen #	Sigma 1	Sigma 2	Sigma 3
1	-	475.3	924.9
2	-	463.9	1141.3
3	-	453.5	1172.5
Avg. (psi)		**458.7**	**1156.9**
Stdev. (psi)			22.08
Max Diff. (psi)			31.23

Table A.4 – 1% fiber content data for TTC testing with HiPer Fiber specimens labeled with the letters HP next to the stress ratio

Stress Ratio: 200-200

	Specimen Failure Stresses (psi)		
Specimen #	Baldwin	Sigma 2	Sigma 3
1	-4266.7	202.4	202.2
2	-4890.3	198.2	198.9
3	-5457.4	185.4	196.2
Avg. (psi)	**-4871.5**	**195.3**	**199.1**
Stdev. (psi)	595.56		
Max Diff. (psi)	-1190.68		

Stress Ratio: 200-200 HP

	Specimen Failure Stresses (psi)		
Specimen #	Baldwin	Sigma 2	Sigma 3
1	-5081.8	195.6	189.1
2	-5715.8	201.8	197.1
3	-5829.1	193.0	192.9
Avg. (psi)	**-5542.2**	**196.8**	**193.0**
Stdev. (psi)	402.77		
Max Diff. (psi)	-747.30		

Stress Ratio: 300-300

	Specimen Failure Stresses (psi)		
Specimen #	Baldwin	Sigma 2	Sigma 3
1	-5868.7	279.2	301.0
2	-4138.0	289.4	306.1
3	-6737.7	275.3	280.7
Avg. (psi)	**-6303.2**	**277.2**	**290.9**
Stdev. (psi)	614.44		
Max Diff. (psi)	-868.95		

Stress Ratio: 400-400 HP

	Specimen Failure Stresses (psi)		
Specimen #	Baldwin	Sigma 2	Sigma 3
1	-2682.0	400.6	396.3
2	-3935.1	395.2	391.0
3	-2445.3	394.5	391.1
Avg. (psi)	**-3020.8**	**396.7**	**392.8**
Stdev. (psi)	800.60		
Max Diff. (psi)	-1489.77		

Stress Ratio: 450-450

	Specimen Failure Stresses (psi)		
Specimen #	Baldwin	Sigma 2	Sigma 3
1	-2323.3	447.2	460.0
2	-2284.0	448.0	454.7
3	-3382.6	444.2	439.7
Avg. (psi)	**-2663.3**	**446.5**	**451.4**
Stdev. (psi)	623.23		
Max Diff. (psi)	-1098.60		

Stress Ratio: 600-300

	Specimen Failure Stresses (psi)		
Specimen #	Baldwin	Sigma 2	Sigma 3
1	-2184.6	287.6	569.9
2	-3479.8	296.6	570.4
3	-3732.2	304.3	586.6
Avg. (psi)	**-3132.2**	**296.1**	**575.6**
Stdev. (psi)	830.27		
Max Diff. (psi)	-1547.57		

Stress Ratio: 600-600

	Specimen Failure Stresses (psi)		
Specimen #	Baldwin	Sigma 2	Sigma 3
1	-969.4	602.0	593.6
2	-	-	-
3	-2448.5	587.3	598.6
Avg. (psi)	**-1709.0**	**594.6**	**596.1**
Stdev. (psi)	1045.90		
Max Diff. (psi)	-1479.12		

Stress Ratio: 600-600 2			
	Specimen Failure Stresses (psi)		
Specimen #	Baldwin	Sigma 2	Sigma 3
1	-2733.4	613.9	602.5
2	-2964.0	615.0	606.5
3	-1057.6	615.8	608.1
Avg. (psi)	**-2848.7**	**614.5**	**604.5**
Stdev. (psi)	163.04		
Max Diff. (psi)	-230.58		

Table A.5 – 2% fiber content data for TTT and TT testing with HiPer Fiber specimens labeled with the letters HP next to the stress ratio

Stress Ratio: 300-300			
	Specimen Failure Stresses (psi)		
Specimen #	Sigma 1	Sigma 2	Sigma 3
1	1343.7	309.7	340.3
2	1249.7	293.1	312.5
3	1222.1	307.9	328.0
Avg. (psi)	**1271.8**	**303.6**	**326.9**
Stdev. (psi)	63.75		
Max Diff. (psi)	121.60		

Stress Ratio: 300-300 HP			
	Specimen Failure Stresses (psi)		
Specimen #	Sigma 1	Sigma 2	Sigma 3
1	1092.8	312.7	335.6
2	933.2	291.6	315.0
3	878.5	305.8	302.4
Avg. (psi)	**905.8**	**298.7**	**308.7**
Stdev. (psi)	38.72		
Max Diff. (psi)	54.76		

Stress Ratio: 500-250

	Specimen Failure Stresses (psi)		
Specimen #	Sigma 1	Sigma 2	Sigma 3
1	1017.8	507.8	252.9
2	1149.4	494.3	273.5
3	1096.7	491.7	264.0
Avg. (psi)	**1088.0**	**498.0**	**263.5**
Stdev. (psi)	66.22		
Max Diff. (psi)	131.58		

Stress Ratio: 600-200

	Specimen Failure Stresses (psi)		
Specimen #	Sigma 1	Sigma 2	Sigma 3
1	1090.9	588.5	228.0
2	1198.4	584.4	227.7
3	1134.5	588.9	227.4
Avg. (psi)	**1141.3**	**587.2**	**227.7**
Stdev. (psi)	54.04		
Max Diff. (psi)	107.46		

Stress Ratio: 600-600

	Specimen Failure Stresses (psi)		
Specimen #	Sigma 1	Sigma 2	Sigma 3
1	1340.5	617.2	614.5
2	1295.7	595.1	598.5
3	1193.5	595.7	612.1
Avg. (psi)	**1276.6**	**602.6**	**608.4**
Stdev. (psi)	75.33		
Max Diff. (psi)	146.96		

Stress Ratio: 600-600 HP

	Specimen Failure Stresses (psi)		
Specimen #	Sigma 1	Sigma 2	Sigma 3
1	1105.5	572.9	566.0
2	1329.2	597.0	587.4
3	1055.8	589.5	599.9
Avg. (psi)	**1080.7**	**581.2**	**582.9**
Stdev. (psi)	35.13		
Max Diff. (psi)	49.68		

Stress Ratio: 700-700

	Specimen Failure Stresses (psi)		
Specimen #	Sigma 1	Sigma 2	Sigma 3
1	1262.1	665.1	682.9
2	1048.6	675.7	701.0
3	1271.2	663.9	697.9
Avg. (psi)	**1266.7**	**664.5**	**690.4**
Stdev. (psi)	6.46		
Max Diff. (psi)	9.13		

Stress Ratio: 800-400

	Specimen Failure Stresses (psi)		
Specimen #	Sigma 1	Sigma 2	Sigma 3
1	1072.6	780.5	377.2
2	1215.7	779.6	417.4
3	1218.8	766.1	397.5
Avg. (psi)	**1169.1**	**775.4**	**397.4**
Stdev. (psi)	83.53		
Max Diff. (psi)	146.21		

Stress Ratio: 800-800

	Specimen Failure Stresses (psi)		
Specimen #	Sigma 1	Sigma 2	Sigma 3
1	1273.3	787.2	810.4
2	1196.2	796.2	815.4
3	1182.0	797.2	816.8
Avg. (psi)	**1217.2**	**793.5**	**814.2**
Stdev. (psi)	49.16		
Max Diff. (psi)	91.38		

Stress Ratio: TT, Proportional

	Specimen Failure Stresses (psi)		
Specimen #	Sigma 1	Sigma 2	Sigma 3
1	-	848.5	890.3
2	-	876.2	840.5
3	-	801.4	784.7
Avg. (psi)		**842.0**	**838.5**
Stdev. (psi)		37.79	52.83
Max Diff. (psi)		74.73	105.60

Stress Ratio: TT, 450

	Specimen Failure Stresses (psi)		
Specimen #	Sigma 1	Sigma 2	Sigma 3
1	-	493.2	1090.7
2	-	-	-
3	-	524.7	997.7
Avg. (psi)		**509.0**	**1044.2**
Stdev. (psi)			65.77
Max Diff. (psi)			93.02

Table A.6 – 2% fiber content data for TTC testing with HiPer Fiber specimens labeled with the letters HP next to the stress ratio

Stress Ratio: 300-300

	Specimen Failure Stresses (psi)		
Specimen #	Baldwin	Sigma 2	Sigma 3
1	-3431.0	307.7	318.6
2	-2528.8	303.8	302.6
3	-3011.7	299.9	303.7
Avg. (psi)	**-2990.5**	**303.8**	**308.3**
Stdev. (psi)	451.49		
Max Diff. (psi)	-902.24		

Stress Ratio: 300-300 2

	Specimen Failure Stresses (psi)		
Specimen #	Baldwin	Sigma 2	Sigma 3
1	-3040.7	297.1	313.7
2	-2541.1	299.7	306.2
3	-2806.7	301.1	314.5
Avg. (psi)	**-2796.2**	**299.3**	**311.5**
Stdev. (psi)	249.96		
Max Diff. (psi)	-499.59		

Stress Ratio: 300-300 HP

	Specimen Failure Stresses (psi)		
Specimen #	Baldwin	Sigma 2	Sigma 3
1	-2218.7	289.2	289.6
2	-1762.5	304.0	311.8
3	-1801.5	293.5	304.6
Avg. (psi)	**-1927.6**	**295.6**	**302.0**
Stdev. (psi)	252.85		
Max Diff. (psi)	-456.15		

Stress Ratio: 300-300 HP 2

	Specimen Failure Stresses (psi)		
Specimen #	Baldwin	Sigma 2	Sigma 3
1	-4556.5	284.9	309.9
2	-5069.7	300.4	299.3
3	-5018.6	301.9	294.4
Avg. (psi)	**-4881.6**	**295.7**	**301.2**
Stdev. (psi)	282.69		
Max Diff. (psi)	-513.17		

Stress Ratio: 450-450

	Specimen Failure Stresses (psi)		
Specimen #	Baldwin	Sigma 2	Sigma 3
1	-3869.7	435.9	476.5
2	-3778.6	448.5	438.9
3	-4794.8	438.6	451.6
Avg. (psi)	**-4147.7**	**441.0**	**455.7**
Stdev. (psi)	562.26		
Max Diff. (psi)	-1016.18		

Stress Ratio: 600-300

	Specimen Failure Stresses (psi)		
Specimen #	Baldwin	Sigma 2	Sigma 3
1	-2363.6	316.2	592.0
2	-2537.1	297.5	585.0
3	-4377.6	297.2	582.1
Avg. (psi)	**-2450.3**	**306.8**	**588.5**
Stdev. (psi)	122.66		
Max Diff. (psi)	-173.47		

Stress Ratio: 600-600

	Specimen Failure Stresses (psi)		
Specimen #	Baldwin	Sigma 2	Sigma 3
1	-1633.8	596.8	602.1
2	-2701.0	603.1	591.9
3	-3246.2	588.5	594.7
Avg. (psi)	**-2973.6**	**595.8**	**593.3**
Stdev. (psi)	385.49		
Max Diff. (psi)	-545.17		

Stress Ratio: 600-600 2

	Specimen Failure Stresses (psi)		
Specimen #	Baldwin	Sigma 2	Sigma 3
1	-1956.6	606.8	589.5
2	-2543.2	611.3	586.2
3	-	-	-
Avg. (psi)	**-2249.9**	**609.0**	**587.9**
Stdev. (psi)	414.78		
Max Diff. (psi)	-586.59		

Stress Ratio: 600-600 HP

	Specimen Failure Stresses (psi)		
Specimen #	Baldwin	Sigma 2	Sigma 3
1	-1833.2	597.9	587.5
2	-591.8	558.0	581.8
3	-1627.1	597.8	606.4
Avg. (psi)	**-1730.1**	**597.8**	**597.0**
Stdev. (psi)	145.76		
Max Diff. (psi)	-206.13		

Stress Ratio: 600-600 HP 2

	Specimen Failure Stresses (psi)		
Specimen #	Baldwin	Sigma 2	Sigma 3
1	-	-	-
2	-3960.1	598.8	589.8
3	-3074.2	602.6	609.5
Avg. (psi)	**-3517.2**	**600.7**	**599.7**
Stdev. (psi)	626.44		
Max Diff. (psi)	-885.92		

Stress Ratio: 700-700

	Specimen Failure Stresses (psi)		
Specimen #	Baldwin	Sigma 2	Sigma 3
1	-	-	-
2	-1092.8	695.6	713.2
3	-1832.8	714.3	696.3
Avg. (psi)	**-1462.8**	**704.9**	**704.7**
Stdev. (psi)	523.26		
Max Diff. (psi)	-740.00		

Table A.7 – 4% fiber content data for TTT and TT testing with HiPer Fiber specimens labeled with the letters HP next to the stress ratio

Stress Ratio: 200-200

	Specimen Failure Stresses (psi)		
Specimen #	Sigma 1	Sigma 2	Sigma 3
1	1180.5	193.6	219.0
2	1303.5	202.4	220.5
3	1139.5	218.2	214.1
Avg. (psi)	**1207.8**	**204.7**	**217.9**
Stdev. (psi)	85.35		
Max Diff. (psi)	164.02		

Stress Ratio: 500-200

	Specimen Failure Stresses (psi)		
Specimen #	Sigma 1	Sigma 2	Sigma 3
1	1401.2	507.8	223.6
2	1389.1	496.1	225.7
3	1341.5	497.1	222.9
Avg. (psi)	**1377.3**	**500.3**	**224.0**
Stdev. (psi)	31.56		
Max Diff. (psi)	59.72		

Stress Ratio: 600-300

	Specimen Failure Stresses (psi)		
Specimen #	Sigma 1	Sigma 2	Sigma 3
1	1403.1	613.8	313.1
2	1305.5	576.3	340.6
3	1351.2	597.2	337.9
Avg. (psi)	**1353.3**	**595.8**	**330.5**
Stdev. (psi)	48.81		
Max Diff. (psi)	97.56		

Stress Ratio: 600-600

	Specimen Failure Stresses (psi)		
Specimen #	Sigma 1	Sigma 2	Sigma 3
1	1314.5	578.2	617.8
2	-	-	-
3	1442.1	589.7	607.2
Avg. (psi)	**1378.3**	**584.0**	**612.5**
Stdev. (psi)	90.17		
Max Diff. (psi)	127.52		

Stress Ratio: 400-400

	Specimen Failure Stresses (psi)		
Specimen #	Sigma 1	Sigma 2	Sigma 3
1	1455.5	400.5	415.0
2	1307.8	408.7	428.6
3	1213.1	401.0	426.2
Avg. (psi)	**1260.5**	**404.8**	**427.4**
Stdev. (psi)	66.90		
Max Diff. (psi)	94.62		

Stress Ratio: 400-400 HP

	Specimen Failure Stresses (psi)		
Specimen #	Sigma 1	Sigma 2	Sigma 3
1	1119.1	393.3	425.4
2	991.2	396.5	413.3
3	1130.7	399.9	427.4
Avg. (psi)	**1080.3**	**396.6**	**422.0**
Stdev. (psi)	77.42		
Max Diff. (psi)	139.50		

Stress Ratio: 700-700 HP

	Specimen Failure Stresses (psi)		
Specimen #	Sigma 1	Sigma 2	Sigma 3
1	1346.2	681.2	690.2
2	1319.1	711.0	703.7
3	1100.1	682.0	723.5
Avg. (psi)	**1332.6**	**696.1**	**696.9**
Stdev. (psi)	19.17		
Max Diff. (psi)	27.11		

Stress Ratio: 800-500

	Specimen Failure Stresses (psi)		
Specimen #	Sigma 1	Sigma 2	Sigma 3
1	1200.1	783.1	498.1
2	1209.1	806.9	529.1
3	1353.5	809.4	532.4
Avg. (psi)	**1254.2**	**799.8**	**519.9**
Stdev. (psi)	86.07		
Max Diff. (psi)	153.40		

Stress Ratio: 800-800

	Specimen Failure Stresses (psi)		
Specimen #	Sigma 1	Sigma 2	Sigma 3
1	-	-	-
2	1195.6	814.3	842.9
3	886.0	814.8	821.9
Avg. (psi)	**1040.8**	**814.6**	**832.4**
Stdev. (psi)	218.95		
Max Diff. (psi)	309.64		

Stress Ratio: 800-800 2

	Specimen Failure Stresses (psi)		
Specimen #	Sigma 1	Sigma 2	Sigma 3
1	1260.3	762.2	771.2
2	1217.5	759.5	771.0
3	1094.2	787.2	824.9
Avg. (psi)	**1190.7**	**769.7**	**789.0**
Stdev. (psi)	86.23		
Max Diff. (psi)	166.06		

Stress Ratio: TT, Proportional

	Specimen Failure Stresses (psi)		
Specimen #	Sigma 1	Sigma 2	Sigma 3
1	-	979.2	1007.1
2	-	876.2	897.0
3	-	791.9	804.0
Avg. (psi)		**927.7**	**952.1**
Stdev. (psi)		72.78	77.87
Max Diff. (psi)		102.92	110.12

Stress Ratio: TT, 600

	Specimen Failure Stresses (psi)		
Specimen #	Sigma 1	Sigma 2	Sigma 3
1	-	588.1	1115.2
2	-	610.2	1186.4
3	-	603.7	1218.7
Avg. (psi)		**600.7**	**1173.4**
Stdev. (psi)			52.95
Max Diff. (psi)			103.48

Table A.8 – 4% fiber content data for TTC testing with HiPer Fiber specimens labeled with the letters HP next to the stress ratio

Stress Ratio: 300-300

	Specimen Failure Stresses (psi)		
Specimen #	Baldwin	Sigma 2	Sigma 3
1	-4793.9	300.7	302.4
2	-8805.0	284.7	300.3
3	-4950.3	300.9	302.8
Avg. (psi)	**-4872.1**	**300.8**	**302.6**
Stdev. (psi)	110.56		
Max Diff. (psi)	-156.36		

Stress Ratio: 300-300 2

	Specimen Failure Stresses (psi)		
Specimen #	Baldwin	Sigma 2	Sigma 3
1	-5871.2	285.7	306.2
2	-2722.5	298.2	307.7
3	-7199.1	302.0	313.3
Avg. (psi)	**-6535.1**	**293.9**	**309.8**
Stdev. (psi)	938.98		
Max Diff. (psi)	-1327.92		

Stress Ratio: 300-300 HP

	Specimen Failure Stresses (psi)		
Specimen #	Baldwin	Sigma 2	Sigma 3
1	-4669.8	296.1	310.9
2	-4274.2	304.0	312.7
3	-3271.6	299.8	296.7
Avg. (psi)	**-4071.9**	**300.0**	**306.8**
Stdev. (psi)	720.71		
Max Diff. (psi)	-1398.19		

Stress Ratio: 400-400

	Specimen Failure Stresses (psi)		
Specimen #	Baldwin	Sigma 2	Sigma 3
1	-5508.4	390.6	382.8
2	-5171.7	371.0	388.8
3	-2400.1	391.3	416.3
Avg. (psi)	**-5340.1**	**380.8**	**385.8**
Stdev. (psi)	238.13		
Max Diff. (psi)	-336.76		

Stress Ratio: 700-350

	Specimen Failure Stresses (psi)		
Specimen #	Baldwin	Sigma 2	Sigma 3
1	-2439.0	347.0	698.1
2	-2275.4	347.8	697.3
3	-4044.2	340.1	694.6
Avg. (psi)	**-2357.2**	**347.4**	**697.7**
Stdev. (psi)	115.68		
Max Diff. (psi)	-163.60		

Stress Ratio: 700-700

	Specimen Failure Stresses (psi)		
Specimen #	Baldwin	Sigma 2	Sigma 3
1	-	-	-
2	-2370.3	703.8	684.6
3	-543.3	708.6	705.6
Avg. (psi)	**-1456.8**	**706.2**	**695.1**
Stdev. (psi)	1291.86		
Max Diff. (psi)	-1826.97		

Stress Ratio: 700-700 HP

	Specimen Failure Stresses (psi)		
Specimen #	Baldwin	Sigma 2	Sigma 3
1	-1803.8	695.5	713.6
2	-1266.2	704.5	705.5
3	-1221.5	704.5	695.5
Avg. (psi)	**-1430.5**	**701.5**	**704.9**
Stdev. (psi)	324.03		
Max Diff. (psi)	-582.22		

Table A.9 – 5% fiber content data for TTT testing

Stress Ratio: 600-300

	Specimen Failure Stresses (psi)		
Specimen #	Sigma 1	Sigma 2	Sigma 3
1	1121.4	596.8	319.0
2	1129.4	600.4	328.5
3	959.6	593.6	320.7
Avg. (psi)	**1125.4**	**598.6**	**323.8**
Stdev. (psi)	5.64		
Max Diff. (psi)	7.98		

Stress Ratio: 600-600

	Specimen Failure Stresses (psi)		
Specimen #	Sigma 1	Sigma 2	Sigma 3
1	1131.1	606.8	607.4
2	1201.8	584.5	600.3
3	986.4	606.9	610.2
Avg. (psi)	**1166.4**	**595.7**	**603.8**
Stdev. (psi)	49.99		
Max Diff. (psi)	70.70		

Stress Ratio: 800-800

	Specimen Failure Stresses (psi)		
Specimen #	Sigma 1	Sigma 2	Sigma 3
1	1131.1	606.8	607.4
2	1201.8	584.5	600.3
3	986.4	606.9	610.2
Avg. (psi)	**1166.4**	**595.7**	**603.8**
Stdev. (psi)	49.99		
Max Diff. (psi)	70.70		

Stress Ratio: 900-900

	Specimen Failure Stresses (psi)		
Specimen #	Sigma 1	Sigma 2	Sigma 3
1	-	-	-
2	927.2	893.7	909.0
3	-	-	-
Avg. (psi)	**927.2**	**893.7**	**909.0**
Stdev. (psi)	-		
Max Diff. (psi)	-		

Table A.10 – 6% fiber content data for TTT testing

Stress Ratio: 400-400

	Specimen Failure Stresses (psi)		
Specimen #	Sigma 1	Sigma 2	Sigma 3
1	1205.6	421.9	411.5
2	1210.9	394.5	419.8
3	1188.5	407.2	405.5
Avg. (psi)	**1201.7**	**407.8**	**412.3**
Stdev. (psi)	11.70		
Max Diff. (psi)	22.38		

Stress Ratio: 600-300

	Specimen Failure Stresses (psi)		
Specimen #	Sigma 1	Sigma 2	Sigma 3
1	988.4	587.3	322.3
2	1114.4	584.1	331.9
3	1173.1	599.4	312.8
Avg. (psi)	**1143.7**	**591.7**	**322.3**
Stdev. (psi)	41.49		
Max Diff. (psi)	58.67		

Stress Ratio: 800-800

	Specimen Failure Stresses (psi)		
Specimen #	Sigma 1	Sigma 2	Sigma 3
1	1252.2	820.8	817.0
2	1016.0	828.6	810.6
3	1034.0	812.2	799.1
Avg. (psi)	**1025.0**	**820.4**	**804.8**
Stdev. (psi)	12.72		
Max Diff. (psi)	17.99		

Stress Ratio: 900-900

	Specimen Failure Stresses (psi)		
Specimen #	Sigma 1	Sigma 2	Sigma 3
1	1132.3	884.5	915.8
2	1252.5	889.2	901.7
3	761.1	900.6	912.9
Avg. (psi)	**1192.4**	**886.8**	**908.8**
Stdev. (psi)	84.96		
Max Diff. (psi)	120.15		

BIBLIOGRAPHY

AISC (American Institute of Steel Construction). 2011. *Steel Construction Manual*. 14th Edition. Chicago, IL: AISC.

Alsalman, A., Dang, C.N., Hale, W.M. 2017. "Development of Ultra-High Performance Concrete With Locally Available Materials." *Construction and Building Materials*, V. 133, pp. 135-145.

ASTM Standard A193/A193M. 2020. "Standard Specification for Alloy-Steel and Stainless Steel Bolting for High Temperature or High Pressure Service and Other Special Purpose Applications." ASTM International, West Conshohocken, PA.

ASTM Standard B209. 2014. "Standard Specification for Aluminum and Aluminum-Alloy Sheet and Plate." ASTM International, West Conshohocken, PA.

ASTM Standard B221. 2020. "Standard Specification for Aluminum and Aluminum-Alloy Extruded Bars, Rods, Wire, Profiles, and Tubes." ASTM International, West Conshohocken, PA.

ASTM Standard C109/C109M. 2020b. "Standard Test Methods for Compressive Strength of Hydraulic Cement Mortars (Using 2-in. or [50 mm] Cube Specimens)." ASTM International, West Conshohocken, PA.

ASTM Standard C1609/C1609M. 2012. "Standard Test Methods for Flexural Performance of Fiber-Reinforced Concrete (Using Beam With Third-Point Loading)." ASTM International, West Conshohocken, PA.

ASTM Standard C1856/C1856M. 2017. "Standard Practice for Fabricating and Testing Specimens for Ultra-High Performance Concrete." ASTM International, West Conshohocken, PA.

ASTM Standard E8/E8M. 2009. “Standard Test Methods for Tension Testing of Metallic Materials.” ASTM International, West Conshohocken, PA.

ASTM Standard E8/E8M. 2021. “Standard Test Methods for Tension Testing of Metallic Materials.” ASTM International, West Conshohocken, PA.

ASTM Standard E691. 2020. “Standard Practice for Conducting an Interlaboratory Study to Determine the Precision of a Test Method.” ASTM International, West Conshohocken, PA.

Campos, R. 2021. “Effect of Fiber Content on Tensile Strength of Non-Proprietary Ultra High Performance Concrete.” M.S. Thesis, The University of Oklahoma, Norman, OK.

Chen, L., Graybeal, B.A. 2012. “Modeling Structural Performance of Ultrahigh Performance Concrete I-Girders.” *Journal of Bridge Engineering*, V. 17(5), pp. 754-764.

Cortese, L., Coppola, T., Campanelli, F., Broggiato, G.B. 2016. “A J2-J3 Approach in Plastic and Damage Description of Ductile Materials.” *International Journal of Damage Mechanics*, V. 25(2), pp. 228-250.

D’Alessandro, K., Robert-Wollmann, C., Cousins, T., Sotelino, E. 2013. “Investigation of Biaxial Stress States of UHPC Bridge Girders Through Small Panel Testing and Finite Element Analysis,” *Designing and Building with UHPFRC*, Chapter 42, pp. 619-637.

Drucker, D.C., Prager, W. 1952. “Soil Mechanics and Plastic Analysis or Limit Design.” *Quarterly of Applied Mechanics*, V. 10, pp. 157-165.

El-Tawil, S., Tai, Y.S., Belcher II, J.A., Rogers, D. 2020. “Open-Recipe Ultra-High-Performance Concrete.” *Concrete Internataionl,* June 2020, pp. 33-38.

eConstruct-WJE-UNL-NCSU. 2020. “implementation of Ultra-High-Performance Concrete in Long-Span Precast Pretensioned Elements for Concrete Buildings and Bridges: Phase I Report.” eConstruct USA, LLC Phase I Report, January 2020.

Engineers Edge. 2021. “Fastener Bolt Thread Stress Tensile Area Table Chart.” Accessed May 1, 2021. https://www.engineersedge.com/fastener_thread_stress_area.htm.

Fehling, E., Leutbecher, T., Roder, F.K., Sturwald, S. 2008. “Structural Behavior of UHPC under Biaxial Loading,” *Structural Materials and Engineering Series No. 10*, Kassel University Press, pp 569-576.

Funk, J.E., Dinger, D.R. 1994. “Predictive Process Control of Crowded Particulate Suspensions.” *Applied to Ceramic Manufacturing,* V. 24(6), pp. 997-1009.

Graybeal, B. 2019. “Design and Construction of Field-Cast UHPC Connections.” FHWA-HRT-19-011.

Graybeal, B.A., Baby, F. 2013. “Development of Direct Tension Test Method of Ultra-High Performance Fiber-Reinforced Concrete.” *ACI Materials Journal,* V. 110(2), pp. 177-186.

Graybeal, B., Davis, M. 2008. “Cylinder or Cube: Strength Testing of 80 to 200 MPa (11.6 to 29 ksi) Ultra-High-Performance Fiber-Reinforced Concrete.” *ACI Materials Journal*, V. 105(6), pp. 603-609.

Haber, Z.B., De la Varga, I., Graybeal, B.A., Nakashoji, B., El-Helou, R. 2018 “Properties and Behavior of UHPC-Class Materials.” FHWA-HRT-18-036.

Haber, Z.B., Munoz, J.F., Graybeal, B.A. 2017. “Field Testing of an Ultra-High Performance Concrete Overlay.” FHWA-HRT-17-096.

Hoek, E., Brown, E.T. 1980. “Empirical Strength Criterion for Rock Masses.” *Journal of the Geotechnical Engineering Division,* V. 106(GT9), pp. 1013-1035.

Kotsovos, M.D. 2015. *Finite-Element Modelling of Structural Concrete: Short-Term Static and Dynamic Loading Conditions*. Boca Raton, FL: CRC Press.

Kupfer, H., Hilsdorf, H.K., Rusch, H. 1969. “Behavior of Concrete Under Biaxial Stresses.” *ACI Journal,* V. 66(8), pp. 656-666.

Kwak, H.G., Na, C.K., Kim, S.W., Kang, S.T. 2009. “Nonlinear Analysis of Ultra Strength Concrete RC Structure.” *Excellence in Concrete Construction through Innovation – Limbachiya & Kew (eds),* Taylor & Francis Group, London, pp. 31-36.

Lee, J.H., Hong, S.G., Joh, C., Kwahk, I., Lee, J.W. 2017. “Biaxial Tension-Compression Strength Beahviour of UHPFRC In-Plane Elements,” *Materials and Structures,* 50:20, pp. 1-17.

Lepissier, K.J.G. 2020. “Tensile Behavior of Ultra-High Performance Concrete Under Direct Tension.” M.S. Thesis, The University of Oklahoma, Norman, OK.

Looney, T., Coleman, R., Funderburg, C., Volz, J., Floyd, R. 2020. “Concrete Bond and Behavior of Nonproprietary Ultrahigh-Performance Concrete Bridge Slab Joints.” *Journal of Bridge Engineering,* V. 26(2).

Looney, T., McDaniel, A., Volz, J., Floyd, R. 2019. "Development and Characterization of Ultra-High Performance Concrete with Slag Cement for Use as Bridge Joint Material." *British Journal of Civil and Architecture Engineering,* V. 1(2).

McDaniel, A.S. 2017. “Development of Non-Proprietary Ultra-High-Performance Concrete Mix Designs.” M.S. Thesis, The University of Oklahoma, Norman, OK.

Menétrey, P., Willam, K.J. 1995. “Traixial Failure Criteria for Concrete and Its Generalization.” *ACI Structural Journal*, May-June, pp. 311-318.

Ottosen, N.S. 1977. “A Failure Criterion for Concrete.” *Journal of the Engineering Mechanics Division*, V. 103(4), pp. 527-535.

Ritter, R., Curbach, M. 2015. “Material Behavior of Ultra-High-Strength Concrete Under Multiaxial Stress States.” *ACI Materials Journal*, Sept.-Oct., pp. 641-652.

Ritter, R., Curbach, M. 2016. “Shape of Hypersurface of Concrete Under Multiaxial Loading.” *ACI Materials Journal*, Jan.-Feb., pp. 55-65.

Russell, H.G., Graybeal, B.A. 2013. “Ultra-High Performance Concrete: A State-of-the-Art Report for the Bridge Community.” FHWA-HRT-13-060.

SAE Standard J429. 2014. “Mechanical and Material Requirements for Externally Threaded Fasteners.” SAE International, Warrendale, PA.

Savino, V., Lanzoni, L., Tarantino, A.M., Viviani, M. 2018. “Tensile Constitutive Behavior of High and Ultra-High Performance Fibre-Reinforced-Concretes,” *Construction and Building Materials*, V. 186, pp. 525-536.

Wang, Y.B., Liew, J.Y.R., Lee, S.C, Xiong, D.X. 2016. “Experimental Study on Ultra-Higher-Strength Concrete Under Triaxial Compression,” *ACI Materials Journal*, Jan.-Feb., pp. 105-112.

Wang, Y.Z., Wang, Y.B., Zhao, Y.Z., Li, G.Q., Lyu, Y.F., Li, H. 2020. “Experimental Study on Ultra-Higher Performance Concrete Under Triaxial Compression.” *Construction and Building Materials*, V. 263.

Wibowo, W., Sritharan, S. 2018. “Use of Ultra-High-Performance Concrete for Bridge Deck Overlays.” IHRB Project TR-683 Report, SPR RB30-015.

Wille, K., Boisvert-Cotulio, C. 2013. “Development of Non-Proprietary Ultra-High Performance Concrete for Use in the Highway Bridge Sector.” FHWA-HRT-13-100.

Wille, K., El-Tawil, S., Naaman, A.E. 2014. “Properties of Strain Hardening Ultra High Performance Concrete (UHP-FRC) Under Direct Tensile Loading.” *Cement and Concrete Composites*, V. 48, pp. 53-66.

Williams, E.M., Graham, S.S., Akers, S.A., Reed, P.A., Rushing, T.S. 2009. “Mechanical Properties of a Baseline UHPC With and Without Steel Fibers,” *WIT Transactions on Engineering Sciences*, V. 64, pp. 93-104.

VITA

Trevor Looney received his Bachelor of Science degree with Summa Cum Laude honors and his Master of Science degree both in civil engineering from the Missouri University of Science and Technology in 2010 and 2012, respectively. Looney worked towards his master's degree under Dr. Jeffery Volz on the effects of bond strength of high-volume fly ash concrete and self-consolidating concrete for infrastructure applications. Upon graduation, he will go on to work at the U.S. Army Corps of Engineers Engineer Research and Development Center in the Concrete and Materials Branch of the Geotechnical and Structures Laboratory.